QUANTUM LIQUIDS AND QUANTUM CRYSTALS

Concentration dependence of the diffusion coefficient in separating dilute solid mixtures of ^{4}He in ^{3}He

V. N. Grigor'ev, V. A. Maĭdanov, A. A. Penzev, É. Ya. Rudavskiĭ, A. S. Rybalko, and Ye. V. Syrnikov*

B. Verkin Institute for Low Temperature Physics and Engineering, National Academy of Sciences of Ukraine, pr. Lenina 47, 61103 Kharkov, Ukraine

(Submitted May 6, 2003)
Fiz. Nizk. Temp. **29**, 1165–1172 (November 2003)

The kinetics of the separation of dilute solid mixtures of ^{4}He in ^{3}He is investigated in the ranges of temperature 100–200 mK, ^{4}He concentration $x=2.2-3.3\%$, and pressure 32–35 bar. It is found that the characteristic time τ required for the separating mixture to come to equilibrium depends substantially on the degree of supercooling. When the mixture is supercooled by more than 40–50 mK relative to the separation temperature of the initial mixture, the characteristic time $\tau<10^3$ s and remains practically unchanged as the temperature is lowered further. At low supercoolings the values of τ reach 4×10^4 s and decrease noticeably with further decrease in temperature. A relation between the measured values of τ and the effective coefficient of mass diffusion is established using the solution of the diffusion problem with allowance for the surface resistance arising when the ^{4}He impurity atoms leave the solution and enter new-phase inclusions. It is shown that an adequate description of the experimental data in the framework of the kinetic theory of tunneling transport of impurities under conditions of an appreciable interaction between them can be obtained under the assumption that the diffusion coefficient of ^{4}He in ^{3}He is proportional to $x^{-4/3}$. The concentration of nuclei and the average size of the region associated to each nucleus are determined. Analysis of the experimental results on the kinetics of nucleation in phase separation shows that they can be explained by the theory of homogeneous nucleation. The values thus obtained for the coefficient of interphase surface tension agree with the existing data. The relaxation time due to the finite resistance to the penetration of an impurity through the boundary between the matrix and new-phase inclusion is determined for the first time. © *2003 American Institute of Physics.*
[DOI: 10.1063/1.1614231]

1. INTRODUCTION

Rather detailed information has by now been obtained about diffusion processes in dilute solid mixtures of ^{3}He in ^{4}He, and practically all the laws of quantum diffusion predicted by Andreev and Lifshits[1] and in a number of subsequent papers[2–5] have been observed. This is made possible by the nonzero nuclear spin of ^{3}He, which allows one to track its motion by means of nuclear magnetic resonance (NMR). The ^{4}He atom does not have nuclear spin, and information about the character of its motion can only be extracted from indirect data. Recently developed methods of quantitative analysis of the kinetics of decomposition of solid solutions at low temperatures[6,7] alter that situation and make it possible to study the diffusion mechanism for mixtures of ^{4}He in ^{3}He as well.

One of the interesting problems in this area is to explore how the motion of the impurities is influenced by the elastic fields that arise in the crystal because of the noticeable difference in the amplitudes of zero-point vibrations of the ^{3}He and ^{4}He atoms and which give rise to an interaction between impurities. For ^{3}He impurities in ^{4}He this problem was considered theoretically in Refs. 8–10 for impurity concentrations large enough that their interaction must be taken into account, and the following concentration dependence of the diffusion coefficient D was predicted:

$$D\sim x^{-4/3}. \tag{1}$$

Relation (1) is in fact the only one of the predicted quantum diffusion relations that has not found confirmation in experiment. The reason is that for mixtures of ^{3}He in ^{4}He this relation holds in an extremely narrow interval of concentrations between the region of band motion of the impurities, where $D\sim x^{-1}$, and the region of self-trapping of impurity excitations, where D is a rapidly falling function. In addition, a dependence $D\sim x^{-4/3}$ is very close to the relation $D\sim x^{-1}$ that obtains at sufficiently low values of x.

It is remarkable that in deriving relation (1), Andreev[8] proceeded from a band picture of the impurity motion while both Landesman[9] and Sacco and Widom[10] considered an incoherent tunneling motion of the impurities, but nevertheless the same result was obtained in all cases:

$$D_x=A\frac{J^2a^2}{V_0x^{4/3}}, \tag{2}$$

where J is the exchange integral for impurity ^{3}He in ^{4}He, a is the distance between nearest neighbors, V_0 is the amplitude of the elastic interaction of impurities, and A is a numerical coefficient for which the expression $A=(16/3)\Gamma(4/3)(8.77)^{-4/3}\approx 0.26$ was obtained in Ref. 9 (here $\Gamma(x)$ is the gamma function). The agreement of the results of Ref. 8 with Refs. 9 and 10 gives us grounds to assume that relation (2) is universal for all cases in which it is necessary to take into account the slowing of the diffusional motion due to the disturbing of the energy levels of the impurities in neighboring lattice sites as a result of the interaction between impurities, and, in particular, it may be used in treating the diffusion of ^{4}He in ^{3}He.

It is known that the random distribution of nuclear spins at temperatures below the nuclear ordering temperature in solid ^{3}He make band motion of the impurities impossible, and therefore ^{4}He atoms in ^{3}He move by random tunneling hops. Motion by this mechanism leads to a diffusion coefficient that is independent of temperature and, at low enough concentrations, independent of concentration as well. Of course, against such a background it is much easier to detect dependence (2), and it is quite promising to look for it in mixtures of ^{4}He in ^{3}He.

2. EXPERIMENTAL TECHNIQUE

In this paper we report an experimental study of the kinetics of separation of dilute solid mixtures of ^{4}He in ^{3}He in the temperature interval 100–200 mK at pressures of 33–35 bar. A method of precision measurement of the change in pressure in the sample upon a stepwise lowering of the temperature is used. The change in pressure ΔP is uniquely related to the change in concentration Δx of the matrix by the Mullin relation.[11] At low concentrations

$$\Delta x = 2.5 V_\mu \beta \Delta P, \tag{3}$$

where V_μ and β are the molar volume (cm^3/mole) and compressibility of the sample.

The samples studied were in the form of disks 9 mm in diameter and 1.5 mm in height and were grown by the the capillary blocking method from an initial mixture containing $x_0=2\%$ ^{4}He. The ^{4}He content in the grown sample was refined with the aid of Eq. (3) from the value of ΔP_0 corresponding to phase separation of the mixture into pure components. After growth the samples were subjected to a kind of heat treatment by repeated temperature cycling in the interval 100–270 mK. It had been established in previous studies that this produces high-quality, uniform samples on which reproducible results can be obtained. In particular, upon the subsequent phase separation of such samples it was possible to obtain impurity concentrations in the matrix which correspond within the error limits to the equilibrium phase diagram.[12] The method of preparing the samples and the measurement technique are described in more detail in Ref. 7.

The samples obtained in this way were subjected to a stepwise cooling in which the pressure in the sample was measured at each step. The change in pressure $P(t)$ was of an exponential character and was described by a dependence

$$P_f - P(t) = (P_f - P_i)\exp(-t/\tau), \tag{4}$$

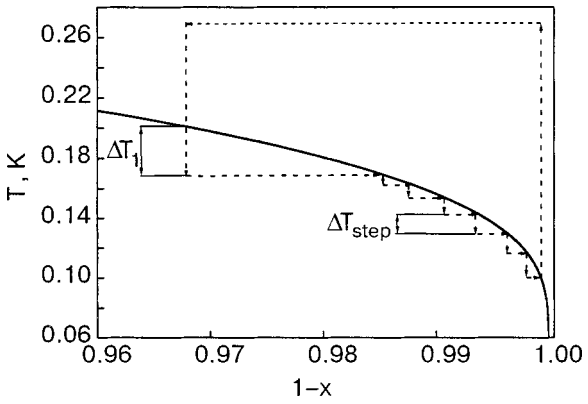

FIG. 1. Diagram of the experimental procedure. The solid curve is a part of the phase diagram according to the data of Edwards and Balibar[23] for $P=33$ bar.

where P_i and P_f are the initial and final (equilibrium) pressure in the sample. The values of P_f and of the characteristic time τ were found by computer processing.

The first steps, corresponding to cooling from the uniform mixture region, had values of ΔT_1 varying from 5 to $\sim$100 mK, while the subsequent steps were 10–15 mK (see Fig. 1). It was found that for ΔT_1 values exceeding 40–50 mK the characteristic time τ was $\sim$500–700 s and remained practically constant as the temperature was lowered further. For small values of ΔT_1 the characteristic time τ was significantly greater, up to 4×10^4 s. Also, in that case a significant decrease of τ in subsequent steps was observed. Figure 2 shows the time dependence of the relative change in pressure in different successive steps for one of the samples at a small value $\Delta T_1=26$ mK. A noticeable increase in the rate of approach to equilibrium with decreasing temperature may be seen, especially at high temperatures.

3. RELATION OF THE SEPARATION TIME CONSTANT TO THE DIFFUSION COEFFICIENT

The presence of short, temperature-independent times τ was noted previously[13] by the authors in connection with the situation when ^{4}He clusters are formed around vacancies in a ^{3}He matrix. It was conjectured[13] that such behavior arises

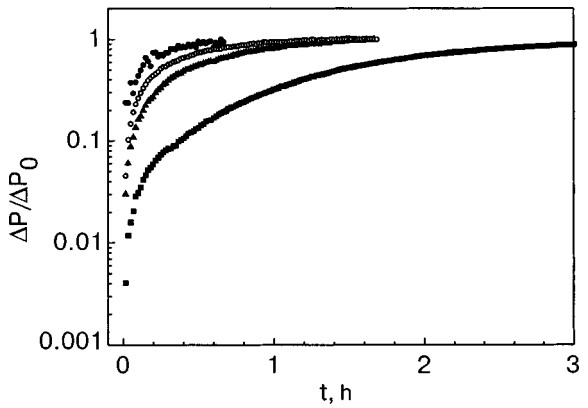

FIG. 2. Dependence of the relative change in pressure with time for a sample with $x_0=3.34\%$ ^{4}He, $V_\mu=24.2$ cm^3/mole, and $\Delta T_1=26$ mK at different temperatures T_i and T_f [mK]: 221 and 195 (■); 195 and 185 (▲); 175 and 162 (○); 121 and 107 (●).

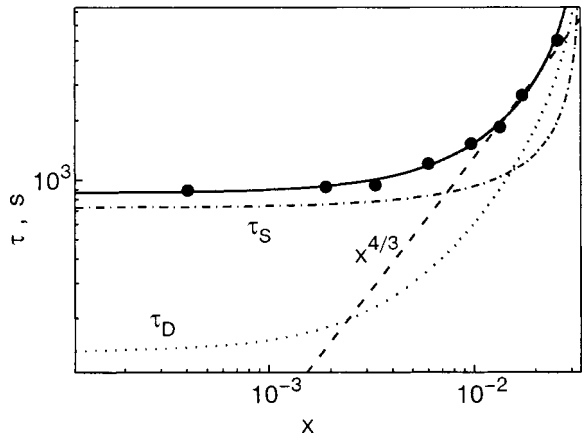

FIG. 3. Dependence of the characteristic separation time on the ^{4}He concentration: experimental points (●); $\tau \sim x^{4/3}$ (---); τ_D [Eq. (12)] (...); τ_S [Eq. (13)] (–·–); Eq. (11) (—).

because the probability that an impurity atom arriving at the boundary will penetrate into the cluster is less than unity. It is natural to assume that a similar situation can arise in the present case as well if the concentration of new-phase nuclei is large enough that the diffusive transport time is less than the time spent by an atom on the surface of a nucleus. Such a picture should obtain at high degrees of supersaturation under conditions of homogeneous nucleation; arguments supporting the existence of such conditions in ^{3}He–^{4}He solid mixtures are given in Refs. 14 and 15.

When the degree of supercooling decreases, the concentration of nuclei falls off rapidly (exponentially), leading to growth of the diffusion time τ_D, which can ultimately be the dominant contribution to τ. The temperature dependence $\tau(T)$ observed in that case is a consequence of the concentration dependence of the diffusion coefficient, since the equilibrium concentration at phase separation is set by the temperature. Figure 3 shows an illustration of the concentration dependence $\tau(x)$ obtained by processing the data of Fig. 2. The concentration for each step was taken as the average between the initial and final concentrations x_i and x_f. It is seen that τ decreases noticeably with concentration, especially at high concentrations. For comparison a plot of the relation $\tau \sim x^{4/3}$ is shown; it is close to the experimental curve in this region. Some characteristics of the sample studied are listed in Table I.

For a quantitative treatment analogous to that given in Ref. 7 for a mixture of ^{3}He in ^{4}He, the solution of the diffusion problem in spherical coordinates, with boundary and initial conditions corresponding to the experimental setup, is used.

The solution of the diffusion equation

$$\frac{\partial x}{\partial t} = D\left(\frac{\partial^2 x}{\partial \rho^2} + \frac{2}{\rho}\frac{\partial x}{\partial \rho}\right) \tag{5}$$

under the initial condition $x(\rho,0) = x_i$ and boundary conditions

$$\left.\frac{\partial x}{\partial \rho}\right|_{\rho=R} = 0, \quad D\left.\frac{\partial x}{\partial \rho}\right|_{\rho=r} = K(x - x_f) \tag{6}$$

has the form (see, e.g., Ref. 16)

TABLE I. Some characteristics of the sample with $x_0 = 3.34\%$ ^{4}He, $V_m = 24.2$ cm^3/mole, and $\Delta T_1 = 26$ mK.

T_f, K	$\tau \cdot 10^{-3}$, s	x_i, % ^{4}He	x_f, % ^{4}He	z	$D_{43} \cdot 10^8$, cm^2/s	$\tau_D \cdot 10^{-3}$, s	$\tau_s \cdot 10^{-3}$, s
0.195	5.01	3.34	1.97	0.201	1.04	3.03	1.98
0.185	2.66	1.97	1.55	0.255	1.64	1.46	1.20
0.175	1.84	1.55	1.19	0.274	2.16	0.81	1.03
0.162	1.52	1.19	0.80	0.289	2.98	0.60	0.92
0.145	1.21	0.80	0.44	0.303	4.44	0.37	0.83
0.132	0.94	0.44	0.25	0.312	6.35	0.20	0.78
0.121	0.925	0.25	0.14	0.316	7.78	0.17	0.76
0.107	0.89	0.14	0.05	0.321	9.49	0.16	0.73

Note: T_f is the final temperature, τ are the characteristic times for establishment of equilibrium according to experiment, x_i and x_f are the initial and final impurity concentrations in the matrix, $z = r/R$ is the ratio of the radius of a new-phase inclusion to the size of the region associated to each nucleus, D_{43} is the effective coefficient of diffusion of ^{4}He in a ^{3}He matrix, τ_D is the characteristic diffusion time according to Eq. (12), and τ_s is the characteristic "surface" time according to Eq. (13).

$$x(\rho,t) = x_f + (x_i - x_f)\sum_{n=1}^{\infty} A_n e^{-D\lambda_n^2 t}\frac{\sin[\lambda_n(\rho - r) + \nu_n]}{\rho}, \tag{7}$$

where x_i and x_f are the initial and final concentrations of ^{4}He in the matrix, r is the radius of a new-phase nucleus, R is the radius of an equivalent sphere of volume equal to the volume from which impurities reach this nucleus, K is a coefficient characterizing the probability of penetration of an impurity into the nucleus, A_n and ν_n are known constant coefficients, and λ_n are the roots of the transcendental equation

$$\tan\lambda_n(R - r) = \frac{\lambda_n(hrR + R - r)}{\lambda_n^2 rR + hr + 1}, \quad h = \frac{K}{D}. \tag{8}$$

The solution of the diffusion problem is obtained for constant r and D; this can be justified by the comparatively small changes of these quantities for each step. The influence of their nonconstancy is partially taken into account by the use of the average values for each step. Estimates show that even at small t one need keep only the first term in Eq. (7). The pressure change measured in the experiment is proportional to the change of the average concentration $\overline{x}(t)$, which can be found by averaging (7) in the interval from r to R:

$$\overline{x}(t) = \frac{3}{(R^3 - r^3)}\int_r^R x(\rho,t)\rho^2 d\rho = x_f + 3\frac{x_i - x_f}{R^3 - r^3}\tilde{A}_1 e^{-t/\tau}, \tag{9}$$

where $\tilde{A}_1$ is a constant.

The time dependence of interest to us is characterized by the quantity

$$\tau = \frac{1}{D\lambda^2}, \quad (\lambda \equiv \lambda_1), \tag{10}$$

where λ is found from the solution of equation (8). This is easily done under the condition $\lambda(R - r) < 1$ by expanding $\tan\lambda(R - r)$ in a series. If terms up to order $\lambda^3(R - r)^3$ are kept in the series expansion and the relation between R and r

is determined by the condition that the ^{4}He is conserved within the volume of the sphere of radius R, one can obtain the following equation:

$$\tau=\frac{1}{D\lambda^2}=\frac{R^2}{3D}\frac{(1-z)^3}{z}+\frac{R}{3K}\frac{1-z^3}{z^2}, \tag{11}$$

where

$$z=\frac{r}{R}=\sqrt[3]{\frac{x_0-\bar{x}}{1-2\bar{x}}}.$$

In practice, formula (11) means that in the approximation considered, the measured relaxation time can be regarded as being the sum of the diffusion time

$$\tau_D=\frac{R^2}{3D}\frac{(1-z)^3}{z} \tag{12}$$

and the ''surface'' time

$$\tau_s=\frac{R}{3K}\frac{1-z^3}{z^2}. \tag{13}$$

We note that the expression for τ_D is exactly that which is obtained for the solution of the diffusion problem in the same approximation in the case when there is no resistance to the transition of an impurity into a nucleus. The dependence of τ_s on the concentration (temperature) is due to the change of the ratio of the volume of the matrix to the total surface area of the new-phase inclusions. It follows from Eq. (11) that

$$\tau D f_1(z)=\frac{R^2}{3}+\frac{RD}{3K}f_2(z), \tag{14}$$

where

$$f_1(z)=\frac{z}{(1-z)^3},\quad f_2(z)=\frac{1}{z}+\frac{3}{(1-z)^2}.$$

Thus if one plots $\tau D f_1(z)$ as a function of $D f_2(z)$, one should obtain a straight line whose intercept with the ordinate can be used to find R and whose slope can be used to determine K.

In processing the electronic data further it is natural to identify the diffusion coefficient appearing in Eq. (11) with D_x from (2). In the case of dilute mixtures of ^{3}He in ^{4}He the quantity J_{34} appearing in (2) can be determined quite reliably in experimental studies of quantum diffusion and turns out to be approximately 5–6 times smaller than the exchange integral J_{33} in pure ^{3}He at the same molar volumes (see, e.g., Ref. 17). The decrease of J_{34} in comparison with J_{33} is due to two factors: the fact that a heavier atom is involved in the tunneling exchange, and the larger amplitude of the zero-point vibrations of the ^{3}He atom, the distance between which and its nearest neighbor is larger than the average lattice spacing. Both of these factors decrease the tunneling probability and bring about the difference found. As to the exchange integral J_{43} of ^{4}He in ^{3}He, there is no reliable information available. However, since in that case the two factors act in opposite directions, one can assume that $J_{43}\approx J_{33}$. Using the known value of J_{33} (Ref. 18) and the value of V_0, which characterizes the interaction of ^{4}He impurities in bcc ^{3}He, estimated by Kal'noĭ and Strzhemechnyĭ[19] (adjusted to our molar volume), we obtain the following expression:

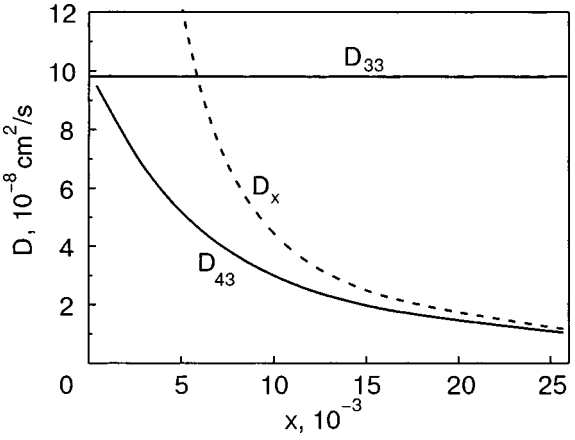

FIG. 4. Dependence of the diffusion coefficient of impurity ^{4}He on the concentration according to Eq. (16).

$$D_x=8.8\times10^{-11}x^{-4/3}\ \text{cm}^2/\text{s}. \tag{15}$$

It should be noted that at small x the value of D_x from (15) is larger than the spin diffusion coefficient D_{33} in pure ^{3}He, as it must not be under our assumption of equal J_{33} and J_{43}, since the diffusion in ^{3}He takes place in the complete absence of retarding elastic interactions. To eliminate such a situation we should use the effective diffusion coefficient

$$D_{43}=\frac{D_x D_{33}}{D_x+D_{33}}, \tag{16}$$

which results in the condition $D_{43}\leqslant D_{33}=5.0\times10^{-34}V_\mu^{19}$ cm^2/s.[20,21] Physically the origin of formula (16) can apparently be regarded as being a consequence of the coexistence of microscopic regions in the sample with a random concentration difference. In regions with lower concentration the impurities do not ''feel'' one another, and the diffusion takes place as in pure ^{3}He, with the coefficient D_{33}, while in regions with higher concentration the interaction of the impurities leads to a dependence of the type (15). The set of such processes can give a diffusion coefficient described by formula (16). Figure 4 shows the concentration dependence of D_{43}. For comparison the value of D_{33} and the function $D_x(x)$ are also plotted. It is seen that D_{43} approaches D_{33} at low concentrations and decreases substantially with increasing x.

A plot of relation (14) under the assumptions mentioned is presented in Fig. 5. One sees a good linear dependence, so that the value of the parameters R and K can be reliably determined: $R=(6.4\pm0.2)\times10^{-3}$ cm, and $K=(2.7\pm0.2)\times10^{-5}$ cm/s. We note that the maximum value found, $\lambda R(1-z)\approx0.7$, justifies the neglect of higher than cubic powers in the expansion of $\tan\lambda(R-r)$ in (8). Substituting the values found for R and K into Eq. (11), we can describe the experimental data obtained. The solid curve in Fig. 3 corresponds to a calculation using Eq. (11). Also shown here are $\tau_D(x)$ and $\tau_s(x)$ according to formulas (12) and (13). As expected, the contribution of τ_D is dominant at high concentrations and that of τ_s is dominant at low concentrations.

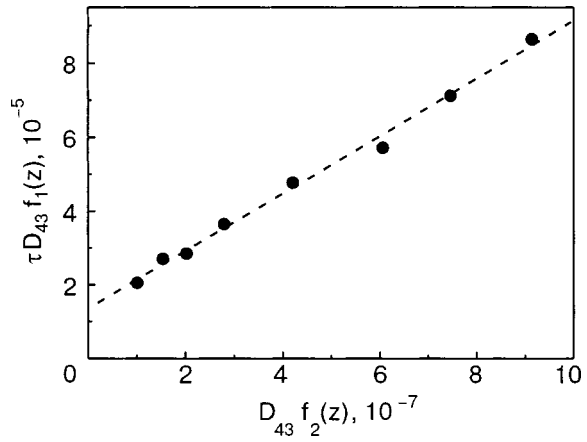

FIG. 5. Plot of $\tau D_{43} f_1(z)$ versus $D_{43} f_2(z)$ according to Eq. (14).

4. CONCENTRATION OF NUCLEI AND THE INTERPHASE TENSION

The R value found can be used to determine the concentration of new-phase nuclei $N_m = \tilde{a}^3/R^3 = 3.6\times 10^{-17}$, $\tilde{a}$ is the interatomic distance determined by the fluctuation $4\pi\tilde{a}^3/3 = V_\mu/N_A$ (N_A is Avogadro's number).

In the framework of the theory of homogeneous nucleation, Slezov and Shmel'tser[22] calculated the concentration of nuclei as a function of the impurity concentration, temperature, and degree of supersaturation. As applied to the separation of a solid mixture of helium isotopes it can be written

$$N_m = \beta^{-3/8} x_i^{7/4} \exp\left\{ -\frac{3\beta^3\left[1+8\dfrac{T_0}{T_f}(x_i - x_f)\right]}{8\ln^2\dfrac{x_i}{x_f}} \right\}, \quad (17)$$

where $\beta = (8\pi/3)(\sigma\tilde{a}^2/T_f)$, T_0 is the temperature of the maximum of the separation curve, T_f is the final temperature, and σ is the surface tension at the boundary of the nucleus.

Formula (17) differs from that given in Refs. 22 and 15 by the presence of the factor in square brackets in the argument of the exponential function; this factor has been introduced to take into account the nonideality of ^{3}He–^{4}He solid mixtures (see Ref. 23). A calculation of N_m with the use of formula (17) shows that in this case practically all the nuclei arise in the first cooling step, so that the number of nuclei and the equivalent radius R can be assumed to be the same in all steps. The N_m value found is approximately two orders of magnitude smaller than in Ref. 15, primarily as a result of the appreciable difference in the degree of supercoooling. An estimate of the interphase surface tension by formula (17) gives $\sigma = 1.9\times 10^{-2}$ erg/cm^2, which is comparable to the value 1.5×10^{-2} erg/cm^2 found in Ref. 14 in a study of the separation kinetics at different degrees of supercooling.[1] The close values of σ obtained in experiments of different types (see also Ref. 15) is, in our view, a weighty argument in favor of the position that homogeneous nucleation conditions are realized in ^{3}He–^{4}He solid mixtures.

5. CONCLUSION

We have carried out studies of the kinetics of separation of dilute solid mixtures of ^{4}He in ^{3}He. We have established that the characteristic separation time τ has a substantial dependence on the degree of supercooling from the region of the uniform mixture. It was found that at high degrees of supercooling the separation time is several hundred seconds and is independent of temperature. At low supercoolings we observed longer times, up to 4×10^3 s at high temperatures, and a noticeable decrease of τ as the temperature was lowered. Such behavior of τ is due to the change of the diffusion coefficient according to the law $D \sim x^{-4/3}$, which has been predicted for impurity diffusion in quantum crystals under conditions of a substantial interaction between impurities. For quantitative processing of the results we used the solution of the diffusion problem with allowance for the finite resistance of the boundary. A comparison of the experimental and calculated results made it possible for the first time to separate out the relaxation time due to the boundary resistance and also to estimate the average size of the region associated to each new-phase nucleus and the concentration of nuclei N_m. The value of N_m was used in the homogeneous nucleation theory to calculate the coefficient of interphase surface tension σ, which turned out to be close to the value found in other experiments. The agreement of the values of σ obtained in different experiments can be taken as evidence of the realization of homogeneous nucleation conditions in rather perfect samples of ^{3}He–^{4}He solid mixtures and an indication of the possibility that this system may serve as an example for the quantitative study of the kinetics of first-order phase transitions.

This study was supported by the State Foundation of Ukraine for Basic Research (Project 02.07/00391, Agreement F7/286-2001).

*E-mail: syrnikov@ilt.kharkov.ua

[1)]Here we have introduced a value of σ corrected for the fact that in the calculation of σ from the value found for β, one uses the parameter $a = (V_\mu/N_A)^{1/3}$ instead of $\tilde{a}$.

[1] A. F. Andreev and I. M. Lifshits, Zh. Éksp. Teor. Fiz. **56**, 2057 (1969) [Sov. Phys. JETP **29**, 1107 (1969)].
[2] V. A. Slyusarev and M. A. Strzhemechnyĭ, in *Low Temperature Physics* [in Russian], Vol. 19, FTINT (1972), p. 85.
[3] A. Widom and M. J. Richards, Phys. Rev. A **6**, 1196 (1972).
[4] Yu. Kagan and M. I. Klinger, J. Phys. C **7**, 2791 (1974).
[5] Yu. M. Kagan and L. A. Maksimov, Zh. Éksp. Teor. Fiz. **84**, 792 (1983) [Sov. Phys. JETP **57**, 459 (1983)].
[6] V. A. Shvarts, N. P. Mikhin, É. Ya. Rudavskiĭ, A. M. Usenko, Yu. A. Tokar', and V. A. Mikheev, Fiz. Nizk. Temp. **21**, 717 (1995) [Low Temp. Phys. **21**, 556 (1995)].
[7] A. N. Gan'shin, V. N. Grigor'ev, V. A. Maĭdanov, N. F. Omelaenko, A. A. Penzev, E. Ya. Rudavskiĭ, A. S. Rybalko, and Yu. A. Tokar, Fiz. Nizk. Temp. **25**, 796 (1999) [Low Temp. Phys. **25**, 592 (1999)].
[8] A. F. Andreev, Usp. Fiz. Nauk **118**, 251 (1976) [Sov. Phys. Usp. **19**, 137 (1976)].
[9] A. Landesman, Phys. Lett. A **54**, 137 (1975).
[10] J. E. Sacco and A. Widom, in *Proceedings of the International Quantum Crystals Conference*, Colorado Univ. (1977), p. C-15; Phys. Rev. B **17**, 204 (1978).
[11] W. J. Mullin, Phys. Rev. Lett. **20**, 254 (1968).
[12] V. A. Gan'shin, V. N. Grigor'ev, V. A. Maĭdanov, N. F. Omelaenko, A. A. Penzev, É. Ya. Rudavskiĭ, and A. S. Rybalko, Fiz. Nizk. Temp. **26**, 1175 (2000) [Low Temp. Phys. **26**, 869 (2000)].

[13] V. A. Gaṇ'shin, V. N. Grigor'ev, V. A. Maĭdanov, N. F. Omelaenko, A. A. Penzev, É. Ya. Rudavskiĭ, A. S. Rybalko, and E. V. Syrnikov, Fiz. Nizk. Temp. **29**, 487 (2003) [Low Temp. Phys. **29**, 362 (2003)].
[14] A. Penzev, A. Ganshin, V. Grigor'ev, V. Maidanov, E. Rudavskii, A. Rybalko, V. Slezov, and Ye. Syrnikov, J. Low Temp. Phys. **126**, 151 (2002).
[15] A. Smith, V. Maidanov, E. Rudavskii, V. Grigor'ev, V. Slezov, M. Poole, J. Saunders, and B. Cowan, Phys. Rev. B (to be published).
[16] B. M. Budak, A. A. Samarskiĭ, and A. N. Tikhonov, in *Problems in Mathematical Physics* [in Russian], Nauka, Moscow (1972).
[17] V. N. Grigor'ev, Fiz. Nizk. Temp. **23**, 5 (1997) [Low Temp. Phys. **23**, 3 (1997)].
[18] M. F. Panczyk and E. D. Adams, Phys. Rev. A **1**, 1356 (1970).
[19] S. E. Kal'noi and M. A. Strzhemechnyi, Fiz. Nizk. Temp. **8**, 1025 (1982) [Sov. J. Low Temp. Phys. **8**, 515 (1982)].
[20] B. N. Esel'son, V. A. Mikheev, and V. N. Grigor'ev, Fiz. Nizk. Temp. **2**, 1229 (1976) [Sov. J. Low Temp. Phys. **2**, 599 (1976)].
[21] V. N. Grigor'ev, *Author's Abstract of Doctoral Dissertation* [in Russian], FTINT, Kharkov (1981).
[22] V. V. Slezov and J. Shmelzer, Fiz. Tverd. Tela (St. Petersburg) **39**, 2210 (1997) [Phys. Solid State **39**, 1971 (1997)].
[23] E. D. Edwards and S. Balibar, Phys. Rev. B **39**, 4083 (1989).

Translated by Steve Torstveit

SUPERCONDUCTIVITY, INCLUDING HIGH TEMPERATURE SUPERCONDUCTIVITY

Superconductivity in quasi-two-dimensional nonadiabatic systems with arbitrary charge-carrier density at $T=0$

M. E. Palistrant*

Institute of Applied Physics, Academy of Sciences of Moldova, 5 Academiei St., 2028 Kishinau, Moldova
(Submitted March 18, 2003)
Fiz. Nizk. Temp. **29**, 1173–1180 (November 2003)

The basic system of equations of the theory of superconductivity at $T=0$ is obtained in an approximation linear in the nonadiabaticity, and analytic solutions for the order parameter Δ and the chemical potential μ are found in two limiting cases: $\mu \gg \Delta$, and $\mu \sim \Delta$. The dependence of these quantities on the density of charge carriers is investigated. It is found that the order parameter Δ can be increased by a factor of four to five in comparison with ordinary superconductors owing to the effects of nonadiabaticity and strong electronic correlations. The influence of the nonadiabaticity on the BCS–Bose crossover in the region of low charge-carrier densities is also investigated. © *2003 American Institute of Physics.*
[DOI: 10.1063/1.1614232]

1. INTRODUCTION

Considerable progress has been made in the study of the properties of materials having high-temperature superconductivity (HTSC). However, because of the complexity of the systems considered, the mechanism of HTSC has still not been established. Theoretical studies must be done on simplified models which take into account individual features of these materials.

Among such features are the overlap of the energy bands at the Fermi surface (see, e.g., Refs. 1–4 and the references cited therein), the presence of van Hove singularities and flat parts in the electron spectrum,[5–7] strong electron–phonon coupling,[8,9] and an anharmonic character of the lattice vibrations.[10] In addition, HTSC materials are characterized by a lowered dimensionality (layered structure), strong electronic correlations, and a low density of charge carriers. These systems are nonadiabatic; the relation $\omega_0 \sim \varepsilon_F$ holds in them (ω_0 is the Debye frequency, and ε_F is the Fermi energy), and at very low charge-carrier densities the relation $\omega_0 \geqslant \varepsilon_F$ can hold.

Such factors as the nonadiabaticity and strong electronic correlations inherent to these materials violate the Migdal theorem[11] and make it necessary to take additional many-particle effects into account as compared with the case of ordinary superconductors, in which the relation $\varepsilon_F \gg \omega_0$ holds. As was shown in Refs. 12 and 13, these effects can be interpreted as the mechanism leading to the high values of T_c.

An important role in the theory of superconductivity is played by the value of the charge-carrier density. At a relatively low charge density a two-dimensional system can undergo a transition from the BCS regime with Cooper pairs to a Schaffroth regime of a Bose condensate of local pairs.[14–20] In Refs. 14–19 the studies were based on a single-band BCS model, while in Ref. 20 the overlap of two energy bands at the Fermi surface was taken into account. In the papers cited above, studies have been done on the basis of a simplified Migdal–Eliashberg theory suitable for adiabatic superconductors ($\omega_0 \ll \varepsilon_F$).

The goal of the present study is to construct a theory of superconductivity for nonadiabatic systems, in which the Migdal theorem[11] is violated because the condition $\omega_0 \ll \varepsilon_F$ does not hold and also because of the presence of strong electronic correlations.

In Sec. 2 expressions are obtained for the diagonal Σ_N and off-diagonal Σ_S parts of the mass operator and for the Green's functions (normal and anomalous) in the linear approximation in the nonadiabaticity. In Sec. 3 a system of equations is obtained for the order parameter Δ at $T=0$ and for the chemical potential μ at arbitrary charge-carrier density, and two limiting cases are considered: $\mu \gg \Delta$, and $\mu \sim \Delta$. Section 4 is devoted to a calculation of the vertex and crossing functions in a two-dimensional system in the weak-coupling approximation and for small values of the exchange momentum q. Numerical results and conclusions are given in Sec. 5.

2. MODEL AND BASIC EQUATIONS OF A NONADIABATIC SYSTEM

We start from a Hamiltonian describing an electron–phonon system:

$$\mathcal{H}=\mathcal{H}_0+\sum_{\sigma} \int d\mathbf{x}\, \psi_{\sigma}^{+}(\mathbf{x}\sigma)\Psi(\mathbf{x}\sigma)\varphi(\mathbf{x}), \tag{1}$$

where $\mathcal{H}_0$ is the Hamiltonian of the free electrons and phonons, the second term corresponds to the electron–phonon interaction, $\Psi(\mathbf{x}\sigma)$ is the annihilation operator for an electron at point $\mathbf{x}$ with spin σ, and $\varphi(\mathbf{x})$ is the phonon operator.

On the basis of perturbation theory[21] at $T=0$, we obtain the following diagram representations for the normal Σ_N and anomalous Σ_S self-energies:

$\Sigma_N(\mathbf{p},\Omega) =$  (2)

$\Sigma_S(\mathbf{p},\Omega) =$  (3)

Here a straight line corresponds to the total electron Green's function—the normal ($\rightarrow$) and the anomalous ($\leftrightarrow$)—and the wavy line to the phonon Green's function. The above perturbation series together with the expressions for ordinary superconductors contain diagrams with a crossing of two lines of electron–phonon interaction; this corresponds to taking into account the vertex and ''crossing'' functions to a first approximation in the nonadiabaticity[13] and, consequently, goes beyond the framework of the Migdal theorem.[11]

For simplicity we choose the Einstein spectrum and write the phonon Green's function in the form

$$D(\mathbf{p}-\mathbf{p}_1,\Omega-\Omega_1)=-|g_{\mathbf{pp}_1}|^2\frac{\omega_0^2}{(\Omega-\Omega_1)^2+\omega_0^2}$$
$$=|g_{\mathbf{pp}_1}|^2 D(\Omega,\Omega_1). \quad (4)$$

The presence of strong electronic correlations in the system due to the Coulomb interaction alters the electron–phonon interaction substantially. In accordance with the studies of Refs. 22 and 23, the value of $|g_{\mathbf{pp}_1}|^2$ increases slowly with increasing exchange momentum $\mathbf{q}=\mathbf{p}-\mathbf{p}_1$ and then falls off sharply. This circumstance allows us to write the electron–phonon coupling constant in the form

$$|g_{\mathbf{pp}_1}|^2=\frac{\pi}{Q_c}g^2\Theta(g_c-|\mathbf{p}-\mathbf{p}_1|);\quad Q_c=\frac{q_c}{2p_F}. \quad (5)$$

Here Θ is the step function, and q_c is the cutoff momentum of the electron–phonon interaction.

The factor of π/Q_c, which corresponds to the case of a two-dimensional system, is introduced in order that averaging over the Fermi surface will give g^2, and so in this model the constant $\lambda=N_0g^2$ is independent of q_c, in agreement with the results of Ref. 22. On the basis of Eqs. (2) and (3) we obtain for the mass operators Σ_N and Σ_S

$$\Sigma_N(\mathbf{p},\Omega)=\frac{1}{\beta V}\sum_{\mathbf{p}_1\Omega_1}V_N(\mathbf{p},\mathbf{p}_1,\Omega,\Omega_1)G(\mathbf{p}_1,\Omega_1), \quad (6)$$

$$\Sigma_S(\mathbf{p},\Omega)=\frac{1}{\beta V}\sum_{\mathbf{p}_1\Omega_1}V_S(\mathbf{p},\mathbf{p}_1,\Omega,\Omega_1)F(\mathbf{p}_1,\Omega_1), \quad (7)$$

where

$$V_N(\mathbf{p},\mathbf{p}_1,\Omega,\Omega_1)=-g^2D(\Omega,\Omega_1)\Theta(q_c-|\mathbf{p}-\mathbf{p}_1|)$$
$$\times\frac{\pi}{Q_c}[1+\lambda P_V(\mathbf{p},\mathbf{p}_1,\Omega,\Omega_1)], \quad (8)$$

$$V_S(\mathbf{p},\mathbf{p}_1,\Omega,\Omega_1)=-g^2D(\Omega,\Omega_1)\Theta(q_c-|\mathbf{p}-\mathbf{p}_1|)\frac{\pi}{Q_c}$$
$$\times[1+2\lambda P_V(\mathbf{p},\mathbf{p}_1,\Omega,\Omega_1)$$
$$+\lambda P_C(\mathbf{p},\mathbf{p}_1,\Omega,\Omega_1)], \quad (9)$$

and P_V and P_C are the vertex and crossing functions, defined by the relations

$$P_V(\mathbf{p},\mathbf{p}_1,\Omega,\Omega_1)=-\frac{\pi}{N_0Q_c}\frac{1}{\beta V}\sum_{p_2,\Omega_2}\Theta(q_c-|\mathbf{p}$$
$$-\mathbf{p}_2|)G(\mathbf{p}_2,\Omega_2)\times G(\mathbf{p}_1+\mathbf{p}_2-\mathbf{p},\Omega_1$$
$$+\Omega_2-\Omega)D(\Omega,\Omega_2). \quad (10)$$

$$P_C(\mathbf{p},\mathbf{p}_1,\Omega,\Omega_1)\approx-\frac{\pi}{N_0Q_c}\frac{1}{\beta V}\sum_{p_2,\Omega_2}\Theta(q_c-|\mathbf{p}-\mathbf{p}_2|)$$
$$\times G(p_2,\Omega_2)G(p_2-p-p_1,\Omega_2$$
$$-\Omega-\Omega_1)D(\Omega,\Omega_2). \quad (11)$$

For the temperature Green's functions, the normal $G(\mathbf{p},\Omega)$ and the anomalous $F(\mathbf{p},\Omega)$, we obtain the relations

$$G(\mathbf{p},\Omega)=-\frac{i\Omega Z+\tilde{\varepsilon}_p}{(\Omega Z)^2+\tilde{\varepsilon}_p^2+|\Sigma_S(\mathbf{p},\Omega)|^2},$$

$$F(\mathbf{p},\Omega)=\frac{\Sigma_S(\mathbf{p},\Omega)}{(\Omega Z)^2+\tilde{\varepsilon}_p^2+|\Sigma_S(\mathbf{p},\Omega)|^2}, \quad (12)$$

where

$$Z=Z(\Omega)=1-\frac{1}{\Omega}\mathrm{Im}\,\Sigma_N(\mathbf{p},\Omega);$$

$$\tilde{\varepsilon}_p=\varepsilon_p+\mathrm{Re}\,\Sigma_N(\mathbf{p},\Omega). \quad (13)$$

In expression (11), which determines the crossing function, where the summation over p_1 and p_2 is mixed, we restrict consideration to the approximation[13] $D(\mathbf{p}_1-\mathbf{p}_2,\Omega_{1-}\Omega_2)\rightarrow D(\mathbf{p}-\mathbf{p}_2,\Omega-\Omega_2)$.

After averaging over the Fermi surface we reduce expressions (6) and (7) to the form

$$\Sigma_N(\Omega)=\frac{1}{\beta V}g^2\sum_{\mathbf{p}_1,\Omega_1}\frac{\omega_0^2}{(\Omega-\Omega_1)^2+\omega_0^2}$$
$$\times[1+\lambda P_V(Q_c,\Omega,\Omega_1)]G(\mathbf{p}_1,\Omega_1), \quad (14)$$

$$\Sigma_S(\Omega)=\frac{1}{\beta V}g^2\sum_{\mathbf{p}_1,\Omega_1}\frac{\omega_0^2}{(\Omega-\Omega_1)^2+\omega_0^2}$$
$$\times[1+2\lambda P_V(Q_c,\Omega,\Omega_1)$$
$$+\lambda P_C(Q_c,\Omega,\Omega_1)]F(\mathbf{p}_1,\Omega_1), \quad (15)$$

where

$$P_{V,C}(Q_c,\Omega,\Omega_1)=\left\langle\frac{\pi}{Q_C}\Theta(q_c-|\mathbf{p}-\mathbf{p}_1|)\right.$$
$$\left.\times P_{V,C}(\mathbf{p},\mathbf{p}_1,\Omega,\Omega_1)\right\rangle_{FS}.$$

3. ORDER PARAMETER AND CHEMICAL POTENTIAL

Let us consider the weak-coupling approximation ($\omega_0 \gg \Delta$), which allows us to neglect the contribution of the last diagram, containing only the anomalous Green's functions, in expression (3). Furthermore, this approximation allows us to obtain analytical expressions for the functions P_V and P_C and for the order parameter Δ and chemical potential μ. Following Ref. 13, we take the functions P_V and P_C out from under the summation sign at $\Omega=0$, $\Omega_1=\omega_0$ and introduce the notation

$$\lambda_Z=\lambda[1+\lambda P_V(Q_c,0,\omega_0)],$$

$$\lambda_\Delta=\lambda[1+2\lambda P_V(Q_c,0,\omega_0)+\lambda P_V(Q_c,0,\omega_0)]. \tag{16}$$

As a result, after formula (12) is substituted in, Eq. (15) becomes

$$\Sigma_S(\Omega)=\lambda_\Delta\frac{1}{N_0}\frac{1}{\beta V}\sum_{\mathbf{p}_1,\Omega_1}\frac{\omega_0^2}{(\Omega-\Omega_1)^2+\omega_0^2} \times\frac{\Sigma_S(\Omega_1)}{(Z\Omega_1)^2+\tilde{\varepsilon}_{p_1}^2+\Sigma_S^2(\Omega_1)}. \tag{17}$$

We use the approximation

$$\frac{\omega_0^2}{(\Omega-\Omega_1)^2+\omega_0^2}\to\frac{\omega_0^2}{\Omega^2+\omega_0^2}\frac{\omega_0^2}{\Omega_1^2+\omega_0^2}$$

and make a series of transformations in (16), as is done in the study of superconducting systems with retardation.[13,24–26] The system of equations for determining the order parameter Δ and the quantity Z can be reduced to the form

$$1=\lambda_\Delta\frac{1}{\beta VN_0}\sum_{\mathbf{p}_1,\Omega_1}\frac{\omega_0^4}{(\Omega_1^2+\omega_0^2)^2}\frac{1}{\Omega_1^2+\overline{\varepsilon}_{p_1}^2+\Delta^2}\frac{1}{Z}, \tag{18}$$

$$Z(\Omega)=1+\lambda_Z\frac{1}{\Omega}\frac{1}{\beta VN_0} \times\sum_{\mathbf{p}_1,\Omega_1}\frac{\omega_0^2}{(\Omega-\Omega_1)^2+\omega_0^2}\frac{\Omega_1}{\Omega_1^2+\overline{\varepsilon}_{p_1}^2+\Delta^2}\frac{1}{Z}, \tag{19}$$

where

$$\overline{\varepsilon}_p=\tilde{\varepsilon}_p/Z,\quad \Delta=\Sigma_S/Z.$$

In these equations we do the integration over energy ($-\mu<\varepsilon_{p_1}<W-\mu$; μ is the chemical potential, W is the width of the energy band) and the integration over Ω_1 between infinite limits in the standard manner. In the approximation of weak electron–phonon coupling we separate out the logarithmic singularity with respect to Δ and in the terms determined by the nonadiabaticity effect we neglect terms $\sim\Delta/\omega_0\ll 1$. In this way expressions (18) and (19) are conveniently reduced to the form

$$\frac{Z}{\lambda_\Delta}=\frac{1}{2}\Bigg[\ln(\overline{W}-\overline{\mu}+\sqrt{(\overline{W}-\overline{\mu})^2+\Delta^2}) -\ln(-\overline{\mu}+\sqrt{\overline{\mu}^2+\Delta^2})-\ln\frac{\overline{\mu}+\omega_0}{\omega_0} -\ln\frac{\overline{W}-\overline{\mu}+\omega_0}{\omega_0}\Bigg]-\frac{1}{4}\Bigg[\frac{\overline{\mu}}{\omega_0+\overline{\mu}}+\frac{\overline{W}-\overline{\mu}}{\omega_0+\overline{W}-\overline{\mu}}\Bigg], \tag{20}$$

$$Z=Z(0)=1+\frac{\lambda_Z}{2}\Bigg[\frac{W-\mu}{W-\mu+\omega_0}+\frac{\mu}{\mu+\omega_0}\Bigg]. \tag{21}$$

We supplement (20) with the expression determining the chemical potential μ for a two-dimensional system:

$$2\varepsilon_F=\frac{n}{N_0}=\overline{W}=\sqrt{(\overline{W}-\overline{\mu})^2+\Delta^2}+\sqrt{\overline{\mu}^2+\Delta^2},$$

$$\overline{W}=W/Z,\quad \overline{\mu}=\mu/Z. \tag{22}$$

where n is the density of charge carriers and $N_0=m/2\pi$ is the electron density of states. The values of Δ and μ are determined by solving the system of equations (20), (22). We shall consider two limiting cases: $\mu\gg\Delta$, and $\mu\sim\Delta$. In the first case Eq. (22) leads to the relation $\varepsilon_F\approx\mu$, as it should. On the basis of (20) we then have

$$\Delta=2\omega_0\sqrt{\frac{\overline{\mu}(\overline{W}-\overline{\mu})}{e(\overline{\mu}+\omega_0)(\overline{W}-\overline{\mu}-\omega_0)}} \times\exp\Bigg(-\frac{Z}{\lambda_\Delta}+\frac{1}{4}\Bigg[\frac{\omega_0}{\overline{\mu}+\omega_0}-\frac{\omega_0}{\overline{W}-\overline{\mu}+\omega_0}\Bigg]\Bigg). \tag{23}$$

Comparing this expression with the value obtained previously for T_c in nonadiabatic systems,[29,30] we obtain the relation known from BCS theory:

$$\frac{\Delta}{T_c}=\frac{\pi}{\gamma_e}\approx 1.76.$$

Consequently, this ratio is not influenced by nonadiabaticity effects in the weak-coupling approximation under consideration.

In the case $\mu\sim\Delta\ll\omega_0$ we introduce the notation

$$A=\frac{2Z_0}{\lambda_\Delta^0}+\ln\frac{\overline{W}+\omega_0}{\omega_0}+\frac{1}{2}\frac{\overline{W}}{\overline{W}+\omega_0} \tag{24}$$

and write Eq. (20) in the form

$$\frac{\overline{W}-\overline{\mu}+\sqrt{(\overline{W}-\overline{\mu})^2+\Delta^2}}{\sqrt{\overline{\mu}+\Delta^2}-\overline{\mu}}=e^A. \tag{25}$$

The solution of the system of equations (22), (25) leads to the relations

$$\Delta^2=\frac{\varepsilon_F(\overline{W}-\varepsilon_F)}{\mathrm{sh}^2(A/2)};\quad \overline{\mu}=\varepsilon_F\coth\frac{A}{2}-\frac{\overline{W}}{2}\Bigg[\coth\frac{\Lambda}{2}-1\Bigg]. \tag{26}$$

If in these formulas we take the limit $\omega_0\to\infty$, we will obtain the results that follow from the BCS model.[27,28] In our case

the quantities appearing in Eq. (26) are redefined because of the nonadiabaticity of the system and the presence of strong electronic correlations.

We consider the weak-coupling approximation ($A \gg 1$). In that approximation we have

$$\Delta = \sqrt{2\varepsilon_F |\varepsilon_b|}, \quad \overline{\mu} = \varepsilon_F - \frac{|\varepsilon_b|}{2}, \tag{27}$$

where the energy of a two-particle bound state is given by the relation

$$|\varepsilon_b| = \frac{2\omega_0}{1+\omega_0/\overline{W}} \exp\left\{ -\frac{2Z_0}{\lambda_\Delta^0} + \frac{1}{2}\frac{1}{1+\omega_0/\overline{W}} \right\}. \tag{28}$$

For systems with wide energy bands ($\omega_0/W \ll 1$) this expression can be rewritten as

$$|\varepsilon_b| = \frac{2\omega_0}{\sqrt{e}} \exp\left\{ -\frac{2Z_0}{\lambda_{\Delta 0}^0} \right\}, \tag{29}$$

where Z_0^0 and $\lambda_{\Delta 0}^0$ are determined from formulas (21) and (16), respectively, for $\mu = 0$ and $W \to \infty$.

The energy of a two-particle bound state in a nonadiabaticity system arises through the exchange of intermediate bosons, leading to the appearance of a pre-exponential factor of ω_0, the energy of the bosons.

Expression (29) differs from the case of adiabatic systems[27,28] by a renormalization of the coupling constant λ and the quantity Z on account of nonadiabaticity effects, and also by the presence of a pre-exponential factor of $e^{-1/2}$ due to the use of a factorization procedure for the phonon Green's function [see the transition from Eq. (17) to Eq. (18)]. The same factor appears in the definition of Δ (23) and T_c (Refs. 29 and 30) for $\varepsilon_F \gg \Delta, T_c$.

We note that the case of adiabatic systems in the factorization approximation presented above is considered in Ref. 31, for example.

Thus the contribution of nonadiabaticity to the definition of Δ and μ (27) in the region of low charge-carrier densities is determined by a redefinition of the value of the binding energy ε_b of the two-particle state. In systems with strong electronic correlations, in which the exchange momentum is small ($q_c \ll 2p_F$), the vertex function P_V is a positive quantity. This circumstance leads to an increase in the coupling constant λ and binding energy $|\varepsilon_b|$ in nonadiabatic systems in comparison with adiabatic ones. Here the order parameter Δ increases in accordance with Eq. (27).

The presence of a two-particle bound state leads to the Schaffroth picture of condensation of local pairs.[16] The absence of such a state leads to the Cooper pairing picture. In band language, the transition from the Cooper to the Schaffroth regime is due to the excursion of the chemical potential μ into the forbidden band, whereupon the energy gap in the superconductor is given by the quantity $\sqrt{\mu^2+\Delta^2}$. In accordance with Eq. (27) we have $\overline{\mu} > 0$ for $\varepsilon_F > |\varepsilon_b|/2$. Such a situation corresponds to the Cooper pairing picture. In the case $\overline{\mu} < 0$ for $\varepsilon_F < |\varepsilon_b|/2$, local-pair condensation arises (the Schaffroth scenario). At the point $\overline{\mu} = 0$, $\varepsilon_F^{\rm cr} = |\varepsilon_b|/2$ there is a crossover from Cooper pairing of particles to a state of condensation of local pairs. This crossover occurs at higher values of ε_F in nonadiabatic systems than in adiabatic systems.

4. VERTEX AND CROSSING FUNCTIONS

To elucidate the dependence of Δ and μ on the charge-carrier density n or Fermi energy ε_F it is necessary to calculate the vertex P_V and crossing P_C functions in accordance with their definition (10), (11).

We use the method of direct calculation developed in Refs. 11–13 with allowance for the small values of the cutoff momentum of the electron–phonon interaction ($q_c \ll 2p_F$). We also consider the weak-coupling approximation ($\Delta \ll \omega_0$), which makes it possible to use in calculating the functions P_V and P_C the expressions for the Green's function (12) for the normal state ($\Sigma_S = \Delta Z = 0$). At values $\mu > 2EQ_c^2$ ($Q_c^2 \ll 1$, $E = 4\varepsilon_F$) we find that the quantities

$$P_{V,C}(Q_c, \Omega, \Omega_1) = \frac{\pi}{Q_c} \ll \Theta(q_c - |\mathbf{p} - \mathbf{p}_1|) \times P_{V,C}(\mathbf{p}, \mathbf{p}_1, \Omega, \Omega_1) \tag{30}$$

are given in the particular case $\Omega = 0$, $\Omega_1 = \omega_0$ (see Refs. 29 and 30 for the more general case) by the expressions

$$P_V(Q_c, 0, \omega_0) = \frac{A(0,\omega_0)}{\omega_0} - \frac{E^2}{\omega_0^2}\left[\frac{A(0,\omega_0)}{\omega_0} - \omega_0 B(0,\omega_0) \right] \frac{1}{2} Q_c^4.$$

$$P_C(Q_C, 0, \omega_0) = \frac{A(0,\omega_0)}{\omega_0} - \frac{E^2}{\omega_0^2}\left[\frac{A(0,\omega_0)}{\omega_0} - \omega_0 B(0,\omega_0) \right] \times \frac{11}{6} Q_c^4 + \frac{E}{\omega_0} C(0,\omega_0) Q_c^2, \tag{31}$$

where

$$\frac{A(0,\omega_0)}{\omega_0} = \frac{\pi}{4} - \frac{1}{2}\left(\tan^{-1}\frac{\omega_0}{\mu+\omega_0} + \tan^{-1}\frac{\omega_0}{W-\mu+\omega_0} \right),$$

$$\omega_0 B(0,\omega_0) = -\frac{\omega_0 - (\mu+\omega_0)[(\mu+\omega_0)^2 + 2\omega_0^2]}{2[(\mu+\omega_0)^2+\omega_0^2]^2} - \frac{\omega_0(W-\mu+\omega_0)}{2[(W-\mu-\omega_0)^2+\omega_0^2]^2}[(W-\mu+\omega_0)^2 + 2\omega_0^2].$$

$$C(0,\omega_0) = \frac{1}{2}\ln\frac{(W-\mu-\omega_0)}{\mu+\omega_0} - \frac{1}{4}\ln\frac{(W-\mu-\omega_0)^2+\omega_0^2}{(\mu+\omega_0)^2-\omega_0^2}. \tag{32}$$

In calculating the functions P_V and P_C at values in the region $\mu \sim \Delta \ll \omega_0$ we can limit consideration to the case $\mu = 0$, $\Delta = 0$, allowing us to set $\varepsilon_F = 0$. In this way we obtain the following expression for $P_{V,C}^0 = P_{V,C}|_{\mu=0}$:

$$P_V^0(Q_c, 0, \omega_0) = P_C^0(Q_c, 0, \omega_0) = \frac{\pi}{8} - \frac{1}{2}\tan^{-1}\frac{\omega_0}{\omega_0 - W}. \tag{33}$$

5. NUMERICAL CALCULATIONS AND CONCLUSIONS

We have considered the behavior of the order parameter Δ and chemical potential μ at $T = 0$ in the whole range of values of the charge-carrier density ($0 < \varepsilon_F < \infty$) in quasi-two-dimensional systems with strong electronic correlations.

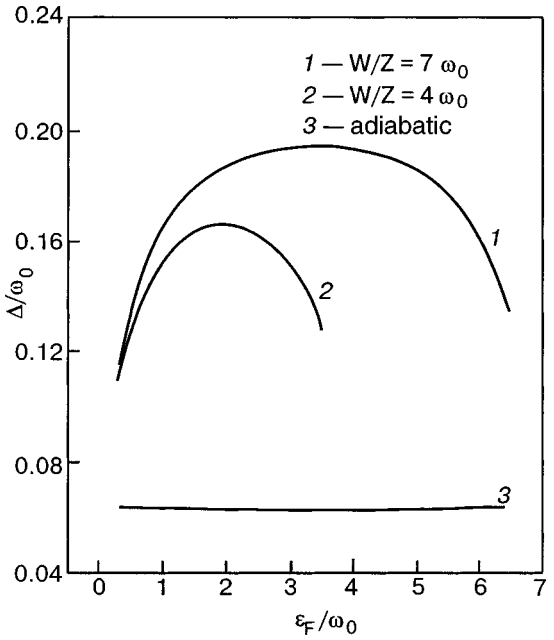

FIG. 1. Dependence of the order parameter Δ on the charge-carrier density (Fermi energy ε_F) in a nonadiabatic system (curves *1* and *2*) and in an adiabatic system (curve *3*).

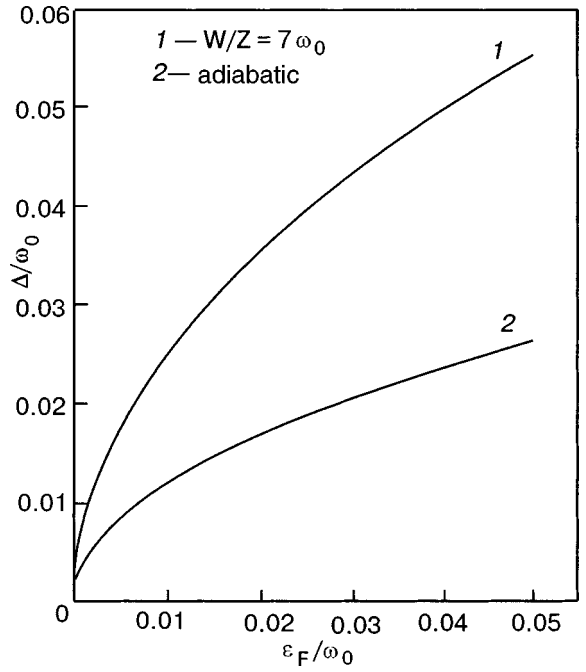

FIG. 2. Dependence of the order parameter Δ on the Fermi energy ε_F in the region of low charge-carrier densities.

The latter were taken into account indirectly through a cutoff of the electron–phonon interaction at a small value of the exchange momentum $q_c < 2p_F$ (Refs. 22 and 23). In the definition of the mass operators Σ_S and Σ_N the terms linear in the nonadiabaticity are taken into account in analogy with Ref. 13, making it possible to estimate the contribution of the many-particle effects that lead to violation of the Migdal theorem[11] and to the corresponding change in the Eliashberg equations.[32]

We have considered the weak-coupling approximation ($\Delta \ll \omega_0$), which made it possible to calculate the vertex and crossing functions (10), (11) and to write the system of equations for determining Δ and μ in the form (20)–(22). This system admits analytical solution. For $\mu \gg \Delta$ Eq. (22) implies that $\mu \approx \varepsilon_F$, and the parameter Δ is given by expression (23).

Figure 1 shows the dependence of Δ on ε_F for all values $\mu \approx \varepsilon_F \gg \Delta$. This region, of course, also includes the values $\varepsilon_F \sim \omega_0$, since $\Delta \ll \omega_0$. We have a bell-shaped dependence of Δ on ε_F. The height and width of this bell curve increase with increasing energy band width W. At points near the maximum the parameter Δ can reach values corresponding to certain oxide ceramics even at an electron–phonon coupling constant $\lambda = 0.5$, the value used in these calculations.

This picture is radically different from the results for adiabatic systems ($P_V = P_C = 0$), which are shown by the straight line *3* in this figure (see Refs. 27 and 28).

We note that a "bell-shaped" dependence of T_c and Δ on the charge-carrier density is observed in numerous experiments on the superconducting materials of today (see, e.g., the review[33]).

In the region of values $\mu \sim \Delta$ ($\varepsilon_F \ll \omega_0$) the solution of the system of equations (20)–(22) in the weak-coupling approximation leads to the results (27). The dependence of Δ and μ on ε_F is presented in Figs. 2 and 3, respectively. Curves *1* in these figures correspond to nonadiabatic systems, while curves *2* correspond to adiabatic systems ($P_V = P_C = 0$). It follows from Fig. 2 that nonadiabaticity effects increase the values of the order parameter Δ by more than a factor of two in comparison with the case of ordinary superconductors in the region of values considered, $\varepsilon_F \ll \omega_0$. However, at values in the region $\varepsilon_F \sim \omega_0$ (see Fig. 1) the nonadiabaticity effects can lead to a 4–5-fold increase in the order parameter in comparison with the results of Migdal–Eliashberg theory. Figure 3 shows the growth of the chemical potential from negative to positive values with increasing ε_F near the crossover from Cooper pairs to the condensation of

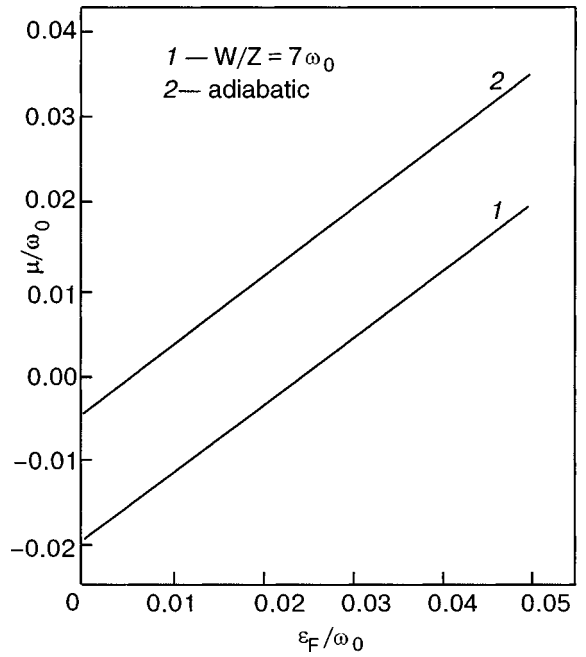

FIG. 3. Relation between the chemical potential μ and the Fermi energy ε_F near the crossover from the BCS state to the condensation of local pairs.

local pairs. Nonadiabaticity effects increase the value of $\varepsilon_F^{\rm cr}$ at which this crossover occurs at the point $\mu=0$. In the weak-coupling approximation ($\Delta \ll \omega_0$) for $\Delta \sim \mu$ the region of the Schaffroth states is small ($\varepsilon_F/\omega_0 \ll 1$).

This transition is more intense for the strong-coupling case ($\Delta \sim \omega_0$), which requires a separate treatment and more effort, since the calculation of P_V and P_C for the case of nonadiabatic systems is complicated, and there is a wider range of ε_F values for which Bose condensation of local pairs can occur. However, by taking into account the substantial contribution of the nonadiabatic corrections for $\varepsilon_F \sim \omega_0$ in the weak-coupling approximation, one can say with certainty that the picture of the dependence of Δ on ε_F is altered both quantitatively and qualitatively in comparison with the case of adiabatic systems.[27,28] Our studies permit us to draw the following conclusions:

(1) Nonadiabatic effects and strong electronic correlations, which violate the Migdal theorem, can be regarded in a wide range of ε_F values (see Fig. 1) as mechanisms which lead to a substantial increase of the order parameter at $T=0$, to values typical of high-T_c superconducting materials.
(2) The dependence of the order parameter on the charge-carrier density has the form of a bell curve, the width and height of which increase with increasing width of the energy band.
(3) For $\mu \sim \Delta$ and $\varepsilon_F \ll \omega_0$ the scenario of superconductivity can change due to a transition from Cooper pairing of particles to the Schaffroth condensation of local pairs. Here in systems with strong electronic correlations the nonadiabatic effects increase the binding energy of the two-particle state, and that in turn leads to an increase of the order parameter and to a decrease of the chemical potential in comparison with ordinary superconductors. The crossover from the BCS to the Schaffroth scenario of superconductivity in nonadiabatic systems with strong electronic correlations takes place at charge-carrier densities (values of the Fermi energy) larger than in ordinary superconductors.

*E-mail: statphys@asm.md

[1] V. A. Moskalenko, M. E. Palistrant, and V. M. Vakalyuk, Usp. Fiz. Nauk **161**, 155 (1991) [Sov. Phys. Usp. **34**, 717 (1991)].
[2] M. E. Palistrant and F. G. Kochorbe, Physica C **194**, 351 (1992).
[3] F. G. Kochorbé and M. E. Palistrant, Zh. Éksp. Teor. Fiz. **104**, 3084 (1993) [JETP **77**, 442 (1993)]; Teor. Mat. Fiz. **26**, 459 (1993) [Theor. Math. Phys. **96**, 1083 (1993)].
[4] V. A. Moskalenko, L. Z. Kon, and M. E. Palistrant, *Low-Temperature Properties of Metals with Band-Spectrum Singularities* [in Russian], Shtiintsa, Kishinev (1989).
[5] J. E. Hirsch and D. J. Scalapino, Phys. Rev. Lett. **56**, 2732 (1986).
[6] J. Friedel, J. Phys.: Condens. Matter **1**, 7757 (1989).
[7] A. A. Abrikosov, J. C. Campuzano, and K. Gofron, Physica C **214**, 73 (1993).
[8] W. Weber, Adv. Solid State Phys. **28**, 141 (1988).
[9] V. A. Ginzburg and E. G. Maksimov, Sverkhprovodimost' (KIAE) **5**, 1453 (1992) [Superconductivity **5**, 1505 (1992)].
[10] G. M. Vujicic, V. L. Aksenov, N. M. Plakida, and S. Stamennovic, Phys. Lett. A **73**, 439 (1979); J. Phys. C **14**, 2377 (1981).
[11] A. B. Migdal, Zh. Éksp. Teor. Fiz. **34**, 1438 (1958) [Sov. Phys. JETP **7**, 996 (1958)].
[12] L. Pietronero, S. Strassler, and C. Grimaldi, Phys. Rev. B **52**, 10516 (1995).
[13] C. Grimaldi, L. Pietronero, and S. Strassler, Phys. Rev. B **52**, 10530 (1995).
[14] N. R. Schaffroth, Phys. Rev. **111**, 72 (1958).
[15] M. Randeria, J. Duan, and L. Shien, Phys. Rev. Lett. **62**, 981 (1989); Phys. Rev. B **41**, 327 (1990).
[16] A. J. Leggett, *Modern Trends in the Theory of Condensed Matter*, Springer-Verlag, Berlin (1980).
[17] É. V. Gorbar, V. P. Gusynin, and V. M. Loktev, Sverkhprovodimost' (KIAE) **6**, 483 (1992); Fiz. Nizk. Temp. **19**, 1171 (1993) [Low Temp. Phys. **19**, 832 (1993)].
[18] A. A. Gorbatsevich and I. V. Tokatly, Zh. Éksp. Teor. Fiz. **103**, 702 (1993) [JETP **76**, 347 (1993)].
[19] E. V. Gorbar, V. M. Loktev, and S. G Sharapov, Fiz. Nizk. Temp. **21**, 421 (1995) [Low Temp. Phys. **21**, 329 (1995)].
[20] M. E. Palistrant, Teor. Mat. Fiz. **105**, 491 (1995); **109**, 137 (1996) [Theor. Math. Phys. **105**, 1593 (1995); **109**, 1352 (1996)]; M. E. Palistrant, J. Supercond.: Incorporation Novel Magnetism **10**, 19 (1997).
[21] A. A. Abrikosov, L. P. Gor'kov, and I. E. Dzyaloshinskiĭ, *Methods of Quantum Field Theory in Statistical Physics*, Prentice-Hall, Englewood Cliffs, New Jersey (1963), Nauka, Moscow (1962).
[22] M. L. Kulik and R. Zeyher, Phys. Rev. B **49**, 4395 (1994).
[23] R. Zeyher and M. L. Kulik, Phys. Rev. B **53**, 2850 (1996).
[24] W. L. McMillan, Phys. Rev. **167**, 331 (1968).
[25] M. E. Palistrant, Teor. Mat. Fiz. **455**, 119 (1999) [Theor. Math. Phys. **119**, 761 (1999)].
[26] M. E. Palistrant and F. G. Kochorbe, J. Supercond.: Incorporation Novel Magnetism **15**, 113 (2002).
[27] V. M. Loktev and S. G. Sharapov, Fiz. Nizk. Temp. **22**, 271 (1996) [Low Temp. Phys. **22**, 211 (1996)]; Preprint ITF-95-18 R (1995) [in Russian].
[28] V. M. Loktev, R. M. Quick, and S. G. Sharapov, Phys. Rep. **349**, 1 (2001).
[29] M. E. Palistrant and F. G. Kochorbe, J. Phys.: Condens. Matter **12**, 2217 (2000).
[30] M. E. Palistrant, Fiz. Nizk. Temp. **26**, 557 (2000) [Low Temp. Phys. **26**, 407 (2000)].
[31] R. Combescot, Phys. Rev. B **42**, 7810 (1990).
[32] G. M. Éliashberg, Zh. Éksp. Teor. Fiz. **38**, 966 (1960) [Sov. Phys. JETP **11**, 696 (1960)].
[33] N. M. Plakida, *High-Temperature Superconductivity*, Springer-Verlag, Berlin (1995), Mezhdunarodnaya Programma Obrazovaniya, Moscow (1996).

Translated by Steve Torstveit

Inhomogeneity of the pseudogap state of a doped layered cuprate antiferromagnet

G. G. Sergeeva*

Kharkov Physicotechnical Institute National Research Center, ul. Akademicheskaya 1, 61108 Kharkov, Ukraine

(Submitted April 18, 2003)
Fiz. Nizk. Temp. **29**, 1181–1188 (November 2003)

The features of the pseudogap state in doped layered cuprate antiferromagnets and underdoped high-T_c superconductors (HTSCs) are investigated. It is shown that the transition to the pseudogap state is a dimensional crossover from three-dimensional motion to two-dimensional motion of charges in the copper–oxygen planes, which leads to the coexistence of light charge carriers and Jahn–Teller polarons and to the development of strong local correlations, as are characteristic for two-dimensional doped Mott–Hubbard insulators. In a doped antiferromagnet the d-wave pairing of light charge carriers and Jahn–Teller polarons leads to the formation of magnetic and bosonic clusters, i.e., substantial inhomogeneity of the copper–oxygen planes arises. It is found that the change in the properties of a doped layered cuprate antiferromagnetic insulator and in the metallic and superconducting states of an underdoped HTSC with decreasing temperature is due to a repeated dynamic reduction of their dimensionality. A model phase diagram in terms of the temperature and dopant concentration is proposed. © *2003 American Institute of Physics.* [DOI: 10.1063/1.1614233]

1. INTRODUCTION

It has become obvious that an understanding of the nature of the pseudogap state of underdoped cuprate high-T_c superconductors (HTSCs) will be the key to the problem of high-temperature superconductivity. This assertion is based on the observation of changes in the density of states at $T \leqslant T^*$ and the formation of a coherent superconducting state at T_c at a practically constant density, and also evidence of the development of superconducting fluctuations at $T^* > T > T_c$ (here $T^*(\delta)$ is the temperature of the transition to the pseudogap state, which depends on the dopant concentration δ). Measurements of the optical conductivity[1–3] and spin susceptibility at $T^* > T > T_c$ (Ref. 4) suggest the coexistence of heavy charge carriers (small polarons) and light charge carriers (holes and electrons, in view of the nesting of the hole and electron parts of the Fermi surface).

Upon doping of cuprate antiferromagnets, because of the Jahn–Teller effect the purely electronic degeneracy is replaced by a more complex vibrational degeneracy of the whole complex around the Cu^{2+} ion, i.e., are strong Jahn–Teller distortions arise. In the present paper it is shown that the transition of a doped layered cuprate antiferromagnet to the pseudogap state is a dimensional crossover from three-dimensional motion to two-dimensional motion of charges in the copper–oxygen (CuO_2) planes. For such an antiferromagnet this two-dimensionality at $T \leqslant T^*$ is responsible for the important role of the Jahn–Teller (JT) distortions, which lead to the formation of two-site Jahn–Teller (TSJT) polarons, which are simultaneously both ''heavy'' charge carriers and carriers of the antiferromagnetic (AF) properties of the CuO_2 planes. Then it becomes important to take into account the strong local correlations characteristic for a two-dimensional doped insulator.[5] We consider the possibility of the formation of local pairs consisting of a TSJT polaron and a light charge carrier at $T \leqslant T^*$, both in a doped AF insulator and in the metallic state of a doped antiferromagnet. This gives rise to local ordering of the spins of the holes and the spins of the Cu^{2+} ion in the CuO_2 planes and leads to the formation of magnetic and bosonic clusters. The magnetic clusters, formed by TSJT polaron–electron pairs in the absence of magnetic field are regions with local AF ordering. The charge of such a cluster is equal to zero, and the total spin is equal to 1 or 0. In the metallic state of a doped antiferromagnet as the temperature is lowered, TSJT polaron–hole pairs are formed, with a charge of $2e$ and a total spin equal to zero; these lead to bosonic clusters and to the development of superconducting fluctuations.

2. DIMENSIONAL CROSSOVER OF THE CHARGE MOTION

For doped AF insulators and underdoped HTSCs at $k_B T > t_c^2(T)/t_{ab}$ the coherent transport of charge along the c axis occurs on account of thermal fluctuations (t_c and t_{ab} are the probability of tunneling of a charge along the c axis and in the CuO_2 plane). As the temperature rises, thermal fluctuations limit the tunneling of charge along the c axis, and the conductivity of charge carriers in the plane increases. This leads to an unscreened long-range Coulomb interaction, which is a characteristic feature for a two-dimensional doped Mott insulator; as a result, the motion of the charge along the c axis is governed by the cooperative motion of charges in the plane.[5,6] Here the tunneling probability t_c is substantially temperature-dependent. With decreasing temperature the thermal fluctuations no longer are sufficient for charge transport along the c axis, so that at

$$k_B T^* = t_c^2(T^*)/t_{ab}$$

a dimensional crossover occurs from three-dimensional motion of the charge to two-dimensional, i.e., the transition to the pseudogap state is a result of a dynamic reduction of the

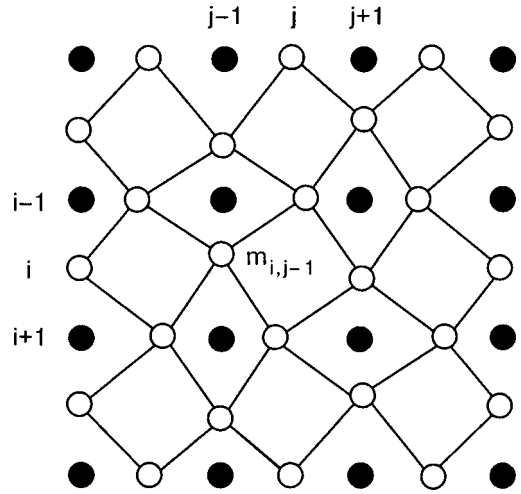

FIG. 1. JT distortions of the positions of the oxygen ions (○) in the copper–oxygen plane around four nearest copper ions (●) due to the JT phonon mode Q_2 of vibrations of the O^{2-} ions of the oxygen complex of two adjacent copper ions, with a common oxygen ion at the site $m_{i,j-1}$ (i and j are the numbers of the rows and columns containing O^{2-} ions).

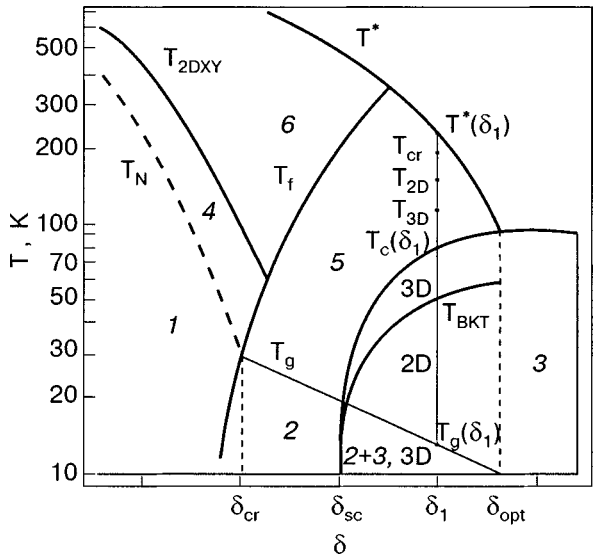

FIG. 2. Model phase diagram of doped layered antiferromagnets and HTSCs in terms of the concentration δ. Here δ_{cr} is the maximum doping that does not destroy the AF state; δ_{sc} is the minimum concentration at which a transition to a superconducting state is observed; δ_{opt} is the optimal dopant concentration of the HTSC; T_N is the Néel temperature for the AF state (region *1*); T_{2DXY} is the temperature of the transition from the magnetically disordered region *6* to two-dimensional XY magnetic ordering of the copper spins (region *4*); T_f is the temperature of the local ordering of the hole spins and spins of the copper in the CuO_2 plane (regions *2,5*); T_g is the temperature of the transition to a three-dimensional cluster-spin-glass state (region *2* in a doped AF insulator and region *2+3* in a three-dimensional superconducting state); T^* is the temperature of the transition to the pseudogap state (region *5*); T_c is the temperature of the transition to a three-dimensional superconducting state (regions 3D and *2+3*); T_{BKT} is the temperature of the Berezinskii–Kosterlitz–Thouless transition to a superconducting state (region 2D). For THSCs with a dopant concentration $\delta_{sc}<\delta<\delta_{opt}$ the formation of local pairs of TSJT polarons and holes occurs at the temperature T_{cr}; T_{2D} and T_{3D} are the temperatures of the transition to 2D and 3D superconducting fluctuations.

dimensionality of the charge motion.[7] For this reason one can assume that the pseudogap is an analog of the dynamic Coulomb gap (Ref. 5).[1)]

The two-dimensional character of the charge motion at $T \leqslant T^*$ leads to a substantial change of the states of hole quasiparticles interacting with JT phonon modes—to the appearance of quasilocal and local hole states—independently of the interaction potential. The interactions of hole excitations with the JT modes Q_4 and Q_5 give rise to the formation of local states—three-spin polarons with spin 1/2 and parallel Cu^{2+} spins, chains of which form narrow stripes in the CuO_2 planes.[7,8] The interaction of holes with the JT mode Q_2 of vibrations of the seven oxygen ions surrounding two adjacent copper ions with a common oxygen ion at the site $m_{i,j-1}$ (i and j are the numbers of rows and columns with O^{2-} ions; Fig. 1) leads to a quasilocal hole state, i.e., to a TSJT polaron with total spin 1/2 (see Ref. 7 and references cited therein). The TSJT polaron is simultaneously a charge carrier and a carrier of AF properties of the plane, i.e., a heavy charge carrier with an AF core. This hole, which moves with low damping in the CuO_2 plane via the oxygen complexes of the two copper ions nearest to the site $m_{i,j-1}$ with Jahn–Teller distortion of the positions of the O^{2-} ions by the Q_2 mode, which corresponds, for example, to the displacements of the TSJT polaron via the sites $m_{i,j-1} \rightarrow m_{i-1,j} \rightarrow m_{i,j+1} \rightarrow m_{i+1,j}$ (Fig. 1). As is seen in Fig. 1, it is only for the 12 oxygen ions at the boundaries of the region around the four copper ions, one of which is divalent, that the position is almost undistorted by the Q_2 mode. For small $\delta < \delta_{cr}$ (δ_{cr} is the maximum doping that does not destroy the AF state; Fig. 2) and $T_{2DXY} < T < T^*$, where T_{2DXY} is the temperature of the two-dimensional XY ordering, the number of charge carriers is small, and the mobility of the TSJT polarons is low.

In doped antiferromagnets the dispersion relations for the holes and electrons typically are nested, the Fermi surface consisting of electron and hole parts which are nearly coincident upon translation in certain directions by a wave vector $\mathbf{Q}$ of the AF cell ($\mathbf{Q}=\mathbf{K}/2$, where $\mathbf{K}$ is a reciprocal lattice vector of the crystal). Allowance for the existence of electrons (light charge carriers from a nesting region of width $\mathbf{Q}$) is especially important for the pseudogap state of a doped AF insulator, when almost all of the holes become polarons, i.e., heavy charge carriers. As the dopant concentration increases and there is more than one charge carrier for each transition metal ion, a doped AF insulator (e.g., WO_{3-x}; Ref. 9) goes into a metallic state with heavy charge carriers (JT polarons) and light charge carriers (holes and electrons from the nesting region). Convincing evidence that the heavy charge carriers for $T \leqslant T^*$ have a magnetic nature both in the AF insulator and in the metallic state is provided by the observation of a doublet structure of the two-magnon absorption band in metallic YBCO films, where the first component of the doublet is identical to the absorption band in the AF insulator.[10] Then it becomes possible in principle for TSJT polaron–light charge carrier pairs to form both in the doped AF insulator for $\delta_{cr} < \delta < \delta_{sc}$ and in the metallic state for $\delta_{sc} < \delta < \delta_{opt}$. Here δ_{sc} is the minimum dopant concentration at which the transition to the superconducting state is observed, and δ_{opt} is the optimal dopant concentration of the HTSC (Fig. 2).

3. FORMATION OF HEAVY–LIGHT CHARGE CARRIER PAIRS IN THE CuO_2 PLANES

For underdoped HTSCs the coexistence of heavy and light charge carriers at $T^*>T>T_c$ has stimulated interest in studying the possibility of their pairing, but the mechanism of suppression of the one-site Coulomb repulsion has been unclear.[11] It was first shown by Kudinov[12] that it is possible in principle for the one-site Coulomb repulsion to be suppressed by the polaron energy shift in the pairing of a Zhang–Rice polaron with a hole. The Kudinov model is easily generalized to TSJT polarons interacting with light charge carriers if all the renormalized interactions between charge carriers are conserved in the Hamiltonian after a canonical transformation. In doped antiferromagnets the number of TSJT polarons $n_p>n_h$ (n_h is the number of holes), and therefore, being interested in the interactions of TSJT polarons with light charge carriers, we must take into account both the hole contribution and the contribution of electrons from the nesting region. The Coulomb interaction between charge carriers,

$$H_c=\sum_{m,\sigma,\sigma'} A(m_1,m_2,m_3,m_4)a^+_{m_1\sigma}a^+_{m_2\sigma}a_{m_3\sigma'}a_{m_4\sigma'}, \tag{1}$$

with $m_1=m_4$, $m_2=m_3$, does not involve actual transport of charge with spin σ from site m_i to site m_j, does not change after the canonical transformation

$$U=\prod_m \exp\left| i\frac{x_0}{\hbar}\sum_\sigma n_{m\sigma}p_m\right|,$$

where x_0 is the coordinate of the oxygen ion about which it is vibrating, and p_m is its momentum.[12] Here $n_{m\sigma}=a^+_{m\sigma}a_{m\sigma}=b^+_{m\sigma}b_{m\sigma}$, $\tilde{n}_{m\sigma}=d^+_{m\sigma}d_{m\sigma}$, with the creation operators for light and heavy charge carriers with spin σ at site m: $a^+_{m\sigma}$ for a hole, $b^+_{m\sigma}=\exp(ix_0p_m)a^+_{m\sigma}$ is a TSJT polaron, and $d^+_{m\sigma}$ for an electron from the nesting region. Assuming that there is no magnetic and charge ordering, we may keep in (1) the one-site terms with Hubbard repulsion $A_{\rm ph}>0$ between the JT polarons and holes, and with the attraction $A_{pe}<0$ between the TSJT polarons and electrons from the nesting region:

$$H_c=2A_{\rm ph}\sum_m n_{m\uparrow}n_{m\downarrow}+2A_{pe}\sum_m n_{m\uparrow}(\tilde{n}_{m\uparrow}+\tilde{n}_{m\downarrow}). \tag{2}$$

Generalization of the Kudinov model[12] for TSJT polarons with spin 1/2 in the lowest approximation in the interactions J between holes and $J_1<J$ between holes and electrons from the nesting region leads to the Hamiltonian

$$\mathcal{H}=\mathcal{H}_H+V+V_1,$$

$$\mathcal{H}_H=\sum_{m,g,\sigma}[2(-E_p+A_{\rm ph})n_{m\uparrow}n_{m\downarrow}+2A_{pe}n_{m\uparrow}(\tilde{n}_{m\uparrow}+\tilde{n}_{m\downarrow})], \tag{3}$$

$$V=J\sum_{m,g,\sigma}(\Lambda a^+_{m\sigma}a_{m+g,\sigma}+\Lambda^{1/2}a^+_{m\sigma}b_{m+g,\sigma}),$$

$$V_1=J_1\sum_{m,g,\sigma}\Lambda^{1/2}b^+_{m\sigma}d_{m+g,\sigma}. \tag{4}$$

Here $\mathcal{H}_H$ is a Hamiltonian with attraction of the Hubbard type, and E_p is the polaron energy shift, which is proportional to the JT stabilization energy. In formulas (4) we have taken into account the renormalization $\Lambda=\exp(-E_p/\hbar\omega)$ of the interaction J between holes by the canonical transformation and the renormalization $\Lambda^{1/2}$ of the interactions of J_1 between light and heavy charge carriers (ω is the frequency of TSJT vibrations of the oxygen ions). It can be seen in (3) that it is possible in principle to form a TSJT polaron–light charge carrier pair, which occupies the TSJT polaron complex. The circumstance that the TSJT polaron is simultaneously a heavy charge carrier and a carrier of the AF properties of the CuO_2 plane requires that the order parameter be symmetry-compatible with the magnetism, i.e., a d-wave symmetry. The formation of local TSJT polaron–hole pairs occurs only in the case when the Coulomb repulsion is compensated by a polaron shift $|E_p|>A_{\rm ph}$ at temperatures $T_{\rm cr}(\delta)\sim|-E_p+A_{\rm ph}|$. For $A_{pe}<0$ the temperature of formation of TSJT polaron–electron pairs, $T_f(\delta)$, can be called the local ordering temperature for the spins of charge carriers and the spins of the copper in the CuO_2 planes of the doped antiferromagnet. In the AF state at low concentrations $\delta<\delta_{\rm cr}$ the ordering processes for the hole and copper spins occur independently—the hole spins order at the temperature $T_f(\delta)$, while the copper spins order at $T_N(\delta)$ (see Fig. 2). With increasing concentration at $\delta>\delta_{\rm cr}$ the local ordering of the spins leads for $T\leqslant T_g(\delta)$ to a transition to a three-dimensional cluster-spin-glass state.[13] For $\delta_{\rm cr}<\delta<\delta_{sc}$ in the pseudogap state of a doped AF insulator, local ordering of the spins of the charge carriers and copper occurs at $T\leqslant T_f(\delta)\leqslant T^*(\delta)$ as a result of the formation of TSJT polaron–electron pairs, which causes a decrease in the number of charge carriers. The charge of such a pair is equal to zero, while the total spin is equal to unity if the spins of the polaron and electron are parallel, or to zero if they are antiparallel. In the metallic state of a doped antiferromagnet for $\delta_{sc}<\delta<\delta_{\rm opt}$, in addition to the TSJT polaron–electron pair, for $T\leqslant T_{\rm cr}(\delta)$ TSJT polaron–hole pairs also form (bosons with charge $2e$).

4. GROUND-STATE WAVE FUNCTIONS

The ground-state wave functions of this system of carriers in the CuO_2 plane for $|-E_p+A_{\rm ph}|\gg J\Lambda^{1/2}$ and $A_{pe}\gg J_1\Lambda^{1/2}$ can be sought in the BCS model by breaking the Hamiltonian (3) into two parts:

$$\mathcal{H}=\mathcal{H}_1+\mathcal{H}_2,$$

$$\mathcal{H}_1=\sum_{m,g,\sigma}2(-E_p+A_{\rm ph})n_{m\uparrow}n_{m\downarrow}+V, \tag{5}$$

$$\mathcal{H}_2=\sum_{m,g,\sigma}2A_{pe}n_{m\uparrow}(\tilde{n}_{m\uparrow}+\tilde{n}_{m\downarrow})+V_1, \tag{6}$$

where $\mathcal{H}_1$ includes only the interaction between TSJT polarons and holes and $\mathcal{H}_2$ that between TSJT polarons and electrons from the nesting region.

There is no long-range order in the plane and there is no phase coherence in k space, since the ground-state wave functions $\Psi_{\rm ph}(\chi)$ of the TSJT polaron–hole pairs (with wave vector equal to zero) and $\Psi_{pe}(\chi,Q)$ of the local pairs be-

tween TSJT polarons and electrons from the nesting region (with pair wave vector Q) depend on the real function $\chi(k) \neq \text{const}$

$$\psi_{\text{ph}}(\chi) = \prod_k \ (u_k + e^{i\chi(k)} v_k a^+_{k\uparrow} b^+_{-k\downarrow}) |0\rangle, \tag{7}$$

$$\psi_{pe}(\chi, Q) = \prod_k \ (u'_k + e^{i\chi(k)} v'_k d^+_{k+Q/2\uparrow} (b^+_{-k+Q/2,\downarrow} + b_{-k+Q/2\uparrow}) |0\rangle, \tag{8}$$

where the variational parameters v_k, u_k and v'_k, u'_k are periodic and analytic functions of the wave vector **k**. After going over to a product over lattice sites in (7) and (8), we have

$$\psi_{\text{ph}}(\chi) = c_1 \prod_m \ \exp \hat{R}_1(m) |0\rangle, \tag{9}$$

$$\hat{R}_1(m) = \frac{1}{2} \sum_G \ S_1(G) (a^+_{m\uparrow} b^+_{m-G,\downarrow} + a^+_{m-G,\uparrow} b^+_{m\downarrow}),$$

$$\Psi_{pe}(\chi, Q) = c_2 \prod_m \ \exp \hat{R}_2(m) |0\rangle, \tag{10}$$

$$\hat{R}_2(m) = \frac{1}{2} \sum_G \ S_2(G) [(d^+_{m\uparrow} b^+_{m-G,\uparrow} + d^+_{m-G,\uparrow} b^+_{m\uparrow}) + (d^+_{m\uparrow} b^+_{m-G,\downarrow} + d^+_{m-G,\uparrow} b^+_{m\downarrow})].$$

Here **G** is an arbitrary lattice vector in the copper–oxygen plane, c_1 and c_2 are arbitrary constants, and the functions

$$S_1(G) = \sum_k \ \frac{v_k}{u_k} \exp i(\mathbf{kG} + \chi(k)),$$

$$S_2(G) = \sum_k \ \frac{v'_k}{u'_k} \exp i[(\mathbf{k} + \mathbf{Q}/2)\mathbf{G} + \chi(k)] \tag{11}$$

for $|G| \to \infty$ fall off faster than any power of $|G|^{-1}$. The contribution to the wave functions $\Psi_{\text{ph}}(\chi)$ and $\Psi_{pe}(X, Q)$ in (9), (10) from states with $|G| \to \infty$ falls off exponentially with a characteristic correlation length $L \sim \hbar v_F / kT_{\text{cr}} > 4R_{\text{Cu–O}}$ (v_F is the velocity on the Fermi surface). The phase incoherence in (11) can be neglected only for sufficiently large $G > \chi(k)/k$, for which the clusters become three-dimensional. Taking the phase incoherence in the CuO_2 plane into account leads to phase fluctuations with a characteristic energy scale $\sim |-E_p + A_{\text{ph}}|$ for the TSJT polaron–hole pairs and $\sim A_{pe}$ for the TSJT polaron–nesting-region electron pairs and also to the formation of bosonic and magnetic clusters at temperatures $T \leqslant T_{\text{cr}}(\delta) \sim |-E_p + A_{\text{ph}}|$ and $T \leqslant T_f(\delta) \sim A_{pe}$, respectively.

The operators $\exp \hat{R}_1(\mathbf{m})$ and $\exp \hat{R}_2(\mathbf{m})$ acting on the vacuum $|0\rangle$ create different clusters, bosonic and two types of magnetic, with a central oxygen ion at site m and a characteristic length L. The bosonic clusters formed by the TSJT polaron–hole pairs are associated with zero-dimensional (0D) superconducting fluctuations for $T \leqslant T_{\text{cr}}(\delta)$. The magnetic clusters formed by the TSJT polaron–electron pairs are associated with local ordering of the spins of the charge carriers and the spins of the copper in the CuO_2 plane. The minimum sizes of these clusters are determined by the sizes of the regions of TSJT distortions within which the TSJT polaron–light charge carrier pair is delocalized, i.e., approximately 3–4 lattice periods of the CuO_2 plane. As we see in Fig. 1, the JT phonon mode Q_2 causes substantial distortions of all twelve O^{2-} ions around the four central copper ions, one of which is divalent. This leads, for example, to displacements of both the TSJT polaron and of the TSJT polaron–light charge carrier pair via the sites $m_{i,j-1} \to m_{i-1,j} \to m_{i,j+1} \to m_{i+1,j}$ (Fig. 1).

Magnetic clusters with total spin $S = 0$ are clusters with local AF order. Magnetic clusters with $S = 1$ can be regarded as vortexlike excitations with an AF core.[2)] It is important that in the pseudogap state both the clusters with local AF order and the vortexlike excitations with an AF core appear in the CuO_2 plane at $\delta > \delta_{\text{cr}}$ in both doped AF insulators and in the metallic state of a doped antiferromagnet. The magnetic clusters coexist with bosonic clusters in regions with a two-dimensional character of the superconducting fluctuations for $T_{3D} < T < T_{2D}$, where T_{3D} is the temperature of the transition to three-dimensional superconducting fluctuations. In underdoped HTSCs, in which the number of TSJT polarons, n_p, is greater than the number of holes, n_h, the vortexlike excitations with an AF core can also exist for $T_g < T < T_{BKT}$, where the superconducting state has a two-dimensional character.[14,15] Here T_{BKT} is the temperature of the Berezinskii–Kosterlitz–Thouless superconducting transition in an isolated CuO_2 plane (Fig. 2).

The structure of the wave functions $\Psi_{\text{ph}}(\chi)$ and $\Psi_{pe}(\chi, Q)$ is characteristic for Mott localization and, as was shown by Kudinov, is inherent not only to the insulating state but also to the superconducting state in the BCS model.[16] This means that for $T \leqslant T^*$ the two-dimensionality of the charge motion in the CuO_2 planes leads to the absence of competition between the formation of local pairs of charge carriers and their delocalization on clusters. The fact that the formation of the local pairs involves TSJT polarons, which are simultaneously both heavy charge carriers and carriers of the AF properties of the CuO_2 plane, requires that the symmetry of the pairing order parameter be compatible with the magnetism, i.e., a d-wave symmetry both in the AF insulator and in the metallic state of the doped antiferromagnet.

Thus in the pseudogap state of a doped layered cuprate antiferromagnet the pair correlations with d-wave symmetry of the order parameter are "built into" the CuO_2 plane and are a consequence of the strong local correlations which are characteristic for a two-dimensional doped Mott–Hubbard insulator.[5,16] The first evidence of strong local correlations and of the existence of dispersion similar to d-wave modulation for the AF gap was obtained[17] in photoemission studies (ARPES) of the insulator $Ca_2CuO_2Cl_2$. In the absence of magnetic field the total spins of individual vortexlike excitations are directed randomly. Under the influence of a field the spins order, and the vortexlike excitations are manifested in the Nernst effect,[18,19] and after the magnetic field is turned off, they can be reduced to a weak residual magnetization of the sample in the pseudogap state.[20,21] For $\delta_{\text{cr}} < \delta < \delta_{\text{opt}}$ the CuO_2 planes are found in an inhomogeneous state with a different local density of states in the bosonic and magnetic clusters. Direct evidence of local pairing in HTSCs with cluster dimensions ~ 14 Å has recently been obtained[22] in

scanning tunneling microscope (STM) measurements of the local density of states and the energy of the superconducting gap in the superconductor $Bi_2Sr_2CaCu_2O_{8+x}$.

5. DYNAMIC REDUCTION OF DIMENSIONALITY IN THE PSEUDOGAP AND SUPERCONDUCTING STATES

In Secs. 3 and 4 it was shown that the dimensional crossover at $T \leqslant T^*$ leads to elimination of the competition between the formation of local TSJT polaron–light charge carrier pairs and their delocalization on clusters. The characteristic correlation length L of the bosonic clusters (i.e., 0D superconducting fluctuations) increases with decreasing temperature, so that at a temperature $T_c < T < T_{2D} < T_{cr}$ they begin to overlap, and a dimensional crossover occurs from the 0D superconducting fluctuations to two-dimensional (2D) ones. As was shown in Ref. 6, this transition leads to temperature dependence of the coherence length in the CuO_2 plane, $\xi_{ab}(T) = \xi_{ab}(T_{BKT})(T/T_{BKT}-1)^{-1/2}$ and of the probability of charge tunneling along the c axis,

$$t_c(T) = \frac{\xi_c^2(T_{BKT})}{\xi_{ab}^2(T_{BKT})}\left(\frac{T}{T_{BKT}}-1\right),$$

where ξ_c is the coherence length along the c axis for $T = T_{BKT}$. The function $t_c(T)$ decreases with decreasing temperature, and at T_{3D} there is a transition to three-dimensional (3D) fluctuations. The superconducting transition occurs as a two-dimensional transition with a bounded region of 3D superconducting fluctuations, while the transition temperature is determined by the Katz inequality $T_c/E_F \geqslant t_c(T_c)$:[6,23]

$$T_c \geqslant T_{BKT}\frac{\xi_c^2 E_F}{\xi_c^2 E_F - \xi_{ab}^2 T_{BKT}},$$

where E_F is the Fermi energy. Indeed, analysis of the results of measurements[6] of the resistance along the c axis in a Bi-2212 single crystal with $T_c = 80$ K showed that the region of 0D+2D superconducting fluctuations $(T_{cr}-T_{3D}) \approx 120$ K and that the region of 3D fluctuations $(T_{3D}-T_c) \approx 10$ K. The value estimated in Ref. 6 for the temperature $T_{BKT} \sim 56$ K agrees with the universal estimate of the region of three-dimensionality of the superconducting state for $T_c > T > T_{BKT} \sim 0.7T_c$, obtained from the results of measurements of the temperature dependence of the magnetic field penetration depth, which has a universal character for underdoped HTSCs with $T_c < T_{c,\max}$ (see relation (7) and Fig. 1 of Ref. 15). Here the transition to 2D superconducting state for $T \leqslant T_{BKT}$ occurs with decreasing temperature when $\xi_c(T)$ becomes less than the distance between CuO_2 planes.

Thus with decreasing temperature the dynamic reduction of dimensionality of underdoped HTSCs with $\delta_{sc} < \delta < \delta_{opt}$ occurs in a pseudogap state at T^*, T_{cr}, T_{2D}, and T_{3D} and is also observed in the superconducting state at T_{BKT} and T_g. In doped AF insulators with $\delta_{cr} < \delta < \delta_{sc}$ the reduction of dimensionality occurs at temperatures T^* and T_g. Reduction of the dimensionality is manifested in changes in the properties of underdoped HTSCs and doped AF insulators at these temperatures and leads to a complex magnetic phase diagram as a function of concentration δ. A model of such a diagram is shown in Fig. 2.[3)] As is seen in Fig. 2, in a doped antiferromagnet the line $T_f(\delta)$ at dopant concentrations $\delta > \delta_{cr}$ separates the region of the disordered state of the copper and hole spins and the region of their local ordering. This ordering for $T \leqslant T_f(\delta)$ leads to a decrease of the number of light and heavy charge carriers and to the appearance of magnetic clusters with local AF order and vortexlike excitations with an AF core. For the pseudogap state their existence region is bounded by the curves $T_f(\delta)$, $T^*(\delta)$, $T_g(\delta)$, and $T_{3D}(\delta)$, and for $T_{cr}(\delta) > T \gg T_{3D}(\delta)$ these excitations coexist with bosonic clusters.

6. CONCLUSION

We have shown that for doped cuprate layered antiferromagnets the transition to the pseudogap state is a result of a dynamic reduction of the dimensionality of the charge motion from three-dimensional to two-dimensional. The two-dimensionality leads to the coexistence of light charge carriers and JT polarons, which are simultaneously both heavy charge carriers and carriers of the antiferromagnetic properties of the copper–oxygen planes. For underdoped HTSCs the coexistence of heavy and light charge carriers plays a decisive role, since the polaron energy shift is compensated by the one-site Coulomb repulsion of the JT polarons and holes and leads to attraction between them for $T < T_{cr}(\delta) < T^*$. We have established that in the pseudogap state it is possible in principle to form local JT polaron–light charge carrier pairs, the symmetry of the order parameter of which must be compatible with the AF core of the JT polarons. Here the pair correlations with d-wave symmetry of the order parameter are ''built into'' the CuO_2 plane and are a consequence of the strong local correlations characteristic for a two-dimensional doped Mott–Hubbard insulator.

We have shown that the d-wave pairing of light and heavy charge carriers in the pseudogap state leads to the formation of clusters with a local AF ordering of the copper spins in them, i.e., to an inhomogeneous state of the CuO_2 planes. In a doped AF insulator the TSJT polaron–electron pairs cause the formation of two types of magnetic clusters. In the metallic state of a doped antiferromagnet the TSJT polaron–hole pairs lead to bosonic clusters for $T < T_{cr}(\delta)$. In the case of a two-dimensional character of the superconducting fluctuations $T_{cr}(\delta) > T > T_{3D}(\delta)$ of the pseudogap state and of the superconducting state $T_g < T < T_{BKT}$, magnetic clusters coexist with bosonic clusters, i.e., the CuO_2 plane is found in a substantially inhomogeneous state.[4)]

We have found that as the temperature is lowered, the changes of the properties of the doped AF insulator and also of the metallic and superconducting states of a doped AF are due to a repeated dynamic reduction of the dimensionality. The superconducting transition occurs as a result of a repeated dynamic reduction of the dimensionality of the superconducting fluctuations (from zero-dimensional to three-dimensional), as a two-dimensional transition with a limited region of three-dimensional superconducting fluctuations and of the three-dimensional superconducting state. A model of the magnetic phase diagram in terms of temperature and the dopant concentration of the antiferromagnet is proposed.

*E-mail: gsergeeva@kipt.kharkov.ua

[1)]It is shown in T. D. Stanesky and P. Phillips, Phys. Rev. Lett. **91**, 017002/1–4 (2003) that the pseudogap state is a manifestation of the finiteness of

the phase space, in which it is important to take into account the strong correlations on neighboring sites.

[2)]The criteria for excitation of such vortices and the possibility of studying them by the Javert method have been discussed previously by the author [Czech. J. Phys. **46**, Suppl. S3, 1667 (1996)].

[3)]In constructing this diagram a universal estimate of the temperature $T_{BKT} \sim 0.7T_c$ (Ref. 15) for underdoped HTSCs with $T_c < T_{c,\max}$ was used. Therefore the diagram in Fig. 2 has a more general character than the diagram given in Ref. 6 for Bi-2212 single crystals.

[4)]The inherent inhomogeneity in the two-component model for cuprates and the formation of two-site clusters were first studied by L. P. Gorkov and A. V. Sokol [JETP Lett. **46**, 420 (1987)] and later by L. P. Gorkov [J. Supercond. **14**, 365 (2001)].

[1] J. Orenstein, G. A. Thomas, A. J. Millis, S. L. Cooper, D. H. Rapkine, T. Timusk, L. F. Schneemeyr, and J. V. Waszchzak, Phys. Rev. B **42**, 6342 (1990).
[2] S. Uchida, T. Ido, A. Takagi, T. Arima, and Y. Takura, Phys. Rev. B **43**, 7942 (1991).
[3] X. X. Bi and P. C. Eklund, Phys. Rev. Lett. **70**, 2625 (1993).
[4] K. A. Muller, G.-M. K. Konder, and H. Keller, J. Phys.: Condens. Matter **10**, L291 (1998).
[5] F. G. Pikus and A. L. Efros, Phys. Rev. B **51**, 16871 (1995).
[6] G. G. Sergeeva, V. Yu. Gonchar, and A. V. Voitsenya, Fiz. Nizk. Temp. **27**, 634 (2001) [Low Temp. Phys. **27**, 468 (2001)].
[7] G. G. Sergeeva and V. L. Vakula, *Abstracts of the International Conference "Present-Day Problems in Theoretical Physics"* [in Russian], Kiev (2002); cond-mat/0301037.
[8] B. I. Kochelaev, J. Supercond. **12**, 53 (1999).
[9] E. Salje and B. Gutter, Philos. Mag. B **50**, 607 (1984).
[10] V. V. Eremenko, V. N. Samovarov, V. L. Vakula, M. Yu. Libin, S. A. Uyutnov, and V. M. Rashkovan, Fiz. Nizk. Temp. **27**, 1327 (2001) [Low Temp. Phys. **27**, 981 (2001)].
[11] A. F. Barabanov, L. A. Maksimov, and A. V. Mikheenkov, JETP Lett. **47**, 328 (2001).
[12] E. K. Kudinov, Fiz. Tverd. Tela (St. Petersburg) **44**, 667 (2002) [Phys. Solid State **44**, 692 (2002)].
[13] C. H. Niedermayer, C. Bernhard, T. Blasius, A. Golnik, A. Moodenbaugh, and J. I. Budnik, Phys. Rev. Lett. **80**, 3843 (1998).
[14] V. N. Krivoruchko, K. Yu. Medvedeva, and Yu. E. Kuzovlev, J. Supercond. **12**, 155 (1999).
[15] G. G Sergeeva, Fiz. Nizk. Temp. **27**, 845 (2001) [Low Temp. Phys. **27**, 624 (2001)].
[16] E. K. Kudinov, Fiz. Tverd. Tela (St. Petersburg) **41**, 1582 (1999) [Phys. Solid State **41**, 1450 (1999)].
[17] F. Ronning, C. Kim, D. L. Feng, D. S. Marshall, A. G. Loeser, L. L. Miller, J. N. Eckstein, I. Bosovic, and Z.-X. Shen, Science **282**, 2067 (1998).
[18] Y. Wang, Z. A. Xu, T. Kakeshita, S. Uchida, S. Ono, Y. Ando, and N. P. Ong, Phys. Rev. B **64**, 224519 (2001).
[19] J. R. Kirtley, Physica C **368**, 55 (2002).
[20] M. S. M. Minhaj, J. Obien, D.-C. Long, J. T. Chen, and L. E. Wenger, J. Supercond. **7**, 715 (1994).
[21] B. G. Lazarev, Ya. D. Starodubov, M. B. Lazareva, L. A. Chirkina, G. G. Sergeeva, and V. S. Okovit, Czech. J. Phys. **46**, 1245 (1996).
[22] Z. Wang, J. R. Engelbrecht, S. Wang, and H. Ding, S. H. Pan, Phys. Rev. B **65**, 064509 (2002).
[23] E. I. Katz, Zh. Éksp. Teor. Fiz. **56**, 1675 (1969) [Sov. Phys. JETP **29**, 897 (1969)].

Translated by Steve Torstveit

Superconductivity, negative magnetoresistance, and anisotropy of the conductivity of YFe_4Al_8 and $ScFe_4Al_8$ single crystals in the frequency range $0-10^8$ Hz

V. M. Dmitriev*

B. Verkin Institute for Low Temperature Physics and Engineering, National Academy of Sciences of Ukraine, pr. Lenina 47, 61103 Kharkov, Ukraine; International Laboratory of High Magnetic Fields and Low Temperatures, 95 Gajowicka St., 53-421, Wroclaw, Poland

N. N. Prentslau, I. V. Zolochevskiĭ, L. A. Ishchenko, and A. V. Terekhov

B. Verkin Institute for Low Temperature Physics and Engineering National Academy of Sciences of Ukraine, pr. Lenina 47, 61103 Kharkov, Ukraine

B. Ya. Kotur

I. Franko Lvov State University, ul. Kirilla i Mefodiya 6, 79005 Lvov, Ukraine

W. Suski

International Laboratory of High Magnetic Fields and Low Temperatures, 95 Gajowicka St., 53-421, Wroclow, Poland; W. Trzebiatowski Institute of Low Temperatures and Structure Research, Polish Academy of Sciences, PO. 1410, 50-950 Wroclaw, Poland

E. Talik

Institute of Physics, University of Silesia, Univertsytecka 4, 40-007 Katowice, Poland
Fiz. Nizk. Temp. **29**, 1189–1199 (November 2003)

The anisotropy of the electrical resistivity of YFe_4Al_8 and $ScFe_4Al_8$ single crystals is investigated for the first time in the frequency range $0-10^8$ Hz and temperature range 300–4.2 K. It is found that the conductivity is higher along the growth axis of the crystals than in the perpendicular direction, while the parameters governing the antiferromagnetic ordering, negative magnetoresistance, and superconductivity effects observed in these single crystals are isotropic. Some effects known previously for polycrystalline high-T_c superconductors containing magnetic impurities are observed in the single crystals investigated and are found to be anisotropic in them. © *2003 American Institute of Physics.*
[DOI: 10.1063/1.1614234]

INTRODUCTION

The $ThMn_{12}$-type crystal structure of the ternary compounds RM_4Al_8 (R is a rare earth, M is a transition metal) was first established back in 1962.[1] Since that time the magnetic and structural properties of these compounds have been studied intensively. Unlike the relatively simple tetragonal body-centered crystal lattice of the $ThMn_{12}$-type compounds, the magnetic structure of RFe_4Al_8 compounds has turned out to be very complex, and to this day the results of studies of this magnetic structure by the various methods are far from complete.[2–4]

It is known that at a certain temperature T_N the iron and rare earth (if magnetic) in the compound undergo antiferromagnetic (AFM) ordering, and for $T<T_N$ the compound is antiferromagnetic, although it is not quite ideal from the standpoint of magnetic ordering.[2–5] It is particularly convenient to study the problem of magnetic interactions when the rare-earth element has no intrinsic magnetic moment. This is because the majority of studies have been devoted to compounds with R=Lu, La, Y, Sc. According to Refs. 4 and 5, a simpler magnetic structure is realized in the compound YFe_4Al_8, and it is the compound that has been investigated most fully. However, it is not only the magnetic structure of the compounds that is of interest, but also the circumstance that at temperatures below T_N a number of polycrystalline compounds have exhibited two very interesting phenomena: negative magnetoresistance at low magnetic fields,[6,7] and superconductivity.[6–9] In this regard the compounds RFe_4Al_8 are of still greater interest.

The resistive and magnetic properties of Czochralski-grown YFe_4Al_8 single crystals were first studied in Ref. 10 (previously only polycrystalline samples of YFe_4Al_8 had been studied). The temperature T_N determined both from the maximum on the temperature dependence of the magnetic susceptibility $\chi(T)$ and from the deviation from a linear temperature dependence of the resistivity $\rho(T)$ was found to be $T_N=195$ K. It became clear from subsequent studies[2–5] that such a high value of T_N attests to the rather good stoichiometric composition of the single crystals. Indeed, it was stated in Ref. 4 that Czochralski-grown (drawn from a stoichiometric melt of the metals) single crystals of the compounds RFe_4Al_8 systematically turn out nonstoichiometric, with an excess of iron, lowering T_N to around $T\approx100$ K. It is important to note that excess iron ($x>4$) leads not only to lowering of the value of T_N but also to a change in the structure of the magnetic ordering. The cycloidal modulation of the Fe magnetic moments, which is characteristic for the

stoichiometric samples ($x=4$), is converted to an amplitude-modulated wave with a much smaller period.[4]

In Ref. 10 the elements of the magnetic anisotropy in YFe_4Al_8 single crystals also were studied for the first time. A rather noticeable anisotropy of the temperature dependence of the magnetic susceptibility χ was found. Remarkably, the values of $\chi(T)$ measured above $T_N=195$ K with the external magnetic field **H** oriented parallel ($\chi_\parallel(T)$) or perpendicular ($\chi_\perp(T)$) to the growth direction of the crystal turned out to be the same. The appreciable anisotropy of $\chi(T)$ arose for $T\leqslant T_N$. Here the value of $\chi_\parallel(T)$ was found to be greater than the value of $\chi_\perp(T)$. At liquid-helium temperatures $\chi_\parallel(T)/\chi_\perp(T)\approx 1.3$. In Refs. 2 and 4 the presence of a weak anisotropy of the magnetic properties of single crystals of $LuFe_4Al_8$ and YFe_4Al_8 was also noted. Thus at the present time the data on the anisotropy of the magnetic properties of RFe_4Al_8 single crystals are clearly inadequate, and the anisotropy of the electrical properties has not been studied at all.

In the present paper we investigate for the first time the anisotropy of the electrical properties of YFe_4Al_8 and $ScFe_4Al_8$ single crystals both in direct current and in alternating fields at frequencies up to 10^8 Hz. These compounds were chosen for the following reasons: both contain nonmagnetic rare earths; YFe_4Al_8 has been studied more and there is some information available about the anisotropy of its magnetic properties; $ScFe_4Al_8$ is quite close to YFe_4Al_8 in its magnetic properties, but nothing is known about its anisotropy properties. It has been shown that the conductivity along the growth axis of the crystals is higher than in the perpendicular direction. The phenomena of superconductivity and negative magnetoresistance observed previously[6,7] in polycrystalline samples also exist in the single crystals studied and turned out to be isotropic with respect to the growth direction of the single crystals.

SAMPLES AND MEASUREMENT TECHNIQUES

Single crystals of YFe_4Al_8 and $ScFe_4Al_8$ were grown by the Czochralski method of pulling from a stoichiometric melt of the initial metals. The YFe_4Al_8 single crystal was in the form a cylinder of diameter 2.1 mm and length 4.7 mm. The $ScFe_4Al_8$ single crystal was in the form a cylinder of diameter 3.5 mm and length 7.7 mm.

The resistivity ρ and total impedance $Z_s=R_s+jX_s$ were measured by the four-contact method in direct current or by a resonator method at the respective frequencies by the technique described in Ref. 11 (R_s and X_s are the active and reactive components of the total impedance Z_s). The geometric factor G of the oscillatory measurement circuit at a high Q of the capacitor was determined by the formula $G=4\pi^2 fLrl^{-1}$, where f is the resonant frequency, L in the inductance of the coil, and r and l are the radius and length of the wire of which the coil is made.

The impedance anomalies were measured from the Q of the circuit, which, in turn, was measured from the variation of the signal amplitude at the resonant frequency with the use of an SK4-59 spectrum analyzer in the long-storage, single-scan mode.

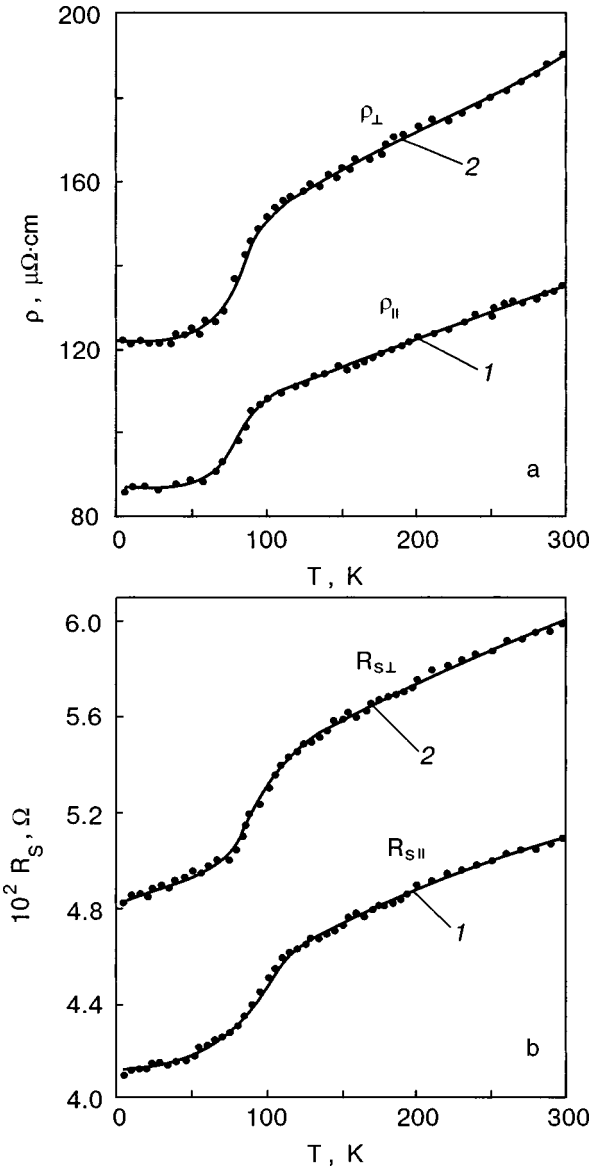

FIG. 1. Temperature dependence of the resistivity ρ (a) and the surface resistance R_s at a frequency of 45 MHz (b), measured parallel ($\parallel$) (curves *1*) and perpendicular ($\perp$) (curve *2*) to the direction of growth of the YFe_4Al_8 single crystal.

EXPERIMENTAL RESULTS

YFe_4Al_8

Figure 1a shows the temperature dependence of the resistivity ρ measured along the growth direction of the crystal ($\rho_\parallel$; curve *1*) and perpendicular to the growth direction ($\rho_\perp$, curve *2*).

It is seen that a good linear dependence of $\rho(T)$ is maintained in both cases down to the AFM ordering temperature $T_N=100$ K. The lower value of T_N in comparison with that obtained in Ref. 10 ($T_N=195$ K) is indicative of some excess Fe.

Figure 1b shows the temperature dependence of the active part R_s of the total impedance $Z_s=R_s+jX_s$ of the YFe_4Al_8 sample at a measurement frequency of 45 MHz. The single crystal was oriented in such a way that the rf current is in one case parallel to the growth direction of the

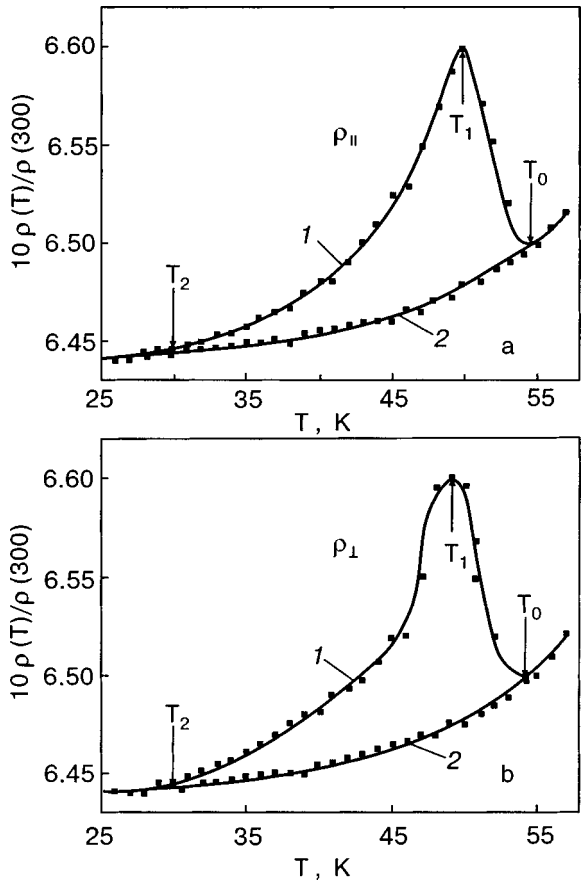

FIG. 2. Temperature dependence of the resistivity ρ measured parallel ($\|$) (a) and perpendicular ($\perp$) (b) to the direction of growth of the YFe_4Al_8 single crystal in the temperature interval where the negative magnetoresistance is observed (curves *1*). Curves *2* were obtained in a static magnetic field $H=50$ Oe.

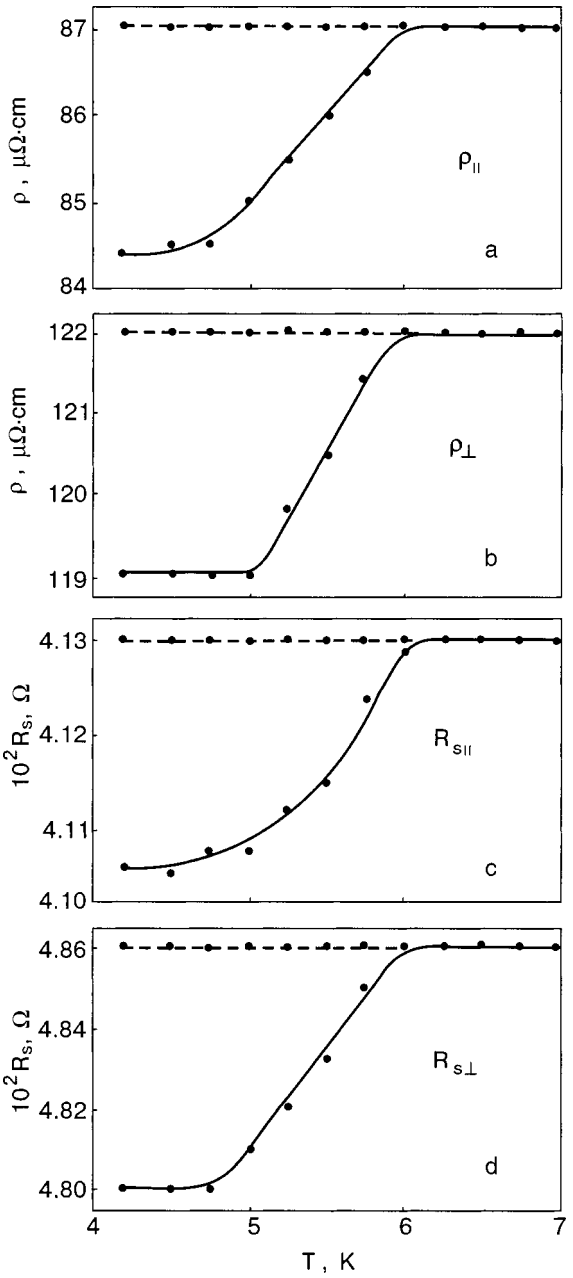

FIG. 3. Temperature dependence of the resistivity ρ (a,b) and surface resistance R_s at a frequency of 45 MHz (c,d), measured parallel ($\|$) and perpendicular ($\perp$) to the growth direction of the YFe_4Al_8 single crystal in the region of the superconducting transition. The dashed lines reflects the dependence measured in a static magnetic field $H=50$ Oe.

crystal ($R_{s\|}$, curve *1*) and in the other case perpendicular to that direction ($R_{s\perp}$, curve *2*).

It is easy to convince oneself that $R_{s\|}/R_{s\perp}\sim(\rho_\|/\rho_\perp)^{1/2}$ in the entire temperature range of the measurements.

It is seen in Fig. 1 that $\rho_\perp>\rho_\|$ ($R_{s\perp}>R_{s\|}$) in the entire temperature range of the measurements, i.e., the resistivity of the YFe_4Al_8 single crystal is approximately 1.4 times higher in the growth direction than in the perpendicular direction. The antiferromagnetic ordering does not cause any additional anisotropic features. The $\rho_{\|,\perp}(T)$ and $R_{s\|,\perp}(T)$ curves change in small jumplike increases, but these anomalies are are expressed weakly in the YFe_4Al_8 samples and cannot be seen on the scale of Fig. 1. For this reason we show in Fig. 2 fragments of the $\rho(T)$ curves of the YFe_4Al_8 single crystal from Fig. 1 on an expanded scale, so that these features may be seen clearly. They are characterized by the following temperatures: $T_0=55$ K, the temperature of the start of the growth of ρ and R_s, and $T_1=50$ K, the temperature at which ρ and R_s reach their peak values. When the temperature is further lowered to $T=30$ K ($T_2<T_1<T_0<T_N$) the values of ρ and R_s decrease. In the temperature region T_0-T_2 one observes negative magnetoresistance at low magnetic fields (of the order of a few to tens of oersteds). Curves *1* were taken in zero magnetic field; curves *2* in a field of $H=50$ Oe. It is seen that the observed effect is isotropic. The features in $R_s(T)$ are not shown, but they have the same form and are observed at the same temperatures. At temperatures in the range from 10 to 85 K the values of $\rho_\perp(T)$ and $\rho_\|(T)$ in a magnetic field increase with temperature as $T^{4.8}$. At a temperature $T_c=6$ K$<T_2$ there is a transition of part of the sample to a superconducting state. The influence of magnetic field on the $\rho(T)$ and $R_s(T)$ curves in this temperature region is shown on an expanded scale in Fig. 3. The points on the solid curves were obtained at $H=0$, while those on the dashed curves were obtained at $H=50$ Oe (the curves are drawn in as an aid to the eye). The data characterizing the $\rho(T)$ curves measured parallel and perpendicular to the growth direction are presented in Table I. Figure 4 shows the frequency dependence of the total impedance Z_s of the YFe_4Al_8 single crystal in the flow of current along the

TABLE I. Main characteristics of the electrical resistance of single crystals.

Compound	T_N	T_0	T_1	T_2	T_c	$\rho_{\parallel}(300)$	$\rho_{\parallel}(4.2)$	$\rho_{\perp}(300)$	$\rho_{\perp}(4.2)$	$\frac{\rho_{\parallel}(300)}{\rho_{\parallel}(4.2)}$	$\frac{\rho_{\perp}(300)}{\rho_{\perp}(4.2)}$	$\partial\rho_{\parallel}/\partial T$	$\partial\rho_{\perp}/\partial T$
	K					μΩ·cm						μΩ·cm/K	
YFe_4Al_8	100	55	50	30	6	135	86	190	121	1.57	1.57	0.135	0.18
YFe_4Al_8 [10]	195	–	–	–	–	125	33	–	–	3.8	–	0.257	–
$ScFe_4Al_8$	210	50	43	25	6	153	118	243	121	1.3	2.0	0.111	0.37

growth direction of the crystal, $Z_{\parallel}$, and in the perpendicular direction, $Z_{\perp}$, measured at temperatures of 300 K (curves *1* (∥) and *2* (⊥) and 10 K (curves *3* (∥) and *4* (⊥). The inset in Fig. 4 shows the initial parts of these curves on an expanded scale. It is seen that the total impedance $Z_{s\perp}$ is higher than $Z_{s\parallel}$, just as was observed in the case of ρ and R_s (see Fig. 1).

$ScFe_4Al_8$

Figure 5a shows the temperature dependence of the resistivity ρ measured along the growth direction of the crystal, $\rho_{\parallel}(T)$, and perpendicular to that direction, $\rho_{\perp}(T)$. The linear trends of $\rho_{\parallel}(T)$ and $\rho_{\perp}(T)$ are disrupted at the same temperature $T_N \approx 210$ K. According to the data of Ref. 12, T_N lies in the temperature range 125–225 K for different samples of $ScFe_4Al_8$, depending on their quality and the methods of measurement. It can therefore be assumed that the $ScFe_4Al_8$ single crystal studied here is rather stoichiometric. Figure 5b shows the temperature dependence of $R_{s\parallel}$ and $R_{s\perp}$, measured at a frequency of 45 MHz (parallel and perpendicular to the growth direction of the single crystal). It is seen that the resistances exhibit anisotropy: $\rho_{\perp} > \rho_{\parallel}$ and $R_{s\perp} > R_{s\parallel}$ in the entire temperature range of the measurements. Not only are the resistances themselves different, their temperature dependence is also different: $\partial\rho_{\perp}/\partial T > \partial\rho_{\parallel}/\partial T$, and $\partial R_{s\perp}/\partial T > \partial R_{s\parallel}/\partial T$. It also follows from Fig. 5 that the $\rho(T)$ and $R_s(T)$ curves exhibit jumplike increases. These are shown for $\rho(T)$ on an expanded scale in

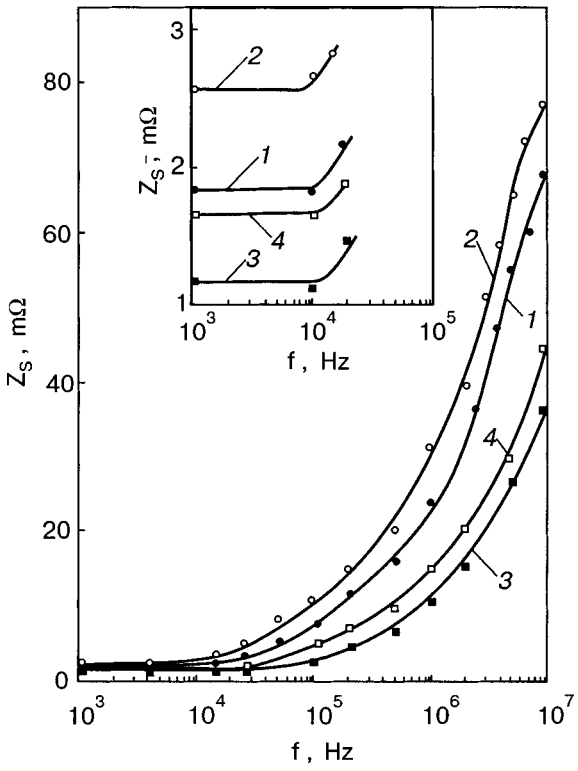

FIG. 4. Frequency dependence of the total impedance Z_s measured parallel to and perpendicular to the growth direction of the YFe_4Al_8 single crystal at temperatures of 300 K (curves *1* ($Z_{s\parallel}$) and *2* ($Z_{s\perp}$)) and 10 K (curves *3* ($Z_{s\parallel}$) and *4* ($Z_{s\perp}$)). The inset shows the initial parts of these curves in an expanded scale.

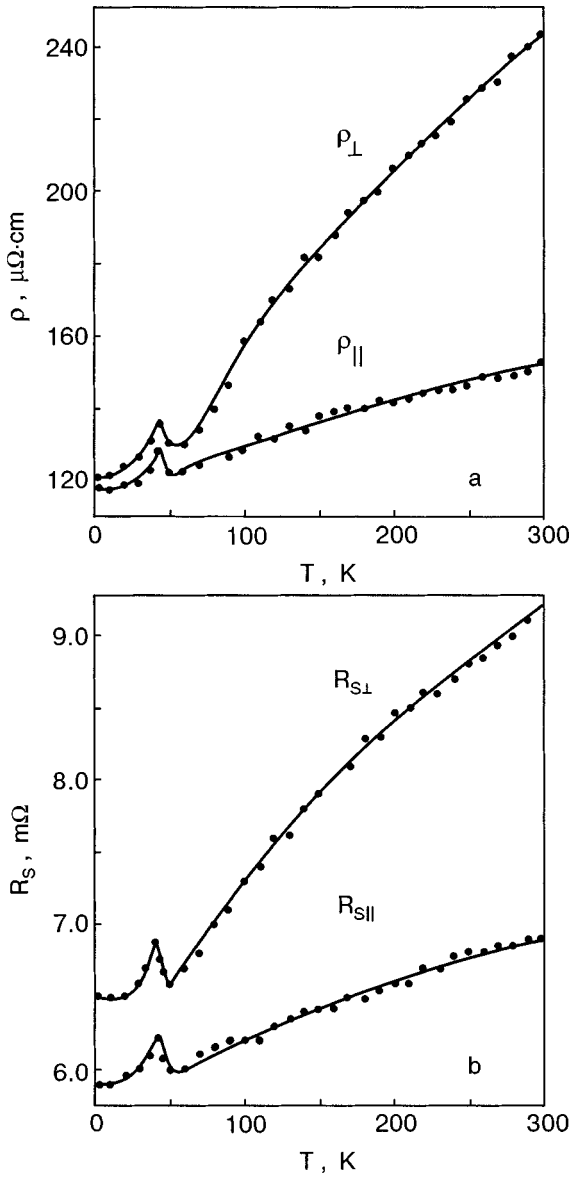

FIG. 5. Temperature dependence of the resistivity ρ (a) and surface resistance $R_s(T)$ at a frequency of 45 MHz (b), measured parallel to and perpendicular to the growth direction of the $ScFe_4Al_8$ single crystal.

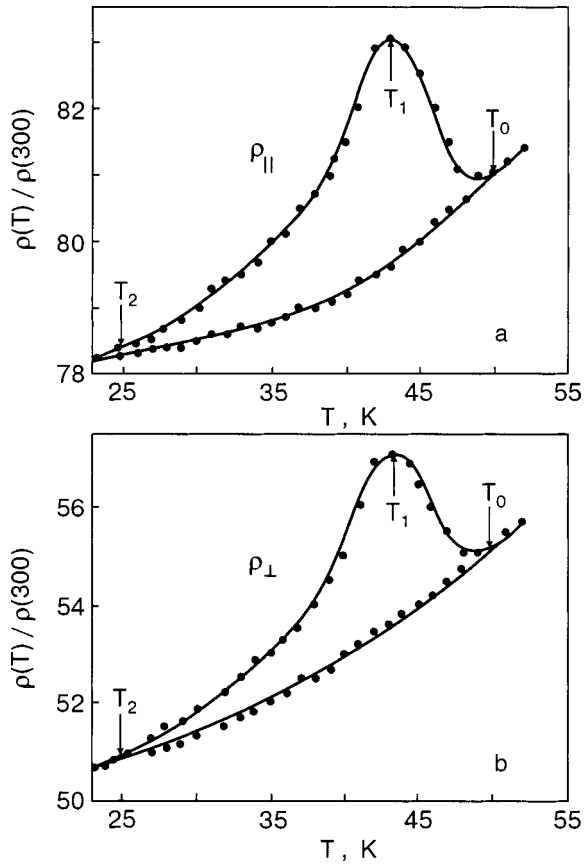

FIG. 6. Temperature dependence of the resistivity ρ measured parallel ($\rho_\parallel$) (a) and perpendicular ($\rho_\perp$) (b) to the growth direction of the $ScFe_4Al_8$ single crystal in the temperature interval where the negative magnetoresistance effect is observed (curves *1*). Curves *2* were obtained in a static magnetic field $H=50$ Oe.

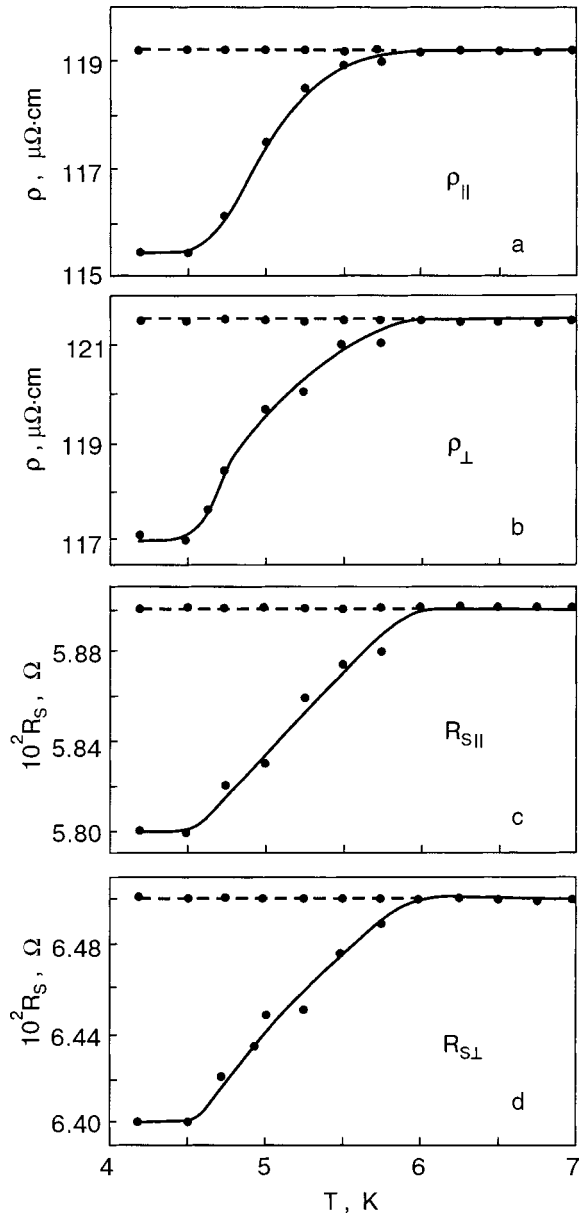

FIG. 7. Temperature dependence of the resistivity ρ (a,b) and surface resistance $R_s(T)$ at a frequency of 45 MHz (c,d), measured parallel ($\parallel$) and perpendicular ($\perp$) to the growth direction of a $ScFe_4Al_8$ single crystal in the region of the superconducting transition. The dashed lines reflect the dependence measured in a static magnetic field $H=50$ Oe.

Fig. 6. The anomalies of $\rho(T)$ and $R_s(T)$ are characterized by the following temperatures: $T_0=50$ K and $T_1=43$ K. Upon further decrease in temperature to 25 K$=T_2<T_1<T_0<T_N$ the values of ρ and R_s decrease. In the temperature interval T_0-T_2 a negative magnetoresistance is observed at low magnetic fields (of the order of a few to tens of oersteds). Curves *1* were taken at zero magnetic field, and curves *2* in a field $H=50$ Oe. At $T_c=6$ K$<T_2$, part of the sample undergoes a transition to the superconducting state. The influence of magnetic field on the $\rho(T)$ and $R_s(T)$ curves in the superconducting transition region are shown in Fig. 7 for the different orientations of the crystal with respect to the direction of the measuring current. The points on the solid curves were obtained at $H=0$, and those on the dashed curves at $H=50$ Oe. It is seen that, independently of the orientation and the manner of measurement, no anisotropy of T_c is observed, nor is any anisotropy of the properties due to the negative magnetoresistive effect. The data characterizing the $\rho(T)$ curves are presented in Table I.

Figure 8 shows the frequency dependence of the total impedance Z_s of the $ScFe_4Al_8$ single crystal, measured along the crystal growth direction, $Z_{s\parallel}$, and in the perpendicular direction, $Z_{s\perp}$, at temperatures of 300 K [curves *1* ($\parallel$) and *1′* ($\perp$)], 100 K [curves *2* ($\parallel$) and *2′* ($\perp$)], and $T=10$ K [curves *3* ($\parallel$) and *3′* ($\perp$)]. The inset in Fig. 8 shows the initial parts of the frequency dependence on an enlarged scale. It is seen that the $Z_\parallel(f)$ and $Z_\perp(f)$ curves are different. The $Z_\parallel(f)$ curves do not cross at any measurement temperature and they have a minimum at a frequency of about 6×10^4 Hz. In contrast to the $Z_\parallel(f)$ curves, the $Z_\perp(f)$ curves do not have a minimum, and the curves taken at different temperatures cross each other. This indicates that the temperature dependence of $Z_\perp(T,f)$ is different at different frequencies. The minimum of $Z_\parallel(f)$, shown on an expanded scale in Fig. 9, can be characterized by three frequencies: f_0, the frequency at which the decrease of $Z_\parallel(f)$ begins, $f_{\min}$, the frequency at which $Z_\parallel(f)$ takes its minimum value, and f_s, the frequency at which $Z_\parallel(f_s)=Z_\parallel(f_0)$.

DISCUSSION OF THE RESULTS

Let us compare the results which we obtained for the $\rho_\parallel(T)$ curves of the YFe_4Al_8 single crystal with the previ-

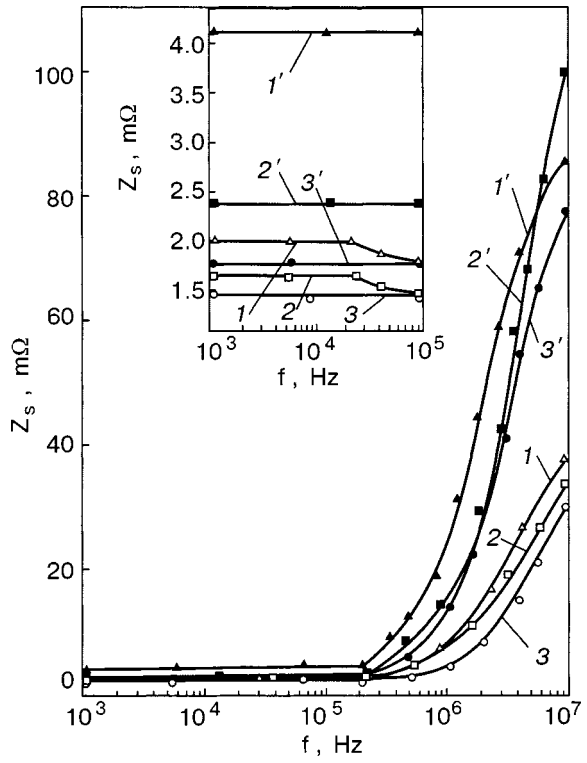

FIG. 8. Frequency dependence of the total impedance $Z_s(f)$ measured parallel (∥) and perpendicular (⊥) to the growth direction of the $ScFe_4Al_8$ single crystal at temperatures $T=300$ K (curves *1* (∥) and *1′* (⊥), $T=100$ K (curves *2* (∥) and *2′* (⊥)), and $T=10$ K (curves *3* (∥) and *3′* (⊥)). The inset shows the initial parts of the curves in an expanded scale.

ously published results (see Fig. 3 of Ref. 10). It follows from our measurements and the data of Ref. 10 that as the temperature is lowered from room temperature the resistivity $\rho_{\parallel}(T)$ decreases by a linear law to the antiferromagnetic ordering temperature T_N. Below T_N the value of $\rho_{\parallel}(T)$ falls off faster, and at still lower temperatures it goes to a plateau. Thus one can state that the results of our measurements of $\rho_{\parallel}(T)$ are in qualitative agreement with the results of Ref. 10. Quantitatively the results of the $\rho_{\parallel}(T)$ measurements differ, as can be seen from Table I. As we have said, the YFe_4Al_8 single crystal studied here apparently contains some excess iron, which lowers T_N appreciably. In addition, we note that

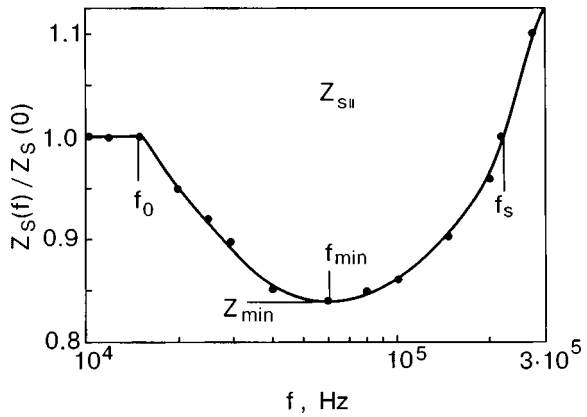

FIG. 9. Fragment of the frequency dependence of the total impedance $Z_s(f)$, Fig. 8, measured parallel (∥) to the growth direction of the $ScFe_4Al_8$ single crystal at temperature $T=300$ K.

excess Fe leads to a higher $\rho(T)$ in comparison with that for a stoichiometric sample.[10] This is especially noticeable in studying the residual resistivity at helium temperatures (see Table I). Thus the transport properties, in the present case the resistivity, is rather sensitive to the stoichiometry of the samples. A departure from stoichiometry leads to disordering of the crystal lattice, a change in the magnetic properties, and, as a result, an enhancement of charge carrier scattering processes.

It follows from Fig. 1a that $\rho(T)$ exhibits anisotropy, with $\rho_{\perp}(T)>\rho_{\parallel}(T)$ at all temperatures from room to helium. On the linear part of the $\rho(T)$ curve the inequality $\partial\rho_{\perp}/\partial T > \partial\rho_{\parallel}/\partial T$, although the difference is small. It follows from the $\rho_{\perp}(T)$ and $\rho_{\parallel}(T)$ curves that $T_N=100$ K for both directions. Interesting, the anisotropy of the resistivity is observed at all measurement temperatures. Anisotropy of the magnetic properties, on the other hand, is observed only for $T<T_N$, as follows from Fig. 4 of Ref. 10. Here the magnetic susceptibility $\chi_{\parallel}(T)$ measured in a magnetic field directed parallel to the crystal growth axis is greater than that measured in a magnetic field perpendicular to the growth axis, $\chi_{\perp}(T)$. When the mutual orientation of the electric currents and their magnetic fields is taken into account, we see that the signs of the anisotropy of the electric and magnetic properties correspond to each other. It follows from Fig. 1b that the anisotropy of the resistivity and its sign are preserved in an alternating electromagnetic field and that the active component of the total impedance has a dependence $R_s \propto \rho^{1/2}$, as is characteristic for pure metals.

As we see in Fig. 3, at helium temperatures the anisotropy of $\rho(T)$ and $R_s(T)$ is preserved, but there the critical temperature T_c of the superconducting transition of part of the sample remains the same in all cases and is equal to 6 K.

The temperature curves of $\rho(T)$ and $R_s(T)$ shown in Fig. 5 are evidence that anisotropy of $\rho(T)$ and $R_s(T)$ is also observed in $ScFe_4Al_8$, but there is a difference in the quantitative values for YFe_4Al_8 and $ScFe_4Al_8$. For example, in YFe_4Al_8 the values of the ratios $\rho_{\perp}(T)/\rho_{\parallel}(T)$ and $R_{s\perp}(T)/R_{s\parallel}(T)$ remain practically unchanged in the temperature interval from room to helium temperatures (see Fig. 1). In contrast to this, the values of these ratios in $ScFe_4Al_8$ decrease with decreasing temperature, i.e., the anisotropic properties of $ScFe_4Al_8$ are less pronounced at helium temperatures than at room temperatures. It can be shown that this is a consequence of the different slopes both of the $\rho_{\perp}(T)$ and $\rho_{\parallel}(T)$ curves and of the $R_{s\perp}(T)$ and $R_{s\parallel}(T)$ curves. Whether this is due to the quality of the sample or is a fundamental fact is a question to be clarified in the future.

Figure 6 shows fragments of the $\rho(T)$ curves from Fig. 5 in an expanded scale in the temperature region 23–52 K. It is seen that the negative magnetoresistance is isotropic and that the characteristic amplitudes and temperatures are the same in both directions. The negative magnetoresistance effect at low magnetic fields is deserving of separate study. Possibly it arises due to a magnetostructural phase transition of the samples in the antiferromagnetic state at $T<T_N$, and such a transition can lead to phase separation (the onset of a stripe state) at very short distances. In the temperature interval from 10 to 100 K the $\rho_{\perp}(T)$ and $\rho_{\parallel}(T)$ curves depend on temperature as $T^{2.5}$ and $T^{2.2}$, respectively. The difference of

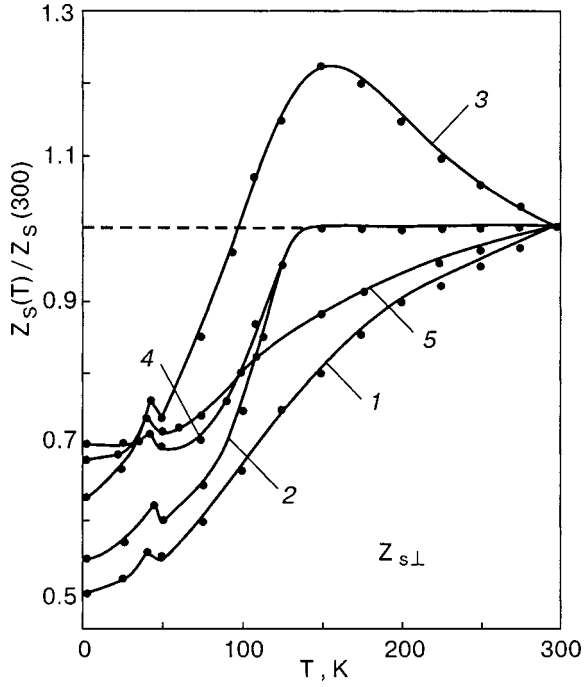

FIG. 10. Temperature dependence of the total impedance $Z_s(T)$ measured in the direction perpendicular ($\perp$) to the growth direction of the $ScFe_4Al_8$ single crystal at frequencies [Hz]: 10^4 (*1*), 5×10^4 (*2*), 2.5×10^5 (*3*), 2.5×10^6 (*4*), 10^7 (*5*).

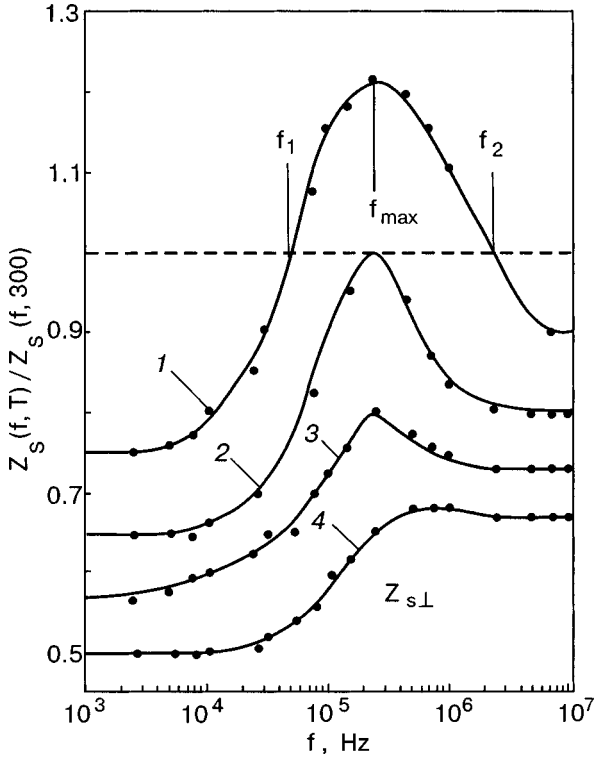

FIG. 11. Frequency dependence of the total impedance $Z_s(f)$ measured in the direction perpendicular ($\perp$) to the growth direction of the $ScFe_4Al_8$ single crystal at temperatures [K]: 150 (*1*), 100 (*2*), 70 (*3*), 10 (*4*).

the temperature dependence of $\rho(T)$ for single crystals of YFe_4Al_8 and $ScFe_4Al_8$ in this temperature interval is most likely due to a different degree of stoichiometry. Both $\rho(T)$ and $R_s(T)$ are indicative of the presence of an isotropic superconducting transition of parts of the samples at $T_c=6$ K (see Figs. 3 and 7).

Thus the anisotropic properties of the resistivity $\rho(T)$ and of the active part $R_s(T)$ of the total impedance of the YFe_4Al_8 and $ScFe_4Al_8$ single crystals are qualitatively similar. They are more pronounced in the $ScFe_4Al_8$ single crystal, possibly because of a higher degree of stoichiometry and a smaller influence of defects on the magnetic and phonon subsystems.

Let us now compare the temperature and frequency dependences of the total impedances Z_s measured in different directions in the YFe_4Al_8 and $ScFe_4Al_8$ single crystals. It follows from Figs. 4 and 8 that, as for ρ and R_s, one has $Z_{s\perp}>Z_{s\parallel}$ for both single crystals. In YFe_4Al_8, however, there is only a quantitative difference between $Z_{s\perp}$ and $Z_{s\parallel}$, while in $ScFe_4Al_8$ there is also a qualitative difference between the curves shown for $Z_{s\perp}$ and $Z_{s\parallel}$. This difference consists in the following: 1. As we have said, the $Z_{s\parallel}(f)$ curve has a minimum (see Figs. 8 and 9). This phenomenon has been observed previously in HTSC materials,[13] but its anisotropy in the single crystals studied here is noted for the first time. This phenomenon is not observed in YFe_4Al_8 (see Fig. 4). 2. As is seen in Fig. 8, the $Z_{s\perp}(f)$ curves measured at different temperatures cross each other. This reflects the fact that not only the value of $\partial Z_{s\perp}/\partial T$ but also the sign of this derivative depend on the measurement frequency. This follows clearly from Fig. 10. Here we show the $Z_{s\perp}(T)$ curves for several characteristic frequencies. Curves *2*, *3*, and *4* in the figure correspond to the frequencies f_1, f_{max}, and f_2 in Fig. 11, which shows the curves of $Z_{s\perp}(f,T)/Z_{s\perp}(f,300)$ measured perpendicular to the growth direction for the $ScFe_4Al_8$ single crystal at temperatures of 150 K (curve *1*), 100 K (curve *2*), 70 K (curve *3*), and $T=10$ K (curve *4*).

Figures 10 and 11 reflect a phenomenon which was observed previously in HTSC materials[14] and in $LuFe_4Al_8$ (Ref. 6) and which was investigated in Refs. 15 and 16. It consists in the fact that the metallic trend of the resistance of the sample in direct current and at low frequencies (curve *1* in Fig. 10) becomes independent of temperature (down to 150 K, curve *2*) as the frequency is increased, and then it becomes semiconductorlike (curve *3*). As the frequency is increased further, the temperature dependence of $Z_{s\perp}(f,T)$ again becomes metallic (curve *5*), passing through $Z_{s\perp}(f,T)=\text{const}$ at a frequency $f_2=2.5\times10^6$ Hz (curve *4*). Here one can speak of three characteristic frequencies: f_1, the frequency of the inflection point on the $Z_{s\perp}(f,T)$ curve, f_{max}, the frequency at which the maximum increase in resistance is observed, and f_2, the frequency at which $Z_{s\perp}(f,T)$ is independent of temperature for $T>150$ K (Fig. 10). These characteristic frequencies are practically independent of temperature, as can be seen from Fig. 11. Interestingly, the $Z_{s,\perp}(f,T)$ curves at the frequencies f_1 and f_2 coincide at temperatures above 125 K. Below that temperature they diverge (see curves *2* and *4* in Fig. 10). There is as yet no definitive physical explanation for this phenomenon, although it can be conjectured that it may be the result of a specific interaction of the charge carriers from two or more different conduction bands.[15,16] If that is also pertinent to the systems under study (since it is observed in $LuFe_4Al_8$ and $ScFe_4Al_8$), then in future studies one should pay attention to the influence exerted on the electric and magnetic properties

TABLE II. Main characteristics of the electrical resistance of polycrystalline alloys.

Compound	$\rho(300)$, $\mu\Omega\cdot$cm	$\rho(4.2)$, $\mu\Omega\cdot$cm	$\frac{\rho(300)}{\rho(4.2)}$	$\partial\rho/\partial T$, $\mu\Omega\cdot$cm/K	Ref.
YFe_4Al_8	114	58	1.96	0.078	[17]
$ScFe_4Al_8$	104	47	2.2	0.08	[18]
$ScFe_4Al_8$	–	–	1.33	–	[19]
$ScFe_4Al_8$	–	–	1.78	–	[20]
$Ce_{0.1}Sc_{0.9}Fe_4Al_8$	110	73	1.5	0.053	[21]

of the compounds RM_4Al_8 by the interaction of the surface groups of electrons with one another, with the magnetic and phonon subsystems, and with the antiferromagnetic correlations, which can be substantial. Not only is it interesting that the phenomenon described above is observed in $ScFe_4Al_8$ samples, it is also interesting that in this case it is anisotropic and is not observed for $Z_{s,\parallel}$, as can be seen in Fig. 8.

The fact that the effects observed in $ScFe_4Al_8$ and presented in Figs. 8, 9, 10, and 11 are absent in YFe_4Al_8 may be a consequence of both nonstoichiometry, excess Fe in the YFe_4Al_8 single crystal, or of a fundamental difference of the magnetic and electronic interactions in YFe_4Al_8 and $ScFe_4Al_8$. This question can be answered in the future by studying high-quality single crystals with different but known iron content. In this context we would like to call attention to the fact that for doing different experiments the requirements on the samples are different. For example, neutron, Mössbauer, magnetic, and x-ray studies and heat capacity measurements do not require high density and uniformity of the samples. For a study of the electrical and heat transport properties the requirements on the density and uniformity of the samples are very high. Unfortunately, the present-day technologies do not satisfy the requirements very well. It may be seen from Tables I and II that, as a rule, the electrical characteristics of single crystals differ little from those for alloys. Moreover, in single crystals the values of $\rho(T)$ are even higher than in alloys, while the ratio $\rho(300)/\rho(4.2)$ for them is approximately the same and is small with a significant scatter of the values. The single crystals differ favorably from the polycrystals only in that the fall of $\rho(T)$ on the linear part of the curve is steeper. With all the scatter of the measured values for the different samples, the slope of $\rho(T)$ on the linear part is approximately twice as large in the single crystals. A good exception is the YFe_4Al_8 single crystal studied in Ref. 10. Its parameters attest to the possibility of growing rather high-quality single crystals by the Czochralski method.

In view of what we have said, we consider the quantitative results of the present study as being of a preliminary nature, and we intend to refine them in a subsequent study with high-quality and well-oriented single crystals.

CONCLUSION

Let us summarize the main results of this study. We have for the first time investigated the anisotropy of the conductivity of crystals with a body-centered lattice of the $ThMn_{12}$ type, for the particular case of the single crystals YFe_4Al_8 and $ScFe_4Al_8$. We have found that the conductivity is higher along the growth direction of the single crystals than in the perpendicular direction. We have investigated the features of the anisotropy of the temperature and frequency dependences of the conductivity parallel and perpendicular to the single-crystal growth direction. Against the background of the conductivity anisotropy the phenomena of antiferromagnetic ordering, negative magnetoresistance, and superconductivity in the single crystals turned out to be isotropic. The features of the frequency–temperature curves of the conductivity known previously for polycrystalline samples of HTSCs[13,14] and $LuFe_4Al_8$ (Ref. 6) have been detected in a $ScFe_4Al_8$ single crystal and turn out to be anisotropic, a change in sign of the temperature dependence of the conductivity at certain characteristic frequencies has been observed, and it was found that at certain frequencies the resistance of the sample can become smaller than the dc resistance. Neither of these effects has yet been given a full and convincing explanation, but the fact that they are anisotropic has been shown here for the first time.

The authors are grateful to V. N. Samovarov for reading the manuscript, for valuable comments, and for a helpful discussion.

*E-mail: dmitriev@ilt.kharkov.ua

[1] O. S. Zarechnyuk and P. I. Kripyakevich, Kristallografiya **7**, 543 (1962) [Sov. Phys. Crystallogr. **7**, 436 (1963)].
[2] J. A. Paixão, S. Langridge, S. A. Søorensen, B. Lebech, A. P. Gonçalves, G. N. Lander, P. J. Prown, P. Burlet, and E. Talik, Physica B **234–236**, 614 (1997).
[3] J. C. Waerenborgh, P. Salamakha, O. Sologub, A. P. Gonçalves, C. Cardoso, S. Serio, M. Godinho, and M. Almcida, Chem. Mater. **12**, 1743 (2000).
[4] J. A. Paixão, M. Ramos Silva, J. C. Wacrenborgh, A. P. Gonçalves, G. N. Lander, P. J. Brown, M. Godinho, and P. Burlet, Phys. Rev. B **63**, 054410 (2001).
[5] P. Schobinger-Papamantellos, K. H. K. Buschow, and C. Ritter, J. Magn. Magn. Mater. **186**, 21 (1998).
[6] A. M. Gurevich, V. M. Dmitriev, V. N. Eropkin, L. A. Ishchenko, N. N. Prentslau, and L. V. Shlyk, Fiz. Nizk. Temp. **25**, 15 (1999) [Low Temp. Phys. **25**, 10 (1999)].
[7] A. M. Gurevich, V. M. Dmitriev, V. N. Eropkin, B. Yu. Kotur, N. N. Prentslau, V. Suski, A. V. Terekhov, and L. V. Shlyk, Fiz. Nizk. Temp. **27**, 1308 (2001) [Low Temp. Phys. **27**, 967 (2001)].
[8] V. M. Dmitriev, L. F. Rybaltchenko, R. Wyder, A. G. M. Jansen, N. N. Prentslau, and W. Suski, Fiz. Nizk. Temp., **28**, 374 (2002) [Low Temp. Phys. **28**, 260 (2002)].
[9] H. Drulis, P. Gaczynski, W. Iwasieczko, W. Suski, and B. Ya. Kotur, Solid State Commun. **123**, 391 (2002).
[10] A. Chelkowski, E. Talik, J. Szade, J. Heimann, A. Winiarska, and A. Winiarski, Physica B **168**, 149 (1991).
[11] V. M. Dmitriev, M. N. Ofitserov, and N. N. Prentslau, Radiotekhnika (Moscow) **No. 97**, 91 (1993).
[12] P. Gaczynski, F. G. Vagizov, W. Suski, B. Kotur, W. Iwasieczko, and H. Drulis, J. Magn. Magn. Mater. **225**, 351 (2001).
[13] V. M. Dmitriev, M. N. Ofitserov, N. N. Prentslau, K. Rogacki, and W. Sadowski, Fiz. Nizk. Temp. **21**, 397 (1995) [Low Temp. Phys. **21**, 308 (1995)].
[14] V. M. Dmitriev, M. N. Ofitserov, and N. N. Prentslau, Fiz. Nizk. Temp. **16**, 387 (1990) [Sov. Low Temp. Phys. **16**, 214 (1990)].
[15] V. P. Galaiko, V. M. Dmitriev, M. N. Ofitserov, and N. N. Prentslau, Fiz. Nizk. Temp. **19**, 135 (1993) [Low Temp. Phys. **19**, 96 (1993)].
[16] V. P. Galaiko and E. N. Bratus', Fiz. Nizk. Temp. **28**, 460 (2002) [Low Temp. Phys. **28**, 321 (2002)].

[17] M. D. Koterlin, B. S. Morokhevs'kiĭ, E. D. Shcherba, and N. V. German, Ukr. Fiz. Zh. (Russ. Ed.) **38(2)**, 362 (1993).
[18] W. Suski, K. Wochowski, and B. Ya. Kotur, Czech. J. Phys. **52**, A 180 (2002).
[19] B. Ya. Kotur, D. Badurski, W. Suski, K. Wochowski, A. Gelewski, and T. Mydlarz, Physica B **254**, 107 (1998).
[20] W. Suski, B. Kotur, and K. Wochowski, Physica B **281–282**, 81 (2000).
[21] P. Gaczynski, F. G. Vagizov, W. Suski, B. Kotur, K. Wochowski, and H. Drulis, J. Magn. Magn. Mater. **214**, 37 (2000).

Translated by Steve Torstveit

LOW-TEMPERATURE MAGNETISM

Structural and magnetic inhomogeneity and the NMR of ^{55}Mn and ^{139}La in the magnetoresistive ceramics $La_{0.7}Ba_{0.3-x}Sn_xMnO_3 \rightarrow La_{0.7-x}Ba_{0.3-x}MnO_3 + 0.5xLa_2Sn_2O_7$

V. P. Pashchenko,* A. A. Shemyakov, M. M. Savosta,† S. I. Khartsev, V. N. Derkachenko, V. K. Prokopenko, V. A. Turchenko, and A. V. Pashchenko

A. A. Galkin Donetsk Physicotechnical Institute, ul. R. Lyuksemburg 72, 83114 Donetsk, Ukraine

V. P. Dyakonov

A. A. Galkin Donetsk Physicotechnical Institute, ul. R. Lyuksemburg 72, 83114 Donetsk, Ukraine; Institute of Physics, Polish Academy of Sciences, 32/46 Al. Lotnikow, O2-668 Warsaw, Poland

Yu. Buhanzev and H. Szymczak

Institute of Physics, Polish Academy of Sciences, 32/46 Al. Lotnikow, O2-668 Warsaw, Poland
(Submitted April 1, 2003)
Fiz. Nizk. Temp. **29**, 1200–1208 (November 2003)

The effects of substitution of barium by tin on the phase composition, structural imperfection, and properties of lanthanum manganite perovskites $La_{0.7}Ba_{0.3-x}Sn_xMnO_3$ ($x=0$, 0.1, 0.15, 0.2, 0.3) are established by comprehensive studies done by x-ray diffraction, resistive, and magnetic (including NMR on ^{55}Mn and ^{139}La) methods. It is shown that the introduction of Sn leads to the formation of a pyrochloric phase $La_2Sn_2O_7$, to an increase in the density of lattice defects of the manganese-enriched main lanthanum manganite phase, and to a substantial decrease of the magnetoresistive effect. The smearing of the metal–semiconductor phase transition temperature is explained by an increase in the inhomogeneity and imperfection of the perovskite structure. The low activation energy is confirmed by a high degree of inhomogeneity and imperfection of the crystal lattice of the samples studied. The broad, asymmetric NMR spectra of ^{55}Mn and ^{139}La attest to high-frequency electron exchange between Mn^{3+} and Mn^{4+} and nonequivalence of the environment of those ions and La^{3+} due both to heterovalent ions and to vacancies and clusters. © *2003 American Institute of Physics.*
[DOI: 10.1063/1.1614235]

INTRODUCTION

The unflagging interest in rare-earth manganites[1–3] and other related metal oxides[4,5] with the perovskite structure, $A^{3+}_{1-x}B^{2+}_xMn^{3+}_{1-x}Mn^{4+}_xO^{2-}_3$ (A=La, Pr, Nd, Sm, ...; B=Ca, Sr, Ba, Pb) is due to the lack of agreement as to the nature of the colossal magnetoresistive (CMR) effect and the prospects for practical application of these materials. The majority of studies have arrived at the conclusion that there is substantial structural, chemical, and magnetic inhomogeneity in these metal oxides, calling particular attention to one form of inhomogeneity or another,[6,10] including inhomogeneity of a cluster[7] or mesoscopic[8] nature and local distortion due to the Jahn–Teller effect.[9,10]

To elucidate the structural imperfection and the nature of the inhomogeneities one must expand the circle of objects and methods of study and obtain a deeper understanding of the real crystal-chemical and magnetic structure of these rare-earth perovskites with CMR.

Among the magnetoresistive rare-earth manganites, the most promising are lanthanum manganite doped with divalent cations, $La^{3+}_{1-x}B^{2+}_xMn^{3+}_{1-x}Mn^{4+}_xO^{2-}_{3\pm\delta}$ with $x=0.3$.[11,12] The least studied of this family, for a number of reasons including the higher synthesis and sintering temperatures and the lower phase transition temperatures, are the Ba-containing lanthanum manganite perovskites. In addition, there are scant data on how the structure and properties of these compounds are affected by an element such as Sn,[13,14] which lowers the synthesis temperature and makes it possible to use the Mössbauer method to study them.[15,16]

In view of what we have said, it is of interest to carry out comprehensive studies of tin-doped lanthanum–barium manganite perovskites with the use of such completely local methods as NMR on ^{55}Mn (Ref. 17) and ^{139}La (Ref. 18) or, even more importantly, on both these nuclei simultaneously and with allowance for the imperfection of the crystal lattice of manganite perovskites, for their structural-chemical and magnetic inhomogeneities, which are related to the electrical conductivity, and for the character and degree of influence of these inhomogeneities on the magnetoresistive effect.

METHODS OF SYNTHESIZING AND STUDYING THE SAMPLES

Ceramic samples of $La_{0.7}Ba_{0.3-x}Sn_xMnO_3$ ($x=0$, 0.1, 0.15, 0.2, 0.3) were obtained from the corresponding mixtures of powders of the oxides La_2O_3 ($Ia3$; $a=11.98$ Å), BaO ($Fm3m$; $a=5.534$ Å), γ-MnO_2 ($a=5.578$ Å, c

TABLE I. Phase compositions of $La_{0.7}Ba_{0.3-x}Sn_xMnO_3$ samples and the molar formulas of ideal (I) and defect (D) magnetoresistive perovskite-like structures.

x	Phase composition of the samples	Molar formulas of the ideal and defect perovskite structure	
0	$La_{0.7}Ba_{0.3}MnO_3$	I	$La^{3+}_{0.7}Ba^{2+}_{0.3}Mn^{3+}_{0.7}Mn^{4+}_{0.3}O^{2-}_3$
		D	$La^{3+}_{0.67}Ba^{2+}_{0.28}Mn^{3+}_{0.67}Mn^{4+}_{0.28}V^{(c)}_{0.10}O^{2-}_{2.85}V^{(a)}_{0.15}$
0.1	$La_{0.6}Ba_{0.2}MnO_3 + 0{,}05La_2Sn_2O_7$	I	$La^{3+}_{0.67}Ba^{2+}_{0.22}Mn^{3+}_{0.89}Mn^{4+}_{0.22}O^{2-}_3$
		D	$La^{3+}_{0.64}Ba^{2+}_{0.21}Mn^{3+}_{0.86}Mn^{4+}_{0.21}V^{(c)}_{0.08}O^{2-}_{2.88}V^{(a)}_{0.12}$
0.15	$La_{0.55}Ba_{0.15}MnO_3 + 0{,}075La_2Sn_2O_7$	I	$La^{3+}_{0.65}Ba^{2+}_{0.18}Mn^{3+}_{1.0}Mn^{4+}_{0.18}O^{2-}_3$
		D	$La^{3+}_{0.63}Ba^{2+}_{0.17}Mn^{3+}_{0.97}Mn^{4+}_{0.17}V^{(c)}_{0.06}O^{2-}_{2.91}V^{(a)}_{0.09}$
0.2	$La_{0.5}Ba_{0.1}MnO_3 + 0{,}1La_2Sn_2O_7$	I	$La^{3+}_{0.62}Ba^{2+}_{0.13}Mn^{3+}_{1.12}Mn^{4+}_{0.13}O^{2-}_3$
		D	$La^{3+}_{0.61}Ba^{2+}_{0.12}Mn^{3+}_{1.10}Mn^{4+}_{0.12}V^{(c)}_{0.05}O^{2-}_{2.92}V^{(a)}_{0.08}$
0.3	$La_{0.4}MnO_3 + 0{,}15La_2Sn_2O_7$	I	$La^{3+}_{0.57}Mn^{2+}_{1.43}O^{2-}_3$
		D	$La^{3+}_{0.54}Mn^{3+}_{1.34}V^{(c)}_{0.12}O^{2-}_{2.82}V^{(a)}_{0.18}$

$=9.33$ Å), and SnO ($P4/nmm$; $a=3.804$ Å, $c=4.826$ Å) after a synthesizing anneal for 24 hours at 850 °C and sintering of the pressings at 1100 °C in a slow heating and cooling regime. The reason for the low annealing temperature is that the Sn-containing oxides are susceptible to thermal dissociation and to the formation of low-melting eutectics. This can lead to an undesirable effect—melting of the samples and volatility of the tin at high synthesis and sintering temperatures. If the economic disadvantage of increasing the synthesis and sintering temperatures is taken into account, the choice of this sort of heat treatment regime is completely justified.

The samples were studied by the following methods:

1) x-ray diffraction on a DRON-2 diffractometer in Cu radiation to determine the phase composition and crystal lattice parameters of the corresponding phases;

2) magnetic, for determining the magnetization and Curie temperature over a wide range of temperatures (4–400 K) and magnetic fields ($H=0.5$–10 kOe);

3) resistive and magnetoresistive (four-probe method), to determine the temperature dependence of the resistance and magnetoresistive effect $[\Delta R/R_0=(R_0-R_H)/R_0]$ for $H=0.5$ kOe in the temperature range $T=77$–400 K;

4) NMR on ^{55}Mn and ^{139}La for determining (at 77 K) the resonance frequency of the local magnetic and valence states of these ions and the nonequivalence of their environment.

The error with which the quantities listed above were determined is as follows: 4% for the phase analysis, 0.05% for the crystal lattice parameters, 0.5% for the resistance, 0.1% for the temperature, 1.5% for the magnetization, 0.5% for the magnetoresistive effect, 0.2% for the NMR frequency of ^{55}Mn, and 0.1% for the NMR frequency of ^{139}La.

RESULTS AND DISCUSSION

According to the x-ray diffraction data, ceramic samples with $x=0$ are practically single-phase, while the others are multiphase, and together with the main rhombohedrally distorted perovskite-like structure ($R\bar{3}c$) they contain small amounts of a phyrochlore-like face-centered phase $La_2Sn_2O_7$ ($Fd3m$; $a=10.702$ Å). This sort of heterophase makeup is due to the fact that Sn does not substitute for Ba in the lanthanum manganite perovskite structure but interacts with La to form a metal oxide with the pyrochlore structure, $La_2Sn_2O_7$. This corresponds to the following reaction:

$$La_{0.7}Ba_{0.3-x}MnO_3 \rightarrow La_{0.7-x}Ba_{0.3-x}MnO_3 + 0.5xLa_2Sn_2O_7.$$

In the samples with $x=0.2$ and 0.3 we detected small amounts of the phase Mn_3O_4, which will be neglected in our further studies.

The phase composition of the ceramic samples with that phase ignored is illustrated in Table I. Also given there, with allowance for the crystal-chemical features of the lanthanum manganite perovskite structure, are the molar formulas for the ideal (I) structure (not containing vacancies) and for the defect (D) lattice, which, according to a single-cycle mechanism of defect formation,[17] contains cationic $V^{(c)}$ and anionic $V^{(a)}$ vacancies. For our case, viz., a two-cycle mechanism of defect formation at temperatures of 850 °C and 1100 °C, the molar formulas of the real defect perovskite structure, with allowance for the distribution of the cations over the A and B positions and for the possible of clustering, are given in Table II. With changing x there are changes in the phase composition (Table I), the Mn^{3+}/Mn^{4+} ratio, and defect content in the main perovskite structure (see Tables I and II).

It is noteworthy that in a real (containing defects in both the cation and anion sublattices) clusterized perovskite structure the manganese ions are found not only in valence states intermediate between 3 and 4 but some of the Mn ions in the clusters are found in a divalent state in distorted polyhedra with a coordination number of 8. According to the principle of local electrical neutrality, the Mn^{2+} ions should be found near anion vacancies, while the Mn^{4+} ions, some of which

TABLE II. Molar formulas of the unclusterized (1) and clusterized (2) defect perovskite structure of $La_{0.7-x}Ba_{0.3-x}MnO_{3\pm\delta}$.

x		Unclusterized and clusterized structures
0	1	$\{La^{3+}_{0.64}Ba^{2+}_{0.28}V^{(c)}_{0.08}\}_A[Mn^{3+}_{0.64}Mn^{4+}_{0.28}V^{(c)}_{0.08}]_B O^{2-}_{2.76}V^{(a)}_{0.24}$
	2	$\{La^{3+}_{0.64}Ba^{2+}_{0.28}V^{(c)}_{0.08}\}_A[Mn^{3+}_{0.60}Mn^{4+}_{0.28}V^{(c)}_{0.08}]_B(Mn^{3+}_{0.02}Mn^{4+}_{0.01}Mn^{2+}_{0.01})_{cl}O^{2-}_{2.76}V^{(a)}_{0.24}$
0.1	1	$\{La^{3+}_{0.60}Ba^{2+}_{0.20}V^{(c)}_{0.20}\}_A[Mn^{3+}_{0.79}Mn^{4+}_{0.20}V^{(c)}_{0.01}]_B O^{2-}_{2.69}V^{(a)}_{0.31}$
	2	$\{La^{3+}_{0.60}Ba^{2+}_{0.20}V^{(c)}_{0.20}\}_A[Mn^{3+}_{0.70}Mn^{4+}_{0.21}V^{(c)}_{0.01}]_B(Mn^{3+}_{0.05}Mn^{4+}_{0.01}Mn^{2+}_{0.02})_{cl}O^{2-}_{2.69}V^{(a)}_{0.31}$
0.15	1	$\{La^{3+}_{0.58}Ba^{2+}_{0.15}V^{(c)}_{0.23}\}_A[Mn^{3+}_{0.90}Mn^{4+}_{0.15}]_B O^{2-}_{2.67}V^{(a)}_{0.33}$
	2	$\{La^{3+}_{0.58}Ba^{2+}_{0.15}V^{(c)}_{0.23}\}_A[Mn^{3+}_{0.76}Mn^{4+}_{0.15}]_B(Mn^{3+}_{0.06}Mn^{4+}_{0.04}Mn^{2+}_{0.04})_{cl}O^{2-}_{2.67}V^{(a)}_{0.33}$
0.2	1	$\{La^{3+}_{0.55}Ba^{2+}_{0.11}V^{(c)}_{0.24}\}_A[Mn^{3+}_{0.99}Mn^{4+}_{0.11}]_B O^{2-}_{2.66}V^{(a)}_{0.34}$
	2	$\{La^{3+}_{0.55}Ba^{2+}_{0.11}V^{(c)}_{0.24}\}_A[Mn^{3+}_{0.80}Mn^{4+}_{0.11}]_B(Mn^{3+}_{0.06}Mn^{4+}_{0.06}Mn^{2+}_{0.06})_{cl}O^{2-}_{2.66}V^{(a)}_{0.34}$
0.3	1	$\{La^{3+}_{0.50}V^{(c)}_{0.24}\}_A[Mn^{3+}_{1.22}Mn^{4+}_{0.03}]_B O^{2-}_{2.64}V^{(a)}_{0.36}$
	2	$\{La^{3+}_{0.50}V^{(c)}_{0.24}\}_A[Mn^{3+}_{0.70}Mn^{4+}_{0.26}]_B(Mn^{4+}_{0.03}Mn^{2+}_{0.26})_{cl}O^{2-}_{2.64}V^{(a)}_{0.36}$

are also found in the clusters, are distributed near cation vacancies.

Table III shows the crystal lattice parameters of the main perovskite-like magnetoresistive lanthanum–barium manganite phase $La_{0.7-x}Ba_{0.3-x}MnO_3$, the metal–semiconductor phase transition temperatures T_{ms}, Curie temperatures T_C, magnetoresistance peak temperatures T_p, and the values of $\Delta R/R_0$. The decrease of the parameter a with increasing x is explained by a decrease in the concentration of the ions La^{3+} ($r=1.36$ Å) and Ba^{2+} ($r=1.61$ Å), which have larger ionic radii[19] than their substituent ions Mn^{3+} ($r=0.645$ Å) and Mn^{4+} ($r=0.53$ Å). The relative changes in the values of the averaged ionic radius ($\Delta r/r_0=2.5\%$), calculated according to the data of Table II, and of the unit cell volume ($\Delta V/V=2.8\%$), determined from the x-ray diffraction data, are in satisfactory agreement.

The temperature dependence of the relative resistance ($R/R_{300\,K}$) of the samples is illustrated in Fig. 1, and the magnetoresistive effect ($\Delta R/R_0$) in Fig. 2. According to these data, the relative resistance increases and the transition temperatures T_{ms}, T_p, and T_C decrease with increasing x (see Table II and Figs. 1 and 2). This character of the change in these parameters with increasing x is apparently due to the increase in the $La_2Sn_2O_7$ content in the intercrystallite zones and the increasing density of crystal lattice defects of both the point ($V^{(c)}, V^{(a)}$) and cluster types in the main perovskite structure. It is noteworthy that for the composition with $x=0.3$ the temperature dependence of $R/R_{300\,K}=f(T)$ exhibits two maxima due to the increased inhomogeneity, phase and/or cluster, of these samples.

Several peaks on the temperature dependence of the resistance of ceramic samples have also been observed in other

TABLE III. Physical properties of the main lanthanum–barium manganite phase $La_{0.7-x}Ba_{0.3-x}MnO_3$.

x	Parameters of the crystal lattice		phase transition temperatures T [K]			$\Delta R/R_0$, %	F, MHz	
	a, Å	α, deg	T_C	T_p	T_{ms}		^{55}Mn	^{139}La
0	7.848	90.32	350	330	330	6,7	355.0 380.0	21
0.1	7.826	90.21	288	280	275	11.5	330.0 352.0 380.0	20
0.15	7.815	90.38	285	270	260	13.0	330.0 352.5 380.0	19.5
0.2	7.806	90.41	284	260	250	14,0	330.0 352.8 380.0	19.0
0.3	7.774	90.53	275	235	230	16,7	358.5 378.0	15.0

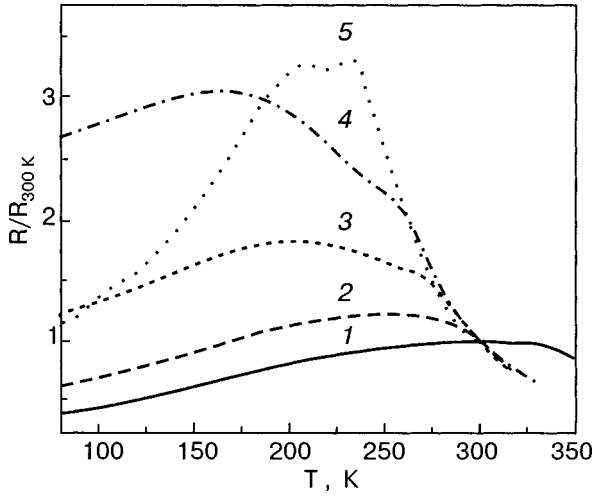

FIG. 1. Temperature dependence of the relative resistance of ceramic samples of $La_{0.7-x}Ba_{0.3-x}Sn_xMnO_3$ of various compositions x: 0 (*1*), 0.1 (*2*), 0.15 (*3*), 0.2 (*4*), 0.3 (*5*).

studies,[13,20,21] the authors of which also attributed them to inhomogeneities but without revealing their crystal-chemical and magnetic nature.

According to the data of Table II, increasing x from 0 to 0.3 leads to an increase in the density of lattice defects of both the point and cluster types. At the same time, the magnetoresistive effect increases by a factor of 2.5 (Fig. 2). The temperature of the peak of the magnetoresistive effect decreases from 330 to 230 K, i.e., by 100 K. Such a substantial lowering of T_{ms}, T_p, and T_C (Figs. 1 and 2; Table III) cannot be explained solely by the decrease of the La and Ba content and increase of the Mn content or even by the lattice defects given in Table I in their point representation. Of particular interest are the differences of the phase transition temperatures $\Delta T = T_C - T_{ms}$. The value of these differences fluctuates strongly: from 0 to 100 K. In our opinion, the cause of these changes and differences may be changes in the Mn^{3+}/Mn^{4+} ratio and, more importantly, imperfection of the crystal lattice, especially its mesoscopic inhomogeneity due to the excess manganese, which leads to an appreciable deficit not only of the cations La^{3+} and Ba^{2+} in the A sublattice and to a lesser degree in the B sublattice, but also to incompleteness of the anion sublattice, i.e., to an increase in the overall imperfection of the crystal lattice.

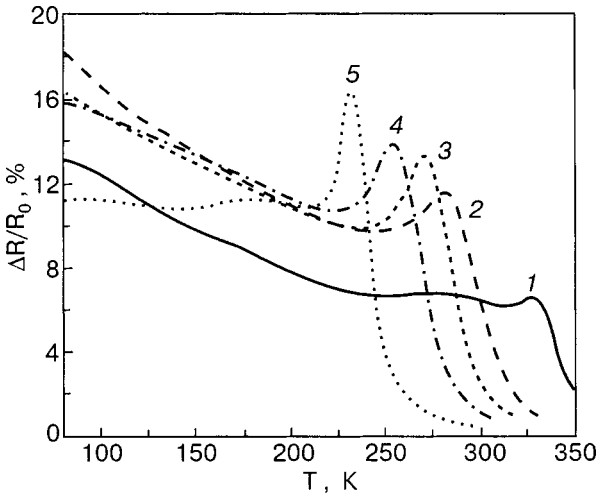

FIG. 2. Magnetoresistive effect ($\Delta R/R$) for ceramic samples of $La_{0.7-x}Ba_{0.3-x}Sn_xMnO_3$ of various compositions x: 0 (*1*), 0.1 (*2*), 0.15 (*3*), 0.2 (*4*), 0.3 (*5*).

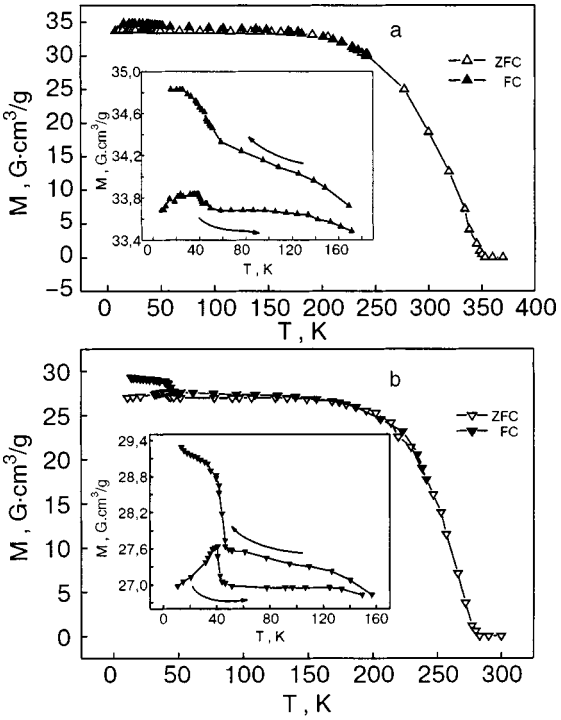

FIG. 3. Temperature dependence of the magnetization at $H = 0.5$ kOe for ceramic samples of $La_{0.7-x}Ba_{0.3-x}Sn_xMnO_3$ of various compositions x: 0 (a), 0.2 (b).

To refine the role of the excess manganese in the formation of clusters and their contribution to the magnetic properties of the samples we made magnetic measurements of the magnetization M over a wide range of temperatures at different magnetic field strengths. Samples of all compositions were studied. As an illustration, in Figs. 3 and 4 we present the results of these magnetic measurements for the samples with $x = 0$ and $x = 0.2$ at low, $H = 0.5$ kOe, and high, $H = 10$ kOe, saturating fields in the temperature interval 10–300 K. A notable feature is the presence of two smeared phase transitions: 1) at $T = 350$ K $= T_C$ ($x = 0$) or 277 K ($x = 0.2$), and 2) at $T = 45$ K. While the phase transition at $T = T_C$ is associated with the Curie temperature of the main perovskite-like phase, the transition at $T = 45$ K, which is practically the same for all the samples, requires a more detailed analysis. According to the data of our previous studies,[17,22] the excess manganese in the magnetoresistive lanthanum manganite perovskite structure can be found not only in the form of an individual phase but also in the form of planar clusters of Mn_3O_4 and/or Mn_2O_3 or a solid solution intermediate between these compositions. This is confirmed by the increase in the jump ΔM at $T = 45$ K from 0.5 G $\cdot$ cm^3/g ($x = 0$) to 1.5 G$\cdot$cm^3/g at $H = 0.5$ kOe for the sample with $x = 0.2$. This phase transition, which is due to a manifestation of cluster magnetism, is suppressed by a strong magnetic field ($H = 10$ kOe). Unlike the Mn_3O_4 phase, a cluster in a weak magnetic field exhibits a sharp drop in magnetization in the temperature interval 42–45 K, and only in a strong magnetic field is there a growth in the magneti-

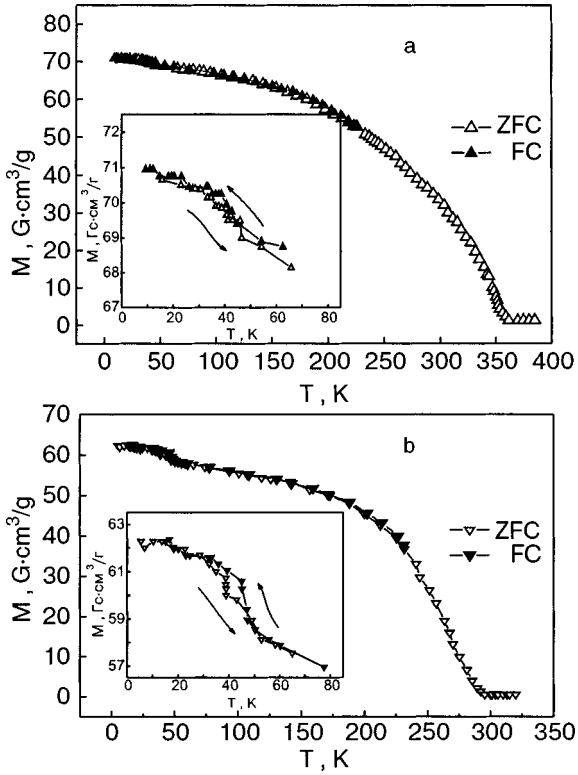

FIG. 4. Temperature dependence of the magnetization at $H=10$ kOe for ceramic samples of $La_{0.7-x}Ba_{0.3-x}MnO_3$ of various compositions x: 0 (a), 0.2 (b).

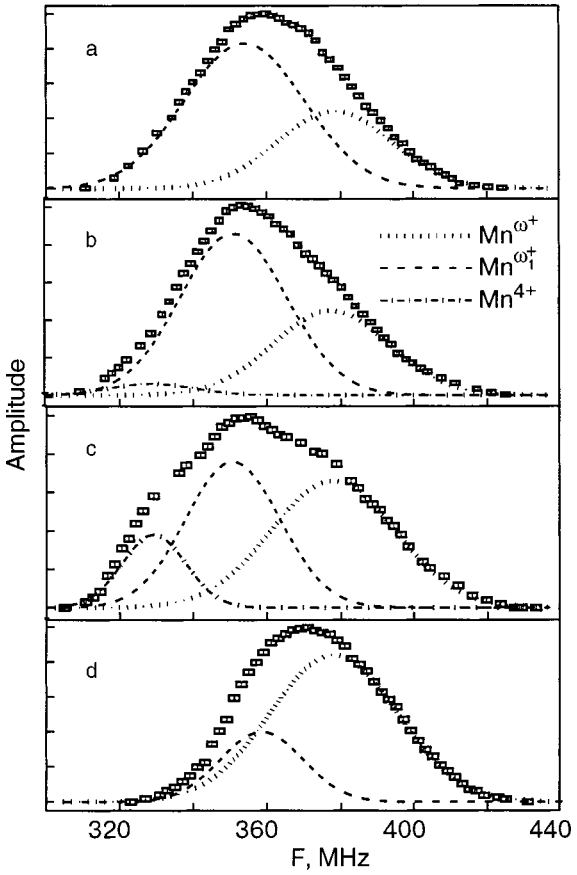

FIG. 5. NMR spectra of ^{55}Mn at 77 K in ceramic samples of $La_{0.7-x}Ba_{0.3-x}MnO_3$ of various compositions x: 0 (a), 0.1 (b), 0.2 (c), 0.3 (d). ω^+ is the averaged valence of the manganese ions in the matrix structure; ω_1^+ is the averaged valence of the manganese ions in the cluster structure.

zation. Another distinctive feature of the cluster state is a pronounced hysteresis appearing in weak fields for the sample with $x=0.2$ (Fig. 3).

The structure and magnetic nature of these clusters, which are coherently connected with the matrix of the perovskite structure, is still under discussion and is attracting more interest.

Our NMR studies on ^{55}Mn (Fig. 5) and ^{139}La (Fig. 6) confirm the high degree of imperfection and inhomogeneity of the lanthanum manganite perovskites $La_{0.7-x}Ba_{0.3-x}MnO_3$. The broad, asymmetric NMR spectrum of ^{55}Mn ($F=320-420$ MHz) attests to nonequivalence of the magnetic (and valence) states of the manganese ions found in rf electron exchange. By decomposing these spectra one can isolate several components due to the different magnetic and valence states of the manganese ions, with an averaged valence $\bar{\omega}=3.5$, and to their different environment, not only in relation to the La^{3+} and Ba^{2+} ions but also to cation vacancies in the A positions. The asymmetrically broadened satellite spectra, in turn, attest to a nonstatistical distribution of ions and defects, confirming the possibility of cluster formation. The decrease of the resonance frequency of the NMR spectrum of ^{139}La (Fig. 6) is also explained by the presence of such (nonmagnetic) clusters, the manganese ions and vacancies of which surround the lanthanum (and partially the barium) ions.

Analogous structural clusters in the form of individual planes of pseudostructural type Mn_3O_4 and/or Mn_2O_3 have been observed by an x-ray method in $La_{1-x}Mn_{1+x}O_3$ (Ref. 17) and by a neutron-diffraction method in $La_{0.63}Ca_{0.27}Mn_{1.1}O_4$ (Ref. 22).

Such a model of the clusterized defect perovskite structure is in agreement with the asymmetrically broadened peaks on the NMR spectra of ^{55}Mn (Fig. 5) and ^{139}La (Fig. 6). Such complex NMR spectrum of ^{55}Mn and ^{139}La have been observed previously in $La_{1-y}Ca_7MnO_3$ (Ref. 23), $La_{0.85}Na_{0.15}MnO_3$ (Ref. 24), $LaMnO_{3+\delta}$ (Refs. 25 and 26), $La_{1-x}Ca_xMnO_3$ (Ref. 27), and $La_{0.9}MnO_3$ (Ref. 28). A computer decomposition of our broad, asymmetric spectrum into the corresponding components attests not only to the non-

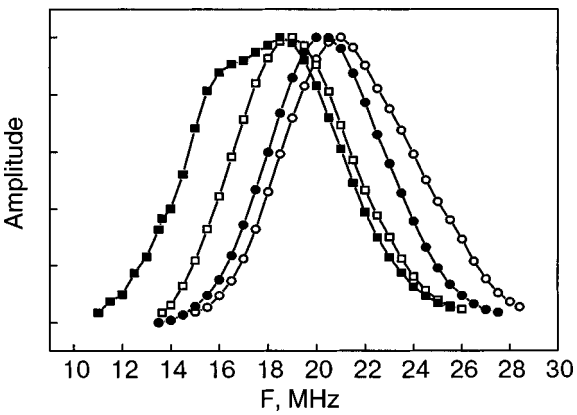

FIG. 6. NMR spectra of ^{139}La at 77 K in ceramic samples of $La_{0.7-x}Ba_{0.3-x}MnO_3$ of various compositions x: 0 (○), 0.1 (●), 0.2 (□), 0.3 (■).

equivalence of the states of the manganese and lanthanum ions but also to distortion of the polyhedra and to structural and magnetic inhomogeneities due to the different environment of these ions, including vacancies and clusters, which disrupt the exchange interactions.

The samples characterized by the maximum inhomogeneity according to the ^{55}Mn NMR data (three-component spectrum) are those with $x=0.1$ and 0.2 (see Fig. 5 and Table II), since in them the manganese ions found in rf electron exchange are surrounded by La^{3+} and Ba^{2+} ions and cation vacancies. Such a character of the inhomogeneity and imperfection of the structure of the main lanthanum–barium manganite phase is attested to by the similarity of the spectrum of our $x=0.3$ sample with those found previously[17] for $La_{1-x}Mn_{1+x}O_3$ ceramics with $x=0.3$ and $x=0.4$, i.e., self-doped lanthanum manganite perovskites of similar composition.

If the excess manganese were not dissolved in the main perovskite-like phase and the defect density did not change with increasing x, then the frequency and width of the peaks on the NMR spectra would not change. Their width should even decrease, since according to Refs. 29 and 30, barium-containing lanthanum manganite perovskites characteristically have a maximal width due to the maximal distortion of the A positions occupied by the Ba^{2+}, with a substantially larger ionic radius ($r=1.61$ Å) in comparison with La^{3+} ($r=1.36$ Å). Another contribution to the additional broadening of the spectra due to the nonequivalence of the environment of the manganese ions (Fig. 5) comes from the predominantly cation vacancies in the A positions, the relative number of which increases from 8% to 24% (Table II), i.e., by 16%. The relative broadening of the NMR lines of ^{139}La and the decrease of their resonance frequency as x is increased from 0 to 0.3 is apparently due predominantly to clusters, the relative number of which increases from 2% to 14.5%, i.e., by 12.5% (Table II).

It is of interest to compare the increase in these imperfections of the crystal lattice with the increase in x from 0 to 0.3 with the increase in the magnetoresistive effect from 6.7% to 16.7%, i.e., by 10% (Table III). The sample with $x=0.3$ is characterized by the maximum concentration of vacancies and clusters, which disrupt the exchange interaction, apparently causing a decrease of the NMR resonance frequency of ^{139}La and a lowering of the phase transition temperatures T_{ms}, T_p, and T_C (Fig. 6). Then the lowering of the phase transition temperatures T_{ms}, T_p, and T_C (Table III) and the increase of the magnetoresistive effect (Fig. 2) and the magnetic moment of the clusters (Fig. 3), the complex NMR spectra of ^{55}Mn (Fig. 5) and ^{139}La (Fig. 6) and also their asymmetric broadening to the low-frequency side can be explained by a change in the Mn^{3+}/Mn^{4+} ratio and to imperfection of the crystal lattice, which is manifested not only in the form of point defects (vacancies) but also as more complex defects (clusters) due to the excess manganese in the main perovskite structure.

Hence one is forced to conclude that the defect state of the crystal lattice of the perovskite-like structure has the governing influence on the CMR. To establish conclusively the predominant influence of one type of defect state or another is impossible; moreover, these defects apparently are ''organically'' related.

TABLE IV. Defect state of the structure of the lanthanum manganite barium perovskite $La_{0.7-x}Ba_{0.3-x}MnO_{3-\delta}$ and the activation energy ^sE_a in the region of semiconductor conduction in the ceramic $La_{0.7-x}Ba_{0.3-x}Sn_xMnO_3$.

x	V, %	$(Mn_3O_4)_{cl}$, %	^sE_a, meV
0	8	2	–
0.1	10	4	150
0.15	11	7	62.8
0.2	12	10	41.6

It must be assumed that for a greater imperfection of the crystal lattice, which contains both cation and anion vacancies simultaneously, the heterovalent manganese ions, which are sources of charge carriers of the n type ($V^{(a)}$, Mn^{2+}, Mn^{3+}) and p type ($V^{(c)}$, Mn^{4+}), the values of the activation energy ^sE_a in the region of semiconductor-type conduction will either be comparable to the data of Ref. 31 or lower.[1,32] In view of the inverse relation between the conductivity σ and resistivity ρ, from the plots of $\ln\rho$ versus $1/T$ we determined the activation energy ^sE_a of the conductivity in the region of semiconductor conduction from the exponential Arrhenius law $\rho=\rho_0\exp(-E_a/kT)$. The values obtained for the activation energy are given in Table IV.

CONCLUSIONS

We have carried out x-ray, magnetic, resistive, and ^{55}Mn and ^{139}La NMR studies of ceramic samples of $La_{0.7}Ba_{0.3-x}Sn_xMnO_3 \rightarrow La_{0.7-x}Ba_{0.3-x}MnO_3 + 0.5xLa_2Sn_2O_7$. We have shown that substitution of barium by tin leads to the formation of both a main perovskite-like ($R\bar{3}c$) lanthanum–barium manganite phase and much smaller amounts of a pyrochlore-like ($Fd3m$) lanthanum–tin phase. The crystal lattice of the magnetoresistive phase $La_{0.7x}Ba_{0.3-x}MnO_3$ contains defects of subtraction (vacancies) in both the cation and anion sublattices and mesoscopically nonuniform formations of a cluster type—planar segregations which are close in composition and structure to Mn_3O_4 or Mn_2O_3, the magnetic phase transition of which occurs in the temperature interval 42–45 K. The strongly smeared temperature dependence of the resistance near the metal–semiconductor phase transition (T_{ms} decreases with increasing x) attests to the increasing inhomogeneity and imperfection. As x increases from 0 to 0.3 the magnetoresistive effect increases by a factor of 2.6. The broad, asymmetric NMR spectra of ^{55}Mn and ^{139}La in $La_{0.7-x}Ba_{0.3-x}MnO_3$ attests to rf electron exchange between Mn^{3+} and Mn^{4+}, to the nonequivalence of their environments and that of La^{3+}, not only in relation to the heterovalent ions but also to cation vacancies and clusters. A substantial influence of the defect state of the structure, in particular that of the cluster type, on the magnetoresistive effect attests to the governing role of such inhomogeneities on the CMR. The low values of the activation energy attest to significant inhomogeneity and imperfection in the samples of the given compositions.

This study was supported in part by Polish Grant 2RO3B 139 18.

*E-mail: pashchen@pashchen.fti.ac.donetsk.ua
†Deceased

[1] R. Mahendiran, S. K. Tiwary, A. K. Raychaudhuri, T. V. Ramakrishnan, R. Mahesh, N. Rangavittal, and C. N. R. Rao, Phys. Rev. B **53**, 3348 (1996).
[2] É. L. Nagaev, Usp. Fiz. Nauk **166**, 833 (1996).
[3] J. Alonso, E. Herrero, J. M. Gonzalez-Calbet, M. Vallet-Regi, J. L. Martinez, J. M. Rojo, and A. Hernando, Phys. Rev. B **62**, 11328 (2000).
[4] T. Egam, Local At. **98**, 116 (2001).
[5] D. M. Edwards, Adv. Phys. **51**, 1259 (2002).
[6] H. L. Ju and Hyunchul Sohn, J. Magn. Magn. Mater. **167**, 200 (1997).
[7] M. R. Ibarra, Gue-mag Zhao, J. M. Teresa, B. Garsia-Landa, Z. Apold, C. Marguina, P. A. Algarabel, H. Keller, and C. Petter, Phys. Rev. B **57**, 74 (1998).
[8] V. V. Runov, D. Yu. Chernyshev, A. I. Kurbakov, M. K. Runova, V. A. Trunov, and A. I. Okorokov, Zh. Éksp. Tear. Fiz. **118**, 1174 (2000) [JETP **91**, 1017 (2000)].
[9] X. Xiong, B. Dabrowski, O. Chmaissem, Z. Bukowski, S. Kolesnik, R. Dybzinski, C. W. Kiwball, and J. D. Jorgensen, Phys. Rev. B **60**, 10186 (1999).
[10] M. T. Causa, G. Alejandro, R. Zysler, F. Prado, A. Caneiro, and M. Tovar, J. Magn. Magn. Mater. **196–197**, 506 (1999).
[11] M. Fath, S. Freisem, A. A. Menovsky, Y. Tomioka, J. Aarts, and J. A. Mydosh, Science **285**, 1540 (1992).
[12] H. L. Ju and Hyunchul Sohn, Solid State Commun. **102**, 463 (1997).
[13] V. N. Krivoruchko, V. P. Pashchenko, Yu. V. Medvedev, S. I. Khartzev, A. A. Shemyakov, M. M. Savosta, V. I. Kamenev, A. D. Loyko, G. K. Volkova, and V. I. Volkov, Phys. Lett. A **245**, 163 (1998).
[14] L. Pi and L. Zhang, Phys. Rev. B **61**, 8917 (2001).
[15] S. Dai, Z. W. Li, A. H. Morrish, X. Z. Zhou, J. G. Zhao, and X. M. Xiong, Phys. Rev. B **55**, 14125 (1997).
[16] Z. W. Li, A. H. Morrish, and J. Z. Jiang, Phys. Rev. B **60**, 10284 (1999).
[17] V. P. Pashchenko, S. I. Khartzev, O. P. Cherenkov, A. A. Shemyakov, Z. A. Samoilenko, A. D. Loyko, and V. I. Kamenev, Neorg. Mater. **35**, 1509 (1999).
[18] K. Kumagai, A. Iwai, Y. Tomioka, H. Kuwahara, Y. Tokura, and A. Yakulovskii, Phys. Rev. B **59**, 97 (1999).
[19] R. P. Shannon, Acta Crystallogr., Sect. A: Cryst. Phys., Diffr., Theor. Gen. Crystallogr. **32**, 751 (1976).
[20] A. Nosov, V. Ustinov, V. Vassiliev, and E. Vladimirova, Fiz. Met. Metalloved. **93**, 25 (2002).
[21] S. S. Kucherenko, V. P. Pashchenko, P. I. Polyakov, V. A. Shtaba, and A. A. Shemyakov, Fiz. Nizk. Temp. **27**, 761 (2001) [Low Temp. Phys. **27**, 559 (2001)].
[22] W. Basela, V. Dyakonov, V. Pashchenko, V. Penc, H. Szymczak, J. H. Hernández-Velasco, and A. Szytula, Phys. Status Solidi **236**, 458 (2003).
[23] G. Allodi, R. De Renzi, G. Guidi, F. Licci, and M. W. Pieper, Phys. Rev. B **56**, 6036 (1997).
[24] M. M. Savosta, V. A. Borodin, P. Novak, Z. Jirak, J. Hejtmanek, and M. Marysko, Phys. Rev. B **57**, 13379 (1998).
[25] Cz. Kapusta and P. C. Riedi, J. Magn. Magn. Mater. **196–197**, 446 (1999).
[26] M. Tovar, G. Alejandro, A. Butera, A. Caneiro, M. T. Causa, F. Prado, and R. D. Sánchez, Phys. Rev. B **60**, 10199 (1999).
[27] G. Papavassiliou, M. Fardis, M. Belesi, T. G. Maris, G. Kallias, M. Pissas, D. Niarchos, C. Dimitropoulos, and J. Dolinsek, Phys. Rev. Lett. **84**, 761 (2000).
[28] K. N. Mikhalev, S. A. Lekomtsev, A. P. Gerashchenko, V. E. Arkhipov, A. V. Korolev, Ya. M. Mukovskiĭ, and A. A. Arsenov, JETP Lett. **72**, 599 (2000).
[29] M. M. Savosta, A. N. Ulyanov, N. Yu. Starostyuk, M. Marysko, and P. Novak, Eur. Phys. J. B **12**, 393 (1999).
[30] V. P. Pashchenko, A. N. Ulyanov, A. A. Shemyakov, S. I. Khartsev, N. N. Mesin, Ju. V. Medvedev, H. V. Gusakov, and V. A. Turchenko, Neorg. Mater. **38**, 302 (2002).
[31] Young Sun, Xiaojun Xu, Lei Zheng, and Yuheng Zhang, Phys. Rev. B **60**, 12317 (1991).
[32] A. K. M. Akther Hossain, L. F. Cohen, F. Damay, N. McN. Aldord, N. D. Mathur, M. G. Blamire, and J. E. Evetts, J. Magn. Magn. Mater. **192**, 263 (1999).
[33] R. Ganguly, I. K. Gopalakrishnan, and J. V. Yakhazi, Phys. Rev. B **235**, 308 (2000).

Translated by Steve Torstveit

Coupling of the magnetic layers and electron spin polarization in four-layer structures of amplitude and nonmagnetic semiconductors

V. V. Zorchenko,* A. Yu. Sipatov, and V. V. Volobuev

National Technical University "Kharkov Physicotechnical Institute," 21 Frunze St., 61002 Kharkov, Ukraine
(Submitted April 15, 2003)
Fiz. Nizk. Temp. **29**, 1209–1222 (November 2003)

The electron energy spectrum, the energy E_m of the exchange coupling between magnetic layers, and the relative polarization β of the electron spins in semiconductor structures with two ferromagnetic barriers and nonmagnetic layers acting as potential wells for electrons are considered. For the example of EuS/PbS(001) structures it is shown that in the case of Fermi statistics E_m is a sign-varying oscillatory function of the width a of the potential well between barriers, and with increasing electron density n_0 in the wells and increasing thickness d of the nonmagnetic sublayers between the barrier and substrate, the extrema of E_m are shifted to smaller a and their amplitudes rapidly increase. As the temperature is lowered from the Curie point, the energy E_m, depending on a, n_0, and d, can increase (in modulus) monotonically or nonmonotonically, change sign from positive to negative, or change sign twice. The polarization β decreases with increasing a, n_0, and d, undergoing sharp jumps when E_m changes sign. For Boltzmann statistics only a ferromagnetic orientation of the barrier magnetizations ($E_m<0$) is possible. © *2003 American Institute of Physics.* [DOI: 10.1063/1.1614236]

1. INTRODUCTION

Since the discovery of interlayer exchange coupling (IEC) in three-layer Fe/Cr/Fe samples,[1] numerous multilayer structures consisting of various ferromagnetic (F) metals separated by nonmagnetic (NM) metal or semiconductor spacer layers or by layers of a rare-earth ferromagnet have been investigated (see, e.g., the review[2]). In those cases the IEC is due to interference between the conduction electrons in the layered structures and to their high concentration.[3] In addition, there are several known studies of the IEC in insulating multilayers containing antiferromagnetic (AF) insulators [Fe_3O_4/MgO (Ref. 4), FeF_2/CoF_2 (Ref. 5), CoO/NiO (Ref. 6)].

The detection of an appreciable exchange coupling between antiferromagnetic layers in the semiconductor superlattices (SLs) MnTe/CdTe,[7,8] MnTe/ZnTe,[8,9] EuTe/PbTe,[10] and somewhat later in EuS/PbS single-crystal SLs[11] and (Ga,Mn)As/(Al,Ga)As/(Ga,Mn)As three-layer samples[12] has been something of a surprise. The limiting thickness of the nonmagnetic spacer layers at which the coupling between magnetic layers is still felt is approximately 30 Å for MnTe/CdTe structures, up to 15 Å for the MnTe/ZnTe structures, up to 70 Å for EuTe/PbTe, and over 30 Å in the structures with (Ga,Mn)As and (Al,Ga)As (see the review[13] for details). For EuTe/PbTe(111) SLs the spins of the Eu ions lie in the (111) planes, the adjacent Eu monolayers having antiparallel magnetization directions. Independently of the thickness of the EuTe and PbTe layers, the coupling of neighboring EuTe layers leads to an antiparallel alignment of the magnetic moments of the Eu monolayers adjacent to the opposite boundaries of the PbTe layer (antiferromagnetic coupling).[14]

In EuS/PbS(001) SLs the magnetizations of neighboring EuS layers are oriented along the layers and are ordered antiparallel at thicknesses of the nonmagnetic spacer layers $d_{PbS} \leqslant 90$ Å,[11,15] while at larger d_{PbS} the sign of the interaction changes to the opposite. This is manifested in a superposition of the neutron-scattering patterns from the antiferromagnetically and ferromagnetically oriented parts of the sample, these different regions arising on account of a slight difference ($\sim 1-2$ monolayers) in the thickness of the PbS layers on different areas of a sample with $d_{PbS}=90$ Å.[16] In EuS/PbS(111) SLs only ferromagnetic ordering of the EuS layers has been observed. Interestingly, in MnTe/ZnTe SLs a change in the sign of the interaction with decreasing temperature of the sample has been observed.[13] These effects have not been explained.

For structures with MnTe there are two models in the literature, according to which the IEC is due to carriers localized at shallow impurities in the nonmagnetic spacer regions.[17,18] However, those models are not applicable to PbS spacers, since PbS does not contain local shallow impurity states in the band gap. The model of Dugaev *et al.*[19] for narrow-gap spacers of IV–VI semiconductors gives too weak a coupling in comparison with that observed experimentally in EuS/PbS(001) SLs, and the coupling is of the opposite sign (always ferromagnetic, as in the models of Refs. 17 and 18). The model of Ref. 19 (and other models considered below) is based on the assumption that there are no free charge carriers in the spacer layer, in direct contradiction to the experimental situation, in which the electron density in the *n*-type PbS layers is rather high (up to $\sim 10^{19}$ cm^{-3}), and it cannot be neglected.

Calculations in the one- and three-dimensional strong-coupling approximations[20,21] have produced results in qualitative agreement with the experimental results for the magnetic ordering in the layers of EuTe/PbTe(111) SLs, but for EuS/PbS(111) SLs the results of the calculations contradict each other: in the 1D model the coupling must be F-type,[20] while in the 3D model it must be AF-type[21] (in contradiction

to the experimental results of Refs. 11, 13, and 15). For EuS/PbS(001) SLs the three-dimensional model gives an AF configuration of adjacent EuS layers but is unable to explain the change in sign of the interaction at larger d_{PbS}. Furthermore, it predicts that the coupling energy J_1 is almost independent of the thickness of the EuTe and EuS magnetic layers, whereas such a dependence should be substantial in the region of small d_{EuS} (see below). For a PbS spacer the value $J_1 \sim 2^{-n}$ was calculated, where n is the number of PbS monolayers in the EuS/PbS(001) SL.[21] The experimental values for $n=1$, 2, and 3 ($J_1=0.063$, 0.031, and 0.019 mJ/m^2, respectively)[15] are an order of magnitude less than the corresponding theoretical values ($J_1=0.77$, 0.33, 0.18 mJ/m^2).[21] At $d_{\mathrm{PbS}} \sim 90$ Å ($n \sim 30$) this model gives a negligibly small value of J_1, in disagreement with experiment. A shortcoming of this type of model is the presence of a set of adjustable fitting parameters and the difficulty of matching the levels of the chemical potential with the carrier density in the SL.[22] Thus at the present time there is no sufficiently clear and reliable explanation for the nature of the coupling in EuS/PbS and EuTe/PbTe superlattices.

We note that in EuTe/PbTe and EuS/PbS SLs the EuTe and EuS layers have a wide band gap [E_g(EuS)=1.65 eV, E_g(EuTe)=2 eV at $T=300$ K],[23] while lead chalcogenides are narrow-gap semiconductors [E_g(PbS)=0.307 eV at $T=77$ K],[24] and therefore europium chalcogenides act as barriers in the corresponding SLs, while the lead chalcogenide layers form quantum wells. Doping of these layers with europium leads to a noticeable increase in E_g [e.g., E_g(PbTe) =0.319 eV, E_g($Pb_{0.927}Eu_{0.073}Te$)=0.63 eV at $T=300$ K],[25] and so there is the possibility of substantially changing the barrier height in such SLs and thereby to control the force coupling the magnetic layers.

In view of the promise of two-barrier structures with ferromagnetic barriers for applications in spintronics[26] and for research now being carried out on EuS/PbS/EuS/PbS/KCl multilayers, in this paper we present the results of a theoretical analysis of the coupling of magnetic layers in structures of this type grown on a sublayer of a quantum-well material formed between the ferromagnetic barriers (such a sublayer is necessary because it is practically impossible to grow single-crystal ferromagnetic insulators directly on an insulating substrate). In the calculations we made use of the circumstance that the energy of an electron in such a structure depends on the mutual orientation of the electron spin direction and the magnetic moments of the ferromagnetic barriers. As in the case of metallic multilayers, the coupling is of an interference nature. Therefore the sign and value of the IEC depend on the parameters of the potential relief (the heights of the barriers, widths of the quantum wells between them, the thicknesses of the sublayers, etc.) and on the electron density and temperature of the sample. Transitions from a ferromagnetic to an antiferromagnetic orientation of the barriers are accompanied by a sharp change in the spin polarization of the electron subsystem of the sample.

2. ELECTRON ENERGY SPECTRUM AND STATISTICS

We shall use the model shown in Fig. 1 for the potential relief for electrons in a four-layer F/NM structure. A similar model has been applied for calculating the size quantization

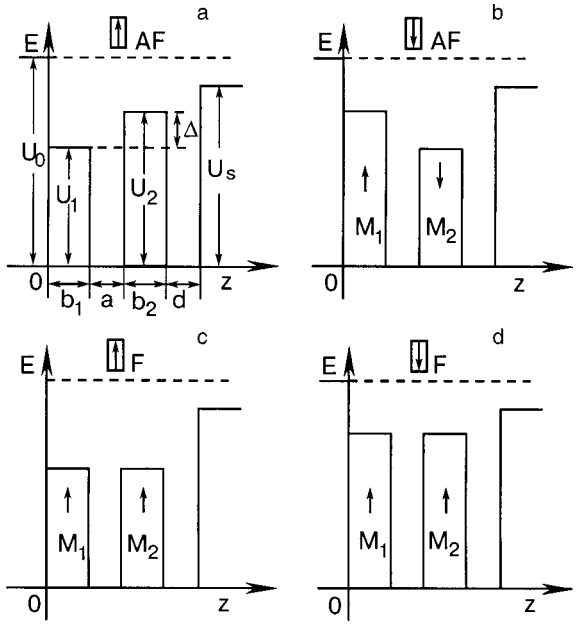

FIG. 1. Potential energy of electrons with spins up (↑) and down (↓) for antiferromagnetic (AF) (a and b) and ferromagnetic (F) (c and d) ordering of the magnetic layers in a four-layer structure F(b_1)/NM(a)/F(b_2)/NM(d) on an insulating substrate. The heavy arrows indicate the direction of the magnetic moments $\mathbf{M}_{1,2}$ of the ferromagnetic barriers. The electron spin orientation is indicated by an arrow in a rectangular frame.

of the electron levels in quantum wells and PbS/EuS SLs.[27] The potential barriers U_0 and U_s of semi-infinite width describe the vacuum and substrate regions. A sublayer of NM material occupies the region $D+d>z>D$, where $D=a+b_1+b_2$. Four types of potential wells for electrons with spins up (↑) and down (↓) in Fig. 1 correspond to antiferromagnetic (a and b) and ferromagnetic (c and d) configurations of the magnetization $\mathbf{M}$ of the ferromagnetic layers, creating barriers in the regions $0<z<b_1$ and $a+b_1<z<D$. As in the description of the tunneling of electrons through an EuS barrier at temperatures below the Curie point T_C of the barrier,[28] the height of the barriers U_1 and U_2 for electrons with spins parallel to and antiparallel to the barrier magnetization $\mathbf{M}$ are given by the relation $U_{2.1}=U \pm (\Delta/2)$, where U is the barrier height for $T>T_C$, and Δ is the exchange splitting of the conduction band of the ferromagnetic semiconductor below T_C.

We shall assume that the electron energy spectrum in the structure under consideration is described by the expression usually used for multilayers:

$$E_n(\mathbf{p}_\perp)=\frac{p_\perp^2}{2m^*}+\varepsilon_n, \quad \mathbf{p}_\perp=\{p_x,p_y\}, \tag{1}$$

in which m^* is the effective mass for motion of the electrons along the layers, and ε_n are the quantum size-effect levels, which are solutions of the Schrödinger equation with the potential $U(z)$ (Fig. 1). In Ref. 27 the miniband spectrum of EuS/PbS SLs with layer orientations (001) and (111) were calculated for the case $T>T_C$, where the potential $U(z)$ is described by the Kronig–Penney model with $U_1=U_2=U$. A study[27] of the photoluminescence spectra of EuS/PbS SLs with wide EuS barriers, in which the minibands degenerate into quantum size-effect levels, showed good agreement of

the observed levels with the calculated values, and we have therefore used for multilayers of EuS and PbS the same technique for calculating ε_n (with allowance for the direction of the electron spin) as in Ref. 27, replacing the SL potential by the potential $U(z)$ shown in Fig. 1.

We denote the effective masses for electron motion transverse to the layers (along the Oz axis) in the quantum-well and barrier regions as m and m_b, respectively. We shall neglect the small difference in the effective masses m_b for electrons with opposite spin directions[29] and use the averaged value for m_b.[27]

Then for electrons in the potential well a in Fig. 1 the eigenvalues ε_n of the Schrödinger equation are determined from the following relation ($\varepsilon < U_s$):

$$\tan(ka) = \gamma k\left[\frac{\chi_1\{1\}+\chi_2\{2\}\tanh(\chi_1 b_1+\alpha_1)}{k^2\{1\}\tanh(\chi_1 b_1+\alpha_1)-\gamma^2\chi_1\chi_2\{2\}}\right], \quad (2)$$

in which

$$\{1\} = \gamma\chi_2\cosh(\chi_2 b_2)\sin(kd+\theta)+k\sinh(\chi_2 b_2)\times\cos(kd+\theta). \quad (3)$$

$$\{2\} = \gamma\chi_2\sinh(\chi_2 b_2)\sin(kd+\theta)+k\cosh(\chi_2 b_2)\times\cos(kd+\theta),$$

$$k=\frac{\sqrt{2m\varepsilon}}{\hbar}, \quad \chi_{1,2}=\frac{\sqrt{2m_b(U_{1,2}-\varepsilon)}}{\hbar},$$

$$\chi_0=\frac{\sqrt{2m_e(U_0-\varepsilon)}}{\hbar}, \quad \chi_s=\frac{\sqrt{2m_s(U_s-\varepsilon)}}{\hbar},$$

$$\tanh\alpha_1=\frac{m_e}{m_b}\frac{\chi_1}{\chi_0}, \quad \tan\theta=\frac{m_s}{m}\frac{k}{\chi_s}, \quad \gamma=\frac{m}{m_b}. \quad (4)$$

Here m_e is the free electron mass, and m_s is the effective mass in the substrate material. For potential wells b, c, and d (Fig. 1) the following replacements must be made in Eqs. (2) and (3): $\chi_1\to\chi_2$ and $\chi_2\to\chi_1$ (well b), $\chi_2\to\chi_1$ (well c), and $\chi_1\to\chi_2$ (well d).

For sufficiently wide potential barriers and energy not too close to U_1 the parameters $\chi_1 b_1 \gg 1$, $\chi_2 b_2 \gg 1$, and therefore the ratio $\{1\}/\{2\}$ and $\tanh(\chi_1 b_1+\alpha_1)$ are practically equal to unity. When these conditions are met for the AF configuration of the barriers, the size-quantization levels for the electrons with spin up, $\varepsilon_n^{\uparrow}(\mathrm{AF})$, and spin down, $\varepsilon_n^{\downarrow}(\mathrm{AF})$, coincide to high accuracy (see below). In that case the parameters of the substrate and the sublayer thickness d do not have an appreciable influence on the electron energy. The following inequalities hold for any values of $\chi_1 b_1$ and $\chi_2 b_2$: $\varepsilon_n^{\uparrow}(\mathrm{F}) < \varepsilon_n^{\uparrow}(\mathrm{AF}) < \varepsilon_n^{\downarrow}(\mathrm{AF}) < \varepsilon_n^{\downarrow}(\mathrm{F})$ $(n=1,2,\ldots)$.

For numerical calculations of the electron spectrum, the IEC energy, and the spin polarization of the electrons we used the typical parameters for EuS/PbS multilayers: $U=1.32$ eV, $U_0=3.5$ eV,[27] and $\Delta(4.2\ \mathrm{K})=0.36$ eV.[28] Since for wide potential barriers the characteristics of the substrate do not have an appreciable effect on the electron spectrum, for the sake of definiteness we took $U_s=2.5$ eV and $m_s=0.6m_e$.

Figure 2 shows the dependence of the first two size-quantization levels on the width a of the quantum well for $b_1=b_2=40$ Å. The difference $\varepsilon_1^{\downarrow}(\mathrm{AF})-\varepsilon_1^{\uparrow}(\mathrm{AF})$ is of the order of $\sim 10^{-11}$ eV for $a=10$ Å, $d=500$ Å and it increases by about twice for the higher-lying level, since the levels $\varepsilon_{1,2}^{\downarrow}(\mathrm{AF})$ and $\varepsilon_{1,2}^{\uparrow}(\mathrm{AF})$ are coincident. It is seen in Fig. 2 that the differences $\varepsilon_{1,2}^{\uparrow\downarrow}(\mathrm{F})-\varepsilon_{1,2}(\mathrm{AF})$ fall off rapidly with increasing a in the region from 10 Å to ~ 30 Å, and that is the reason for the rapid decrease in the exchange coupling energy with increasing width of the quantum well between barriers. For $d=100$ and 500 Å the difference of the corresponding levels is extremely slight. For example, for $a=10$ Å the difference $\varepsilon_{1F}^{\downarrow}(d=500\ \text{Å})-\varepsilon_{1F}^{\downarrow}(d=100\ \text{Å}) \cong 6.3\times 10^{-6}$ eV, i.e., the levels differ by approximately 1.5×10^{-3}%.

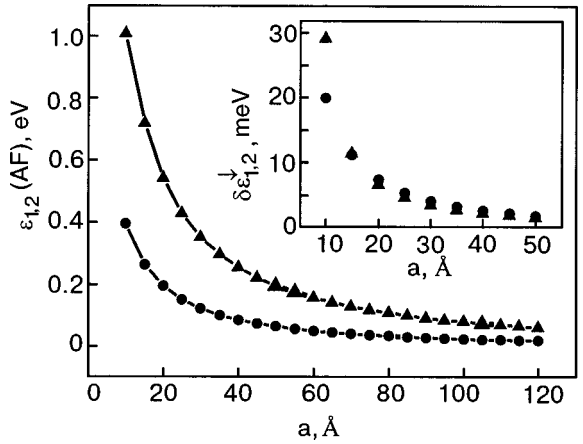

FIG. 2. Plots of the 1st (dots) and 2nd (triangles) electron energy levels $\varepsilon_{1,2}(\mathrm{AF})$ in a four-layer structure of PbS and EuS with AF orientation of the magnetic layers as functions of the width a of the potential well between the ferromagnetic barriers, calculated from Eq. (2) for a temperature $T=4.2$ K and $b_1=b_2=40$ Å, $d=500$ Å. The inset shows the difference $\delta\varepsilon_{1,2}^{\downarrow}(\mathrm{F}) = \varepsilon_{1,2}^{\downarrow}(\mathrm{F})-\varepsilon_{1,2}(\mathrm{AF})$ of the corresponding levels for F and AF configurations of the barriers. The values of $\delta\varepsilon_{1,2}^{\downarrow}(\mathrm{F})$ plotted on the graph are reduced from their calculated values by a factor of two. For electrons with spin up, the analogous differences $\varepsilon_{1,2}(\mathrm{AF})-\varepsilon_{1,2}^{\uparrow}(\mathrm{F})$ turned out to be just barely less than $\delta\varepsilon_{1,2}^{\downarrow}(\mathrm{F})$. For the 1st level in the region $a \geqslant 10$ Å and for the 2nd level at $a \geqslant 17$ Å the difference is not more than 5.5%; $\varepsilon_2^{\uparrow}(\mathrm{F})-\varepsilon_2(\mathrm{AF}) \cong 44.8$ meV at $a=10$ Å.

We note that because of the layer-by-layer mechanism of the growth of EuS and PbS on each other, one can prepare multilayer samples with a spacer-layer thickness of a single unit cell ($a_{\mathrm{PbS}} \cong 5.94$ Å). However, for such structures our macroscopic approach, based on the use of the bulk-state parameters of the materials, becomes incorrect; we therefore restricted the calculations to values $a \geqslant 10$ Å. At sufficiently low temperatures (temperatures much less than the spacings between adjacent levels) the upper limit of a for which one can still observe the quantum size effects is determined by electron collision processes, which destroy the interference pattern. Therefore, in the case of sufficiently thick sublayers and wide potential wells, our calculations of the coupling energy of the magnetic layers loses meaning. For EuS/PbS SLs[27] the photoluminescence data at $T=4.2$–80 K confirm the presence of size quantization at least to the largest quantum-well widths in the samples studied (~ 200 Å).

It should be taken into account in calculating the IEC that the Curie temperature T_C of the ferromagnetic layers (and the value of the exchange splitting Δ) depend on their thickness. In particular, for EuS/PbS(001) SLs on KCl with an EuS layer thickness of 200 monolayers it has the value

$T_C = 17.3$ K,[30] which is considerably higher than the Curie temperature of bulk samples of EuS ($T_C = 16.6$ K), whereas for EuS/PbS(111) SLs grown on BaF_2, T_C is lower than the bulk value ($T_C = 13.6$ K). For both types of SLs, when the thickness of the EuS layers is decreased to about 20 monolayers, the Curie temperature initially varies weakly and then falls noticeably to $T_C \sim 10$ K for d_{EuS} equal to two monolayers.[30] Such behavior of T_C is explained by the appreciable deformation of the EuS layers in these SLs and by the difference in the environments of the Eu ions found on the surface and in the interior of the EuS film.[30,31] Since the energy splitting Δ is determined by the magnetization of the ferromagnetic barrier material, i.e., by the ratio T/T_C, this sort of thickness effect must be kept in mind when analyzing the temperature dependence of the IEC. Therefore, the conclusion reached in Ref. 21 that the IEC depends weakly on the thickness of the ferromagnetic layers is clearly incorrect for EuS/PbS SLs with relatively thin EuS layers.

The IEC energy is largely determined by the electron density in the structure. The electron surface density n_S (the number of electrons per unit area of the sample) is described in the case of Boltzmann and Fermi statistics, respectively, by the relations

$$n_S = \frac{T}{\xi}\sum_n \left\{ \exp\left(\frac{\mu-\varepsilon_n^{\uparrow}}{T}\right) + \exp\left(\frac{\mu-\varepsilon_n^{\downarrow}}{T}\right)\right\},$$

$$\exp\left(\frac{\mu-\varepsilon_1^{\uparrow}}{T}\right) \ll 1, \tag{5}$$

$$n_S = \frac{1}{\xi}\left[\sum_{n=1}^{k_1}(\mu-\varepsilon_n^{\uparrow}) + \sum_{n=1}^{k_2}(\mu-\varepsilon_n^{\downarrow})\right], \quad \xi = \frac{2\pi\hbar^2}{N_e m^*}, \tag{6}$$

where $\varepsilon_n^{\uparrow\downarrow}$ is the energy of the nth quantum size-effect level, k_1 and k_2 are the numbers of electron-filled subbands ($\uparrow$) and ($\downarrow$) ($k_2 \leqslant k_1$), μ is the chemical potential, N_e is the number of equivalent valleys of the electron spectrum in the well material (we are not considering the case when there is more than one group of equivalent valleys with equal inclinations of the principal axes with respect to the interface between layers, as in EuS/PbS(111) SLs[32]). For PbS layers there are four energy ellipsoids, oriented along directions of the [111] type, with which we shall compose the spectrum (1).[27] In EuS/PbS(001) SLs all the ellipsoids are inclined equally to the interfaces between layers ($N_e = 4$), while in a SL with the (111) orientation there are three ellispsoids with identical inclination and the fourth is orthogonal to the layers.

From here on we limit consideration to the case of relatively wide potential barriers (in reality $b_1, b_2 > 20$ Å), when one can assume that $\varepsilon_n^{\uparrow}(\mathrm{AF}) = \varepsilon_n^{\downarrow}(\mathrm{AF}) = \varepsilon_n(\mathrm{AF})$. For thin barriers the behavior of the IEC energy as a function of the quantum well width a, electron density n_S, and temperature T will be qualitatively the same as in the case of wide barriers.

Expression (6) for n_S was obtained from the exact relation

$$n_S = \sum n_S(n), \quad n_S(n) \sim \left\{ \ln\left[1+\exp\left(\frac{\mu-\varepsilon_n^{\uparrow}}{T}\right)\right] + \ln\left[1+\exp\left(\frac{\mu-\varepsilon_n^{\downarrow}}{T}\right)\right]\right\}$$

under the assumption that for a ferromagnetic configuration of the barriers, one of the following pairs of inequalities holds:

$$\frac{\mu-\varepsilon_{k_1}^{\uparrow}}{T} \gg 1, \quad \frac{\varepsilon_{k_1}^{\downarrow}-\mu}{T} \gg 1,$$

$$\frac{\mu-\varepsilon_{k_1}^{\downarrow}}{T} \gg 1, \quad \frac{\varepsilon_{k_1+1}^{\downarrow}-\mu}{T} \gg 1. \tag{7}$$

These two pairs of inequalities pertain to the cases when the chemical potential lies between levels $\varepsilon_{k_1}^{\downarrow}$ and $\varepsilon_{k_1}^{\uparrow}$ ($k_2 = k_1 - 1$) or $\varepsilon_{k_1+1}^{\uparrow}$ and $\varepsilon_{k_1}^{\downarrow}$ ($k_2 = k_1$). For an antiferromagnetic configuration the second pair of inequalities should hold. Estimates show that expression (6) describes the situation well in cases when the chemical potential μ lies more than a distance of $2T$ from the levels $\varepsilon_n^{\uparrow\downarrow}$. Since we are considering the low-temperature region, the intervals of μ in which inequality (7) does not hold is rather narrow. If the distance between the two levels nearest to the chemical potential in the well is much greater than $4T$, then for simplicity we can neglect the width of these intervals and assume that the filling of the subbands $\varepsilon_n^{\uparrow\downarrow}$ begins when the chemical potential crosses the corresponding levels.[33]

Fermi statistics will be applicable in the region of well widths a of interest to us (up to ~ 100 Å) (except for narrow intervals where condition (7) does not hold), if the following inequality holds for the lowest subband:

$$\frac{\mu-\varepsilon_1^{\uparrow}}{T} = \frac{\xi n_S}{T} \gg 1. \tag{8}$$

Assuming that $N_e = 4$, $m^* = 0.093 m_e$,[27] and $T = 10$ K, we obtain $\xi n_S/T \cong 1.5\times 10^{-11} n_S$ (cm^{-2}). If we ignore the small contribution to n_S from the electrons of the ferromagnetic semiconductor which have passed over into the quantum-well regions during the formation of the multilayers, then $n_S = n_0(a+d)$, where n_0 is the electron density (number per unit volume) in the initial n-type material from which the quantum wells were formed. The electron density n_0 in the PbS layers for the EuS/PbS SL structures investigated in Refs. 11, 15, 23, and 24 could vary over the limits $\sim 2\times 10^{18} - 3\times 10^{19}$ cm^{-3}. Assuming that $a + d = 100$ Å and $n_0 = 2\times 10^{18}$ cm^{-3}, we obtain $\xi n_S/T \cong 29.9$ for T = 10 K. Since usually $d \sim 100-500$ Å, the case of Boltzmann statistics can be realized only at rather low densities n_0, which can be obtained in EuS/PbS multilayers with the aid of special vacuum condensation technologies.

Let us now consider the filling of the subbands as the width a of the quantum well increases. Here and below, in order to clarify the overall picture of this process, we shall neglect the finiteness of the width a of the regions in which condition (7) does not hold (which we shall call transition regions), since in those regions as a increases a gradual "turning on" (filling) of the corresponding subbands occurs.

For a ferromagnetic configuration of the barriers in the case of extremely narrow wells, one can assume that only the lowest subband $\varepsilon_1^{\uparrow}(\mathrm{F})$ is filled. As the well width increases, the subbands $\varepsilon_1^{\downarrow}(\mathrm{F})$, $\varepsilon_2^{\uparrow}(\mathrm{F})$, $\varepsilon_2^{\downarrow}(\mathrm{F})$, etc. begin to fill. The well width a at which the chemical potential touches the bottom of subband $\varepsilon_k^{\uparrow}(\mathrm{F})$ or $\varepsilon_k^{\downarrow}(\mathrm{F})$ (i.e., the filling of these subbands begins) can be calculated assuming in (7) that $k_1=k$, $k_2=k-1$ or $k_1=k_2=k$ and equating μ to the corresponding energies.[33] The same can be said about the filling of the subbands in the case of an antiferromagnetic configuration of the barriers.

3. COUPLING ENERGY OF MAGNETIC BARRIERS AS A FUNCTION OF THE QUANTUM WELL WIDTH

The surface energy E_S of an electron gas (the energy per unit area of the sample) for Boltzmann and Fermi statistics has the form

$$E_S=n_S T+n_S\frac{\Sigma_n\left[\varepsilon_n^{\uparrow}\exp\left(-\frac{\varepsilon_n^{\uparrow}}{T}\right)+\varepsilon_n^{\downarrow}\exp\left(-\frac{\varepsilon_n^{\downarrow}}{T}\right)\right]}{\Sigma_n\left[\exp\left(-\frac{\varepsilon_n^{\uparrow}}{T}\right)+\exp\left(-\frac{\varepsilon_n^{\downarrow}}{T}\right)\right]}. \quad (9)$$

$$E_S=\frac{1}{2\xi}\left[\sum_{n=1}^{k_1}(\mu^2-\varepsilon_n^{\uparrow 2})+\sum_{n=1}^{k_2}(\mu^2-\varepsilon_n^{\downarrow 2})\right]. \quad (10)$$

The energy of the IEC is determined by the energy difference $E_m=E_S(\mathrm{F})-E_S(\mathrm{AF})$ (see Ref. 3). It is seen from relation (9) that for Boltzmann statistics, as a consequence of the inequalities $\varepsilon_n^{\uparrow}(\mathrm{F})<\varepsilon_n(\mathrm{AF})$ the energy E_m is negative, i.e., experimentally the F configuration of the barriers will be observed. In the case of small a the energy E_m will be quite perceptible. For example, for $n_0=10^{17}$ cm^{-3}, $a=10$ Å, and $d=500$ Å, one has $n_S\varepsilon_1^{\uparrow}(\mathrm{F})\cong 0.31$ mJ/m^2.

For Fermi statistics, upon filling of the subbands $\varepsilon_1^{\uparrow}(\mathrm{F})$ and $\varepsilon_1(\mathrm{AF})$, i.e., under the condition $\xi n_S\leqslant\varepsilon_1^{\downarrow}(\mathrm{F})-\varepsilon_1^{\uparrow}(\mathrm{F})$, the energy E_m is equal to

$$E_m=\frac{n_S}{4}\{\xi n_S-4[\varepsilon_1(\mathrm{AF})-\varepsilon_1^{\uparrow}(\mathrm{F})]\} \quad (11)$$

and only F-type coupling of the magnetic layers can be observed, since $\varepsilon_1^{\downarrow}(\mathrm{F})-\varepsilon_1^{\uparrow}(\mathrm{F})\cong 2[\varepsilon_1(\mathrm{AF})-\varepsilon_1^{\uparrow}(\mathrm{F})]$ (see Fig. 2). As the width of the quantum well increases, the subband $\varepsilon_1^{\downarrow}(\mathrm{F})$ will be filled. Then

$$E_m=\frac{1}{\xi}\left\{\xi n_S\left[\frac{\varepsilon_1^{\uparrow}(\mathrm{F})+\varepsilon_1^{\downarrow}(\mathrm{F})}{2}-\varepsilon_1(\mathrm{AF})\right]-\left[\frac{\varepsilon_1^{\downarrow}(\mathrm{F})-\varepsilon_1^{\uparrow}(\mathrm{F})}{2}\right]^2\right\},$$

$$2\varepsilon_2^{\uparrow}-[\varepsilon_1^{\uparrow}(\mathrm{F})+\varepsilon_1^{\downarrow}(\mathrm{F})]\geqslant\xi n_S\geqslant\varepsilon_1^{\uparrow}(\mathrm{F})-\varepsilon_1^{\downarrow}(\mathrm{F}). \quad (12)$$

In this interval of well widths satisfying conditions (12), a change in the sign of E_m occurs (from negative to positive). Upon further increase in the well width the filling of the subbands $\varepsilon_2^{\uparrow}(\mathrm{F})$, $\varepsilon_2(\mathrm{AF})$, $\varepsilon_2^{\downarrow}(\mathrm{F})$, etc. begins. For a ferromagnetic configuration of the barriers upon filling of the uppermost subband $\varepsilon_k^{\uparrow}(\mathrm{F})$ and $\varepsilon_{k-1}^{\downarrow}(\mathrm{F})$ $[\varepsilon_k^{\uparrow}(\mathrm{F})>\mu\geqslant\varepsilon_k^{\downarrow}(\mathrm{F})]$ the chemical potential is described by the expression

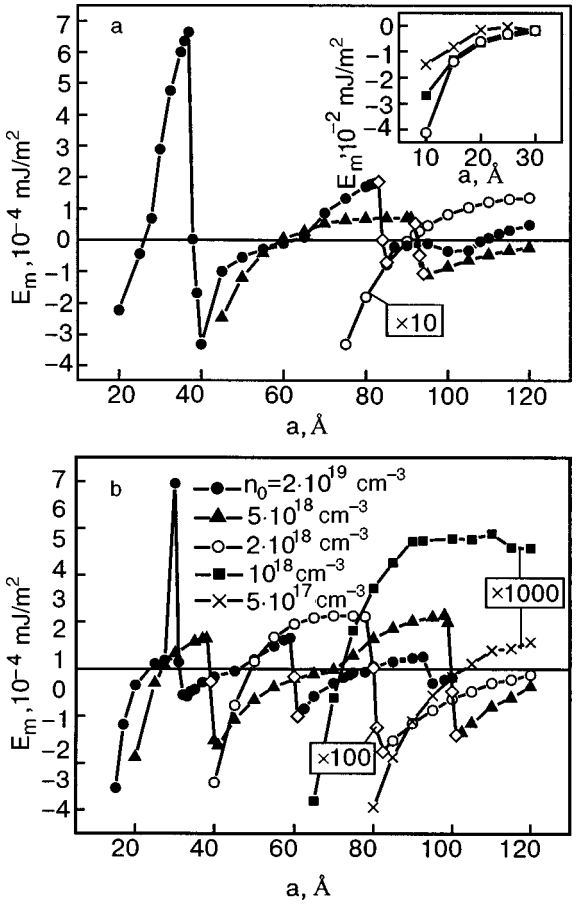

FIG. 3. Energy of the IEC as a function of the width of the potential well between barriers of EuS for different electron densities n_0 in the PbS wells at PbS sublayer thicknesses $d=100$ (a) and 500 Å (b) ($b_1=b_2=40$ Å, $T=4.2$ K). The numbers in the rectangular frames here and in the subsequent figures give the factor by which the values of E_m plotted on the graph must be multiplied to get the calculated values. In addition, the values of the IEC energy in Fig. 3a for $n_0=2\times10^{19}$ cm^{-3} in the regions where $E_m<0$ have been reduced by a factor of 10 from the calculated values, while in Fig. 3b the values of $E_m(a)$ on the parts $a>46$ Å and $a<49$ Å for $n_0=2\times10^{19}$ and 5×10^{18} cm^{-3}, respectively, have been magnified by a factor of 10 (for $n_0=5\times10^{18}$ cm^{-3} the values of $E_m(a)$ in the region $a>49$ Å are 100 times the calculated values). The points falling in the transition regions of a are indicated by diamonds. The inset shows the initial parts of the $E_m(a)$ curves for $n_0=5\times10^{17}$, 10^{18}, 2×10^{18} cm^{-3}, $d=100$ Å.

$$\mu_F=\frac{1}{2k-1}[C_k(\mathrm{F})-\varepsilon_k^{\downarrow}(\mathrm{F})],$$

$$C_k(\mathrm{F})=\xi n_S+\sum_{n=1}^{k}[\varepsilon_n^{\uparrow}(\mathrm{F})+\varepsilon_n^{\downarrow}(\mathrm{F})], \quad (13)$$

and upon filling of the subbands $\varepsilon_k^{\uparrow}(\mathrm{F})$ and $\varepsilon_k^{\downarrow}(\mathrm{F})$ we obtain $[\varepsilon_{k+1}^{\uparrow}(\mathrm{F})>\mu\geqslant\varepsilon_k^{\uparrow}(\mathrm{F})]$

$$\mu_F=\frac{1}{2k}C_k(\mathrm{F}). \quad (14)$$

For an antiferromagnetic configuration of the magnetic layers in the case of wide barriers the chemical potential μ_{AF} is given by relation (14).

Using these formulas and relation (10), we have calculated the dependence of the energy E_m on the width a of the potential well for various electron densities n_0 and for two thicknesses d of the sublayers (Fig. 3). It is seen in Fig. 3

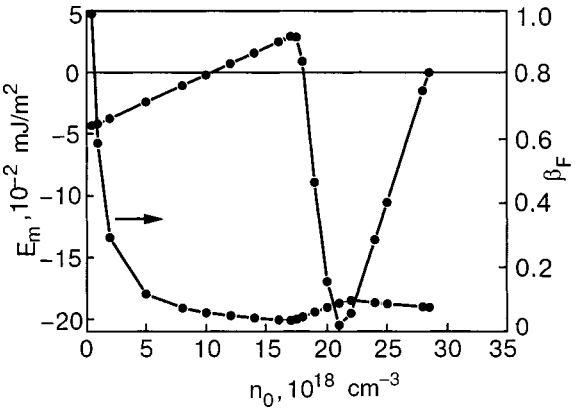

FIG. 4. IEC energies E_m and relative electron polarization β_F for a ferromagnetic configuration of the EuS barriers versus the electron density n_0 in the PbS layers for $a=10$ Å, $b_1=b_2=40$ Å, $d=500$ Å; $T=4.2$ K.

that the IEC energy E_m in the general case is a nonmonotonic, sign-varying function of the well width. The maxima and subsequent minima of the function $E_m(a)$ correspond to the start of filling of the subbands $\varepsilon_k^{\uparrow}$(F) and $\varepsilon_k^{\downarrow}$(F), respectively. The extrema $E_m(a)$ have an asymmetric shape. The change in sign of E_m occurs when the width a of the quantum well changes by $\sim 1-2$ Å. The width of the a regions in which antiferromagnetic ordering of the barriers should be observed is relatively small.

For samples with fixed a, b_1, and b_2 one can obtain both a ferromagnetic and an antiferromagnetic configuration of the magnetic layers by choosing the appropriate electron density n_0 and layer thickness d. This is seen, e.g., in Fig. 4, which shows the change of E_m as n_0 increases for the sample with $a=10$ Å, $b_1=b_2=40$ Å. The energy of the antiferromagnetic coupling of magnetic layers here reaches a value of $+2.91\times10^{-2}$ mJ/m^2, comparable to the IEC energy in SLs with metallic layers and of the same scale as in EuS/PbS(001) SLs with PbS spacer layers 2 monolayers thick ($+3.1\times10^{-2}$ mJ/m^2).[15] This last circumstance provides indirect evidence in support of the view that our model gives at least the right energy scale for the IEC. The value of E_m at the minimum (-0.205 mJ/m^2) is almost an order of magnitude greater in modulus than the value of E_m at the maximum. The antiferromagnetic coupling is manifested in a rather narrow density interval $n_0\approx(1.4-1.8)\times10^{19}$ cm^{-3}. As in the case of $E_m(a)$, the maximum and minimum here correspond to the start of filling of the subbands $\varepsilon_2^{\uparrow}$(F) and $\varepsilon_2^{\downarrow}$(F). The sharp fall of the functions $E_m(a)$ and $E_m(n_0)$ with increasing a and n_0 is explained by the fact that when a new subband $\varepsilon_n^{\uparrow}$(F) starts to fill, the energy of the ferromagnetic configuration of the barriers decreases rapidly, favoring the establishment of the F state.

It is seen in Fig. 3 that at high electron concentrations n_0 and large sublayer thicknesses d the IEC will be perceptible even in samples with $a\sim100$ Å. With increasing n_0 and d the maxima shift to smaller a, while the values of E_m at the maxima increase appreciably. This is not surprising, since the sublayer plays the role of a reservoir of electrons, contributing to the surface density $n_S=n_0(a+d)$. If we denote by $E_m^{(n)}$ the value of the IEC energy at the nth maximum, then for $n_0=2\times10^{19}$ cm^{-3} the ratios $E_m^{(1)}(d=500\text{ Å})/E_m^{(1)}(d=100\text{ Å})\cong59.5$, $E_m^{1/2}(d=500\text{ Å})/E_m^{(2)}(d=100\text{ Å})\cong3.6$. For $d=500$ Å the value of $E_m^{(1)}$ falls off by approximately 55.7 times as n_0 decreases from 2×10^{19} to 5×10^{18} cm^{-3} and by 5.7 times as n_0 decreases from 5×10^{18} to 2×10^{18} cm^{-3}. For $d=100$ Å the fall of $E_m^{(1)}$ with decreasing n_0 is less ponderous: by 9.4 times as n_0 decreases from 2×10^{19}cm^{-3} to 5×10^{18} cm^{-3}. For $d=500$ Å and $n_0=2\times10^{19}$ cm^{-3} the second maximum $E_m^{(2)}$ is much lower than the first: $E_m^{(1)}/E_m^{(2)}\cong60.2$, whereas $E_m^{(2)}/E_m^{(3)}\cong2.6$. Thus with increasing a there is first a sharp decrease of the IEC energy and then a relatively slow decay of E_m.

In the region of extremely small a the energy E_m increases sharply with increasing a. The sign of E_m in Fig. 3 (for the given values of n_0) is negative in the region of small a. However, as is seen in Fig. 4, even for this region there can exist an interval of densities n_0 for which $E_m>0$. Therefore one cannot state that for small a a ferromagnetic configuration of the magnetic layers will always be observed.

The values of $E_m(a)$ in the transition regions of a, calculated using the approximate formulas (6) and (10) (denoted by the diamond symbols in Fig. 3), can differ appreciably from the exact values E_m. However, as is seen in Fig. 3, such an approximation, gives a fair description of the behavior of the function $E_m(a)$ in transition regions of a with a width of $\sim1-2$ Å.

We note that theoretical calculations of the IEC for (GaMn)As/GaAs SLs[34] (in which essentially the same approach to the problem of the IEC as in our model is used) have given qualitatively similar results: at small a a ferromagnetic coupling of the magnetic layers is manifested; E_m is an oscillatory sign-varying function of $2k_Fd$, where d is the period of the SL and k_F is the Fermi wave number corresponding to the averaged electron density over the SL. However, in this model there are practically no barriers for $T>T_C$. Barriers appear as a result of the exchange splitting of the conduction band in the (GaMn)As layers for $T<T_C$. Therefore, in the model of Ref. 34 an antiferromagnetic coupling can be realized only at very high electron densities, leading to a high level of T_C and appreciable splitting Δ.

Our calculations of the IEC can be easily extended to the case of SLs. If the potential barriers are wide enough, the minibands of the SL essentially become discrete levels, and the calculations of the IEC can be done using the same formulas (10), (13), and (14) for E_m and μ, with the energies $\varepsilon_n^{\uparrow\downarrow}$ for the SL substituted in and with $n_S=n_0(a+d)$ replaced by $n_S=n_0a$ (a is the width of the nonmagnetic spacer layers). Here E_S will have the meaning of the surface energy per period of the SL. One therefore expects the appearance of oscillations on the $E_m(a)$ and $E_m(n_0)$ curves. Experimental data for several samples of EuS/PbS SLs ($d_{\mathrm{PbS}}\leqslant90$ Å) show the presence of antiferromagnet ordering of the EuS layers. However, that does not mean that the energy E_m is positive for other values of d_{PbS} as well, as can be inferred from the change in sign of E_m for samples with $d_{\mathrm{PbS}}>90$ Å.

4. TEMPERATURE DEPENDENCE OF THE IEC ENERGY

The energies of the size-quantization levels and the IEC for a given sample are determined by the value of the exchange splitting $\Delta(T)$ in the barrier material, which depends on the sample temperature. For $T\leqslant T_C$ the value of Δ varies

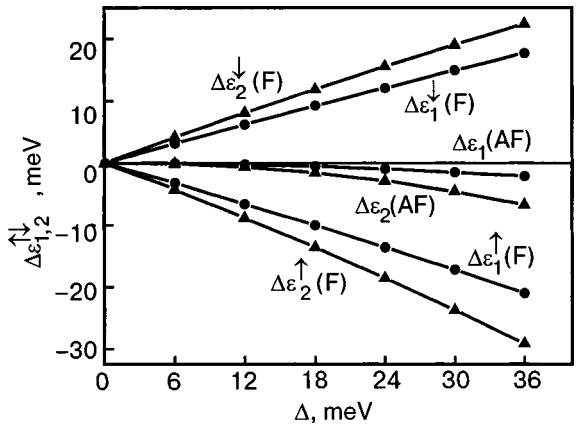

FIG. 5. Shift of the energies of the 1st and 2nd size-quantized levels, $\Delta_{1,2}=\varepsilon_{1,2}(\Delta)-\varepsilon_{1,2}(0)$, with increasing exchange splitting Δ of the conduction band in the EuS layers for electrons with spins up ($\uparrow$) and down ($\downarrow$) for F (triangles) and AF (dots) configurations of the magnetic layers ($a=10$ Å, $b_1=b_2=40$ Å, $d=500$ Å, $\varepsilon_1(0)=0.3994$ eV, $\varepsilon_2(0)=1.0239$ eV, $\Delta(4.2\text{ K})=0.36$ eV).

from zero to $\Delta_{\max}$ as the temperature is lowered from T_C to $T_{\min}$, the minimum temperature at which the measurements of E_m are made. The dependence of the first two size-quantization levels on Δ for a four-layer structure with $a=10$ Å, $d=500$ Å, and $b_1=b_2=40$ Å are shown in Fig. 5, from which it is seen that the energies of the levels $\varepsilon^{\uparrow}_{1,2}(\mathrm{F})$ and $\varepsilon_{1,2}(\mathrm{AF})$ decrease monotonically with increasing Δ and that the levels $\varepsilon^{\downarrow}_{1,2}(\mathrm{F})$ are higher than the corresponding values $\varepsilon_{1,2}(0)$ for $T=T_C$ ($\Delta=0$). The splitting of the first level, $\varepsilon^{\downarrow}_1(\mathrm{F})-\varepsilon^{\uparrow}_1(\mathrm{F})$, at $T=4.2$ K reaches a value of 38.64 meV, i.e., more than 10% of the value of the splitting $\Delta(T=4.2\text{ K})=0.36$ eV.

Let us analyze the behavior of the energy E_m as the temperature decreases and $\Delta(T)$ grows for the particular example of the sample with $a=10$ Å, $d=500$ Å, $b_1=b_2=40$ Å. For simplicity we shall neglect the finiteness of the width Δ of the transition region in which inequality (7) does not hold. Such an approximation, which leads to some distortion of the function $E_m(\Delta)$ in the transition regions, does not qualitatively alter its behavior.

We assume that at the temperature $T=T_C$ the chemical potential $\mu(0)$ is found near the lower level $\varepsilon_1(0)$. Then with increasing Δ the split-off sublevel $\varepsilon^{\downarrow}_1(\mathrm{F})$ can turn out to lie above the level $\mu_F(T)$, i.e., in a certain temperature region a transition occurs from filling of the levels $\varepsilon^{\uparrow\downarrow}_1(\mathrm{F})$ and $\varepsilon_1(\mathrm{AF})$ to filling of the levels $\varepsilon^{\uparrow}_1(\mathrm{F})$ and $\varepsilon_1(\mathrm{AF})$. For such a transition to take place, the condition $\mu_F(T)<\varepsilon^{\downarrow}_1(\mathrm{F})$ must hold, if only in a small part of the investigated temperature interval, i.e.,

$$\xi n_S<\varepsilon^{\downarrow}_1(\mathrm{F})-\varepsilon^{\uparrow}_1(\mathrm{F}). \tag{15}$$

If we take $T=T_{\min}=4.2$ K, then condition (15) gives $\xi n_S<0.0386$ eV. In this case the energy E_m is determined by relation (11). In the region of high temperatures and small Δ, when the subbands $\varepsilon^{\uparrow\downarrow}_1(\mathrm{F})$ and $\varepsilon_1(\mathrm{AF})$ are filled and inequality (15) do not hold, the energy E_m is described by relation (12). As we have said, in the low-temperature state, when inequality (15) is satisfied, one will observe a ferromagnetic type of coupling of the magnetic layers ($E_m<0$). If condition (15) does not hold (high temperatures or $\xi n_S>0.0386$ eV), then the sign of E_m can be positive or negative, depending on the value of ξn_S. It follows from relation (12) that a change in sign of E_m will occur at the temperature for which

$$\xi n_S=\frac{(\varepsilon^{\downarrow}_1(\mathrm{F})-\varepsilon^{\uparrow}_1(\mathrm{F}))^2}{2[(\varepsilon^{\uparrow}_1(\mathrm{F})+\varepsilon^{\downarrow}_1(\mathrm{F}))-2\varepsilon_1(\mathrm{AF})]}=f(\Delta). \tag{16}$$

For $\xi n_S>f(\Delta)$ the antiferromagnetic orientation of the magnetic layers will be dominant. Numerical calculations show that the function $f(\Delta)$ in the temperature interval from T_C to $T_{\min}$ behaves as follows: for $\Delta=0$ the function $f(\Delta)$ has its lowest value, $f(0)=(\xi n_S)_{\min}\cong 0.668$ eV; as the temperature is lowered, $f(\Delta)$ reaches a maximum at $\Delta\cong 0.04$ eV ($f=(\xi n_S)_{\max}\cong 0.695$ eV) and then decreases monotonically to a value $f(\Delta_{\max})=(\xi n_S)_p\cong 0.687$ eV. Since $(\xi n_S)_{\min}$ clearly exceeds the limiting value $\xi n_S=0.0386$ eV up to which inequality (15) holds, the energy E_m for $\xi n_S<(\xi n_S)_{\min}$ will always be negative. In the case when the conditions $(\xi n_S)_p>\xi n_S>(\xi n_S)_{\min}$ hold, one will observe a change in sign of E_m from positive to negative with increasing Δ. On the other hand, if $(\xi n_S)_{\max}>\xi n_S>(\xi n_S)_p$, the sign of E_m will change twice. For $\xi n_S>(\xi n_S)_{\max}$ an antiferromagnetic type of coupling of the magnetic layers will be manifested in the entire temperature interval from T_C to $T_{\min}$. The above-described modification of the behavior of the function $E_m(\Delta)$ with increasing ξn_S is shown in Fig. 6a. We note that the electron densities n_0 corresponding to the values $(\xi n_S)_{\min}$, $(\xi n_S)_p$, and $(\xi n_S)_{\max}$ lie in a rather narrow interval of values and are equal to 1.014×10^{19}, 1.044×10^{19} (the zero of the function $E_m(n_0)$ in Fig. 4), and 1.057×10^{19} cm^{-3}. Therefore, to observe the effect of the sign change of E_m in this region of electron densities one must use a sample with small fluctuations of n_0 over the area of the sample. In addition, the value of E_m in the sign-change region is very small, making it difficult to observe the effects in question in an experiment.

Using expressions (13) and (14) for μ_F and μ_{AF}, one can easily show that with increasing ξn_S at a fixed temperature the chemical potential $\mu_F(T)$ initially occurs above the level $\varepsilon^{\uparrow}_{2F}(T)$, and, further, the chemical potential $\mu_{AF}(T)$ touches the level $\varepsilon_{2AF}(T)$. Thus electrons begin to fill the subbands $\varepsilon^{\uparrow}_{2F}(T)$ and $\varepsilon_{2AF}(T)$ in the quantum wells with F and AF configurations of the barriers, respectively. For a given temperature T the start of the filling of these subbands will correspond to values $\xi n_S=2\varepsilon^{\uparrow}_{2F}(T)-[\varepsilon^{\uparrow}_{1F}(T)+\varepsilon^{\downarrow}_{2F}(T)]$ and $\xi n_S=2[\varepsilon_{2AF}(T)-\varepsilon_{1AF}(T)]$. In the investigated temperature interval the lowest values of ξn_S satisfying those relations will be reached at the temperature $T=T_{\min}=4.2$ K, and these minimal ξn_S are equal to $(\xi n_S)_{2F\uparrow}=1.136$ eV and $(\xi n_S)_{2AF}=1.226$ eV. For $T=T_C$ the filling of the subband $\varepsilon_2(0)$ begins at a value $\xi n_S=(\xi n_S)_2=2[\varepsilon_2(0)-\varepsilon_1(0)]=1.249$ eV. As the temperature is lowered, however, the $\varepsilon^{\downarrow}_{2F}(T)$ level begins to empty, since its energy increases with increasing $\Delta(T)$ (Fig. 5). Therefore, for $\xi n_S>(\xi n_S)_2$ the subband $\varepsilon^{\downarrow}_{2F}(T)$ turns out to be filled only above a certain minimum temperature at which $\mu_F(T)=\varepsilon^{\downarrow}_{2F}(T)$, i.e., when $\xi n_S=3\varepsilon^{\downarrow}_{2F}(T)-[\varepsilon^{\uparrow}_{1\mathrm{F}}(T)+\varepsilon^{\downarrow}_{1F}(T)+\varepsilon^{\uparrow}_{2F}(T)]$. The right-hand side of this last equation reaches its largest value $(\xi n_S)_{2\uparrow\downarrow}=1.445$ eV and $T=T_{\min}$. Here the

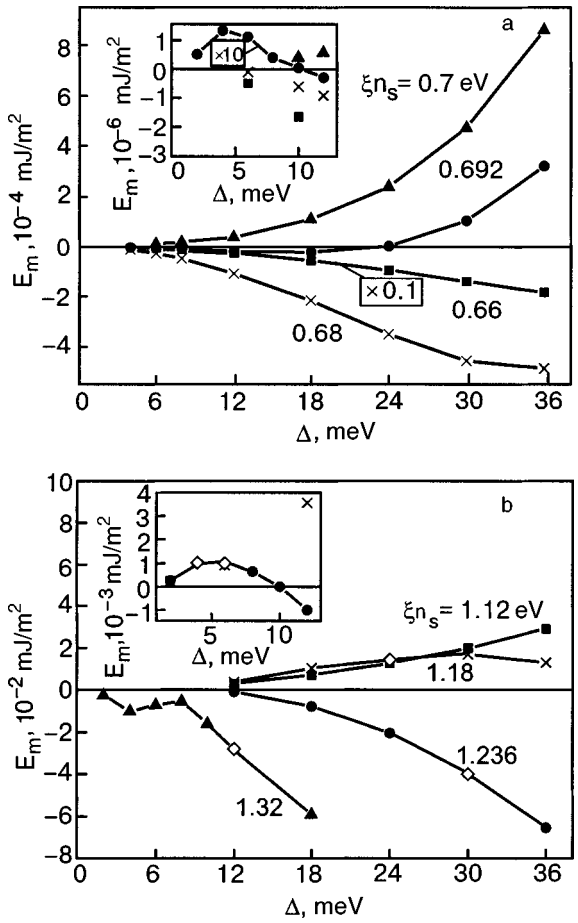

FIG. 6. IEC energy E_m for $a=10$ Å, $b_1=b_2=40$ Å, $d=500$ Å versus the exchange splitting Δ of the conduction band in the EuS layers for different values of ξn_S, corresponding to finding the level of the chemical potential far from the 1st and 2nd size-quantization levels (a) and close to the 2nd level (b). The insets show the initial parts of the $E_m(\Delta)$ curves.

subband ε_2(AF) will be filled in the entire temperature interval under consideration, starting with $\xi n_S=(\xi n_S)_2$, since in this situation $\mu_{AF}(T)\geqslant\varepsilon_{2AF}(T)$. Therefore for $\xi n_S>(\xi n_S)_{2\uparrow\downarrow}$ the upper subbands $\varepsilon_2^{\uparrow\downarrow}$(F) and ε_2(AF) will be filled in the entire temperature interval from T_C to $T_{\min}$.

The behavior of the function $E_m(\Delta)$ will vary depending on the relationship of ξn_S to the special values of ξn_S indicated above (Fig. 6). For $(\xi n_S)_{\max}<\xi n_S<(\xi n_S)_{2F\uparrow}$ the function $E_m(\Delta)$ increases monotonically with increasing Δ. If, however, $(\xi n_S)_{2AF}>\xi n_S>(\xi n_S)_{2F\uparrow}$, then the original growth of $E_m(\Delta)$ gives way to a drop due to the filling of the subband $\varepsilon_2^{\uparrow}$(F). In the interval $(\xi n_S)_2>\xi n_S>(\xi n_S)_{2AF}$ the function $E_m(\Delta)$ initially grows and then starts to fall off rapidly, changing sign from positive to negative. For $(\xi n_S)_{2\uparrow\downarrow}>\xi n_S>(\xi n_S)_2$ the value of E_m is negative, and one observes a nonmonotonic fall of $E_m(\Delta)$ with increasing Δ. Upon further increase in ξn_S, when $\xi n_S>(\xi n_S)_{2\uparrow\downarrow}$, $E_m<0$ (until the 3rd size-quantization level comes into play). The particular points of ξn_S at which the transformation of the shape of the function $E_m(\Delta)$ occurs correspond to rather high electron densities n_0: 1.726×10^{19} (the maximum of $E_m(n_0)$ in Fig. 4), 1.864×10^{19}, 1.898×10^{19}, and 2.196×10^{19} cm^{-3}. In this region of electron densities a change in the sign of E_m can be detected experimentally, since positive values of $E_m(\Delta)$ reach a value $\sim10^{-3}$ mJ/m^2 before the sign of E_m changes to negative.

The examples considered show that the behavior of the function $E_m(\Delta)$ (or $E_m(T)$) for a sample with a fixed geometric parameters of the layers (a, $b_1=b_2=b$, d) changes qualitatively in certain intervals of values of the electron density n_0 that depend on those layer parameters. The above-noted change in sign of E_m for MnTe/ZnTe SLs[13] upon lowering of the temperature is apparently due to the fact that for that sample the electron density happened to lie in one of the special intervals of n_0.

We note that the exchange splitting Δ for ferromagnetic semiconductors is proportional to the magnetization M, and near T_C it varies according to a power law, $\Delta\sim\tau^{\alpha}$ (Ref. 35), where $\tau=(T_C-T)/T_C$. According to Ref. 36, for EuS in the temperature interval $0.1>\tau>0.01$ the exponent $\alpha=0.33\pm0.015$. At lower temperatures the splitting $\Delta(T)$ can be described by a Brillouin function.[35] In a neighborhood of the Curie point the spontaneous fluctuations of the magnetization lead to corresponding fluctuations of Δ, which cause a strong change in the optical width of the band gap in EuS, starting at $T\sim25$ K.[35] The model considered in the present paper does not take fluctuations of the barrier height into account, and the value of Δ is proportional to the time-averaged magnetization, and therefore $\Delta=0$ for $T\geqslant T_C$.

Matching the parts of the $\Delta(T)$ curve near T_C with the low-temperature part at the point $\tau=0.1$ and assuming that $\Delta(4.2\text{ K})=0.36$ eV, $T_C=16.6$ K for samples with the parameters chosen above, we find that the values $\Delta=0.06$, 0.12, 0.18, 0.24, and 0.3 eV are reached at temperatures of 16.52, 15.94, 14.55, 12.68, and 9.73 K. We see from these estimates that the change in sign of E_m from positive to negative in the case of a double sign change should be observed in a region of temperatures near T_C, while a repeated sign change can occur at temperatures all the way down to $T_{\min}$.

5. POLARIZATION OF THE ELECTRON SPINS

At present there are several methods for determining the electron spins in the surface layers of a sample, e.g., SEMPA (scanning electron microscopy with polarization analysis), which has been successfully used to study Fe/Cr/Fe and Fe/Au/Fe three-layer structures.[37] It is of interest in this regard to estimate the spin polarization of electrons in the four-layer structure under consideration.

We characterize the relative polarization of the electron spins by the parameter

$$\beta=\frac{n_S^{\uparrow}-n_S^{\downarrow}}{n_S},\quad n_S=n_S^{\uparrow}+n_S^{\downarrow}. \tag{17}$$

Since in the case of Boltzmann statistics only a ferromagnetic type of coupling of the magnetic barriers is realized, the electron spins will be oriented predominantly along the direction of magnetization of the barriers. The relative polarization will fall off smoothly with increasing width of the potential well:

$$\beta=\frac{\sum_n\left(\exp\left(-\frac{\varepsilon_n^{\uparrow}}{T}\right)-\exp\left(-\frac{\varepsilon_n^{\uparrow}}{T}\right)\right)}{\sum_n\left(\exp\left(-\frac{\varepsilon_n^{\uparrow}}{T}\right)+\exp\left(-\frac{\varepsilon_n^{\downarrow}}{T}\right)\right)}. \tag{18}$$

For Fermi statistics the mutual orientation of the barrier magnetizations in the absence of external magnetic field will vary with increasing well width, and therefore the parameter β will be an oscillatory function of a. Since for wide enough barriers one has $\varepsilon_n^{\uparrow}(\mathrm{AF})=\varepsilon_n^{\downarrow}(\mathrm{AF})$, one can assume that β is nonzero only in those regions of a values for which a ferromagnetic ordering of the barriers is realized. Therefore one should calculate the function $\beta_F(a)$ and use its values in the corresponding regions of a and assume $\beta=0$ in the regions of antiferromagnetic orientation of the magnetic layers. In the case of an antiferromagnetic type of coupling, the imposition of a relatively weak magnetic field will cause the magnetic moments of the barriers to orient along the field direction, leading to a change in polarization of the electron spins from zero to the value $\beta_F(a)$. This effect can be used in spintronic devices.[26]

The parameter β_F has the form

$$\beta_F=\frac{1}{\xi n_S}\left[\sum_{n=1}^{k_1}(\mu-\varepsilon_n^{\uparrow})-\sum_{n=1}^{k_2}(\mu-\varepsilon_n^{\downarrow})\right]_F. \tag{19}$$

For small enough a, d, and n_0, when only the subband $\varepsilon_1^{\uparrow}(\mathrm{F})$ is filled, the electron spin polarization reaches 100%. In the region of well widths a corresponding to the filling of the upper subbands $\varepsilon_k^{\uparrow}(\mathrm{F})$ and $\varepsilon_{k-1}^{\downarrow}(\mathrm{F})$ the polarization β_F has the value

$$\beta_F=\frac{1}{\xi n_S}\left\{\frac{1}{(2k-1)}[C_k-\varepsilon_k^{\downarrow}]_F+\sum_{n=1}^{k}(\varepsilon_n^{\downarrow}-\varepsilon_n^{\uparrow})_F-\varepsilon_k^{\downarrow}(F)\right\} \tag{20}$$

and in the adjacent region of a, in which the filling of the $\varepsilon_k^{\downarrow}(\mathrm{F})$ subband occurs,

$$\beta_F=\frac{1}{\xi n_S}\left[\sum_{n=1}^{k}(\varepsilon_n^{\downarrow}-\varepsilon_n^{\downarrow})\right]_F. \tag{21}$$

Figure 7 shows the curves of $\beta_F(a)$ for samples with different electron densities and sublayer thicknesses d. The polarization β_F decreases rather rapidly with increasing a, making sharp jumps from the minimum values at the start of the filling of the subbands $\varepsilon_n^{\uparrow}(\mathrm{F})$ to maximum values when the subbands $\varepsilon_n^{\downarrow}(\mathrm{F})$ are "turned on." The intervals of antiferromagnetic ordering of the barriers on the $\beta_F(a)$ curves correspond to regions of a which begin approximately halfway between the maxima and minima of $\beta_F(a)$ and end around the minima of $\beta_F(a)$. The amplitude of the spikes of the relative polarization β in the regions of ferromagnetic ordering in Fig. 7 does not exceed 0.04.

From an analysis of the behavior of the function $E_m(\Delta)$ for different n_0 one can reach the following conclusions as to the possible form of the temperature dependence $\beta(T)$. If in the interval under study, from T_C to $T_{\min}$, the energy E_m is negative, then the polarization β will increases monotonically from zero to the largest values $\beta(T_{\min})$, except for cases when the functions $E_m(\Delta)$ and $\beta(\Delta)$ behave nonmonotonically (see the curve for $\xi n_S=1.32$ eV in Fig. 6b). If instead $E_m>0$, the polarization is equal to zero. In the case of a change in sign of E_m the polarization β becomes nonzero at temperatures below that at which the sign change of E_m occurs. If E_m changes sign twice (see the curve for $\xi n_S=0.692$ eV in Fig. 6a) the polarization $\beta(T)$ is nonzero only in the region lying between the points at which E_m changes sign. Thus, depending on n_0, a, and d, the function $\beta(T)$ can exhibit five qualitatively different types of behavior.

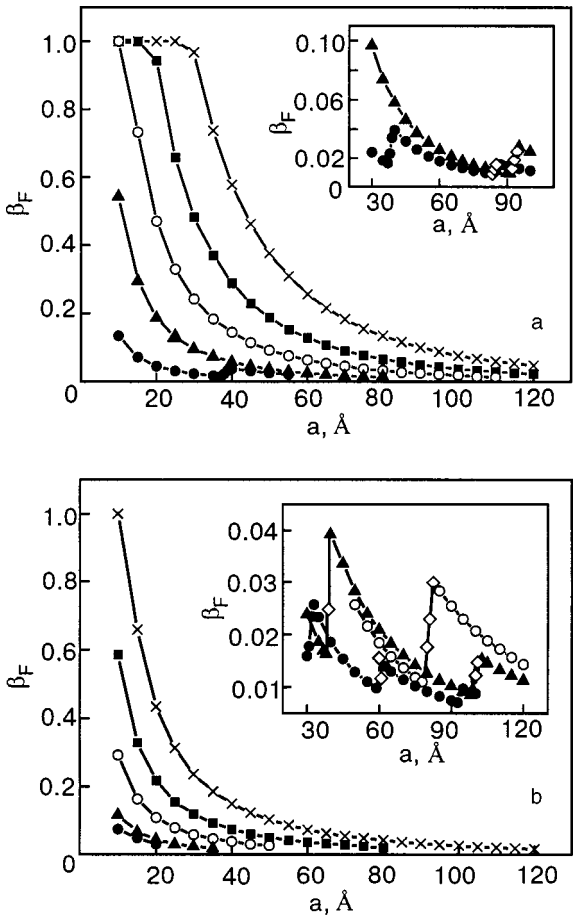

FIG. 7. Relative spin polarization β_F of the electrons for F orientation of the magnetic layers as a function of the width a of the quantum well between the EuS barriers for a PbS sublayer thickness $d=100$ (a) and 500 Å (b) and different electron densities n_0 (see Fig. 3 for notation); $b_1=b_2=40$ Å; $T=4.2$ K. The insets show parts of the $\beta_F(a)$ curves in an expanded scale.

6. CONCLUSIONS

For a simple model of the potential energy of electrons in a four-layer structure of the type I/NM/F/NM/F (I is an insulating substrate and NM is a nonmagnetic spacer layer), in which the ferromagnetic layers act as potential barriers for the motion of electrons and the nonmagnetic semiconductor spacers are potential wells, we have calculated the energy spectra of electrons with opposite spin directions for the cases of ferromagnetic-field and antiferromagnetic ordering of the magnetizations of the magnetic layers. Because of the exchange splitting of the conduction band of the ferromagnetic layers, the barrier height depends on the mutual orientation of the electron spin and barrier magnetization and also on temperature, which governs the value of the splitting. Because of the difference of the potential relief for electrons

in the cases of ferromagnetic and antiferromagnetic orientations of the barrier magnetizations, the spectra of the electrons in the sample will be different for these orientations. For sufficiently wide barriers the electron spectrum is practically independent of the sublayer thickness d and the characteristics of the insulating substrate. The difference of the surface energies of the electrons for ferromagnetic, $E_S(\mathrm{F})$, and antiferromagnetic, $E_S(\mathrm{AF})$, ordering of the barriers, $E_m = E_S(\mathrm{F}) - E_S(\mathrm{AF})$, is a characteristic of the energy of exchange coupling of the magnetic layers.

In the case of Boltzmann statistics the energy $E_m < 0$, and one should always observe ferromagnetic ordering of the magnetic layers. The absolute value of E_m and the relative spin polarization β of the electrons will grow rapidly with decreasing temperature and decreasing width a of the potential well between the barriers ($\beta \sim 1$ for narrow potential wells and temperatures far from the Curie temperature T_C of the barriers).

For Fermi statistics the energy E_m is a sign-varying oscillatory function of the quantum well width a, and with increasing electron density in the wells (n_0) and sublayer thickness the extrema of E_m are shifted to smaller values of a, and their amplitudes rapidly increase. For EuS/PbS(001) multilayers the calculated values of E_m in the case of narrow potential wells ($a \sim 10$ Å) and electron densities $n_0 \sim 10^{19}$ cm^{-3} are on the same scale ($E_m \sim 10^{-2}$ mJ/m^2) with the experimentally determined values of E_m for EuS/PbS(001) superlattices.[15]

The calculations show that, depending on the values of a, d, and n_0, the temperature dependence of E_m can be qualitatively different. There can be a monotonic (or nonmonotonic) increase or decrease of E_m from zero to $E_m(T_{\min})$ as the temperature is lowered from T_C to $T_{\min}$, where $T_{\min}$ is the lowest temperature at which E_m is measured. At fixed a and d there are certain intervals of electron densities n_0 in which the energy E_m can change sign from positive to negative or change twice as the temperature is lowered. The sign change of E_m has been observed experimentally for MnTe/ZnTe SLs.[13]

The polarization β is nonzero only in regions of ferromagnetic ordering of the barriers and decreases rapidly with increasing a and n_0, undergoing sharp spikes and dips when E_m changes sign. The character of the temperature dependence of $\beta(T)$ is determined by the behavior of the energy $E_m(T)$: either $\beta = 0$ (antiferromagnetic ordering of the barriers in the entire temperature interval $T_C - T_{\min}$), or β increases monotonically (or nonmonotonically) with decreasing temperature (ferromagnetic ordering), or it becomes nonzero at temperatures below that at which the sign change of E_m occurs, or $\beta \neq 0$ in the temperature interval lying between the points at which E_m changes sign.

Such a diversity of behavior of E_m and β upon change in the width of the quantum well, electron density n_0, and temperature is due to the nonsimultaneous filling of the corresponding spin-dependent subbands of the size quantization in the cases of ferromagnetic and antiferromagnetic orientation of the magnetic barriers. The oscillations of $E_m(a)$ and $\beta(a)$ are of the same nature as the known quantum size effects in films of semiconductors and semimetals.[34] For semiconductor SLs with wide ferromagnetic barriers, in which the minibands degenerate to a system of discrete energy levels, one expects qualitatively similar effects to be manifested as in the four-layer structures investigated here.

This study was supported by the grant CRDF UP2-2444-KH-02.

*E-mail: zorch@kpi.kharkov.ua

[1] P. Grünberg, R. Schreiber, Y. Pang, M. B. Brodsky, and H. Sower, Phys. Rev. Lett. **57**, 2442 (1986).
[2] R. E. Camley and R. L. Stamps, J. Phys.: Condens. Matter **5**, 3727 (1993).
[3] P. Bruno, Phys. Rev. B **52**, 411 (1995).
[4] P. A. A. van der Heijden, P. J. H. Bloemen, J. M. Metselaar, R. M. Wolf, J. M. Gaines, J. T. W. W. van Eemeren, P. J. van der Zaag, and W. J. M. de Jonge, Phys. Rev. B **55**, 11569 (1997); P. A. A. van der Heijden, C. H. W. Swüste, W. J. M. de Jonge, J. M. Gaines, J. T. W. W. van Eemeren, and K. M. Schep, Phys. Rev. Lett. **82**, 1020 (1999).
[5] C. A. Ramos, D. Lederman, A. R. King, and V. Jaccarino, Phys. Rev. Lett. **65**, 2913 (1990).
[6] J. A. Borchers, M. J. Carey, R. W. Erwin, C. F. Majkrzak, and E. Berkowitz, Phys. Rev. Lett. **70**, 1878 (1993).
[7] V. Nunez, T. M. Giebultowicz, W. Faschinger, G. Bauer, H. Sitter, and J. K. Furdyna, J. Magn. Magn. Mater. **140–144**, 633 (1995).
[8] L. E. Stumpe, J. J. Rhyne, H. Kaiser, S. Lee, U. Bindley, and J. K. Furdyna, J. Appl. Phys. **87**, 6460 (2000).
[9] J. J. Rhyne, J. Lin, J. K. Furdyna, and T. M. Giebultowicz, J. Magn. Magn. Mater. **177–181**, 1195 (1998); J. Lin, J. J. Rhyne, J. K. Furdyna, and T. M. Giebultowicz, J. Appl. Phys. **83**, 6554 (1998).
[10] T. M. Giebultowicz, V. Nunez, G. Springholz, G. Bauer, J. Chen, M. S. Dresselhaus, and J. K. Furdyna, J. Magn. Magn. Mater. **140–144**, 635 (1995).
[11] H. Kepa, J. Kutner-Pielaszek, A. Twardowski, A. Yu. Sipatov, C. F. Majkrzak, T. Story, R. R. Gałazka, and T. M. Giebultowicz, J. Magn. Magn. Mater. **226–230**, 1795 (2001).
[12] N. Akiba, F. Matsukura, A. Shen, Y. Ohno, H. Ohno, A. Oiwa, S. Katsumoto, and Y. Iye, Appl. Phys. Lett. **73**, 2122 (1998); D. Chiba, N. Akiba, F. Matsukura, Y. Ohno, and H. Ohno, Appl. Phys. Lett. **77**, 1873 (2000).
[13] T. M. Giebultowicz, H. Kepa, J. Blinowski, and P. Kacman, Physica E (Amsterdam) **10**, 411 (2001).
[14] J. J. Chen, Z. H. Wang, M. S. Dresselhaus, G. Dresselhaus, G. Springholz, and G. Bauer, Solid-State Electron. **37**, 1073 (1994); J. J. Chen, G. Dresselhaus, M. S. Dresselhaus, G. Springholz, C. Pichler, and G. Bauer, Phys. Rev. B **54**, 402 (1996); L. Bergomi and J. J. Chen, Phys. Rev. B **56**, 3281 (1997).
[15] H. Kepa, J. Kutner-Pielaszek, J. Blinowski, A. Twardowski, C. F. Majkrzak, T. Story, P. Kacman, R. R. Gałazka, K. Ha, H. J. M. Swagten, W. J. M. de Jonge, A. Yu. Sipatov, V. V. Volobuev, and T. M. Giebultowicz, Europhys. Lett. **56**, 54 (2001); L. Kowalczyk, M. Chernyshova, T. Story, J. K. Ha, V. V. Volobuev, and A. Yu. Sipatov, Acta Phys. Pol. A **100**, 357 (2001).
[16] H. Kepa and T. M. Giebultowicz, to be published.
[17] P. Shevchenko, L. Swierkowski, and J. Oitmaa, J. Magn. Magn. Mater. **177–181**, 1168 (1998).
[18] T. M. Rusin, Phys. Rev. B **58**, 2107 (1998).
[19] V. K. Dugaev, V. I. Litvinov, W. Dobrowolski, and T. Story, Solid State Commun. **110**, 351 (1999).
[20] J. Blinowski and P. Kacman, Acta Phys. Pol. A **92**, 719 (1997).
[21] J. Blinowski and P. Kacman, Phys. Rev. B **64**, 045302 (2001).
[22] M. Wilczyhski and R. Swirkowicz, Phys. Status Solidi B **212**, 165 (1999).
[23] P. Wachter, in *Handbook on the Physics and Chemistry of Rare Earths*, K. A. Gscheider Jr. and L. Eyring (eds.), North-Holland, Amsterdam (1997), Chap. 19.
[24] Yu. I. Ravich, B. A. Efimova, and I. A. Smirnov, *Methods of Semiconductor Research in Application to the Lead Chalcogenides PbTe, PbSe, and PbS*, [in Russian] Nauka, Moscow (1968).
[25] L. D. Hicks, T. C. Harman, K. Sun, and M. S. Dresselhaus, Phys. Rev. B **53**, R10493 (1996).
[26] H. Ohno, F. Matsukura, and Y. Ohno, JSAP International **5**, 4 (2002).
[27] I. V. Kolesnikov, V. A. Litvinov, A. Yu. Sipatov, A. I. Fedorenko, and A. É. Yunovich, Zh. Éksp. Teor. Fiz. **94**, 239 (1988) [Sov. Phys. JETP **67**, 1431 (1988)]; L. Kowalczyk, J. Sadowski, R. R. Gałazka, A. Stachow-Wójcik,

A. Yu. Sipatov, V. V. Volobuev, V. A. Smirnov and V. K. Dugaev, Acta Phys. Pol. A **94**, 397 (1998).
[28] X. Hao, J. S. Moodera, and R. Meservey, Phys. Rev. B **42**, 8235 (1990).
[29] S. J. Cho, Phys. Rev. B **1**, 4589 (1970).
[30] A. Stachow-Wójcik, T. Story, W. Dobrowolski, M. Arciszewska, R. R. Gałazka, M. W. Kreijveld, C. H. W. Swüste, H. J. M. Swagten, W. J. M. de Jonge, A. Twardowski, and A. Yu. Sipatov, Phys. Rev. B **60**, 15220 (1999).
[31] R. Swirkowicz and T. Story, J. Phys.: Condens. Matter **12**, 8511 (2000).
[32] I. V. Kolesnikov and A. Yu. Sipatov, Fiz. Tekh. Poluprovodn. **23**, 954 (1989) [Sov. Phys. Semicond. **23**, 598 (1989)].
[33] B. M. Askerov, *Electron Transport Phenomena in Semiconductors* [in Russian], Nauka, Moscow (1985).
[34] T. Jungwirth, W. A. Atkinson, B. H. Lee, and A. H. MacDonald, Phys. Rev. B **59**, 9818 (1999).
[35] A. Mauger and C. Godart, Phys. Rep. **141**, 51 (1986).
[36] P. Heller and G. Benedek, Phys. Rev. Lett. **14**, 71 (1965).
[37] J. Unguris, R. J. Celotta, and D. T. Pierce, Phys. Rev. Lett. **67**, 140 (1991); **79**, 2734 (1997).

Translated by Steve Torstveit

ELECTRONIC PROPERTIES OF METALS AND ALLOYS

Properties of low-temperature ytterbium condensates grown in a medium of gaseous helium

V. M. Kuz'menko and A. N. Vladychkin

*Kharkov Physicotechnical Institute National Research Center, ul. Akademicheskaya 1, 61108 Kharkov, Ukraine**

(Submitted March 7, 2003)
Fiz. Nizk. Temp. **29**, 1223–1230 (November 2003)

The features of the electronic properties and mechanisms of crystallization of amorphous ytterbium films obtained by low-temperature condensation in a medium of gaseous helium (at a partial pressure of 2.3×10^{-3}–7 Pa) are investigated. The changes of the conductivity, magnetoresistance, and Hall effect upon annealing of the films are investigated. The corresponding changes in the density and mobility of charge carriers are calculated in a two-band model. A model of the structural transformation of low-temperature condensates of gas-saturated ytterbium in the annealing process is proposed. © *2003 American Institute of Physics.*
[DOI: 10.1063/1.1614237]

INTRODUCTION

The configuration of the outer electrons of neutral ytterbium atoms in their ground state can be written as $4f^{14}6s^2$. Since the $4f$ level in ytterbium is close to the Fermi level, an additional anisotropic coupling arises due to the strong mixing of the $4f$ states with the conduction band. The $5d$ band of ytterbium is empty and also overlaps with the s band. Since ytterbium, as a rule, is a divalent metal, its electronic properties are mainly determined by the degree of overlap of the s and p bands. Ordinarily, if the lattice constant of divalent fcc and bcc metals is increased significantly, the width of the two bands decreases and at some point in the process their overlap can vanish—the substance becomes a semiconductor. In some divalent metals the overlap of the bands can decrease with decreasing lattice constant, and the substance becomes a semiconductor at sufficiently high pressures. In particular, such behavior is observed in ytterbium. Up to a pressure $p\sim3\times10^9$ Pa the resistivity of ytterbium increases with pressure, and ytterbium acquires semiconductor properties.[1,2] In the framework of a divalent model the density of carriers in fcc Yb (single crystals with a ratio of resistivities at temperatures of 293 and 4.2 K in the range $\rho_{293}/\rho_{4.2}=4-22$) decreases as the pressure is increased from 0 to 1.7×10^9 Pa by approximately 5 times.[2] The number of charge carriers at atmospheric pressure and $T\approx2$ K for the samples obtained was $(0.3-4)\times10^{20}$ cm^{-3} (depending on $\rho_{293}/\rho_{4.2}$). It is thought that most likely an energy gap between the s valence band and the empty p conduction band arises in ytterbium under pressure. Thus a metal–nonmetal transition will occur in a cubic divalent metal if some parameter influencing the width of the band gap (e.g., the lattice constant) is varied to a sufficient degree. By means of thermal expansion one can achieve an increase in the lattice constant of only a few percent. A considerably wider range of variation of the interatomic distances can be achieved in noncrystalline glassy substances.

It is known that the condensation of ytterbium vapor in ultrahigh vacuum onto a substrate cooled by liquid helium results in the formation of an amorphous modification of ytterbium.[3,4] The transition to the fcc modification ($a-k$ transition) occurs at $T_{a-k}\approx15-20$ K or in the process of condensation when the film reaches a critical thickness (in the latter case a mechanism of avalanche (explosive) crystallization is realized[5]).

We note that in this paper we will be discussing only amorphous ytterbium and its fcc modification. We did not observe even a trace of the low-temperature hcp modification of this metal, which has been observed at temperatures near and below room temperature in high-purity ytterbium ($\rho_{293}/\rho_{4.2}\approx100$).[6] In the present study we used bulk annealed ytterbium with $\rho_{293}/\rho_{4.2}=11$ (purity 99.7%). The electronic properties of pure ytterbium films in the amorphous and crystalline states at low temperatures have been studied previously.[7]

In particular, the density and mobility of carriers as functions of temperature and film thicknesses have been determined in the two-band model. The temperature dependence of the effective coupling between electrons $g(T)$ found in Ref. 8 is indicative of the possibility that a superconducting transition exists in amorphous Yb at low temperatures. Nevertheless, superconductivity has not been found in amorphous ytterbium films down to $T=0.35$ K.[9] Granted, the films, prepared at $p\approx1.3\times10^{-4}$ Pa, could have been contaminated with appreciable amounts of YbH_2 and Yb_2O_3 (Ref. 10).[1)]

The present paper is devoted to a study of the electronic properties of low-temperature Yb–He condensates. On the one hand, the increase in the number of scattering centers in view of the appreciable difference of the scattering potentials of the Yb and He atoms should lead to an increase of ρ with increasing He concentration. On the other hand, the embedding of helium atoms into the ytterbium structure can result

in an increase of the average interatomic distance for ytterbium. In that case, judging from the behavior of fcc Yb under pressure, one can expect an increase in the overlap of the $6s$ and $6p$ bands and a decrease of ρ. Importantly, unlike active interstitial impurities (H, O, N, C, B), a transition of electrons from the interstitial helium atoms to the empty $5d$ subshell of ytterbium or the formation of chemical compounds is impossible; this is important for making a more objective assessment of the change in the electronic properties of ytterbium under the influence of the interstitial helium atoms.

The goal of this study is to check the possibility of a superconducting transition in the amorphous system Yb–He, to investigate the influence of helium on the electronic properties (the Hall effect, resistivity, magnetoresistance) of amorphous and fcc ytterbium, and to study the influence of helium on the stability and mechanisms of crystallization of the amorphous phase of Yb.

TECHNIQUES

The techniques used to obtain amorphous films of pure metals and to study their electronic properties are described in detail in Refs. 12 and 13. Welded glass ampoules were used, having a flat polished substrate to which platinum wire leads were welded to provide for electrical measurements of the metallic layer condensed on the substrate. After a preliminary pumping down to a pressure of 1.3×10^{-4} Pa the ampoule was filled to the required pressure with pure gaseous helium, hermetically sealed with a gas torch, and detached from the vacuum apparatus. The ampoule was mounted in a helium cryostat which was then flooded with liquid helium; this created an ultrahigh vacuum ($\sim1.3\times10^{-10}$ Pa) in the ampoule with respect to all air components at a partial pressure of helium in the interval from 2.3×10^{-3} Pa to 7 Pa. Since the substrate was washed by liquid helium, its temperature did not exceed 5 K during the Yb condensation process. The geometry of the films for the resistivity and Hall-effect studies was determined by the shape of the cutouts in a stainless-steel mask placed on the substrate (Fig. 1). The magnetic field used in the Hall-effect and magnetoresistance studies was produced by a superconducting solenoid with an induction $B=1.6$ T and was imposed perpendicular to the film plane. To check the field dependence of the Hall voltage and magnetoresistance we used a solenoid with $B\approx4.0$ T. The resistivity and Hall voltage were measured by a compensation method with the use of a potentiometer. The films studied were more than 50 nm thick. At such a thickness practically all the measurable characteristics of Yb–He films cease to depend on the thickness.[7,12] The thickness of the films was determined after the experiment was completed and the ampoule was opened, using an interferometric method and, for $d=50-70$ nm, from the optical density. The maximum error in these measurements was around 15%. This error was the main determinant of the error in the calculated values of the Hall coefficient and electrical conductivity. The temperature of the film in the interval 4.2–293 K was measured by a platinum resistance thermometer.

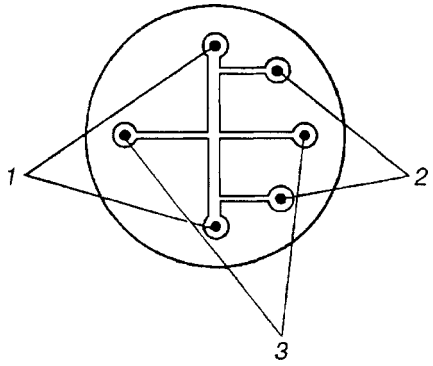

FIG. 1. Shape of the films for measurement of the resistivity and Hall voltage: current contacts (*1*), potential contacts (*2*), and contacts for measurement of the Hall potential difference (*3*).

EXPERIMENTAL RESULTS

It was found that at a partial pressure of gaseous helium in the working ampoule of less than 1.7×10^{-1} Pa and a rate of condensation of 4–10 nm/min, such film parameters as the resistivity in the amorphous state (ρ_a) and in the state crystallized at $T=T_{a-k}$ (ρ_{a-k}) and the galvanomagnetic characteristics (the Hall coefficient R_H and magnetoresistance $\Delta\rho/\rho$) did not differ from those of pure Yb film within the error limits. The activation energy for crystallization, E, determined by the method of the ratio of the angular coefficients from the isothermal $\rho(t)$ curves at different temperatures during annealing of a single sample[14] for amorphous Yb–He films (grown at $p<1.7\times10^{-1}$ Pa) also practically coincide with the values for pure Yb films. The velocity U_f

TABLE I. Physical parameters of Yb and Yb–He films.

Samples	Rate of condensation, nm/min	d, nm	T_{a-k}, K	$\frac{\Delta\rho_{a-k}}{\rho_a}$, %	ρ_a, μΩ·cm	ρ_{a-k}, μΩ·cm	ρ_{293}, μΩ·cm	U_f, m/s	E, kJ/mole
Yb	5–10	50–70	13.2	86	125	17	23	9.0	3.35
Yb–He-1	4.5–8.5	50–70	14.0	87	117	15	21	8.7	3.30
Yb–He-2	≤10	110	17.0	67	350	117	24.5	–	–
Yb–He-3	9.5	190	18.0	54	397	181	25.3	–	–
Yb–He-4	11.5	115	19.0	57	414	178	25	–	4.20
Yb–He-5	>100	700	18.0	38	900	558	25	–	4.80

Note: $\Delta\rho_{a-k}=\rho_{a-k}-\rho_a$.

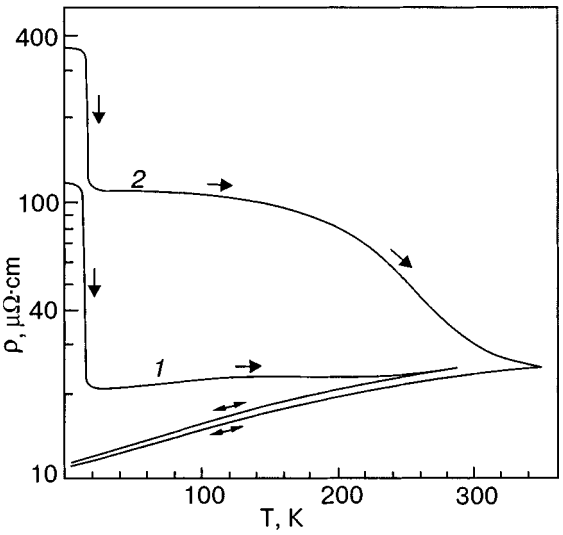

FIG. 2. Variation of the resistivity of films of pure Yb (*1*) and the film Yb–He-2 (*2*) on heating.

of the front of avalanche crystallization initiated in the Yb–He films by a local current pulse[14] did not differ appreciably from the value of U_f for pure films (Table I). The first column of Table I corresponds to the averaged values for 15 pure Yb films in the thickness interval 50–70 nm. The second column corresponds to the averaged values for five Yb–He films of the same thickness, obtained at the following partial pressures of He [Pa]: 0.9×10^{-4}, 2.3×10^{-3}, 5.7×10^{-2}, 8.9×10^{-2}, 1.7×10^{-1}. For each individual film the values given in the first two columns of Table I differ from the averaged values by $\pm10\%$. A substantial increase in ρ_a, ρ_{a-k}, T_{a-k}, and E was observed for the Yb–He films obtained at helium partial pressures in the working ampoule greater than 2.7×10^{-1} Pa. Self-sustaining avalanche crystallization in these samples was not realized at all; i.e., the initiating current pulse passed through a local region of the film and brought it to a crystalline state (see Ref. 14) but the crystallization front did not propagate in a self-sustaining manner to the rest of the film. The third column of Table I gives the parameters of the film Yb–He-2, which was condensed at a partial pressure in the ampoule equal to 3.3×10^{-1} Pa, and columns 4–6 give those for films condensed at a He partial pressure of $\approx4.4\times10^{-1}$ Pa (these films are denoted by Yb–He-3...5, respectively).

Figure 2 shows the variation of the resistivity in the course of annealing for a pure film (curve *1*) and the film Yb–He-2 (curve *2*). The parts of the curves for $T\leqslant20$ K correspond to a transition of the samples from the amorphous to the crystalline state. One sees a sharp difference of the resistivities of these samples both in the amorphous state and immediately after the transition. However, after annealing to 350 K the resistivity of the film Yb–He-2 at room temperature was practically no different from that of the pure Yb film and the bulk annealed metal used in this study.[2)] The film Yb–He-5, which was obtained at a high rate of condensation, had $\rho\approx900\mu\Omega\cdot$cm in the as-condensed state. In the $a-k$ transition process at a temperature of 18–20 K the resistivity decreases by 37% and then declined slowly to $\sim50\mu\Omega\cdot$cm at 320 K. After the ampoule was placed in a furnace at a temperature of ≈450 K and held at that temperature for several minutes, the resistivity of this film at room temperature agreed (within error limits) with the value of ρ for the pure films and the initial bulk metal, i.e., $\approx25\mu\Omega\cdot$cm.

At a helium partial pressure in the working ampoule of ≈7 Pa a black condensate with an even surface formed on the substrate. It was easily scratched through to the glass by a copper or even a wooden point. Clearly in this case a ytterbium powder was formed, the black color of which is explained by the circumstance that the size of the grains is much less than the wavelength of light and the absorption coefficient of the powder is close to unity. Nevertheless, there was good contact between the powder grains, so that immediately after condensation the resistivity of this condensate was a few thousand $\mu\Omega\cdot$cm, $R_H\approx6.5\times10^{-10}$ m^3/C, and after annealing to room temperature $\rho_{4.2}\approx151\mu\Omega\cdot$cm, $\rho_{293}/\rho_{4.2}\approx1.15$, $R_H=12.7\times10^{-10}$ m^3/C (see the film Yb–He-6 in Table II). None of the Yb–He samples showed signs of superconductivity down to 1.5 K.

It is known that fcc Yb is a compensated metal,[15] i.e., in terms of the two-band model[16–18] it has an equal number of mobile electrons and holes. At different stages of their annealing the resistivity, magnetoresistance, and Hall coefficient of the crystallized films Yb–He-1...5 were measured at $T=4.2$ K. The field dependence of the magnetoresistance was close to quadratic ($\Delta\rho/\rho\sim H^2$), and we used the formulas of the two-band model for calculating the carrier density and mobility in these films:

$$\sigma=\rho^{-1}=en(\mu_e+\mu_h);$$

$$R_H=\frac{1}{en}\,\frac{\mu_h-\mu_e}{\mu_h+\mu_e};\quad \frac{\Delta\rho}{\rho B^2}=\mu_e\mu_h.$$

Here σ is the conductivity, $n=n_e=n_h$ is the number of elec-

TABLE II. Electronic characteristics of the Yb and Yb–He films.

Sample	d, nm	T_w, K	$\rho_{4.2}$, μΩ·cm	R_H, 10^{-10} m^3/C	$\frac{\Delta\rho}{\rho}$ (1.6 T), 10^{-4}	μ_e, 10^{-2} m^2/(V·s)	μ_h, 10^{-2} m^2/(V·s)	$n_e=n_h$, 10^{20} cm^{-3}
Yb	105.0	25	24.4	8.9	4.7	1.20	1.57	9.23
Pure		293	11.6	7.6	15.8	2.21	2.87	10.60
Yb – He-2	110.0	25	117.0	6.35	1.3	0.72	0.77	3.58
		350	11	8.20	17.6	2.32	3.07	10.53
Yb – He-6	540.0	293	151	12.7	0,6	0.47	0.55	4.06

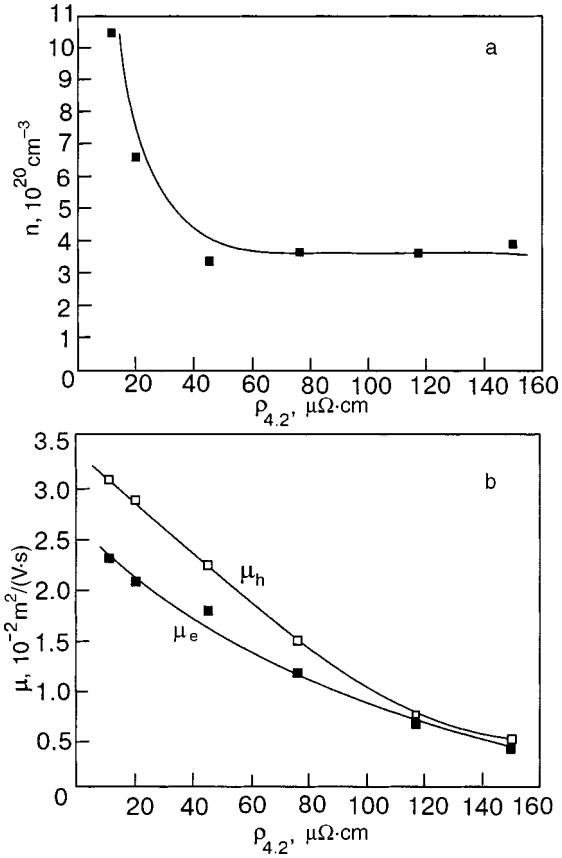

FIG. 3. Increase in the density (a) and mobility (b) of charge carriers at 4.2 K with decreasing resistivity in crystalline films Yb–He-2 and Yb–He-3 annealed at temperatures from 25 to 350 K.

trons or holes per unit volume, μ_e and μ_h are the electron and hole mobilities, and B is the magnetic induction.

We note that in the amorphous state the magnetoresistance of Yb films[8] and of the Yb–He films investigated in the present study is anomalous because of the quantum corrections to the Boltzmann conductivity.[19] In this case the applicability of the two-band model is not indisputable, although a description was attempted[7] with the use of this model back before the development of a theory of the quantum corrections.

For comparison Table II gives the electronic characteristics of a pure Yb film and of the film Yb–He-2 at $T=4.2$ K immediately after the $a-k$ transition and after annealing to temperatures close to room temperature. The main difference lies in the fact that the carrier density in the pure crystalline Yb films after annealing to 25 K increased only slightly (by 10–20%) on heating to room temperature. A more more substantial growth of the parameter n (correlated with a decrease in ρ) is observed in the annealed films Yb–He-(2...5). Interestingly, the carrier density at 4.2 K in the sootlike sample Yb–He–6 after annealing to room temperature was close in order of magnitude to that for the pure films (see Table II).

The variation of the carrier density and mobility of the Yb–He films at 4.2 K as functions of the resistivity at different stages of annealing is showed in Fig. 3. Interestingly, the carrier density is practically constant in the resistivity interval 150–50$\mu\Omega\cdot$cm, and it only increases rapidly to values close to those for the pure films as a result of further annealing (Fig. 3a). At the same time, the electron and hole mobilities increase monotonically with decreasing ρ (Fig. 3b).

DISCUSSION OF THE RESULTS

It is known that impurities of oxygen, nitrogen, carbon, boron, phosphorus, etc. substantially retard the growth of crystals in amorphous films of pure metals.[12,20] It follows from the present study that the stabilizing ability of helium atoms is much less. There have been several hypotheses attempting to explain the mechanism of stabilization of the amorphous state of a metal by the admixture of a second component.[20] According to the hypothesis of Bennet *et al.*,[21] for crystallization to occur the impurity atoms occupying pores in the amorphous structure of the metal must move at least one interatomic distance. Then the growth of the crystals will be limited by the hopping frequency of impurity atoms to the positions ensuring a higher degree of local order of the metal atoms. The time constant τ for this process should be on a level with the time constant for the diffusion of the impurity atoms.[22] That is, the value of τ should be much larger than for the motion of the amorphous metal–crystal interphase surface in pure systems, which occurs by much shorter atomic displacements (by a diffusionless mechanism[5]). Therein, according to Ref. 21, lies the mechanism of stabilization of the amorphous state of a metal by impurities. However, in the case of low-temperature ytterbium–helium condensates a different picture is observed.

In the condensation of ytterbium vapor in a residual atmosphere of helium on a liquid-helium-cooled substrate, the helium atoms enter the metallic condensate through cryocapture:[23] the helium atoms falling on the substrate are buried by the oncoming flow of metal atoms. In fcc Yb the radius of the octahedral interstitial site is approximately 0.08 nm, while that of the tetrahedral one is 0.043 nm,[24] and there is one octahedral interstitial site per fcc Yb atom. Since the density of amorphous ytterbium is lower than the density of fcc Yb (in amorphous ytterbium at the same shortest interatomic distances as in fcc Yb the coordination number is smaller[4]), one can propose the presence of a large number of submicropores, with a size >0.08 nm. Numerous papers on positron annihilation also attest that the structure of amorphous substances contains vacancy-like defects with a radius up to $0.7r_0$,[25] where r_0 is the radius of an atom of the main component ($r_0=0.199$ nm for Yb). These submicropores apparently fill with helium atoms (the radius of which is 0.122 nm), having little effect on the electronic properties of the condensate when the pressure in the ampoule is not over 1.7×10^{-1} Pa and the condensation rate is less than 10 nm/min. In this case the crystallization parameters—the activation energy of the transformation and the velocity of the avalanche crystallization front—differ little from those of the pure films (see Table I). In the process of crystallization of the ytterbium the helium atoms apparently come to occupy the octahedral interstitial sites of the fcc lattice. This process should apparently be diffusionless, since the activation energy for crystallization of the Yb–He-1 series of films under discussion is the same as in the case of pure ytterbium films.

Indeed, if the transition of the ytterbium atoms through the boundary between the amorphous and crystalline phases in the processes of crystallization of the ytterbium–helium samples depended on the diffusion of helium atoms, then the activation energy of the transformation would correspond to the activation energy for diffusion of helium in ytterbium. It is clear that the high stabilizing ability of interstitial atoms of O, N, C, P, and B in the amorphous metal structure is due (unlike the case of a helium impurity) not only to the necessity of their diffusion in order for crystallization to occur but also to the existence of a strong interaction of the active atoms of the impurity with the atoms of the metal.[20,21]

As was shown above, increasing the helium partial pressure in the ampoule to $p > 2.7\times10^{-1}$ Pa and the rate of condensation to $v \geqslant 10$ nm/min will lead to a situation in which the resistivity of the unannealed films (Yb–He-2...5) is several times higher than in the pure ytterbium films. The higher resistivity of the film Yb–He-5 in comparison with the films Yb–He-3 and 4 (even though they were all grown at the same helium partial pressure) is due to the higher rate of condensation of that film. Increasing the rate of evaporation at a constant gas pressure acts in an analogous way to increasing the pressure at a constant rate of evaporation.[26]

In the case of the films Yb–He-2...5, instead of the molecular-stream condensation characteristic for higher vacuum, we observed signs of deposition of metal particles by bulk condensation, specifically: smearing of the boundaries of the molecular shadow as a result of scattering of the molecular stream. The interaction between atoms of the metal does not require an activation energy. Therefore, practically any encounter between evaporated ytterbium atoms in the poor vacuum will lead to their joining together on the way to the substrate. Colliding with one another, the metal atoms can form particles consisting of two, three, and, in general, diverse numbers of atoms. The simultaneous deposition on the substrate of the disperse particles formed as a result of bulk condensation and condensation of the molecular stream, which at the same time bring about the incorporation of powder particles, leads to the formation of film materials with a high concentration of micropores and a developed specific surface.[27] These factors can, in the main, account for the high resistivity and substantially lower carrier density (in comparison with pure ytterbium films) in the samples Yb–He-2...5 immediately after their crystallization (see Table II). The influence on the resistivity of a possible increase in the interatomic distance (because of the incorporation of helium atoms in the Yb lattice) should apparently be the opposite, since the value of ρ in fcc Yb increases with pressure.[1,2]

It is known that under conditions of intense release of a latent heat of transition (and poor heat transfer) a self-acceleration of the crystallization of amorphous substances is possible, when the velocity of a single transformation front reaches tens of meters per second. The nature of this effect, which is called avalanche or explosive crystallization, has been studied in amorphous films of a number of substances,[5,28] including amorphous films of pure ytterbium.

It appears that the main reason for the absence of an avalanche crystallization mechanism in the Yb–He-2...5 samples is the considerably smaller latent heat of transition per unit volume of the films as compared with the Yb and Yb–He-1 films as a result of the higher microporosity.

For pure amorphous metals the heat released in the crystallization process is approximately one-half the heat of fusion (see Refs. 5 and 12). It can be assumed that the heat of crystallization per unit volume of a ytterbium–helium film is substantially smaller than for pure ytterbium films for more reasons than just the presence of micro- and submicropores. Judging from the high values of the resistivity of the films Yb–He-2...5 after crystallization (larger than ρ for liquid Yb[29]), they probably retain a high disordering energy, which decreases by means of heat release during the long annealing time. Such a situation is observed, for example, in the annealing of pure films of tin, lead, copper, and gold which are maximally distorted as a result of condensation at 4.2 K but which do not form an amorphous phase.[30] The trend of the $\rho(T)$ curves of low-temperature condensates of these metals[20,31] in the interval 4.2–300 K is the same as in the films Yb–He-2...5 after the $a-k$ transition (see curve *2* in Fig. 2). The fact that the carrier density in the films Yb–He-2...5 is practically independent of their resistivity in the interval 50–150$\mu\Omega\cdot$cm (see Fig. 3a) may be due to the circumstance that that the concentration of micropores remains constant there, while the decrease of ρ (curve *2* in Fig. 2) is due to improvement of the Yb lattice. The latter is accompanied by an increase in the carrier mobility (Fig. 3b). Further decrease of the resistivity and growth of the carrier density with increasing annealing temperature is apparently due to the escape of helium from the sample and the healing of micropores, as in the case of annealing of selenium films obtained by laser deposition in an oxygen atmosphere.[32] In Ref. 32 the stage of crystallization of selenium films was preceded by a stage in which the excess gas was released in the form of bubbles buried in the amorphous matrix. The formation of oxygen (or argon[33]) bubbles has also been observed during the crystallization (at $T \approx 362$ K) of amorphous gold films grown at a partial pressure of the gas $\geqslant 90$ Pa and a substrate temperature close to room temperature. Very low values of the temperature and activation energy for crystallization of the films Yb–He-2...5 (see Table I) eliminates the need for helium diffusion in order for the transition to occur. The formation of helium bubbles in the crystalline films Yb–He-2...5, if it occurs at all, occurs at temperatures substantially higher than T_{a-k}. However, it cannot be ruled out that the possibility of activationless subbarrier tunneling of He atoms at low temperatures has an influence on the morphology of the films.

Unfortunately, we do not have the technical means at our disposal (in particular, a low-temperature electron microscope) necessary in order to track the dynamics of the change in morphology of the Yb–He films in the course of their annealing from 4.2 to 300–350 K and to link this change to a change in the electronic parameters of the films studied.

We took x-ray diffraction patterns in chromium radiation for Yb–He films with parameters close to those of the film Yb–He-5 after its annealing to room temperature ($\rho_{293} = 60\mu\Omega\cdot$cm). The diffraction lines all belong exclusively to fcc Yb. Photometry of the x-ray patterns showed that the lattice constant of this film is practically no different from the values for the initial bulk ytterbium.

CONCLUSION

The electronic characteristics of ytterbium films grown by low-temperature condensation at a helium partial pressure below 1.7×10^{-1} Pa (and $p\leqslant1.3\times10^{-10}$ Pa for the residual gases) are practically no different from the characteristics of ytterbium films grown in ultrahigh vacuum. The mechanisms of crystallization of the Yb–He films are also ordinary in this case—both isothermal crystallization on heating and avalanche crystallization initiated at 4.2 K by a local current pulse or arising spontaneously when the film reaches a critical thickness are possible. The change of the electronic properties of ytterbium and the suppression of the self-sustaining avalanche crystallization mechanism in it occur when it is evaporated at a helium partial pressure $p>2.7\times10^{-1}$ Pa. In this case besides condensation of a molecular stream one also observes bulk condensation of complexes of atoms, which obviously leads to a substantial increase in the porosity of the condensate (a less-close packing). Nevertheless, even here upon heating to $T=350-450$ K the parameters of the Yb films become close to those of films grown in ultrahigh vacuum. At a helium partial pressure above 7 Pa the condensate has a black powdery form. However, it retains the hallmarks of a metal—metallic conduction and a high density of charge carriers, indicating that the powder grains are pure metal and maintain contact with one another. No signs of superconductivity were detected in the Yb–He films down to 1.5 K.

*E-mail: marbor@roket.kharkov.ua

[1)]The valence of 3 in the latter compound is due to the excited state $5d^16s^2$, which arises as a result of a transition of one electron from the $4f$ to the $5d$ level.[11]

[2)]The value of ρ for the initial Yb after rolling was $35.7\mu\Omega\cdot$cm, and after annealing at $T=400\,^\circ$C for 2 hours it was $\approx22.4\mu\Omega\cdot$cm.

[1] M. N. Pavlovskiĭ, Zh. Éksp. Teor. Fiz. **73**, 237 (1977) [Sov. Phys. JETP **46**, 122 (1977)].
[2] S. Minomura, G. Fujii, O. Shimomura, H. Nagano, and S. Tanuma, in *Proceedings of the 12th International Conference on Low Temperature Physics, Kyoto, 1970*; publ. Tokyo (1971), p. 567.
[3] B. G. Lazarev, V. M. Kuz'menko, A. I. Sudovtsov, and R. F. Bulatova, Dokl. Akad. Nauk SSSR **184**, 587 (1969) [Sov. Phys. Dokl. **184**, 7 (1969)].
[4] Yu. F. Komnik and L. A. Yatsuk, in *Filamentary Crystals and Thin Films* [in Russian], Part 2, Voronezh (1975), p. 85.
[5] V. A. Shklovskiĭ and V. M. Kuz'menko, Usp. Fiz. Nauk **157**, 311 (1989) [Sov. Phys. Usp. **32**, 163 (1989)].
[6] E. Bucher, P. H. Schmidt, A. Jayaraman, K. Antres, J. P. Maita, K. Nassan, and P. D. Dernier, Phys. Rev. B **2**, 3911 (1970).
[7] V. M. Kuz'menko, V. I. Mel'nikov, and A. I. Sudovtsov, Zh. Éksp. Teor. Fiz. **71**, 1503 (1976) [Sov. Phys. JETP **44**, 786 (1976)].
[8] V. M. Kuz'menko, A. N. Vladychkin, V. I. Mel'nikov, and A. I. Sudovtsov, Zh. Éksp. Teor. Fiz. **86**, 180 (1984) [Sov. Phys. JETP **59**, 102 (1984)].
[9] N. Jacobsen, C. G. Granqvist, T. Claeson, Z. Phys. B **25**, 265 (1976).
[10] A. E. Curzon and O. J. Singh, Less-Common Metals **39**, 227 (1975).
[11] K. N. R. Taylor and M. Darby, *Physics of Rare-Earth Solids*, Chapman and Hall, London (1972), Mir, Moscow (1974).
[12] V. M. Kuz'menko, B. G. Lazarev, V. I. Mel'nikov, and A. I. Sudovtsov, Ukr. Fiz. Zh. (Russ. Ed.) **21**, 883 (1976).
[13] V. M. Kuz'menko and A. N. Vladychkin, Fiz. Tverd. Tela (St. Petersburg) **41**, 177 (1999) [Phys. Solid State **41**, 155 (1999)].
[14] V. M. Kuz'menko and V. I. Mel'nikov, Zh. Éksp. Teor. Fiz. **82**, 802 (1982) [Sov. Phys. JETP **55**, 474 (1982)].
[15] W. R. Datars and S. Tanuma, Phys. Lett. A **27**, 182 (1968).
[16] E. H. Sondheimer and A. H. Wilson, Proc. R. Soc. London, Ser. A **190**, 435 (1947).
[17] E. H. Sondheimer, Proc. R. Soc. London, Ser. A **193**, 484 (1948).
[18] M. Kohler, Ann. Phys. (Leipzig) **6**, 18 (1949).
[19] B. L. Al'tshuler, A. G. Aronov, A. I. Larkin, and D. E. Khmel'nitskiĭ, Zh. Éksp. Teor. Fiz. **81**, 768 (1981) [Sov. Phys. JETP **54**, 411 (1981)].
[20] Yu. F. Komnik, Fiz. Nizk. Temp. **8**, 3 (1982) [Sov. J. Low Temp. Phys. **8**, 1 (1982)].
[21] C. H. Bennet, D. E. Polk, and D. Turnbull, Acta Metall. **19**, 1295 (1971).
[22] T. Masumoto, K. Suzuki, H. Fujimori, and K. Hashimoto, *Elements of Amorphous Metals* [in Japanese], Ohm-sha, Tokyo (1982), Metallurgiya, Moscow (1987).
[23] É. Trendelenburg, *Ultrahochvakuum*, G. Braun Verlag, Karlsruhe (1963), Mir, Moscow (1966).
[24] E. Fromm and E. Gebhardt, *Gase und Kohlenstoff in Metallen*, Springer Verlag, Berlin (1976), Metallurgiya, Moscow (1980).
[25] Yu. V. Barmin and I. V. Zolotukhin, in *Physical Chemistry of Amorphous (Glassy) Metallic Materials* [in Russian], Nauka, Moscow (1987), p. 80.
[26] J. Hengevoss and E. A. Trendelenburg, Z. Naturforsch. Teil A **18**, 481 (1963).
[27] L. S. Palatnik, I. Kh. Tartakovskaya, and O. I. Kovaleva, Dokl. Akad. Nauk SSSR **260**, 335 (1981) [Sov. Phys. Dokl. **26**, 889 (1981)].
[28] V. M. Kuz'menko, Zarubezhnaya Radioélektronika. Uspekhi Sovremennoĭ RadioÉlektroniki, No. 5, 17 (2002).
[29] H. J. Güntherodt, E. Hauser, and H. U. Künzi, Phys. Lett. A **50**, 313 (1974).
[30] W. Mönch, Z. Phys. **164**, 229 (1961).
[31] K. A. Neĭgebauér, in *Physics of Thin Films* [Russian translation], Vol. 2, Mir, Moscow (1967), p. 13.
[32] A. G. Bagmut, V. D. Sarana, and Yu. G. Mashkarov, Voprosy Atomnoĭ Nauki i Tekhniki, Ser.: Yaderno-Fizicheskie Issledovaniya, No. 1(27), 63 (1994).
[33] A. G. Bagmut, Izv. Akad. Nauk, Ser. Fiz. **57**, 112 (1993).

Translated by Steve Torstveit

"High-temperature" oscillations of the magnetoresistance of bismuth: a possible alternative explanation

Yu. F. Komnik*

B. Verkin Institute for Low Temperature Physics and Engineering, National Academy of Sciences of Ukraine, pr. Lenina 47, 61103 Kharkov, Ukraine

(Submitted March 11, 2003; revised May 6, 2003)
Fiz. Nizk. Temp. **29**, 1231–1236 (November 2003)

It is shown that the known experimental results on the properties of the "high-temperature" oscillations of the magnetoresistance of bismuth—in particular, the angular dependence of the oscillation periods on the direction of the magnetic field—can be described by the Polyanovskiĭ theory with the use of the condition that the cyclotron frequencies are equal or multiples. © *2003 American Institute of Physics.* [DOI: 10.1063/1.1614238]

The goal of this communication is to explain the unusual "high-temperature" oscillations (HTOs) of the magnetoresistance of bismuth on the basis of the Polyanovskiĭ theory,[1–3] which, with some additional assumptions, can provide an adequate description of the experimental results.

The observation of new quantum oscillations of the magnetoresistance of bismuth, with a period in the inverse magnetic field, ΔH^{-1}, which is 2–3 times shorter than that of the Shubnikov–de Haas oscillations and with an order-of-magnitude smaller amplitude but a slower temperature decay was reported by Bogod and Krasovitskiĭ in 1973.[4] Since then the new oscillations have been studied in detail in crystals of Bi and the alloys $Bi_{1-x}Sb_x$ and also in crystals with donor (Te) and acceptor (Sn) impurities.[5–14] Experiments have been done to study the manifestation of the oscillations in the thermopower[15,16] and the behavior under pressure and uniaxial deformation[17,18] and in strong magnetic fields.[19–21] Based on the data of these experiments it was concluded that the period of the HTOs is not determined directly by the Fermi energy of the electrons E_F^e or holes E_F^h but is somehow related to the value of the band overlap $E_{\rm ov}$. The latter conclusion served as a stimulus for the dubious assertion[22] that the HTOs are "quantum oscillations of the probability of quasielastic intervalley scattering of charge carriers with deep-lying energies," specifically, with states at the bottom of the electron band E_c^e and the top of the hole band E_c^h. However, the deep-lying states are traditionally considered to be completely filled. Although it was shown in a subsequent paper[23] that the deep-lying states in connection with "collisional" broadening of the energy levels can contribute to the conduction, the scope of that work did not encompass a treatment of the detailed picture of the observed oscillation periods in different crystallographic directions and their weak temperature decay.

Polyanovskiĭ[1–3] singled out from the magnetoconductance the term involving intervalley transitions and describing the properties of the HTOs—a small period ΔH^{-1} and weak temperature decay. Meanwhile, Polyanovskiĭ's theory was not accepted by the authors of the experimental papers (see the critique in Ref. 14), since the physical cause of the new oscillations remained unclear. Recently Kirichenko and Kozlov[24] obtained a result similar to Polyanovskiĭ's in an analysis of a completely different object—a layered conductor in which, as in bismuth, there are two types of extremal sections that govern oscillations of the magnetoconductance.

Bismuth is a semimetal, with a weak overlap of the valence and conduction bands, as a result of which electron and hole valleys form. Taking the spectrum of a semimetal in a magnetic field as

$$E_n^e=\left(n+\frac{1}{2}\right)\hbar\Omega^e+\frac{p_z^{e^2}}{2m^e}$$

and

$$E_n^h=E_{\rm ov}-\left(n+\frac{1}{2}\right)\hbar\Omega^h-\frac{p_z^{h^2}}{2m^h}$$

($E_{\rm ov}$ is the overlap energy of the bands), Polyanovskiĭ[1–3] obtained for the conductivity in a magnetic field two terms describing interband transitions, σ^{ee} and σ^{hh}, which determine the Shubnikov–de Haas oscillations[25,26] for the electron and hole valleys, and a term σ^{eh} describing the interband transitions. The last term contains the product of the densities of states in different valleys. This product of two oscillatory characteristics gives rise not only to terms describing the Shubnikov–de Haas oscillations in each of the valleys but also to a "cross" term with combination parameters, arising as a result of the interference of the densities of states in the different valleys. This term in the conductivity can serve as an explanation for the "high-temperature" oscillations of the magnetoresistance of bismuth. It has the form[27]

$$\sigma^{eh}=\frac{3}{8}\sigma_{\rm cl}\frac{\hbar(\Omega^e+\Omega^h)}{E_{\rm ov}}\sum_{k,l=1}^{\infty}\frac{(-1)^{k+l}}{\sqrt{kl}}\times\left\{A\left[\frac{2\pi^2k_BT}{\hbar}\left(\frac{k}{\Omega^e}-\frac{1}{\Omega^h}\right)\right]\sin\frac{2\pi}{\hbar}\times\left(k\frac{E_F^e}{\Omega^e}+l\frac{E_{\rm ov}-E_F^e}{\Omega^h}\right)+A\left[\frac{2\pi^2k_BT}{\hbar}\left(\frac{k}{\Omega^e}+\frac{l}{\Omega^h}\right)\right]\times\cos\frac{2\pi}{\hbar}\left(k\frac{E_F^e}{\Omega^e}-l\frac{E_{\rm ov}-E_F^e}{\Omega^h}\right)\right\}. \quad (1)$$

Here Ω^e and Ω^h are the cyclotron frequencies of the electrons and holes, $A(x)=x/\sinh(x)\approx x\exp(-x)$ for $x\gg 1$.

Taking into consideration that

$$\frac{2\pi E_F^e}{\hbar\Omega^e}=\frac{cS^e}{\hbar eH},\quad \frac{2\pi E_F^h}{\hbar\Omega^h}=\frac{cS^h}{\hbar eH},\quad E_{\rm ov}-E_F^e=E_F^h,$$

we obtain Polyanovskiĭ's result:

$$\sigma^{eh}=\frac{3}{8}\sigma_{\rm cl}\frac{\hbar(\Omega^e+\Omega^h)}{E_{\rm ov}}\sum_{k,l=1}^{\infty}\frac{(-1)^{k+l}}{\sqrt{kl}}\times\left\{A\left(\frac{2\pi^2k_BT}{\hbar\Omega^-}\right)\sin\left(\frac{cS^+}{\hbar eH}\right)+A\left(\frac{2\pi^2k_BT}{\hbar\Omega^+}\right)\cos\left(\frac{cS^-}{\hbar eH}\right)\right\}. \tag{2}$$

Equation (2) contains the combination areas

$$S^{\pm}=kS^e\pm lS^h \tag{3}$$

and the combination inverse cyclotron frequencies

$$\frac{1}{\Omega^{\pm}}=\frac{k}{\Omega^e}\pm\frac{1}{\Omega^h}. \tag{4}$$

According to Eq. (2) there are two series of oscillations, with periods

$$\Delta H^{-1}=\frac{2\pi\hbar e}{cS^{\pm}}, \tag{5}$$

the temperature decay of which is governed by the factor

$$\exp\left(-\frac{2\pi^2k_BT}{\hbar\Omega^{\mp}}\right). \tag{6}$$

We are mainly interested in the oscillations determined by the combination area S^+, for which the period ΔH^{-1} is smaller than for the Shubnikov–de Haas oscillations and the temperature decay determined by the combination frequency Ω^- is slower than for the Shubnikov–de Haas oscillations. These oscillations can explain the HTOs. The second type of oscillations—long-period, with faster temperature decay, have not been detected in experiment.

The results obtained explain well the whole complex of experimental observations. For example, adding a donor impurity (Te) to bismuth increases the electron concentration and decreases the hole concentration. Additionally, E_F^e increases and E_F^h decreases, but the period of the HTOs remains unchanged,[13] since the sum of the areas (3) remains practically unchanged. An analogous result is obtained when an acceptor impurity (Sn) is added to bismuth. When the isovalent impurity antimony is added to bismuth, both energies E_F^e and E_F^h decrease, and accordingly both areas S^e and S^h decrease, leading to an increase in the oscillation period ΔH^{-1} (Ref. 12). Similarly, one can explain the results of a study[18] on the influence of uniaxial deformation on the periods of the HTOs and also the fact that the ultraquantum limit at high magnetic field is reached simultaneously for both the Shubnikov–de Haas and ''high-temperature'' oscillations.[19] (Note that this would not be the case if the HTOs were related to some energy other than the Fermi energy, as in the model of Ref. 22).

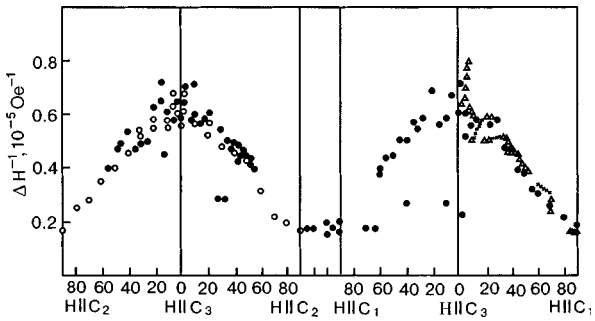

FIG. 1. Angular dependence of the periods ΔH^{-1} of the ''high-temperature'' oscillations in bismuth, obtained in measurements of the diagonal and off-diagonal components of the magnetoresistance tensor (●—data of Ref. 7; △—mean period;[9] ×—period obtained from the angular shift of the extrema[9]) and from thermopower measurements (○—Ref. 16).

The most important result of the experimental study of HTOs is the dependence of the oscillation periods ΔH^{-1} on the orientation of the magnetic field with respect to the crystallographic directions[7,9,16] (Fig. 1). Let us discuss these findings.

As was noted in Refs. 1–3, the HTOs are due to intervalley transitions of electrons which occur at resonant values of the magnetic field, fields at which Landau levels in the different valleys are simultaneously found near the Fermi energy. However, the frequency with which such events occur as the magnetic field is varied is determined exclusively by the frequency with which Landau levels pass through the Fermi energy in the band with the higher cyclotron frequency (lower cyclotron mass), and so this does not give rise to a new period ΔH^{-1} of the magnetoresistance oscillations. The new period is due to the appearance of a combination of cyclotron processes in the two valleys. Polyanovskiĭ's theory, of a formal mathematical construction, does not allow one to understand the physical nature of the simultaneous oscillatory terms. As we have said, the crossing terms appear as a result of the interference of the oscillatory dependences of the densities of states in the different valleys. The reason why the amplitudes of these oscillations are not small (undetectable) is apparently of a quantum nature, like that which was pointed out by Adams and Holstein[26] in an analysis of the Shubnikov–de Haas oscillations in the single-band case, having to do with the influence of electric field on the collision integral.

It is important to note that for the intervalley conversion transitions, the density of states has features (maxima) in both the initial and final states. In addition, expression (2) for the ''high-temperature'' oscillations, unlike the case of the Shubnikov–de Haas oscillations,[26] does not contain the value of the chemical potential, and the energies E_F^e and E_F^h are related through a constant, nonoscillatory quantity—the overlap energy $E_{\rm ov}$. For this reason the amplitude of the oscillations is not very sensitive to temperature smearing of the Fermi boundary, i.e., the temperature decay of the oscillation amplitude is weak.[27]

Experimental observations show that the amplitude of the HTOs in bismuth increases with temperature in the range 1.5–10 K, passes through a maximum (at 10 K), and then falls off slowly.[9,14] The authors justifiably surmised that high-frequency thermal phonons excited at the higher tem-

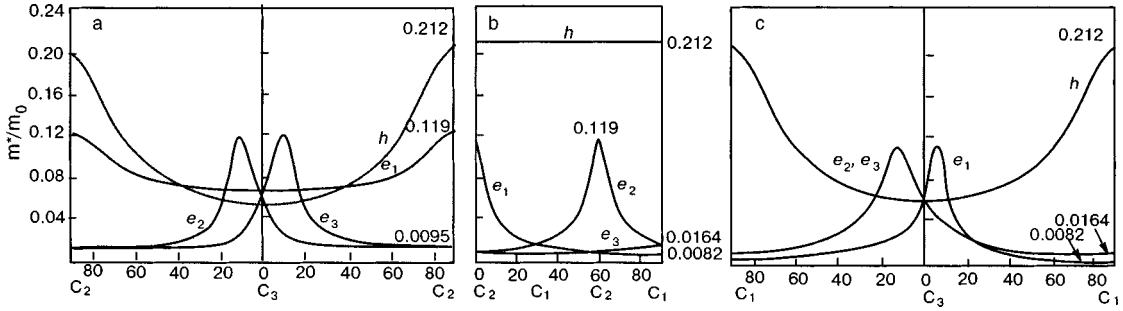

FIG. 2. Angular dependence of the cyclotron mass in bismuth, constructed from the data of Refs. 28–30.

peratures play a role in the formation of the HTOs. This role may reduce to the circumstance that the turning on of electron–phonon scattering leads to the appearance of free electron states below the Fermi energy, which are needed for isoenergetic intervalley transitions.

The possibility of electron intervalley conversion transitions is obvious when the cyclotron frequencies on the extremal orbits in the different valleys are equal, since in that case the electron states remain coherent. That was the case considered in the paper by Kirichenko and Kozlov.[24] However, in bismuth it is only when the magnetic field direction is along the trigonal axis C_3 that the cyclotron frequencies of electrons and holes are approximately equal (the cyclotron effective masses are equal to $0.0630m_0$ for electrons and $0.0639m_0$ for holes). When the field deviates from the C_3 axis, and especially for a field direction along the bisector C_1 and binary C_2 axes, the cyclotron effective masses of electrons and holes are considerably different. Meanwhile, the HTOs in bismuth are observed for arbitrary directions of the magnetic field.

We note that the possibility of electron intervalley conversion transitions remains present for multiples of the cyclotron frequencies as well. Indeed, if the cyclotron frequencies for the two valleys are multiples of each other, then, with a frequency equal to the lower of the two cyclotron frequencies, the coherence of the electron states is periodically recovered, i.e., the conditions for a resonant transition of an electron from an orbit in one valley to an orbit in another valley are restored.

We choose the harmonics k and l in formula (2) such that their ratio corresponds to a multiple of the cyclotron frequencies, i.e., we let

$$\frac{k}{l}=\frac{\Omega^e}{\Omega^h}=\frac{m^h}{m^e}=K, \tag{7}$$

where $K=1,2,3...$ are integers. This assumption was also made in Refs. 1 and 2.

To check stated assumptions we calculated the possible oscillation periods according to Eq. (5) with the use of relation (7). Figure 1 illustrates the experimental data for the periods ΔH^{-1} of the HTOs in bismuth upon variation of the magnetic field direction. The angular dependence of the periods ΔH^{-1} for the bisector plane C_3C_2 was taken from Refs. 7 and 16 and for the binary plane C_3C_1 from Refs. 7 and 9. It is seen that the values of the HTO periods ΔH^{-1} have a considerably larger scatter than for the Shubnikov–de Haas oscillations (see Ref. 7); in particular, the pattern for the bisector plane C_3C_2 does not have mirror symmetry. In Ref. 9, observations of the HTOs were made as the angle of rotation of the magnetic field in the binary plane C_3C_1 was varied with a step of $1-2°$, and it was found that in many cases two close periods were observed, and in some directions oscillations were not detected.

The results of calculations of the periods ΔH^{-1} according to formulas (5) and (3) with the use of (7) are extremely sensitive to the initial data for the cyclotron masses m^* and the cross-sectional areas S in bismuth, and for this reason we give in Figs. 2 and 3 the angular dependences of m^* and S adopted in the calculations. The angular dependences for the masses were constructed according to the data of cyclotron resonance studies,[28–30] the data for the areas were generalized according to studies[31–34] of the Shubnikov–de Haas and de Haas–van Alfven effects in bismuth. The values of m^* and S for the principal directions of the magnetic field (along the C_1, C_2, and C_3 axes) correspond to the numbers given in the review by Edelman.[35]

If the periods ΔH^{-1} are calculated according to Eqs. (5) and (3) for the values of the harmonics $k=l=1$, then good agreement with experiment is obtained only for $\mathbf{H}\|\mathbf{C}_3$

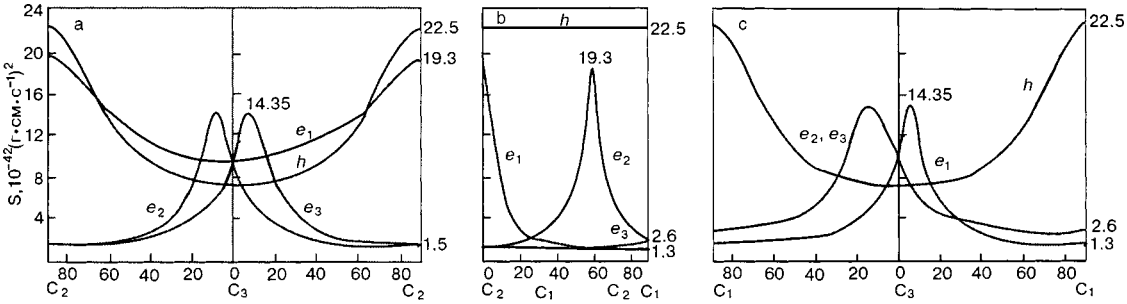

FIG. 3. Angular dependence of the areas of sections through the hole and electron ellipsoids in bismuth, constructed according to the data of Refs. 31–34.

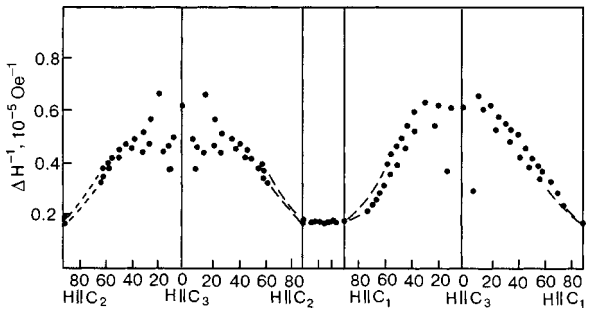

FIG. 4. Angular dependence of the calculated values of the periods ΔH^{-1} of the ''high-temperature'' oscillations in bismuth. For the trigonal plane C_1C_2, as in Fig. 1, a 30° sector is given; the rest of the pattern is mirror symmetric.

($\Delta H^{-1}=0.63\times10^{-5}$ Oe^{-1}). For the direction $\mathbf{H}\|\mathbf{C}_2$ the calculated value of ΔH^{-1} (0.253×10^{-5} Oe^{-1}) is almost one and a half times larger than the experimentally observed value (0.18×10^{-5} Oe^{-1}). For the direction $\mathbf{H}\|\mathbf{C}_1$ the difference reaches a factor of 2.5: the calculation gives 0.44×10^{-5} Oe^{-1} while the experimental value is approximately 0.18×10^{-5} Oe^{-1}. Accordingly, the angular dependences of ΔH^{-1} for the bisector (C_3C_2) and especially for the binary (C_3C_1) planes differ appreciably from the picture observed experimentally. Consequently, this version of Polyanovskiĭ's theory does not give numerical agreement with experiment.

A completely different result is obtained when condition (7) is used. Figure 4 shows the results of calculations of the periods ΔH^{-1} with the use of that condition.

The calculations were done for values up to $K=10$, since beyond that the error of the calculations grows strongly. The dashed curves in Fig. 4 show proposed extensions of the calculated curves of ΔH^{-1} to values for magnetic field directions along the C_1 and C_2 axes. It is seen that the calculated picture (Fig. 4) reproduces the experimentally observed picture (Fig. 1) to a satisfactory degree of approximation. (One must consider the error of both the experimental observations and of the initial data for the calculations.)

We note that in the case when high harmonics participate in the formation of the oscillations (for a strong deviation of the field from the C_3 axis), the oscillations take on a less perfect sinusoidal form and their amplitude decreases.[6,9,16,18,19]

On account of the Dingle smearing of the levels, oscillations of an interference nature can be observed not only at exact integer values of the ratio m^h/m^e but also close to these values. For an exact integer value of the ratio $k/l=m^h/m^e$ the inverse combination cyclotron frequency tends toward zero, i.e., the temperature suppression of the oscillations because of smearing of the Fermi distribution vanishes, and only the Dingle smearing remains. The same result was obtained by Kirichenko and Kozlov[24] in considering a layered conductor in which the cyclotron frequencies on two cross sections are equal.

We note that the oscillations shown by the dark dots in Fig. 4 cannot be designated as hole or electron; they are of an interference nature and are combination oscillations.

We note another important result of the calculations: for the planes (C_3C_1) and (C_3C_2) (see Fig. 4) the calculated points form two chains of possible oscillation periods with slightly different values, as has been noted repeatedly by the authors of experimental papers (see Refs. 9 and 13, etc.)

Thus formulas (2)–(5), which were obtained by Polyanovskiĭ for explaining the ''high-temperature'' oscillations of the magnetoresistance in bismuth, give a completely successful description of the properties of those oscillations and, in particular, describe the angular dependences of the oscillation periods ΔH^{-1} with respect to the magnetic field direction. In our view it remains necessary to solidify the physical grounds for the nature of the combination areas and to explain the temperature dependence of the oscillation amplitude at lower temperatures (<10 K). The above considerations are only of a preliminary character.

We are grateful to V. B. Krasovitskiĭ, Yu. A. Kolesnichenko, V. G. Peschanskiĭ, and A. A. Slutskin for a helpful discussion of the problem, and to I. V. Kozlov for communicating valuable information.

*E-mail: komnik@ilt.kharkiv.ua

[1] V. M. Polyanovskiĭ, JETP Lett. **46**, 132 (1987).
[2] V. M. Polyanovskiĭ, Ukr. Fiz. Zh. (Russ. Ed.) **33**, 1575 (1988).
[3] V. M. Polyanovskiĭ, Ukr. Fiz. Zh. (Russ. Ed.) **34**, 459 (1989).
[4] Yu. A. Bogod, Vit. B. Krasovitskiĭ, Preprint FTINT AN USSR (1973) [in Russian].
[5] Yu. A. Bogod, Vit. B. Krasovitskiĭ, and V. G. Gerasimechko, Zh. Éksp. Teor. Fiz. **66**, 1362 (1974) [Sov. Phys. JETP **39**, 667 (1974)].
[6] Yu. A. Bogod, Vit. B. Krasovitskii, and V. G. Gerasimechko, Fiz. Tverd. Tela (Leningrad) **17**, 1799 (1975) [Sov. Phys. Solid State **17**, 1172 (1975)].
[7] Yu. A. Bogod, V. G. Gerasimechko, and Vit. B. Krasovitskii, Fiz. Nizk. Temp. **1**, 1472 (1975) [Sov. J. Low Temp. Phys. **1**, 707 (1975)].
[8] Yu. A. Bogod and Vit. B. Krasovitskiĭ, JETP Lett. **24**, 543 (1976).
[9] Yu. A. Bogod, Vit. B. Krasovitskiĭ, and S. A. Mironov, Zh. Éksp. Teor. Fiz. **78**, 1099 (1980) [Sov. Phys. JETP **51**, 554 (1980)].
[10] Yu. A. Bogod, Vit. B. Krasovitskii, and E. T. Lemeshevskaya, Fiz. Nizk. Temp. **7**, 1530 (1981) [Sov. J. Low Temp. Phys. **7**, 739 (1981)].
[11] Yu. A. Bogod, Vit. B. Krasovitsky, and E. T. Lemeshevskaya, Fiz. Nizk. Temp. **9**, 34 (1983) [Sov. J. Low Temp. Phys. **9**, 16 (1983)].
[12] Yu. A. Bogod, Vit. B. Krasnovitskiĭ (Krasovitsky), and E. T. Lemeshevskaya, Fiz. Nizk. Temp. **9**, 832 (1983) [Sov. J. Low Temp. Phys. **9**, 431 (1983)].
[13] Yu. A. Bogod, Vit. B. Krasovitskii, and E. T. Lemeshevskaya, Fiz. Nizk. Temp. **12**, 610 (1986) [Sov. J. Low Temp. Phys. **12**, 345 (1986)].
[14] Yu. A. Bogod and Vit. B. Krasovitskii, Fiz. Nizk. Temp. **16**, 900 (1990) [Sov. J. Low Temp. Phys. **16**, 527 (1990)].
[15] Yu. A. Bogod, Vit. B. Krasovitski, and E. T. Lemeshevskaya, Fiz. Nizk. Temp. **12**, 435 (1986) [Sov. J. Low Temp. Phys. **12**, 248 (1986)].
[16] Yu. A. Bogod, Vit. B. Krasovitskii, V. Ya. Levantovskii, and E. T. Lemeshevskaya, Fiz. Nizk. Temp. **14**, 1252 (1988) [Sov. J. Low Temp. Phys. **14**, 692 (1988)].
[17] A. G. Budarin, V. A. Venttsel', A. V. Rudnev, Yu. A. Bogod, and Vit. B. Krasovitskiĭ, Fiz. Nizk. Temp. **14**, 875 (1988) [Sov. J. Low Temp. Phys. **14**, 481 (1988)].
[18] Vit. B. Krasovitskii and V. V. Khotkevich, Fiz. Nizk. Temp. **17**, 710 (1991) [Sov. J. Low Temp. Phys. **17**, 374 (1991)].
[19] Vit. B. Krasovitsky, V. V. Khotkevich, A. G. M. Jansen, and P. Wyder, Fiz. Nizk. Temp. **25**, 903 (1999) [Low Temp. Phys. **25**, 677 (1999)].
[20] Yu. A. Bogod and A. Libinson, Solid State Commun. **96**, 609 (1995).
[21] Yu. A. Bogod and A. Libinson, Phys. Status Solidi B **197**, 137 (1996).
[22] Yu. A. Bogod, Fiz. Nizk. Temp. **12**, 1004 (1986) [Sov. J. Low Temp. Phys. **12**, 569 (1986)].
[23] Yu. A. Bogod, L. Yu. Gorelik, and A. A. Slutskin, Fiz. Nizk. Temp. **13**, 626 (1987) [Sov. J. Low Temp. Phys. **13**, 353 (1987)].
[24] O. V. Kirichenko and I. V. Kozlov, Fiz. Nizk. Temp. **28**, 690 (2002) [Low Temp. Phys. **28**, 509 (2002)].
[25] I. M. Lifshits and A. M. Kosevich, Zh. Éksp. Teor. Fiz. **33**, 88 (1957) [Sov. Phys. JETP **6**, 67 (1958)].
[26] E. N. Adams and T. D. Holstein, J. Phys. Chem. Solidi, **10**, 254 (1959)

[*Voprosy kvantovoĭ teorii neobratimykh protsessov*, V. L. Bonch-Bruevich (Ed.), Izd-vo inostr. lit. (1961), p. 255].
[27] I. V. Kozlov, private communication.
[28] Yi-Han Kao, Phys. Rev. **129**, 1122 (1963).
[29] R. J. Dinger and A. W. Lawson, Phys. Rev. B **7**, 5215 (1973).
[30] V. S. Édel'man and M. S. Khaĭkin, Zh. Éksp. Teor. Fiz. **49**, 405 (1965) [*sic*].
[31] N. B. Brandt, T. F. Dolgolenko, and N. N. Stupochenko, Zh. Éksp. Teor. Fiz. **45**, 1320 (1963) [Sov. Phys. JETP **18**, 635 (1964)].
[32] Y. Eckstein and J. Ketterson, Phys. Rev. **137**, 1777 (1965).
[33] R. N. Bhargava, Phys. Rev. **156**, 785 (1967).
[34] R. D. Brown, Phys. Rev. B **2**, 929 (1970).
[35] V. S. Edelman, Adv. Phys. **25**, 555 (1976) [V. S. Édel'man, Usp. Fiz. Nauk **123**, 257 (1977)].

Translated by Steve Torstveit

High-frequency characteristics of contactless electromagnetic excitation of transverse sound in quasi-two-dimensional conductors

O. Galbova, G. Ivanovski,* and D. Krstovska

Faculty of Natural Sciences and Mathematics, Institute of Physics, P.F. 162, 1000 Skopje, Republic of Macedonia

(Submitted March 26, 2003)
Fiz. Nizk. Temp. **29**, 1237–1243 (November 2003)

The contactless electromagnetic excitation of transverse sound with frequency ω in the semi-infinite space ($z \geqslant 0$) of a quasi-two-dimensional conducting medium is considered. The distribution of the displacement field $u(z)$, the electronic damping of sound, and the asymptotic behavior of the displacement field of an anomalous sound wave under conditions of the anomalous skin effect are calculated. © *2003 American Institute of Physics.*
[DOI: 10.1063/1.1614239]

Electromagnetic and sound waves in conductors form a coupled system that permits their interconversion.[1,2] The method of direct electromagnetic excitation of sound, which is based on this phenomenon, has become an important method of theoretical and experimental research on metals and has opened up the possibility of contactless excitation of high-frequency sound[3] through the action of various kinds of forces on the elastic medium.[1,2] At high frequencies in the absence of a constant magnetic field the main forces are strain-related. Here two mechanisms of conversion are possible. The first is the excitation of a so-called ordinary sound wave (OSW), the damping length of which is greater than both the skin depth δ of the electromagnetic field and the mean free path l of the conduction electrons. Such a wave propagates at the sound velocity s, and all the electrons participate in its excitation.[4] The second mechanism is due to the dragging of the sound field directly by the conduction electrons. The excitation of such a wave involves the participation of the electrons of the reference points and the electrons of the Fermi surface, for which the velocity component in the direction of propagation of the sound reaches the highest value.[5,6] This is a so-called anomalous sound wave (ASW). The electrons incident on the surface of the conducting medium at any angles participate in the conversion of electromagnetic energy into sound; because of this, the conversion coefficient depends substantially on the character of the scattering of electrons by the boundaries of the sample.[7,8] Thus the conversion of electromagnetic energy into sound energy can be counted among the effects which are sensitive to the surface quality of the conducting medium.

The search for new superconducting materials in the 1960s brought attention to conductors of organic origin, having a layered or filamentary structure. In addition to the great practical value of layered structures and the possibility of using them in modern electronics and computational technique, these conductors are in large measure attractive in connection with their unusual behavior in strong magnetic fields and their having a series of phase transitions at comparatively low pressures.

The propagation of both electromagnetic fields and high-frequency longitudinal acoustic waves in quasi-two-dimensional conductors has been quite well studied theoretically.[9] At the same time, the contactless conversion of electromagnetic energy into sound energy in quasi-two-dimensional conductors has not been adequately studied. In view of both the theoretical and practical value, in this paper we consider the high-frequency characteristics of contactless electromagnetic excitation of sound in quasi-two-dimensional conductors. The acoustic field of OSWs and the asymptotics of the acoustic field of the ASWs are calculated, and the electronic damping of sound is analyzed.

A number of quasi-two-dimensional organic conductors are now known;[10] these have typical metallic conduction in a certain plane and anomalously low conduction along the normal to that plane. The anisotropy of the electrical conductivity is due to anisotropy of the electron energy spectrum of such objects: the Fermi surface of a quasi-two-dimensional conductor can be represented in the form a slightly corrugated open cylinder, the smallness of its corrugation η reflecting the weak conduction in the open direction.

Thus the energy $\varepsilon(\mathbf{p})$ of the conduction electrons in the unstrained conductor can be written in the form

$$\varepsilon(\mathbf{p}) = \sum_{n=0}^{\infty} \varepsilon_n(p_x, p_y) \cos \frac{anp_z}{\hbar}, \tag{1}$$

where $\hbar$ is Planck's constant, $\mathbf{p}$ is the momentum of the conduction electrons, a is the distance between conducting layers, $\varepsilon_n(p_x, p_y)$ are arbitrary functions of their arguments, the maximum value $\varepsilon_n^{\max}$ on the Fermi surface falling off substantially with increasing n, so that $\varepsilon_1^{\max} = \eta\varepsilon_F$ and $\varepsilon_{n+1}^{\max} \ll \varepsilon_n^{\max}$.

Suppose that an electromagnetic wave of frequency ω ($E_x = E$, $E_y = E_z = 0$) is incident normally on a conducting half space ($z \geqslant 0$). For such a configuration only a transverse sound wave is excited, traveling in the positive z direction. Here the displacement vector $\mathbf{u}$ of the ions is directed along the x axis ($u_x = u$, $u_y = u_z = 0$). The problem is to calculate the amplitude of the wave. The total system of equations describing the propagation of coupled electromagnetic and sound waves in a conducting medium consists of the continuity equation for the nonequilibrium term $f(\mathbf{p}, \mathbf{r}, t)$ added to the equilibrium distribution function $f_0(\varepsilon)$ of the electrons,

Maxwell's equations, and the equations for the vibration of the elastic medium under the force density exerted on the lattice by the electric field and electrons.[1,2] In the chosen geometry this system has the form

$$\frac{\partial f}{\partial z} - i\frac{\omega^*}{v_z} f = \frac{e v_x}{v_z} E - \frac{i\omega}{v_z}\Lambda_{xz}\frac{\partial u}{\partial z}, \tag{2}$$

$$\frac{\partial^2 E}{\partial z^2} + i\omega\mu_0\langle v_x f\rangle = 0, \tag{3}$$

$$\frac{\partial^2 u}{\partial z^2} + q^2 u = \frac{1}{\rho s_t^2}\left[e\left\langle \frac{v_x\Lambda_{xz}}{v_z} E\right\rangle + i\omega^*\left\langle \frac{\Lambda_{xz}}{v_z} f\right\rangle\right], \tag{4}$$

where $\omega^* = \omega + i\nu$, ω and $\nu = 1/\tau$ are the frequency of the field and the frequency of collisions of the conduction electrons; $q = \omega/s$, s is the velocity of transverse sound; ρ is the density of the medium; $\mu_0 = 4\pi\times 10^{-7}$ N/m is the magnetic permeability of the vacuum; e is the charge, and v is the velocity of the conduction electrons. The angle brackets denote integration over the Fermi surface:

$$\langle \ldots\rangle = -\frac{2}{(2\pi\hbar)^3}\int (\ldots)\frac{\partial f_0}{\partial\varepsilon} d^3\mathbf{p}.$$

The system of equations (2)–(4) must be supplemented with the boundary condition on the surface:

$$f_-(\mathbf{p},\, z=0) = P f_+(\mathbf{p},\, z=0), \tag{5}$$

where f_- and f_+ are the nonequilibrium terms due to the conduction electrons incident on and reflected from the surface $z=0$, and P is the Fuchs phenomenological specularity parameter, which depends on the angle of incidence Θ of the electron on the surface of the sample[11] and is defined in such a way that $P=1$ for purely specular reflection and $P=0$ for purely diffuse reflection.

The electromagnetic wave is assumed monochromatic, so that f, E, and u are proportional to $\exp(-i\omega t)$.

Here we use the simplest form of quasi-two-dimensional dispersion relation for the charge carriers:

$$\varepsilon(\mathbf{p}) = \frac{p_x^2 + p_y^2}{m} + \eta\frac{\hbar}{a} v_0 \cos\frac{a p_z}{\hbar}, \tag{6}$$

where m is the effective mass and v_0 is the Fermi velocity of the conduction electrons. Elastic straining of the crystal leads to a renormalization of the charge carrier energy by an amount

$$\delta\varepsilon = \Lambda_{ij}(\mathbf{p}) u_{ij}, \tag{7}$$

where $u_{ij} = \partial u_i/\partial x_j$ is the strain tensor of the crystal. In the calculation we need the Λ_{xz} component of the deformation potential, which we write in the form

$$\Lambda_{xz}(\mathbf{p}) = \eta m v_x^2 L\cos\frac{a p_z}{\hbar} - m\eta v_0 v_x D\sin\frac{a p_z}{\hbar}. \tag{8}$$

The dimensionless parameters L and D are related to the genesis of the electron energy spectrum in the strained crystal.[1)] We shall assume that the parameters L and D are specified. The nonequilibrium term f added to the equilibrium distribution function f_0 of the conduction electrons satisfies boundary condition (5); the boundary conditions on equations (3) and (4) are the usual electrodynamic ones (continuity of the tangential component of the electric and magnetic fields) and the dynamic theory of elasticity. The boundary condition for the displacement u is obtained from the expression for the momentum flux density,[1,2] and with the use of condition (5) can be written in the form

$$\left.\frac{\partial u}{\partial z}\right|_{z=0} + \frac{P-1}{P+1}\frac{1}{\rho s^2}\left\langle \frac{v_z\Lambda_{xz}}{|v_z|} f_s\right\rangle\Bigg|_{z=0} = 0, \tag{9}$$

where

$$f_s = \frac{1}{2}[f(v_z,z) + f(-v_z,z)] \tag{10}$$

which is symmetric with respect to the component v_z of the nonequilibrium term in the distribution function.

The system of equations (2)–(4) with the appropriate boundary conditions will be solved by the Fourier method. In calculating the electromagnetic wave amplitude in the sample we will drop the second term in Eq. (2), which is quadratic in the small parameter characterizing the interconversion of electromagnetic and sound waves. However, that term must be kept when obtaining an expression for the electronic damping coefficient of sound. We obtain the following equations for the Fourier components E^k of the electric field and u^k of the displacement field:

$$E^k[k^2 + i\omega\mu_0\sigma(\omega,k)] + \frac{1}{\pi}E'(0) = \int_{-\infty}^{\infty} K(\omega,k,r)E^r dr, \tag{11}$$

$$u^k[q^2 - k^2] = \frac{e}{\rho s^2}E^k L_1(\omega,k) - \frac{i}{2\pi}\frac{(P-1)e\omega^*}{\rho s^2}\int_{-\infty}^{\infty} L_2(\omega,k,r)E^r dr, \tag{12}$$

$E'(0) = dE/dz|_{z=0}$ is the derivative at $z=0$, and

$$K(\omega,k,r) = -i\omega\mu_0 e^2\frac{P-1}{2\pi} \times\left\langle \frac{(\omega^*)^2 v_x^2 v_z^2}{|v_z|[(kv_z)^2 - (\omega^*)^2]\left[\left(\frac{v_z}{r}\right)^2 - (\omega^*)^2\right]}\right\rangle, \tag{13}$$

$$L_1(\omega,k) = k^2\left\langle \frac{\Lambda_{xz} v_z v_x}{(kv_z)^2 - (\omega^*)^2}\right\rangle.$$

$$\sigma(\omega,k) = ie^2\omega^*\left\langle \frac{v_x^2}{(kv_z)^2 - (\omega^*)^2}\right\rangle, \tag{14}$$

$$L_2 = \left\langle \frac{k^2 v_z^3 v_x\Lambda_{xz}}{|v_z|[(kv_z)^2 - (\omega^*)^2]\left[\left(\frac{v_z}{r}\right)^2 - (\omega^*)^2\right]}\right\rangle. \tag{15}$$

It follows from Eq. (12) that the surface scattering of conduction electrons influences the value of the acoustic field in two ways. First, through the electric field, which is determined as the solution of the integral equation (11): the kernel $K(\omega,k,r)$ of the integral equation, according to Eq.

(13), depends on the conditions for scattering of conduction electrons (through the value of the parameter P). Second, by the presence of a δ-function-like surface force,[7,8] due to the second term on the right-hand side of Eq. (12). The integration in (13)–(15) can be done exactly using the expressions for the dispersion relation (6) and deformation potential (8). One obtains the following expressions:

$$K(\omega,k,r)=i\frac{P-1}{\pi^2\delta_a^3}\frac{1}{k^2-r^{-2}} \times\left[\frac{\arcsin(\eta v_0|k|/\omega^*)}{\sqrt{(\omega^*/k\eta v_0)^2-1}}-\frac{\arcsin(\eta v_0/\omega^*|r|)}{\sqrt{(\omega^* r/\eta v_0)^2-1}}\right], \tag{16}$$

$$\sigma(\omega,k)=i\frac{2}{3}\frac{\nu\sigma_0}{\omega^*}\frac{1}{\sqrt{1-(k\eta v_0/\omega^*)^2}},$$

$$\sigma_0=\frac{ne^2}{m\nu},\quad n=\frac{p_0^2}{4\pi^2\hbar^2 a}, \tag{17}$$

$$L_1(\omega,k)=-D\frac{2}{3}\frac{m\nu\sigma_0}{e^2}\left[1-\frac{1}{\sqrt{1-(k\eta v_0/\omega^*)^2}}\right], \tag{18}$$

$$L_2(\omega,k,r)=-D\frac{4}{3}\frac{m\nu\sigma_0}{\pi e^2\eta v_0}\frac{1}{r^{-2}-k^2} \times\left[-\frac{\arcsin\left\{\dfrac{\eta v_0|k|}{\omega^*}\right\}}{\sqrt{(\omega^*/k\eta v_0)^2-1}} +(kr)^2\frac{\arcsin\left\{\dfrac{\eta v_0}{\omega^*|r|}\right\}}{\sqrt{(\omega^* r/\eta v_0)^2-1}}\right], \tag{19}$$

where

$$\delta_a=\left(\frac{3}{2}\frac{\eta v_0}{\omega\mu_0\sigma_0\nu}\right)^{1/3} \tag{20}$$

is the skin depth under conditions of the extremely anomalous skin effect:

$$\eta|\ell^*|\gg\delta_a,\quad \ell^*=\frac{\ell}{1-i\omega\tau},\quad \ell=v_0\tau. \tag{21}$$

Under conditions of the anomalous skin effect (21) the electromagnetic field interacts efficiently with conduction electrons, which ''glide'' in the skin layer. Such electrons feel the surface of the sample only weakly, and the scattering of the conduction electrons is almost specular.[13] Because of this the term due to the surface character of the scattering on the right-hand side of Eq. (11) is a small quantity. This allows one to solve equation (11) by the method of successive approximations, in which the following asymptotic expression must be used for the conductivity $\sigma(\omega,k)$:

$$\sigma(\omega,k)\simeq\frac{2}{3}\frac{\sigma_0}{|k|\eta\ell}. \tag{22}$$

Keeping this in mind, we emphasize that the smallness of the term on the right-hand side of Eq. (11) is unrelated to the value of the specularity parameter P. Nevertheless, because of dispersion relation (6), $1-P\simeq\eta$, i.e., the reflection is almost specular.

The diffuseness of the scattering, as it turns out, give a correction of the same order to the field and to the surface force. Therefore, the electric field must be calculated to second-order accuracy.

The Fourier component of the displacement, u^k, is conveniently represented in the form of a sum of three terms:

$$u^k=u_v^k+(u_v^k)_s+u_s^k. \tag{23}$$

The term

$$u_v^k=-\frac{1}{\pi}\frac{e}{\rho s_t^2}\frac{E'(0)}{q^2-k^2}\frac{L_1(\omega,k)}{k^2+i\omega\mu_0\sigma(\omega,k)} \tag{24}$$

is conditioned by the bulk mechanisms. The term

$$(u_v^k)_s=-\frac{1}{\pi}\frac{e}{\rho s_t^2}\frac{E'(e)}{q^2-k^2}\frac{L_1(\omega,k)}{k^2+i\omega\mu_0\sigma(\omega,k)} \times\int_{-\infty}^{\infty}K(\omega,k,r)\frac{dr}{r^{-2}+i\omega\mu_0\sigma(\omega,r)} \tag{25}$$

describes the influence of the diffuseness of the scattering of conduction electrons on the elastic field via the correction to the electric field E^k due to the diffuseness of the scattering. The last term in Eq. (23)

$$u_s^k=\frac{i}{2\pi^2}e\omega^*\frac{(P-1)}{\rho s_t^2}\frac{E'(0)}{q^2-k^2}\int_{-\infty}^{\infty}L_2(\omega,k,r) \times\frac{dr}{r^{-2}+i\omega\mu_0\sigma(\omega,r)} \tag{26}$$

is due to the surface force arising on account of the diffuseness of the scattering of the conduction electrons.

The acoustic field $u(z)$ is obtained using the inverse Fourier transformation:

$$u(z)=\int_{-\infty}^{\infty}u^k e^{ikz}dk, \tag{27}$$

where u_k is given by formulas (23)–(26). Since the conversion of electromagnetic energy into sound energy is a process involving all the electrons, in calculating the integral (27) we used the exact expressions (16), (18), and (19). According to Eqs. (24)–(26), the integrand in (27) has simple poles which are determined by the zeros of the dispersion relations for coupled electromagnetic and sound waves. To obtain it one needs the second term on the right-hand side of Eq. (2). Owing to the weak coupling between the electromagnetic and sound waves, the wave vector of the sound wave is close to the unperturbed value $q=\omega/s$ and is determined by the equation

$$k^2=q^2+\frac{1}{\rho s^2}\frac{2m^2\nu\sigma_0}{3e^2}D^2\left(1-\frac{1}{\sqrt{1+(k\eta\ell^*)^2}}\right) \times\left[\omega\omega^*-\frac{2}{3}\frac{\nu\sigma_0\mu_0\omega^2}{k^2\sqrt{1+(k\eta\ell^*)^2}+i\eta\ell^*\delta_a^{-3}} \times(\sqrt{1+(k\eta\ell^*)^2}-1)\right]. \tag{28}$$

The OSW damping γ is determined by the imaginary part of the wave vector. It must be taken into account when writing the final form of the OSW amplitude. Besides poles, the integrand of expression (27) has a branch point $k=k_1=\omega^*/\eta v_0$. In the case of a quasi-two-dimensional electron spectrum, when the Fermi surface is a slightly corrugated cylinder open in the direction of propagation of the acoustic field, the branch point is due to a belt on the Fermi surface with the maximum value of the electron velocity $v_z^{\max}$. The branch point determines the ASWs.

Let us investigate the electronic damping of transverse sound. Since it is known[7,8] that the nonuniformity of the electromagnetic field in a sample promotes the conversion of electromagnetic energy into sound energy, the coefficient of electronic absorption will be studied under conditions of the anomalous skin effect (21). For the case of an isotropic dispersion relation of the conduction electrons, the electronic damping coefficient has been studied by many authors. It has been shown[14,15] that the frequency dependence of the electronic damping coefficient of sound, $\gamma(\omega)$, requires a more exact analysis as a function of the mean free path l than the use of the single condition $ql\gg 1$. For this let us analyze the expression for γ, using the spacing between characteristic frequencies of the electron gas and the electrodynamic frequency ω_{em} (the frequency at which the wavelength of the sound is equal to the penetration depth of the electromagnetic field[4]). For the anomalous skin effect (21), we obtain using the asymptotics of the conductivity (22), the following expression for the electromagnetic frequency:

$$\omega_{em}=\frac{s}{\delta_0}\left(\frac{2}{3\eta}\frac{s}{v_0}\right)^{1/2},\quad \delta_0=\frac{c}{\omega_0}, \tag{29}$$

where ω_0 is the plasma frequency. Depending on the mean free path of the conduction electrons, ω_{em} falls into one of the following frequency intervals: if $(\eta v_0/s)^{1/2}\delta_0 \ll \eta\ell \ll \delta_0(\eta v_0/s)^{3/2}$ then $(s/\eta v_0)\nu \ll \omega_{em} \ll \nu$, while if $\eta\ell \gg \delta_0(\eta v_0/s)^{3/2}$, then $\omega_{em}\gg\nu$.

Considering the second term of (28) as a small correction to q^2, we obtain the following frequency dependence for the coefficient of electronic damping of sound:

$$\gamma\equiv \operatorname{Im} k\simeq qD^2\frac{m^2\nu\sigma_0}{3\rho e^2}\times\left\{\frac{1}{\omega t}+\eta q\ell\frac{\omega\tau+1/(\omega\tau)}{[1+(\omega\tau)^2][1+(q\delta_a)^6]}\right\}. \tag{30}$$

With the use of the spacing of the characteristic frequencies, Eq. (30) yields rather simple formulas. If $(\eta v_0/s)^{3/2}\delta_0 \gg \eta\ell \gg \delta_0(\eta v_0/s)^{1/2}$, then

$$\gamma_1\simeq \eta D^2\frac{m^2\omega_0^2 v_0}{3\rho e^2 s^2}\omega,\quad \omega\ll\omega_{em}; \tag{31}$$

$$\gamma_2\simeq\frac{4}{3\eta}D^2\frac{m^2\omega_0^6 s^4}{\rho e^2 c_0^4 v_0}\frac{1}{\omega^3},$$

$$\omega_{em}\ll\omega\ll\omega_{em}\left(\eta\frac{s}{v_0}\frac{\ell^2}{\delta_0^2}\right)^{1/6};$$

$$\gamma_3\simeq D^2\frac{m^2\omega_0^2\nu}{3\rho e^2 s},\quad \omega\gg\omega_{em}\left(\eta\frac{s}{v_0}\frac{\ell^2}{\delta_0^2}\right)^{1/6}.$$

Here the frequency ω can be lower or higher than the collision frequency ν. The first two formulas in (31) describe the collisionless Landau absorption: the coefficient of electronic damping of sound first grows linearly with increasing frequency, reaches a maximum at $\omega=\omega_{em}$, and then falls off by an ω^{-3} law. For higher frequencies $\gamma\sim\nu$. If $\eta l \gg \delta_0(\eta v_0/s)^{3/2}$ the frequency part on which $\gamma\sim\nu$ is shifted to higher frequencies. However, in this case it is necessary to take other mechanisms besides the strain mechanism into account. Such a frequency dependence also takes place in the case of an isotropic dispersion relation for the conduction electrons.[14,15] The difference is that in the case of the quasi-two-dimensional dispersion relation under conditions of collisionless Landau damping, γ is a function of the corrugation parameter η.

Let us determine the amplitude of OSWs. For this we calculate the contribution of the poles of the integrand in (27). Using (24)–(26) and also the coefficient of electronic damping of sound (31), we obtain the following result for the contribution to the sound amplitude from the purely bulk mechanisms of conversion of electromagnetic energy into sound energy:

$$u_v^{USW}\simeq D\frac{m\eta v_0 E'(0)}{e\rho\mu_0 s^2\omega}e^{i\omega z/s}e^{-\gamma_1 z},$$

$$\omega\ll\omega_{em}; \tag{32}$$

$$u_v^{USW}\simeq D\frac{m\eta v_0 E'(0)}{e\rho\mu_0 s^2\omega}e^{i\omega z/s}e^{-\gamma_2 z}(q\delta_a)^{-3},$$

$$\omega_{em}\ll\omega\ll\omega_{em}\left(\eta\frac{s}{v_0}\frac{\ell^2}{\delta_0^2}\right)^{1/6};$$

$$u_v^{USW}\simeq D\frac{m\eta v_0 E'(0)}{e\rho\mu_0 s^2\omega}e^{i\omega z/s}e^{-\gamma_3 z}(q\delta_a)^{-3},$$

$$\omega\gg\omega_{em}\left(\eta\frac{s}{v_0}\frac{\ell^2}{\delta_0^2}\right)^{1/6}.$$

Substituting the Fourier components (25) and (26) into the integrand of (27), we obtain the contribution to the sound amplitude due to the diffuseness of the scattering of conduction electrons from the surface of the sample. We obtain

$$u_s^{USW}\simeq D\frac{m\eta v_0 E'(0)}{e\rho\mu_0 s^2\omega}\frac{P-1}{\pi^2}e^{i\omega z/s}\ln\left(\frac{\delta_a}{\eta\ell^*}\right)\times\ln(q\delta_a)e^{-\gamma_1 z},\quad \omega\ll\omega_{em};$$

$$u_s^{USW}\simeq D\frac{m\eta v_0 E'(0)}{e\rho\mu_0 s^2\omega}\frac{P-1}{\pi^2}e^{i\omega z/s}e^{-\gamma_2 z}(q\eta\ell^*)^{-1},$$

$$\omega_{em}\ll\omega\ll\omega_{em}\left(\eta\frac{s}{v_0}\frac{\ell^2}{\delta_0^2}\right)^{1/6};$$

$$u_s^{USW}\simeq D\frac{m\eta v_0 E'(0)}{e\rho\mu_0 s^2\omega}\frac{P-1}{\pi^2}e^{i\omega z/s}e^{-\gamma_3 z}(q\eta\ell^*)^{-1},$$

$$\omega \gg \omega_{em}\left(\eta\frac{s}{v_0}\frac{\ell^2}{\delta_0^2}\right)^{1/6}. \tag{33}$$

For $\omega \ll \omega_{em}$ the contribution of the purely bulk mechanism, by virtue of the relation $1-P \simeq \eta$, exceeds the contribution from mechanisms due to the surface scattering of conduction electrons. At higher frequencies, when $\omega \gg \omega_{em}$, because of the strong nonuniformity of the field, the parameter $(q\delta_a)^3/(q|l^*|) \gg 1$ can become much greater than unity. In this case the conversion of electromagnetic energy into sound energy on account of diffuse scattering mechanisms exceeds the contribution from purely bulk mechanisms. Under the given conditions such behavior also occurs for an isotropic dispersion relation of the conduction electrons.[8] We note that in the case of an isotropic dispersion relation, the two effects are of the same order for $\omega \ll \omega_{em}$. The asymptotic behavior of the OSWs at large distances from the surface of the sample is governed by an exponentially decaying function. At low temperatures and for pure samples the main damping mechanism is the electronic one. The other mechanisms can be taken into account phenomenologically.

The amplitude of the ASWs is determined by the integrals along the two banks of the branch cut, from the branch point $k_1 = \omega^*/\eta v_0$ to infinity. Performing the necessary manipulations, we obtain the following asymptotic expression for the amplitude of the displacement of the ASWs due to purely bulk mechanisms at large distances from the surface of the sample:

$$u_v^{ASW}(z) \simeq \sqrt{\frac{2}{\pi}} D \frac{m v_0 \eta E'(0)}{e\rho\mu_0 s^2 \omega} \frac{1}{(q\eta\ell^*)^{1/2}} \times \frac{1}{(qz)^{3/2}} e^{-z/\eta\ell} e^{i\omega z/\eta v_0}. \tag{34}$$

The corresponding contribution to the asymptotics of the displacement, because of the diffuse character of the scattering of conduction electrons, is determined by the expression

$$u_s^{ASW}(z) \simeq \frac{2\sqrt{2}}{\pi^2\sqrt{\pi}} D \frac{m v_0 \eta E'(0)}{e\rho\mu_0 s^2 \omega} \frac{P-1}{(q\eta\ell^*)^{1/2}} \times \frac{\ln^2(\delta_a/\eta\ell^*)}{(qz)^{3/2}} e^{-z/\eta\ell} e^{i\omega z/\eta v_0}. \tag{35}$$

Expressions (34) and (35) were obtained under conditions where inequality (21) holds. At distances z satisfying the inequality $|\eta l^*| \geqslant z \gg 1/\gamma$, where $1/\gamma$ is the OSW damping length and ηl is the mean free path of the conduction electrons in the direction of propagation of the sound wave, the asymptotics of the acoustic field is determined by the asymptotics of the ASWs, i.e., formulas (34) and (35). This asymptotics is a power-law function $z^{-3/2}$, i.e., the acoustic field falls off nonexponentially at large distances from the surface of the sample. We recall that in the case of an isotropic dispersion relation the asymptotics is determined by a power-law function z^{-2}, i.e., the damping is faster.

Let us briefly list the main results. The general theory of direct electromagnetic excitation of transverse sound, proposed in Refs. 7 and 8 for the case of an isotropic dispersion relation of the conduction electrons, finds confirmation in the case of a quasi-two-dimensional electron energy spectrum, as one may be convinced. The conversion of electromagnetic energy into sound energy is a process in which all the electrons participate, and the efficiency of the strain mechanism increases with increasing nonuniformity of the electromagnetic field in the sample. Therefore the frequency dependence and the influence of the surface on the conversion effect are the same as in the case of an isotropic dispersion relation of the conduction electrons. However, owing to the quasi-two-dimensionality of the electron energy spectrum, which is specified by the corrugation parameter η, the electrons almost glide toward the surface of the sample, and therefore over a mean free path l they traverse a slightly nonuniform field. Because of this the results obtained here for the displacement field of an OSW when $\omega \ll \omega_{em}$ are smaller by a factor of η in relation to the corresponding results in the case of an isotropic dispersion relation. At high frequencies, for $\omega \gg \omega_{em}$, the results are independent of η and agree in order of magnitude with the corresponding expressions for an isotropic dispersion relation.

At large distances from the surface, such that $|\eta l^*| \geqslant z \gg 1/\gamma$, the acoustic field at $\omega\tau \gg 1$ falls off nonexponentially, by a $z^{-3/2}$ law, and is determined by the amplitude of the ASW. We recall that in the case of an isotropic dispersion relation the field of the ASW decays by a z^{-2} law.[5,6] The contribution to the amplitude of the ASW from bulk mechanisms exceeds the contribution from the surface mechanisms by a factor of $1/\eta$. In the case of the OSW, under conditions of the anomalous skin effect and $\omega \gg \omega_{em}$ the surface mechanisms of conversion can become the governing mechanisms. For this it is necessary that the electron mean free paths satisfy the condition $l \gg \delta_0(v_0/s)^{1/2}$.

In electronics, in connection with the existing interest in quasi-two-dimensional conductors, we emphasize once again the importance of studying the contactless electromagnetic conversion of sound in such media. The method permits excitation of high-frequency sound, which cannot be done using contact methods. It can be used for nondestructive quality control. This is especially important for studying the surface quality, since the conversion effect is sensitive to roughness of the sample surface. Finally, the influence of the spectrum on the sound characteristics allows one to draw conclusions about the parameters of the spectrum and also about the electron–phonon coupling.

We wish to thank V. G. Peschansky and O. V. Kirichenko for helpful discussions.

*E-mail: gorgiiv@iunona.pmf.ukim.edu.mk

[1)] Although, strictly speaking, the expression for the deformation potential (8) does not agree completely with the dispersion relation adopted for the conduction electrons, this model can nevertheless be used to obtain qualitative results.

[1] V. M. Kontorovich, Zh. Éksp. Teor. Fiz. **45**, 1638 (1963) [Sov. Phys. JETP **18**, 1125 (1964)].
[2] V. M. Kontorovich, Zh. Éksp. Teor. Fiz. **59**, 2116 (1970) [Sov. Phys. JETP **32**, 1146 (1971)].
[3] A. N. Vasil'ev and Yu. P. Gaĭdukov, Usp. Fiz. Nauk **141**, 431 (1983) [Sov. Phys. Usp. **26**, 952 (1983)].
[4] M. I. Kaganov and V. B. Fiks, Zh. Éksp. Teor. Fiz. **62**, 1461 (1972) [Sov. Phys. JETP **35**, 767 (1972)].
[5] G. Ivanovski and M. I. Kaganov, Zh. Éksp. Teor. Fiz. **83**, 2320 (1982) [Sov. Phys. JETP **56**, 1345 (1982)].

[6] G. Ivanovski and O. Galbova, Phys. Status Solidi B **134**, 815 (1986).
[7] G. Ivanovski, M. I. Kaganov, and V. B. Fiks, Fiz. Tverd. Tela (Leningrad) **15**, 1441 (1973) [Sov. Phys. Solid State **15**, 972 (1973)].
[8] G. Ivanovski and M. I. Kaganov, Fiz. Tverd. Tela (Leningrad) **18**, 2704 (1976) [Sov. Phys. Solid State **18**, 1576 (1976)].
[9] V. M. Gohfeld and V. G. Peschansky, "Nonlocal acoustoelectronic effects in metals and layered conductors," in *Soviet Science Reviews, Section A. Physics*, I. M. Khalatnikov (Ed.), Harwood Academic Publishers, Switzerland–USA (1993).
[10] J. Singelton, Rep. Prog. Phys., 116 (2000).
[11] K. Fuchs, Cambridge Philos. Soc. **1**, 100 (1938).
[12] B. Abeles, Phys. Rev. Lett. **19**, 1181 (1967).
[13] G. E. H. Reuter and E. H. Sondheimer, Proc. R. Soc. London, Ser. A **195**, 336 (1948).
[14] G. Ivanovski and M. I. Kaganov, Fiz. Tverd. Tela (Leningrad) **15**, 3304 (1973) [Sov. Phys. Solid State **15**, 2201 (1973)].
[15] G. Ivanovski, Phys. Status Solidi B **72**, K53 (1975).

Translated by Steve Torstveit

Phonons in conductors with magnetoimpurity electron states

A. M. Ermolaev* and G. I. Rashba

V. N. Karazin Kharkov National University, pl. Svobody 4, 51077 Kharkov, Ukraine
(Submitted April 15, 2003)
Fiz. Nizk. Temp. **29**, 1244–1255 (November 2003)

A study is made of the changes in on the phonon spectrum and damping in a conductor in a quantizing magnetic field under the joint influence of quasilocal vibrations of impurity atoms in the lattice and magnetoimpurity electron states at those atoms. A system of equations for the electron and ion Green's function is obtained on the basis an electron–ion model of a nonideal conductor in a magnetic field with the quasilocal vibrations and the magnetoimpurity states taken into account. At a low concentration of impurity atoms the magnetoimpurity states give resonance contributions to the polarization operator. They have a substantial influence on the phonon spectrum and damping. The magnetoimpurity states cause a crossover splitting of the phonon dispersion curves and give rise to new branches in the spectrum of elastic vibrations. © *2003 American Institute of Physics.* [DOI: 10.1063/1.1614230]

INTRODUCTION

The description of the dynamic properties of conductors is based on separation of the electron and ion subsystems and taking the coupling of these subsystems into account. After separation of the problem, the low-temperature properties of conducting systems are treated using the Frohlich model[1] and the adiabatic approximation.[2] However, it is well known that both of those methods have some drawbacks. In particular, the use of the Frohlich Hamiltonian does not permit a correct investigation of the ion subsystem. In turn, the adiabatic approximation is poorly suited for studying the electron subsystem, although the dynamics of the ions may be studied to high accuracy in that approach. Another drawback of the adiabatic approximation is the absence of a convenient diagram technique for calculating the nonadiabatic corrections to the observable quantities. It can be stated that a consistent microscopic theory of the electron–ion interaction in degenerate conductors is far from completion, although attempts to create such a theory have been undertaken for a long time now. The situation is more complicated in real conductors, which contain impurities and other lattice defects,[3–8] and in organic conductors.[9]

The problem of the influence of impurity atoms on the properties of crystals was raised to a higher level in the famous series of papers by I. M. Lifshits on the theory of vibrations of nonideal crystal lattices, which were written in the 1940s.[3] In them he stated and solved the problem of the influence of impurity atoms on the phonon spectrum, predicted local vibrations of a nonideal lattice, and developed a method of calculating the physical composition of systems perturbed by impurity atoms. Before long that theory had been used to study impurity states of other quasiparticles—electrons and magnons.[10]

Ordinarily impurity states of phonons and electrons are studied separately. This can be done if the energy of an electron on a quasilocal level is substantially different from the frequency of quasilocal vibrations of the lattice. Under certain conditions, however, these quantities can become comparable.[11] The effects of the coupling of a quasilocal electron with the optimum degrees of freedom of an impurity ion have been studied since long ago. It has been shown[12] that the electron–phonon coupling has a substantial influence on the shape of the curve of the cross section for scattering of an electron on an impurity atom as a function of the electron energy. This is related to the electron mobility in an impure conductor. The problem of the scattering of an electron or hole on a resonant impurity center in the presence of electron–phonon coupling was considered in Ref. 13. The influence of this coupling on the scattering cross section for electrons on an impurity atom was found. The electron–phonon coupling in impure conductors was studied in Ref. 14. Using the Keldysh diagram technique, the authors of that paper obtained the collision integrals describing the relaxation of electrons and phonons in impure normal metals and superconductors.

The electron–phonon coupling in metals in a quantizing magnetic field was considered in Ref. 15, where the features of the phonon spectrum and damping due to the Landau quantization were investigated on the basis of the Frohlich model. Nonadiabatic effects in the phonon spectrum of pure conductors in a magnetic field were considered in Ref. 16 with allowance for Fermi-liquid effects. As a natural continuation of the studies on this topic, impurity states of electrons in a magnetic field were studied in Refs. 17 and 18.

The problem of impurity states of electrons in a magnetic field **H** has the peculiarity that an impurity that attracts electrons can localize a particle in a three-dimensional sample only in the case when the uncertainty of the energy of the particle in the impurity potential well does not exceed the well depth:[19]

$$\frac{1}{mr_0^2} < U_0, \tag{1}$$

where m is the mass of the electron and r_0 and U_0 are the radius and depth of the well. Here and below the quantum constant is taken equal to unity. If condition (1) does not hold, then the states do not form, and only potential scattering of the electron by the impurity atoms occurs, accompa-

nied by a slight phase shift in its wave function. In the presence of a magnetic field the situation changes. The motion of an electron in a magnetic field is similar to one-dimensional, and in the one-dimensional case a potential well of arbitrarily small intensity can localize a particle.[19] In a magnetic field field impurity states exist even in the case when inequality (1) does not hold. An attractive impurity, by partially lifting the degeneracy of the electron energy levels with respect to the position of the center of the Larmor ''orbits,'' splits sublevels off from each Landau level. The sublevels that are split off from the ground Landau level go into the forbidden energy region and are local. The sublevels split off from the higher Landau subbands hybridize with the states of the continuous spectrum and remain quasilocal. These states are due to the joint influence of the attractive impurities and magnetic field on the electrons, and they are therefore called magnetoimpurity states.[17,18,20] It was shown in Refs. 20 and 21 that magnetoimpurity states make it possible for new types of collective excitations, called magnetoimpurity waves,[20] to propagate in conductors.

As we have said, the quasilocal states of the phonons and electrons are considered separately. Meanwhile, an impurity atom can be a source of both quasilocal lattice vibrations and quasilocal electron states. The joint study of the impurity states of electrons and phonons is a topical problem in solid-state physics. Here we consider the effects on the phonon spectrum and damping in degenerate conductors due to the combined influence of the quasilocal lattice vibrations with heavy impurity atoms and the magnetoimpurity electron states. In Sec. 1 we describe the model used—an electron–ion model of a nonideal metal in a quantizing magnetic field. Section 2 is devoted to the derivation of the main equations of the theory by the temperature Green's function method. In Sec. 3 we consider the influence of the magnetoimpurity electron states on the phonon polarization operator. The phonon spectrum and damping in conductors with quasilocal lattice vibrations and magnetoimpurity electron states are considered in Sec. 4.

1. MODEL

We consider a system of conduction electrons in a simple crystal lattice of ions. We write the radius vector of an ion in the form $\mathbf{r}_n=\mathbf{r}_n^0+\mathbf{u}_n$, where $\mathbf{r}_n^0$ is the equilibrium position of the ion and $\mathbf{u}_n$ is the displacement vector. At some sites there are impurity ions. We introduce the occupation numbers of the sites:

$$c_n=\begin{cases}1, & \text{site } n \text{ impurity},\\ 0, & \text{site } n \text{ host}\end{cases}$$

The mass of the ion at the nth site will be given by

$$M_n=M_0+(M_1-M_0)c_n,$$

where M_0 is the mass of a host ion and M_1 is the mass of an impurity ion.

The Hamiltonian of the ion subsystem in the harmonic approximation is[5,6]

$$\frac{1}{2M_0}\sum_{n\nu}(\hat{p}_n^{\nu})^2+\frac{1}{2}\sum_{nn'\nu\nu'}\Phi_{nn'}^{\nu\nu'}\hat{u}_n^{\nu}\hat{u}_{n'}^{\nu'}+\frac{1}{2}\left(\frac{1}{M_1}-\frac{1}{M_0}\right)\sum_{n\nu}c_n(\hat{p}_n^{\nu})^2, \tag{2}$$

where

$$\hat{p}_n^{\nu}=M_n\hat{u}_n^{\nu}$$

is the momentum operator of the ion at site n, $\Phi_{nn'}^{\nu\nu'}$ is the dynamic matrix, and $\hat{u}_n^{\nu}$ is the operator of Cartesian components of the displacement vector $\mathbf{u}_n$ of the ion at site n ($\nu=x,y,z$). The first two terms on the right-hand side of Eq. (2) represent the Hamiltonian of the ideal lattice, and the third term is the part due to the impurity perturbation. We assume that the impurities do not perturb the dynamic matrix Φ (the isotopic approximation for the vibrational spectrum) but do scatter electrons. It should be noted that in the case of a large difference between masses M_0 and M_1 that approximation is rather accurate. That is because a local adjustment of the properties of the lattice occurs near an impurity ion, substantially reducing the relative change in the force constants, especially in the presence of conduction electrons.[6]

The Hamiltonian of an electron in the field of the ions and in a magnetic field has the form

$$\hat{h}=\frac{1}{2m_0}\left(-i\nabla-\frac{e}{c}\mathbf{A}\right)^2+\sum_n u_n(\mathbf{r}-\mathbf{r}_n)-\hat{\boldsymbol{\mu}}\mathbf{H},$$

where m_0 and e are the mass and charge of a free electron, $\hat{\boldsymbol{\mu}}$ is the spin magnetic moment operator, $\mathbf{A}=(0,Hx,0)$ is the vector potential in the Landau gauge, $u_n(|\mathbf{r}-\mathbf{r}_n|)$ is the potential energy of the electron in the field of the nth ion, and c is the speed of light. We assume that the ions execute small vibrations about the equilibrium positions and we keep in the expansion of $u_n(\mathbf{r}-\mathbf{r}_n)$ only the terms linear in the displacements $\mathbf{u}_n$. Then the electron Hamiltonian becomes

$$\hat{h}=\frac{1}{2m_0}\left(-i\nabla-\frac{e}{c}\mathbf{A}\right)^2+\sum_n u_0(\mathbf{r}-\mathbf{r}_n^0)+\sum_n c_n[u_1(\mathbf{r}-\mathbf{r}_n^0)-u_0(\mathbf{r}-\mathbf{r}_n^0)]+\sum_n \hat{\mathbf{u}}_n\mathbf{a}_n(\mathbf{r}-\mathbf{r}_n^0)-\hat{\mu}\mathbf{H}, \tag{3}$$

where

$$a_n^{\nu}(\mathbf{r}-\mathbf{r}_n^0)=-\frac{\partial}{\partial x_{\nu}}u_n(\mathbf{r}-\mathbf{r}_n^0),$$

and u_0 and u_1 are the energies of interaction of an electron with a host or impurity ion, respectively. The second term in formula (3) is the energy of interaction of an electron with the ideal lattice. Thus the first two terms in Hamiltonian (3) correspond to the problem of a Bloch electron in a magnetic field. Using the effective-mass approximation, we replace m_0 by the effective mass m of an electron in the lattice. The third term in formula (3) is the impurity potential, which scatters electrons. The fourth term in (3) describes the inter-

action of the electron with vibrations of the ions. We write the Hamiltonian of the electrons and ions in second-quantized form as

$$\hat{\mathcal{H}}=\hat{\mathcal{H}}_0+\hat{V},$$

where

$$\hat{\mathcal{H}}_0=\frac{1}{2M_0}\sum_{n\nu}(\hat{p}_n^{\nu})^2+\frac{1}{2}\sum_{n\nu n'\nu'}\Phi_{nn'}^{\nu\nu'}\hat{u}_n^{\nu}\hat{u}_{u'}^{\nu'}+\sum_{\kappa\sigma}\xi_{\kappa\sigma}\hat{a}_{\kappa\sigma}^{+}\hat{a}_{\kappa\sigma}$$

is the part that is unperturbed by the impurity atoms, and

$$\hat{V}=\frac{1}{2}\left(\frac{1}{M_1}-\frac{1}{M_0}\right)\sum_{n\nu}c_n(\hat{p}_n^{\nu})^2+\sum_{\mathbf{q}n}\mathrm{e}^{-i\mathbf{q}\mathbf{r}_n^0}\sum_{\kappa\kappa'\sigma}I_{\kappa'\kappa}(\mathbf{q})\hat{a}_{\kappa'\sigma}^{+}\hat{a}_{\kappa\sigma}\times[\Delta u(\mathbf{q})c_n-i(\mathbf{q}\hat{\mathbf{u}}_n)u_n(\mathbf{q})]$$

is the interaction Hamiltonian. Here $\kappa=(n,k_y,k_z)$ are the Landau quantum numbers, σ is the spin quantum number, $\xi_{\kappa\sigma}=\varepsilon_{\kappa\sigma}-\mu$ is the energy of an electron measured from the chemical potential μ, $\varepsilon_{\kappa\sigma}$ is the Landau spectrum, $\hat{a}_{\kappa\sigma}$ and $\hat{a}_{\kappa\sigma}^{+}$ are the annihilation and creation operators for electrons in states $|\kappa\sigma\rangle$, $u_n(\mathbf{q})$ is a Fourier component of the potential, $\Delta u=u_1-u_0$, and $I_{\kappa'\kappa}(\mathbf{q})=\langle\kappa'|\mathrm{e}^{i\mathbf{q}\cdot\mathbf{r}}|\kappa\rangle$ are the matrix elements of a plane wave in the Landau basis. Here and below the volume of the system will be taken equal to unity. In these formulas we have used the second-quantized representation for the electrons, while the Hamiltonian of the ion subsystem is written in first-quantized form.

2. BASIC EQUATIONS

To derive the equations describing the dynamic properties of an electron–impurity conductor, we use the temperature Green's function technique.[22] For this purpose we introduce the electron and ion Green's functions

$$G_{\sigma\sigma'}(\kappa\tau,\kappa'\tau')=-\langle T_\tau\{\hat{a}_{\kappa\sigma}(\tau)\hat{\bar{a}}_{\kappa'\sigma'}(\tau')\}\rangle, \tag{4}$$

$$D_{nn'}^{\nu\nu'}(\tau,\tau')=-\langle T_\tau\{\hat{u}_n^{\nu}(\tau)\hat{u}_{n'}^{\nu'}(\tau')\}\rangle, \tag{5}$$

where $\hat{u}_n^{\nu}(\tau)$, $\hat{a}_{\kappa\sigma}(\tau)$, and $\hat{\bar{a}}_{\kappa\sigma}(\tau)$ are the Matsubara operators for the ion displacement and electron annihilation and creation, τ is the Matsubara "time" ($0\leqslant\tau\leqslant\beta$, where β is the inverse temperature), T_τ is the symbol for chronological ordering of the operators, and the angle brackets denote averaging over a Gibbs canonical ensemble.

The equation of motion for the electron Green's function (4) has the form

$$\left(-\frac{\partial}{\partial\tau}-\xi_{\kappa\sigma}\right)G_{\sigma\sigma'}(\kappa\tau,\kappa'\tau')=\delta_{\kappa\kappa'}\delta_{\sigma\sigma'}\delta(\tau-\tau')+\sum_{\mathbf{q}n\kappa_1}\mathrm{e}^{-i\mathbf{q}\mathbf{r}_n^0}I_{\kappa\kappa_1}(\mathbf{q})\Delta u(\mathbf{q})c_nG_{\sigma\sigma'}(\kappa_1\tau,\kappa'\tau')+i\sum_{\mathbf{q}n\nu\kappa_1}\mathrm{e}^{-i\mathbf{q}\mathbf{r}_n^0}I_{\kappa\kappa_1}(\mathbf{q})q^{\nu}u_n(\mathbf{q})\times\langle T_\tau\{\hat{a}_{\kappa_1\sigma}(\tau)\hat{\bar{a}}_{\kappa'\sigma'}(\tau')\hat{u}_n^{\nu}(\tau)\}\rangle. \tag{6}$$

The analogous equation for the ion Green's function is

$$-\frac{\partial^2}{\partial\tau^2}D_{nn'}^{\nu\nu'}(\tau,\tau')=-\frac{1}{M_n}\delta_{nn'}\delta_{\nu\nu'}\delta(\tau-\tau')-\frac{1}{M_n}\sum_{n_1\nu_1}\Phi_{nn_1}^{\nu\nu_1}D_{n_1n'}^{\nu_1\nu'}(\tau,\tau')-\frac{i}{M_n}\sum_{\mathbf{q}}q^{\nu}u_n(\mathbf{q})\mathrm{e}^{-i\mathbf{q}\mathbf{r}_n^0}\sum_{\kappa\kappa'\sigma}l_{\kappa'\kappa}(\mathbf{q})\times\langle T_\tau\{\hat{\bar{a}}_{\kappa'\sigma}(\tau)\hat{a}_{\kappa\sigma}(\tau)\hat{u}_{n'}^{\nu'}(\tau')\}\rangle. \tag{7}$$

The function D is related to the Green's function D_0 of the ideal lattice by Dyson's equation[22,23]

$$D_{nn'}^{\nu\nu'}(\tau,\tau')=\overset{0}{D}{}_{nn'}^{\nu\nu'}(\tau,\tau')+\sum_{n_1\nu_1}\int_0^{\beta}d\tau_1\sum_{n_2\nu_2}\int_0^{\beta}d\tau_2\times\overset{0}{D}{}_{nn_1}^{\nu\nu_1}(\tau,\tau_1)\Pi_{n_1n_2}^{\nu_1\nu_2}(\tau_1,\tau_2)D_{n_2n'}^{\nu_2\nu'}(\tau_2,\tau'), \tag{8}$$

where Π is the polarization operator.

The right-hand sides of equations (6) and (7) contain the mixed Green's function

$$P_{\sigma\sigma'}^{\nu_1}(\kappa\tau,\kappa'\tau',n_1\tau_1)=\langle T_\tau\{\hat{a}_{\kappa\sigma}(\tau)\hat{\bar{a}}_{\kappa'\sigma'}(\tau')\hat{u}_{n_1}^{\nu_1}(\tau_1)\}\rangle.$$

It is related to the vertex function Γ as

$$P_{\sigma\sigma'}^{\nu_1}(\kappa\tau,\kappa'\tau',n_1\tau_1)=\sum_{\kappa_1'\sigma_1'}\int_0^{\beta}d\tau_1'\sum_{\kappa_2'\sigma_2'}\int_0^{\beta}d\tau_2'\sum_{n_3'\nu_3'}\int_0^{\beta}d\tau_3'\times G_{\sigma\sigma_1'}(\kappa\tau,\kappa_1'\tau_1')\Gamma_{\sigma_1'\sigma_2'}^{\nu_3'}(\kappa_1'\tau_1',\kappa_2'\tau_2',n_3'\tau_3')\times G_{\sigma_2'\sigma'}(\kappa_2'\tau_2',\kappa'\tau')D_{n_3'n_1}^{\nu_3'\nu_1}(\tau_3',\tau_1).$$

After a Fourier transformation with respect to τ, we can write Eq. (8) in the form

$$D_{nn'}^{\nu\nu'}(\omega_m)=\overset{0}{D}{}_{nn'}^{\nu\nu'}(\omega_m)+\sum_{\substack{n_1\nu_1\\ n_2\nu_2}}\overset{0}{D}{}_{nn_1}^{\nu\nu_1}(\omega_m)\times\Pi_{n_1n_2}^{\nu_1\nu_2}(\omega_m)D_{n_2n'}^{\nu_2\nu'}(\omega_m), \tag{9}$$

where ω_m are the even Matsubara frequencies. The Fourier component of the polarization operator is

$$\Pi^{\nu_1\nu_2}_{n_1n_2}(\omega_m)=(M_1-M_0)c_{n_1}\omega_m^2\delta_{n_1n_2}\delta_{\nu_1\nu_2}$$
$$-i\sum_{\mathbf{q}} q^{\nu_1}u_{n_1}(\mathbf{q})\mathrm{e}^{-i\mathbf{q}\mathbf{r}^0_{n_1}}\sum_{\kappa\kappa'\sigma} I_{\kappa'\kappa}(\mathbf{q})$$
$$\times\sum_{\kappa_1'\sigma_1'}\sum_{\kappa_2'\sigma_2'}\frac{1}{\beta}\sum_s G_{\sigma\sigma_1'}(\kappa\kappa_1',\zeta_s)$$
$$\times\Gamma^{\nu_2}_{\sigma_1'\sigma_2'}(\kappa_1'\kappa_2'n_2;\zeta_s,\zeta_s-\omega_m)$$
$$\times G_{\sigma_2'\sigma}(\kappa_2'\kappa',\zeta_s-\omega_m), \qquad (10)$$

where ζ_s are the odd Matsubara frequencies.

Doing the Fourier transform with respect to τ in (6), we obtain

$$(i\zeta_s-\xi_{\kappa\sigma})G_{\sigma\sigma'}(\kappa\kappa',\zeta_s)$$
$$=\delta_{\kappa\kappa'}\delta_{\sigma\sigma'}+\sum_{\mathbf{q}n\kappa_1}\mathrm{e}^{-i\mathbf{q}\mathbf{r}^0_n}I_{\kappa\kappa_1}(\mathbf{q})\Delta u(\mathbf{q})c_n$$
$$\times G_{\sigma\sigma'}(\kappa_1\kappa',\zeta_s)+i\sum_{\mathbf{q}n\nu\kappa_1}\mathrm{e}^{-i\mathbf{q}\mathbf{r}^0_n}I_{\kappa\kappa_1}(\mathbf{q})q^{\nu}u_n(\mathbf{q})$$
$$\times\sum_{\sigma_1'\kappa_1'}\sum_{\sigma_2'\kappa_2'}\sum_{\nu_3'n_3'}\frac{1}{\beta}\sum_{m=-\infty}^{\infty}G_{\sigma\sigma_1'}(\kappa_1\kappa_1',\zeta_s+\omega_m)$$
$$\times\Gamma^{\nu_3'}_{\sigma_1'\sigma_2'}(\kappa_1'\kappa_2'n_3';\zeta_s+\omega_m,\zeta_s)$$
$$\times G_{\sigma_2'\sigma'}(\kappa_2'\kappa',\zeta_s)D^{\nu_3'\nu}_{n_3'n}(\omega_m). \qquad (11)$$

This equation can be written in the form

$$G_{\sigma\sigma'}(\kappa\kappa',\zeta_s)=G^0_{\sigma}(\kappa,\zeta_s)\delta_{\kappa\kappa'}\delta_{\sigma\sigma'}$$
$$+G^0_{\sigma}(\kappa,\zeta_s)\sum_{\kappa_1\sigma_1}\Sigma_{\sigma\sigma_1}(\kappa\kappa_1,\zeta_s)$$
$$\times G_{\sigma_1\sigma'}(\kappa_1\kappa',\zeta_s), \qquad (12)$$

where $G^0_{\sigma}(\kappa,\zeta_s)$ is the Fourier component of the single-particle Green's function of an ideal electron gas, and

$$\Sigma_{\sigma_1\sigma_2}(\kappa_1\kappa_2,\zeta_s)$$
$$=\sum_{\mathbf{q}}\Delta u(\mathbf{q})\sum_n c_n\mathrm{e}^{-i\mathbf{q}\mathbf{r}^0_n}I_{\kappa_1\kappa_2}(\mathbf{q})\delta_{\sigma_1\sigma_2}$$
$$+i\sum_{\mathbf{q}n\nu\kappa}q^{\nu}\mathrm{e}^{-i\mathbf{q}\mathbf{r}^0_n}I_{\kappa_1\kappa}(\mathbf{q})u_n(\mathbf{q})$$
$$\times\sum_{\sigma_1'\kappa_1'}\sum_{n_2'\nu_2'}\frac{1}{\beta}\sum_{m=-\infty}^{\infty}G_{\sigma_1\sigma_1'}(\kappa\kappa_1',\zeta_\sigma+\omega_m)$$
$$\times\Gamma^{\nu_2'}_{\sigma_1'\sigma_2'}(\kappa_1'\kappa_2'n_2';\zeta_s+\omega_m,\zeta_s)D^{\nu_2'\nu}_{n_2'n}(\omega_m) \qquad (13)$$

is the self-energy function. Using the electron–ion model of a nonideal conductor in a magnetic field, we obtain an exact system of equations (9), (10), (12), and (13) for the electron and ion Green's functions. In this model, as in Ref. 16, the phonons are not introduced *a priori* but are obtained as a result of solution of the dispersion relation. The main difficulty in solving these equations is to calculate the vertex function Γ. It appears not only in the expression for the self-energy part (13) of the electron Green's function but also in the exact ion polarization operator (10).

3. CONTRIBUTION OF THE MAGNETOIMPURITY STATES TO THE POLARIZATION OPERATOR

In this paper we ignore the Coulomb interaction of the electrons. In addition, following Ref. 1, we replace the total vertex function by a simple one. It has the form

$$\overset{0}{\Gamma}{}^{\nu_2}_{\sigma_1\sigma_2}(\kappa_1\kappa_2n_2;\zeta_s,\zeta_s-\omega_m)$$
$$=\delta_{\sigma_1\sigma_2}\int d\mathbf{r}_1\varphi^*_{\kappa_1}(\mathbf{r}_1)\varphi_{\kappa_2}(\mathbf{r}_1)a^{\nu_2}_{n_2}(\mathbf{r}_1-\mathbf{r}^0_{n_2})$$
$$=-i\delta_{\sigma_1\sigma_2}\sum_{\mathbf{q}} q^{\nu_2}u_{n_2}(\mathbf{q})I_{\kappa_1\kappa_2}(\mathbf{q})\mathrm{e}^{-i\mathbf{q}\mathbf{r}^0_{n_2}}. \qquad (14)$$

where $\varphi_{\kappa}(\mathbf{r})$ is the orbital wave function of the electron in a magnetic field. Substituting the simple vertex (14) into (10), we obtain the temperature polarization operator of the ions in the isotopic approximation:

$$\Pi^{\nu_1\nu_2}_{n_1n_2}(\omega_m)=(M_1-M_0)c_{n_1}\omega_m^2\delta_{n_1n_2}\delta_{\nu_1\nu_2}$$
$$+\sum_{\mathbf{q}_1\mathbf{q}_2}q_1^{\nu_1}q_2^{\nu_2}u^*_{n_1}(\mathbf{q}_1)u_{n_2}(\mathbf{q}_2)\mathrm{e}^{i(\mathbf{q}_1\mathbf{r}^0_{n_1}-\mathbf{q}_2\mathbf{r}^0_{n_2})}$$
$$\times\sum_{\kappa\kappa'\sigma}I^*_{\kappa\kappa'}(\mathbf{q}_1)\sum_{\kappa_1'\kappa_2'\sigma_1'}\frac{1}{\beta}\sum_s$$
$$\times G_{\sigma\sigma_1'}(\kappa\kappa_1',\zeta_s)I_{\kappa_1'\kappa_2'}(\mathbf{q}_2)$$
$$\times G_{\sigma_1'\sigma}(\kappa_2'\kappa',\zeta_s-\omega_m). \qquad (15)$$

The first term on the right-hand side of this formula is found in Refs. 4–6. The second term is due to the electron–ion interaction in impure conductors. In a graphical representation of the polarization operator it corresponds to an electron loop with the exact functions G.

Using in (15) the spectral representation of the electron Green's function (4), we do the summation over s by the contour integration method.[22] As a result we obtain

$$\Pi^{\nu_1\nu_2}_{n_1n_2}(\omega_m)=(M_1-M_0)c_{n_1}\omega_m^2\delta_{n_1n_2}\delta_{\nu_1\nu_2}$$
$$+\sum_{\mathbf{q}_1\mathbf{q}_2}q_1^{\nu_1}q_2^{\nu_2}u^*_{n_1}(\mathbf{q}_1)u_{n_2}(\mathbf{q}_2)\mathrm{e}^{i(\mathbf{q}_1\mathbf{r}^0_{n_1}-\mathbf{q}_2\mathbf{r}^0_{n_2})}$$
$$\times\sum_{\kappa\kappa'\sigma\kappa_1'}\sum_{\kappa_2'\sigma_1'}I^*_{\kappa\kappa'}(\mathbf{q}_1)I_{\kappa_1'\kappa_2'}(\mathbf{q}_2)$$
$$\times\int_{-\infty}^{\infty}d\xi_1\rho_{\sigma\sigma_1'}(\kappa\kappa_1',\xi_1)\int_{-\infty}^{\infty}d\xi_2$$
$$\times\rho_{\sigma_1'\sigma}(\kappa_2'\kappa',\xi_2)\frac{f(\xi_2)-f(\xi_1)}{i\omega_m+\xi_2-\xi_1}. \qquad (16)$$

Here ρ is the spectral density of the single-particle temperature Green's function, and f is the Fermi function.

The deformation of the phonon spectrum of the crystal and the phonon damping due to the first term in formula (16) have been studied previously.[4–6] Here we are interested in the influence of the resonance scattering of electrons by impurity atoms on the phonon spectrum and damping of a conductor in a magnetic field. This effect is described by the second term on the right-hand side of formula (16). For this purpose we drop the first term on the right-hand side of (16). This can be done if the quasilocal frequency of the vibrations of the impurity atom are substantially different from the frequencies of the resonance transitions of the electrons between magnetoimpurity levels and the Landau levels. We shall neglect the contribution of the vibrations of the impurity ions in the second term of (16). This effect has been studied in the papers of Kagan and Zhernov (see, e.g., Ref. 8). On the right-hand side of Eq. (11) only the first two terms remain. They are due to the elastic impurity scattering of electrons in a magnetic field. In order to take the electron impurity states into account, we must go beyond the Born approximation in the electron–impurity interaction in calculating the scattering amplitude. For this we write Eq. (12) in the usual form

$$G_{\sigma\sigma'}(\kappa\kappa',\zeta_s)=G^0_\sigma(\kappa,\zeta_s)\,\delta_{\kappa\kappa'}\delta_{\sigma\sigma'} + G^0_\sigma(\kappa,\zeta_s)\sum_{\kappa_1\sigma_1} U_{\kappa\kappa_1}G_{\sigma_1\sigma'}(\kappa_1\kappa',\zeta_s), \tag{17}$$

where $U_{\kappa\kappa_1}$ are the matrix elements of the operator for the electron–impurity interaction energy. The solution of this equation can be obtained by using the standard iterative procedure. Doing the averaging of Eq. (17) over positions of the impurity atoms,[22] we obtain

$$G_{\kappa\sigma}=G^0_{\kappa\sigma}+(G^0_{\kappa\sigma})^2T_{\kappa\sigma}, \tag{18}$$

where $T_{\kappa\sigma}$ is the average value of the operator for the scattering of electrons by impurity atoms. Since we are interested in impurity states of the electrons in the field of isolated impurity atoms, we can limit consideration to the linear approximation in the series interval of $T_{\kappa\sigma}$ in powers of the concentration n_i of the impurity atoms. In the graphical representation this means that among the diagrams for $T_{\kappa\sigma}$, only those with one cross are important (the single-center approximation). Taking such diagrams into account means that the amplitude of multiple scattering of electrons by an isolated impurity atom is calculated exactly. This allows us to take into account the poles of the amplitude, which correspond to magnetoimpurity electron states. In this approximation we obtain

$$T_{\kappa\sigma}=n_it_{\kappa\sigma}(\zeta_s).$$

where

$$t_{\kappa\sigma}(\zeta_s)=\frac{u_0}{1-u_0\sum_{\kappa_1}G^0_{\kappa_1\sigma}(\zeta_s)} \tag{19}$$

is the temperature operator for single-center scattering. In deriving this formula we have limited consideration to short-range impurity atoms, when one needs to keep only the Fourier component of the electron–impurity interaction potential for $\mathbf{q}=0$: $u(\mathbf{q})=u_0$. The methods of removing the divergence of the series that appears here were discussed in Ref. 24.

Carrying out an analytical continuation of expression (18) with a discrete set of points $i\zeta_s$ on the real energy axis, we can see that the retarded and advanced electron Green's functions have additional poles which are roots of the Lifshitz equation.[3,10] They correspond to magnetoimpurity electron states that must be taken into account in calculating the polarization operator.

We also average expression (16) over configurations of impurity atoms in the sample. Here we shall neglect the difference by $u_0(\mathbf{q})$ and $u_1(\mathbf{q})$. We omit the vertex corrections arising in the averaging of the product of spectral densities.[22] Then the integrand in (16) contains the product of densities averaged over configurations of the impurities:

$$\langle\rho_{\sigma\sigma'}(\kappa\kappa',\varepsilon)\rangle_c=\delta_{\sigma\sigma'}\delta_{\kappa\kappa'}\rho_\sigma(\kappa,\varepsilon).$$

We do the analytical continuation of expression (16) according to the rule $i\omega_m\to\omega+i0$. Then the retarded phonon polarization operator in an isotropic crystal has the form

$$\Pi^{\nu_1\nu_2}_{n_1n_2}(\omega)=\frac{\delta_{\nu_1\nu_2}}{3}\sum_{\mathbf{q}} q^2|u_0(\mathbf{q})|^2e^{i\mathbf{q}(\mathbf{r}^0_{n_1}-\mathbf{r}^0_{n_2})} \times\sum_{\kappa\kappa'\sigma}|I_{\kappa\kappa'}(\mathbf{q})|^2\int_{-\infty}^{\infty}d\varepsilon_1\int_{-\infty}^{\infty}d\varepsilon_2 \times\rho_\sigma(\kappa,\varepsilon_1)\rho_\sigma(\kappa',\varepsilon_2)\frac{f(\varepsilon_2)-f(\varepsilon_1)}{\omega+i0+\varepsilon_2-\varepsilon_1}. \tag{20}$$

The method of calculating the spectral density with allowance for bound and quasibound states of the electrons in a plasma is set forth in the monograph by Kraeft *et al.*[25] We apply that method to the electron–impurity system in a magnetic field. Following Refs. 21 and 25, we expand ρ in a series about the point at which the damping of the electrons vanishes. Such an approximation is sufficient for considering the high-frequency properties of conductors provided that the frequency of the external field is greater than the electron collision frequency. To remove the divergence of the series in (19), we use a self-consistent approximation. This means that an electron undergoing multiple collisions with impurities is not free but is all the time sensitive to their presence.[22,25] Graphically this corresponds to replacing the fine electron lines in the diagrams for the electron Green's function by heavy lines.

In the approximation linear in the concentration of impurity ions the spectral density of the averaged electron Green's function is equal to

$$\rho=\rho^0+\delta\rho,\quad\text{where}\quad\rho^0_\sigma(\kappa,\varepsilon)=\delta(\varepsilon-\varepsilon_{\kappa\sigma});$$

and the impurity contribution $\delta\rho\sim n_i$ has the form

$$\delta\rho_\sigma(\kappa,\varepsilon)=\frac{1}{\pi}\frac{\gamma_\sigma(\varepsilon)}{[\varepsilon-\varepsilon_{\kappa\sigma}-\Delta_\sigma(\varepsilon)]^2+\gamma^2_\sigma(\varepsilon)} -\delta(\varepsilon-\varepsilon_{\kappa\sigma}). \tag{21}$$

Here $\Delta_\sigma - i\gamma_\sigma$ is the retarded self-energy function due to the electron–impurity interaction. The real part Δ_σ determines the shift of the Landau levels, and the imaginary part γ_σ the damping. In the case of short-range impurity atoms that scatter solutions independently, we find

$$\gamma_\sigma(\varepsilon)=\frac{\pi u_0^2 n_i g_\sigma(\varepsilon)}{[1-u_0F_\sigma(\varepsilon)]^2+[\pi u_0 g_\sigma(\varepsilon)]^2}, \tag{22}$$

where $g_\sigma(\varepsilon)$ is the density of electron states in the magnetic field, and

$$F_\sigma(\varepsilon)=P\int_{-\infty}^{+\infty}d\varepsilon'\frac{g_\sigma(\varepsilon')}{\varepsilon-\varepsilon'}.$$

In the Born approximation the denominator in formula (22) must be replaced by unity. Then γ_σ goes over to the known collision frequency for electrons with the impurity atoms.[22] We see from (21) and (22) that the spectral density has complex poles at points which are roots of the Lifshitz equation. They correspond to magnetoimpurity electron states. Their characteristics are found in Ref. 20. The distance between a Landau level and the magnetoimpurity level split off from it is given by

$$\Delta=\frac{1}{2}\Omega\left(\frac{a}{l}\right)^2,$$

where Ω is the cyclotron frequency, l is the magnetic length, and a is the scattering length. The width of the Nth magnetoimpurity level is equal to

$$\Gamma_N=2\Delta\sqrt{\frac{\Delta}{\Omega}}\sum_n (N-n)^{-1/2}.$$

The residue of the electron–impurity scattering amplitude at the pole is

$$r=\frac{2^{5/2}\pi\Delta^{3/2}}{m^{3/2}\Omega}.$$

These formulas have been obtained for $\Delta\ll\Omega$. The concrete form of the function γ_σ (22) will not be used below. Only the fact of the existence of poles of the spectral density will be used. The characteristics of the magnetoimpurity states presented here will be used only for numerical estimates.

In the approximation linear in the concentration of impurity atoms we obtain $\Pi=\Pi_0+\delta\Pi$, where Π_0 describes the change and damping of the phonon spectrum due to the electron–phonon interaction in the ideal conductor, and $\delta\Pi$ is an impurity contribution. The term Π_0 for the longitudinal phonons with $\mathbf{q}\|\mathbf{H}$ is obtained in Ref. 15:

$$\mathrm{Re}\,\Pi_0(\mathbf{q},\omega)=\frac{m^2g^2\Omega}{4\pi^2q_z}\sum_{nn'\sigma}^{N_\sigma}C_{nn'}(q_\perp)\times\ln\left|\frac{\left[\left(\frac{q_z}{k_0}-x_{n'\sigma}\right)^2-x_{n\sigma}^2\right]^2-\left(\frac{\omega}{\mu_0}\right)^2}{\left[\left(\frac{q_z}{k_0}+x_{n'\sigma}\right)^2-x_{n\sigma}^2\right]^2-\left(\frac{\omega}{\mu_0}\right)^2}\right|, \tag{23}$$

$$\mathrm{Im}\,\Pi_0(\mathbf{q},\omega)=\frac{m^2g^2\Omega}{4\pi|q_z|}\sum_{nn'\sigma}C_{nn'}(q_\perp)[f(\varepsilon_{nk_2^0\sigma})-f(\varepsilon_{n'(k_2^0-q_z)\sigma})], \tag{24}$$

where $g\sim\mu_0/d$ is the constant of the deformation potential (μ_0 is the chemical potential of the electrons and d is the density of the conductor),[23] $x_{n\sigma}=(1-\varepsilon_{n\sigma}/\mu_0)^{1/2}$, $\varepsilon_{n\sigma}$ are the Landau levels, $k_0=(2m\mu_0)^{1/2}$, N_σ is the number of filled Landau levels,

$$k_z^0=\frac{m}{q_z}[\omega_+-\Omega(n-n')],\quad \omega_+=\omega+\frac{q_z^2}{2m},$$

$$\sum_{k_yk_y'}|I_{\kappa\kappa'}(\mathbf{q})|^2=\frac{m\Omega}{2\pi}\delta_{q_z,k_z-k_z'}C_{nn'}(q_\perp),$$

and $q_\perp=(q_x^2+q_y^2)^{1/2}$. Expression (23) was obtained at zero temperature. We note that in formulas (23) and (24) we have used the normalization of the polarization operator adopted in Ref. 23. It differs from ours (15) by an additional factor of q^2d. This is because our Green's function (5) is constructed on the displacement operators of the ions, while in Ref. 23 it was constructed on density fluctuations. Formulas (23) and (24) can be obtained from (20) if the spectral density ρ_0 of an ideal conductor is used, and $u_0(\mathbf{q})$ is replaced by a constant.

Using the resonance character of the imaginary part (22) of the self-energy of the electrons, we write the contribution $\delta\Pi$ in the form

$$\delta\Pi(\mathbf{q},\omega)=-\frac{mg^2n_i\Omega}{(2\pi)^2}\sum_{N\sigma}r_{N\sigma}\sum_{nn'}\int_{-\infty}^{\infty}dk_z\times\frac{f(\varepsilon_{N\sigma})-f(\varepsilon_{nk_z\sigma})}{[\varepsilon_{n'(k_z+q_z)\sigma}-\varepsilon_{N\sigma}]^2}C_{nn'}(q_\perp)\times\left(\frac{1}{\varepsilon_{nk_z\sigma}-\varepsilon_{N\sigma}-\omega-i\Gamma_{N\sigma}}+\frac{1}{\varepsilon_{nk_z\sigma}-\varepsilon_{N\sigma}+\omega+i\Gamma_{N\sigma}}\right). \tag{25}$$

Here $\varepsilon_{N\sigma}$ and $\Gamma_{N\sigma}$ are the position and width of the Nth magnetoimpurity electron energy level with spin projection σ; $r_{N\sigma}$ is the residue of the scattering amplitude for electrons on an impurity atom at the pole of $\varepsilon_{N\sigma}-i\Gamma_{N\sigma}$. In this paper we are ignoring the broadening of the Landau levels.

The effect we are interested in is due to the poles of the integrand in (25), which are roots of the equations $\varepsilon_{nk_z\sigma}-\varepsilon_{N\sigma}\pm\omega\pm i\Gamma_{N\sigma}=0$. Here the upper sign corresponds to transitions of the electrons in the field of the vibrating lattice from the Landau levels to the magnetoimpurity levels, and the lower sign corresponds to the inverse transitions.

We now specialize to the case $\mathbf{q}\|\mathbf{H}$. Near the frequencies ω_s of the resonance transitions of the electrons from the magnetoimpurity levels to the Landau levels, the contribution (25) has the form

$$\delta\Pi_s(\omega)=-i\frac{\alpha_s}{(\omega-\omega_s+i\Gamma)^{1/2}}, \tag{26}$$

where $\omega_s=\omega_0+s\Omega$ $(s=0,1,\ldots)$ are the transition frequencies, $\omega_0=\Delta$, and

$$\alpha_s=\frac{m^{3/2}g^2\Omega n_i r}{2^{1/2}\pi\omega_s^2}\sum_N\,[f(\varepsilon_N)-f(\varepsilon_N+\omega_s)]. \tag{27}$$

The values of α_s play the role of oscillator strengths of the resonance transitions. In formulas (26) and (27) we neglect the dependence of Δ, Γ, and r on the number of the Landau level. This is allowable if $\Delta\ll\Omega$. The square-root singularities of (26) reproduce the singularities of the density of states of the electrons at the Landau levels involved in the transitions, and the difference of the Fermi functions in (27) takes the Pauli principle into account. Near the frequencies of the resonance transitions of the electrons from the Landau levels to the magnetoimpurity levels the polarization operator contains the contribution

$$\delta\Pi_p(\omega)=-i\frac{\beta_p}{(\omega_p-\omega-i\Gamma)^{1/2}}, \tag{28}$$

where $\omega_p=p\Omega-\omega_0$ $(p=1,2,\ldots)$ are the transition frequencies, and

$$\beta_p=\frac{m^{3/2}g^2\Omega n_i r}{2^{1/2}\pi\omega_p^2}\sum_N\,[f(\varepsilon_N-\omega_p)-f(\varepsilon_N)]$$

are the oscillator strengths. In the formulas for the oscillator lengths strengths we neglect the spin splitting of the energy levels.

It is seen from formulas (26) and (28) that the magnetoimpurity states of electrons give rise to resonance contributions to the real and imaginary parts of the phonon polarization operator. The imaginary part of the contribution (26) has a square-root singularity at $\omega\to\omega_s+0$, and the real part has one at $\omega\to\omega_s-0$. This means that the magnetoimpurity states have a substantial influence on the damping of phonons with frequencies $\omega\geqslant\omega_s$. In the case of transitions at frequencies ω_p the situation is reversed: the phonons are strongly damped in the region $\omega\leqslant\omega_p$.

Let us consider the limiting case $H=0$. We assume that the electron energy spectrum has is only one resonance level ε_r of width Γ, and the residue of the scattering amplitude of electrons on impurity atoms is equal to r. Then, passing to the limit $H\to 0$ in formula (20), we obtain $\delta\Pi=\delta\Pi_1+\delta\Pi_2$, where

$$\delta\Pi_1(q,\omega)=-i\frac{\sqrt{2}m^{3/2}g^2 r n_i}{\pi}[f(\varepsilon_r)-f(\varepsilon_r+\omega)]\times\frac{(\varepsilon_r+\omega+i\Gamma)^{1/2}}{(\omega_++i\Gamma)^2-4\varepsilon_q(\varepsilon_r+\omega+i\Gamma)},$$

$$\delta\Pi_2(q,\omega)=-i\frac{\sqrt{2}m^{3/2}g^2 r n_i}{\pi}[f(\varepsilon_r-\omega)-f(\varepsilon_r)]\times\frac{(\varepsilon_r-\omega-i\Gamma)^{1/2}}{(\omega_-+i\Gamma)^2-4\varepsilon_q(\varepsilon_r-\omega-i\Gamma)},$$

$\omega_\pm=\omega\pm q^2/2m$; $\varepsilon_q=q^2/2m$. The contribution $\delta\Pi_1$ is due to transitions of electrons from the resonance level to the band, and $\delta\Pi_2$ is due to the inverse transitions. As in the case $H\neq 0$, the contributions $\delta\Pi_1$ and $\delta\Pi_2$ are proportional to the density of electron band states. The imaginary part $i\Gamma$ is due to the natural width of the resonance line.

4. PHONON SPECTRUM AND DAMPING IN CONDUCTORS WITH MAGNETOIMPURITY ELECTRON STATES

The ion Green's function (5), averaged over positions of the impurity atoms, satisfies Dyson's equation[23,23]

$$\langle D\rangle_c=\frac{1}{D_0^{-1}-\langle\Pi\rangle_c}.$$

In Refs. 4–6 the averaged polarization operator $\langle\Pi\rangle_c$ is calculated in a linear approximation in the concentration of impurity atoms. Such an approximation is based on the selective summation of diagrams for $\langle D\rangle_c$. Diagrams are summed which take into account the multiple scattering of elastic waves by an isolated isotopic defect. This result can be obtained from Eq. (7) in which the last term on the right-hand side is neglected. In the previous Section we set $\langle\Pi\rangle_c=\Pi_0+\delta\Pi$, where the term $\delta\Pi$ (25) is also calculated in the linear approximation in the concentration of impurity atoms. In the calculation we restricted the summation of diagrams for $\langle G\rangle_c$ to those with one cross,[22] which take into account multiple scattering of electrons by isolated impurity atoms.

The dispersion relation for the phonon spectrum in conductors with magnetoimpurity electron states has the form

$$\frac{\omega^2-u^2q^2}{q^2d}-\mathrm{Re}\,\delta\Pi(q,\omega)=\mathrm{Re}\,\Pi_0,$$

where u is the renormalized sound velocity. The term $\mathrm{Re}\,\delta\Pi$ takes into account the influence of magnetoimpurity states of electrons on the phonon spectrum.

As in Sec. 3, we limit consideration to longitudinal phonons propagating along the magnetic field. Near the frequency ω_0 of the resonance transitions of electrons from the magnetoimpurity level to the adjacent Landau level, the dispersion relation for such longitudinal phonons has the form

$$A\left(x^2-\frac{u^2q^2}{\omega_0^2}\right)+B(1-x)^{-1/2}-Cx^2(x^2-x_k^2)^{-1}=\ln E, \tag{29}$$

where

$$x=\omega/\omega_0,\quad A=2\pi^2\left(\frac{\Delta}{\mu_0}\right)^2\frac{k_0}{q}\left(\frac{l^2d}{mk_0}\right),$$

$$B=16\pi^2\left(\frac{l}{a}\right)^2 ql^4n_i,$$

$$C=2\pi^2n_ia_0^3\left(\frac{\omega_D}{\mu_0}\right)^2\frac{k_0}{q}\left(\frac{l^2d}{mk_0}\right),$$

$$E=\left|\left(\frac{q}{k_0}-2x_0\right)^2-\left(\frac{\Delta}{\mu_0}\frac{k_0}{q}x\right)^2\right|\left|\left(\frac{q}{k_0}+2x_0\right)^2-\left(\frac{\Delta}{\mu_0}\frac{k_0}{q}x\right)^2\right|^{-1},$$

$x_k=\omega_k/\omega_0$ (ω_k is the frequency of quasilocal vibrations), a_0 is the lattice constant, ω_D is the Debye frequency, and $x_0=(1-\Omega/2\mu_0)^{1/2}$. The second term on the left-hand side of

dispersion relation (29) is due to the magnetoimpurity states, and the third term takes into account the quasilocal vibrations of heavy impurity atoms in the lattice.[4–6] The spin splitting of the Landau and magnetoimpurity levels has not been taken into account in these formulas, and only one term in the sum (23) is being considered. A graphical analysis of Eq. (29) shows that in the case $A(uq/\omega_0)^2>2\ln F^{-1}$ in the parabolic window of transparency ($x<x_-$) of the conductor for elastic waves in the absence of magnetoimpurity states there exists a longitudinal vibrational branch of the spectrum. There

$$x_\pm=\frac{\mu_0}{\omega_0}\frac{q}{k_0}\left(2x_0\pm\frac{q}{k_0}\right),\quad F=\left|\frac{q}{k_0}-2x_0\right|\left(\frac{q}{k_0}+2x_0\right)^{-1}.$$

When the magnetoimpurity states are taken into account, a crossover splitting of the dispersion curve under consideration occurs which is analogous to the crossover situation in a lattice with quasilocal vibrations.[5] This occurs if the following inequalities hold:

$$x_->1,\quad A\left(\frac{uq}{\omega_0}\right)^2-B>2\ln F^{-1}.$$

In the parabolic window the spectrum has not one but two branches: a low-frequency branch and a high-frequency branch. The frequency of the low-frequency branch lies in the interval $\omega<\omega_0$, and that of the high-frequency branch, between ω_0 and the boundary of the transparency window. If instead

$$A\left(\frac{u^2q^2}{\omega_0^2}-1\right)<\ln E^{-1}(x=1),$$

then the high-frequency branch vanishes. Only a lowering of the frequency of the initial branch of vibrations occurs.

Let us clarify what happens to the phonon spectrum described above when the quasilocal vibrations are taken into account. Let $1<x_k<x_-$. Then it follows from Eq. (29) that for

$$A\left(\frac{u^2q^2}{\omega_0^2}-1\right)-C(x_k^2-1)^{-1}<\ln E^{-1}(x=1)$$

the crossover situation described above is preserved. A further decrease of the vibrational frequency occurs in the interval $x<1$, while the frequency of the high-frequency branch increases. Its frequency lies between ωk and the boundary of the transparency window.

Near the frequency of the electron transitions from the Landau level to the magnetoimpurity level $\omega_1=\Omega-\omega_0$ the dispersion relation has the form

$$A_1(x^2-x_1^2)-B_1(x-1)^{-1/2}-C_1x^2(x^2-x_{k_1}^2)^{-1}=\ln E_1,\tag{30}$$

where

$$A_1=\left(\frac{\Omega}{\omega_0}\right)^2A,\quad B_1=2^{-5/2}\left(\frac{a}{l}\right)^5,\quad C_1=C,$$

$$x_1=\frac{uq}{\Omega},\quad x_{k_1}=\frac{\omega_k}{\Omega},$$

and E_1 is obtained from E by replacing ω_0 with Ω in the argument of the logarithm. It follows from this equation that in the case

$$A_1x_1^2<2\ln F^{-1},\quad x_->1$$

there are no solutions of the dispersion relation in the parabolic transparency window in the absence of magnetoimpurity states. If magnetoimpurity states do exist, such a solution appears. The root of the dispersion relation lies in the interval $(1, x_-)$. It corresponds to magnetoimpurity phonons. As in the case of electromagnetic waves,[20,21] magnetic localization of electrons on impurity atoms promotes the propagation of vibrations in conductors. Taking the magnetoimpurity states into account leads to a lowering of the phonon frequency in the collisionless damping resistivities $x_-<x<x_+$ and to growth of the vibrational frequency in the region $x>x_+$. If $x_{k_1}<1$, $C_1(1-x_{k_1}^2)^{-1}<\ln E_1^{-1}(x=1)$, the third term on the left-hand side of dispersion relation (30) causes a splitting of the magnetoimpurity phonon branch. The low-frequency branch lies in the interval $(x_{k_1},1)$ and the high-frequency branch at $1<x<x_-$. The vibrational frequency decreases in the region $x_-<x<x_+$ and increases for $x>x_+$. If instead $C_1(1-x_{k_1}^2)^{-1}>\ln E_1^{-1}(x=1)$, the low-frequency branch vanishes and the high-frequency branch remains.

The phonon damping decrement γ is related to the imaginary part of the retarded polarization operator by the relation[1,23]

$$\gamma(q)=-\frac{dq}{2u}\operatorname{Im}\Pi(q,\omega_q),\tag{31}$$

where ω_q is the phonon spectrum. It follows from formula (26) that near the resonance frequency ω_s the damping decrement contains a contribution due to the magnetoimpurity states. It is equal to

$$\delta\gamma_s(q)=\frac{\alpha_sqd}{2^{3/2}ua_s(\omega_q)}[a_s(\omega_q)+(\omega_q-\omega_s)]^{1/2},\tag{32}$$

where

$$a_s(\omega)=[(\omega-\omega_s)^2+\Gamma^2]^{1/2}.$$

If we neglect the width of the magnetoimpurity level, expression (32) has a square-root singularity for $\omega\to\omega_s$ from above and is equal to zero below ω_s. Taking Γ into account leads to a smoothing of this singularity. The absorption line of the phonons is asymmetric. It is shifted to higher frequencies with respect to ω_s. A maximum of the sound absorption coefficient analogous to that predicted here has been observed in InSb samples doped with donor impurities.[26] It can be explained as an activation by the field of the sound wave of electrons which had been magnetically frozen at the local levels.

Near the frequency ω_p the contribution to the phonon damping decrement has the form

$$\delta\gamma_p(q)=\frac{\beta_pqd}{2^{3/2}ua_p(\omega_q)}[a_p(\omega_q)+(\omega_p-\omega_q)]^{1/2}.$$

This expression has a square-root singularity as the frequency goes to ω_p from below. The corresponding absorption line is also asymmetric, shifted to lower frequencies with respect to ω_p.

It is seen from formula (24) that for $\omega < qv_0 - q^2/2m$, when $v_0 = [2/m(\mu_0 - \Omega/2)]^{1/2}$, there is no collisionless damping in a degenerate conductor. In this region the ratio of the maximum value of the damping decrement (32) with frequency ω_0 to the damping of the quasilocal vibrations[5] is of the order of

$$\left(\frac{M_0}{M_1 - M_0}\right)^{3/2}\left(\frac{\mu_0}{\Delta}\right)^2 \sqrt{\frac{\Delta}{\Gamma}}\,\frac{\omega_0}{\omega_k}\,\frac{q}{ua_0^3 d}.$$

If the parameter values $\mu_0/\Delta = 10$, $\Delta/\Gamma = 10$, $\omega_0/\omega_k = 0.8$, $q/(ua_0^3 d) = 10^{-2}$, and $M_1/M_0 = 3$, which are typical of semimetals and degenerate semiconductors, are substituted into this expression, we obtain a value of 0.9 for this ratio. If

$$qv_0 - q^2/2m < \omega < qv_0 + q^2/2m,$$

then the phonons undergo collisionless damping. The ratio of the maximum value of the decrement (32) at frequency ω_0 to the value found in Ref. 15 for the contribution from the region $x_- < x < x_+$ is of the order of

$$2^{7/2}\pi\left(\frac{l}{a}\right)^2 \sqrt{\frac{\Delta}{\Gamma}}\,(ql)(l^3 n_i).$$

At the parameter values indicated above and $l/a = 25$, $ql = 10^{-2}$, and $l^3 n_i = 10^{-2}$, this ratio is equal to 7.

5. CONCLUSION

Usually quasilocal vibrations of the crystal lattice and quasilocal (resonance) states of electrons in impure conductors are considered separately. Meanwhile, the same impurity can be a source of both quasilocal vibrations and resonance electron states. In semimetals and degenerate semiconductors the frequency of quasilocal vibrations can turn out to be comparable to the energy of the electron resonance. Then these resonances must be taken into account simultaneously.

In this paper we have shown that quasilocal vibrations of heavy impurity atoms and resonance electron states at those atoms influence the phonon spectrum and damping in impure conductors in the presence of a quantizing magnetic field. The treatment is done on the basis of an electron–ion model of a nonideal conductor in a magnetic field. In this model the phonons are not introduced *a priori* but arise as a result of solution of the dispersion relation. The magnetoimpurity electron states at isolated impurity atoms are taken into account. In the framework of this model we have obtained equations for the electron and ion Green's functions by the temperature Green's function method. We have shown that at a low concentration of impurity atoms in a conductor, magnetoimpurity states give resonance contributions to the phonon polarization operator. They depend on the type of transitions of electrons between the Landau levels and the magnetoimpurity levels in the field of an elastic wave. The magnetoimpurity states have a substantial influence on the phonon spectrum and damping. When the vibrational frequency coincides with the frequency of resonance transitions of the electrons, a crossover splitting of the phonon dispersion curve into two branches occurs. Under certain conditions new branches of the vibrational spectrum can exist in the windows of transparency for elastic waves; these branches are absent in conductors without magnetoimpurity states. The corresponding phonons are called magnetoimpurity phonons. Their damping is due to the scattering of electrons and elastic waves by the impurity atoms in the conductor.

This study was supported in part by the INTAS program (Grant INTAS-01-0791) and the program European Network of Excellence in ''Fundamentals of Nanoelectronics.''

*E-mail: alexander.m.ermolaev@univer.kharkov.ua

[1] A. B. Migdal, Zh. Éksp. Teor. Fiz. **34**, 1438 (1958) [Sov. Phys. JETP **7**, 996 (1958)].
[2] E. G. Brovman and Yu. M. Kagan, Usp. Fiz. Nauk **112**, 369 (1974) [Sov. Phys. Usp. **17**, 125 (1974)].
[3] I. M. Lifshits, *Physics of Real Crystals and Disordered Systems. Collected Works* [in Russian], Nauka, Moscow (1987).
[4] I. M. Lifshitz and A. M. Kosevich, Rep. Prog. Phys. **29**, 217 (1966).
[5] A. M. Kosevich, *Theory of Crystal Lattice*, Springer-Verlag (1995), Vishcha Shkola, Kharkov (1988).
[6] Yu. M. Kagan, in *Physics of Crystals with Defects*, Vol. 2, Tbilisi (1966), p. 93.
[7] E. G. Maksimov, Tr. Fiz. Inst. Akad. Nauk SSSR (FIAN) **86**, 101 (1975).
[8] A. P. Zhernov, N. A. Chernoplekov, and É. Mrozan, *Metals with Nonmagnetic Impurity Atoms* [in Russian], Énergoatomizdat, Moscow (1992).
[9] V. M. Gokhfel'd, O. V. Kirichenko, and V. G. Peschanskii, Fiz. Nizk. Temp. **19**, 3 (1993) [Low Temp. Phys. **19**, 1 (1993)].
[10] I. M. Lifshits, S. A. Gredeskul, and L. A. Pastur, *Introduction to the Theory of Disordered Systems*, Wiley, New York (1988), Nauka, Moscow (1982).
[11] V. I. Kaĭdanov and Yu. I. Ravich, Usp. Fiz. Nauk **145**, 51 (1985) [Sov. Phys. Usp. **28**, 31 (1985)].
[12] B. A. Volkov and S. V. Sharov, Zh. Éksp. Teor. Fiz. **102**, 1693 (1992) [JETP **75**, 916 (1992)].
[13] L. I. Glazman and R. N. Shekhter, Zh. Éksp. Teor. Fiz. **94**, 309 (1988) [Sov. Phys. JETP **67**, 163 (1988)].
[14] M. Yu. Reizer and A. V. Sergeyev, Zh. Éksp. Teor. Fiz. **90**, 1056 (1986) [Sov. Phys. JETP **63**, 616 (1986)].
[15] A. Ya. Blank and É. A. Kaner, Zh. Éksp. Teor. Fiz. **50**, 1013 (1966) [Sov. Phys. JETP **23**, 673 (1966)].
[16] É. A. Kaner and L. V. Chebotarev, Zh. Éksp. Teor. Fiz. **73**, 1813 (1977) [Sov. Phys. JETP **46**, 953 (1977)].
[17] A. M. Ermolaev and M. I. Kaganov, JETP Lett. **6**, 395 (1967).
[18] A. M. Ermolaev, Zh. Éksp. Teor. Fiz. **54**, 1259 (1968) [Sov. Phys. JETP **27**, 1266 (1968)].
[19] L. D. Landau and E. M. Lifshitz, *Quantum Mechanics: Non-Relativistic Theory*, 3rd ed., Pergamon Press, Oxford (1977), Nauka, Moscow (1989).
[20] É. A. Kaner and A. M. Ermolaev, Zh. Éksp. Teor. Fiz. **92**, 2245 (1987) [Sov. Phys. JETP **65**, 1266 (1987)].
[21] N. V. Gleizer, A. M. Ermolaev, and G. I. Rashba, Fiz. Nizk. Temp. **20**, 1169 (1994) [Low Temp. Phys. **20**, 919 (1994)].
[22] A. A. Abrikosov, L. P. Gor'kov, and I. E. Dzyaloshinskiĭ, *Methods of Quantum Field Theory in Statistical Physics*, Prentice-Hall, Englewood Cliffs, New Jersey (1963), Fizmatgiz, Moscow (1962).
[23] L. D. Landau and E. M. Lifshitz, *Statistical Physics*, 3rd ed., Vol. 2 (by E. M. Lifshitz and L. P. Pitaevskii), Pergamon Press, Oxford (1980), Nauka, Moscow (1978).
[24] M. I. Kaganov and S. Klama, Fiz. Tverd. Tela (Leningrad) **20**, 2360 (1978) [Sov. Phys. Solid State **20**, 1361 (1978)].
[25] W. D. Kraeft, D. Kremp, W. Ebeling, and G. Röpke, *Quantum Statistics of Charged Particle Systems*, Plenum Press, New York (1986), Mir, Moscow (1988).
[26] H. Tokumoto and R. Mansfield, Jpn. J. Appl. Phys. Suppl. **22**, 196 (1983).

Translated by Steve Torstveit

LOW DIMENSIONAL AND DISORDERED SYSTEMS

Spin–plasma wave in a one-dimensional metal

V. M. Gokhfeld*

A. A. Galkin Donetsk Physicotechnical Institute, ul. R. Lyuksemburg 72, 83114 Donetsk, Ukraine
(Submitted May 19, 2003)
Fiz. Nizk. Temp. **29**, 1256–1259 (November 2003)

It is shown that a new type weakly damped acoustic plasmons can propagate in a quasi-one-dimensional conductor in an external static magnetic field **H**. These are due to the presence of spin subbands in the electron spectrum and are accompanied by forced oscillations of the magnetic moment of the sample. The dependence of the velocity and amplitude of these waves on the magnetic field strength H is found. © *2003 American Institute of Physics.*
[DOI: 10.1063/1.1614241]

1. INTRODUCTION

A number of conducting crystals are now known which are so anisotropic that they can be regarded to a known degree of accuracy as one-dimensional (1D) metals with a charge carrier spectrum that depends only on the projection of the quasimomentum **p** on the **C** axis, the direction of maximum conductivity. Some of these materials, e.g., $TaSe_3$, the polymers $(SN)_x$, and organic polymers of the type $(TVTSF)_2CeO_4$, do not undergo a Peierls transition and remain metallic at all temperatures;[1,2] obviously, these are normal (nonsuperconducting) metals in rather high magnetic fields. The kinetic coefficients of a 1D electron gas can be calculated in an elementary manner, and their behavior in an external (static and uniform) magnetic field—independently of the direction of **H**—is determined solely by the spin[1)] splitting of the levels:

$$\varepsilon_{\pm}(\mathbf{p}) = p_C^2/2m_C \pm \beta H; \tag{1}$$

$\beta \equiv e\hbar/2mc$ is the Bohr magneton.

Adopting spectrum (1) (i.e., restricting discussion for simplicity to a 1D model in the effective-mass approximation), we shall show that weakly damped longitudinal plasma waves, similar to acoustic plasmons in an ordinary conductor,[2)] can propagate in such a metal at low temperatures. However, the wave velocity here depends on the magnetic field strength, and that circumstance can in principle be used in constructing adjustable wideband ''delay lines'' for rf signals.

2. NONLOCAL CONDUCTIVITY AND THE "ACOUSTIC" MODE

Let us calculate the contribution of each of the subbands (1) to the longitudinal conductivity:

$$\sigma_{\pm}(k,\omega) = \frac{\tilde{\omega}e^2}{ik^2}\left\langle \frac{kv_C}{kv_C - \tilde{\omega}} \right\rangle \equiv \frac{\tilde{\omega}e^2}{ik^2} P_{\pm}, \tag{2}$$

where $\mathbf{v} \equiv \partial\varepsilon/\partial\mathbf{p}$; the angle brackets denote integration over the Fermi surface[3)] with a weight $|\mathbf{v}|^{-1}(2\pi\hbar)^{-3}$, $\tilde{\omega} \equiv \omega + i/\tau$, and τ—the relaxation time with respect to both the momenta and the spin variable—is assumed constant and large in comparison with the period $2\pi/\omega$ of the external perturbation. Formula (2) follows directly from the kinetic equation in the **k** representation and the definitions of current density and the nonequilibrium carrier density:

$$i(\mathbf{k}\cdot\mathbf{v} - \tilde{\omega})\psi_k = -e\mathbf{v}\cdot\mathbf{E}_k;$$

$$\mathbf{j}_k = -e\langle \mathbf{v}\psi_k \rangle;$$

$$\langle \psi_k \rangle = (ieE_k/k)P. \tag{3}$$

To within constant common factors, the contributions of the subbands to the conductivity are proportional to

$$\sigma_{\pm} \propto \frac{\sqrt{\mu_{\pm}}}{1 - 2k^2\mu_{\pm}/m_C\tilde{\omega}^2},$$

and the reduced chemical potential $\mu_{\pm}(H) \equiv \mu(H) \pm \beta H$ (the filling depth of each of the subbands) is determined by the condition that the equilibrium particle number density N be equal in a magnetic field and in zero field (subscript 0):

$$\sqrt{\mu_+} + \sqrt{\mu_-} = 2\sqrt{\mu_0},$$

$$\mu_{\pm} = \mu_0\left(1 \pm \frac{\beta H}{2\mu_0}\right)^2 \equiv \mu_0(1 \pm h)^2. \tag{4}$$

It is easy to see that the total conductivity $\sigma_+ + \sigma_-$ vanishes for a wave with a linear dispersion relation

$$k(\omega) = K \equiv \frac{\tilde{\omega}}{v_0\sqrt{1-h^2}}. \tag{5}$$

Its velocity $V_1 = v_0\sqrt{1-h^2}$, where $v_0 \equiv \sqrt{2\mu_0/m_C}$, is the geometric mean of the Fermi velocities for each of the subbands; $V_1 \to 0$ as H approaches the critical value $H_1 = 2\mu_0/\beta$ for which the carriers leave the upper spin band. The wave damping decrement is of a collisional nature and is independent of frequency.

3. ELECTRIC FIELD DISTRIBUTION IN A SEMI-INFINITE SAMPLE

Let us estimate the value of the effect, assuming that the wave is excited by an electric field $E(0)\exp(-i\omega t)$ applied normal to the surface of a semi-infinite conductor ($x_C \geqslant 0$) with an ideal boundary that reflects the conduction electrons in a specular manner. The Fourier transform of the longitudinal electric field inside such a sample is known to be (see, e.g., Refs. 5 and 6)

$$E_k = \frac{2E(0)}{ik\epsilon(k,\omega)}, \tag{6}$$

where $\epsilon(k,\omega) \equiv 1 + 4\pi i\sigma(k,\omega)/\omega$ is the dielectric function, and the total conductivity calculated according to formula (2) can be written in the form

$$\sigma(k,\omega) = \frac{\tilde{\omega}e^2}{ik^2}(P_+ + P_-)$$

$$= \sigma(0,\omega)\frac{1 - z^2(1-h^2)}{[1-z^2(1+h)^2][1-z^2(1-h)^2]}, \tag{7}$$

where

$$\sigma(0,\omega) = iNe^2/m_C\tilde{\omega}; \quad z \equiv kv_0/\tilde{\omega}. \tag{8}$$

At frequencies small compared to the plasma frequency, expression (6) has a pole that practically coincides with K defined in Eq. (5); the residue at that pole gives the following expression for the electric field in the wave:

$$\delta E(x_C,t) \approx \frac{\omega}{i\pi\sigma(0,\omega)}E(0)\frac{h^2}{1-h^2}$$

$$\times \exp\left(\frac{i\tilde{\omega}x_C}{v_0\sqrt{1-h^2}} - i\omega t\right). \tag{9}$$

For a general value of the reduced magnetic field h [see Eq. (4)] the pre-exponential factor here is of the same order of magnitude as in the always-present homogeneous term:[4)]

$$E_\infty(t) = \frac{E(0)}{\epsilon(0,\omega)}\exp(-i\omega t)$$

$$\approx -\frac{\omega E(0)}{4\pi i\sigma(0,\omega)}\exp(-i\omega t); \tag{10}$$

therefore, conductors with a comparatively low density of free carriers (and, accordingly, low wave conductivity $\sigma(0,\omega)$) are the preferred objects of study. However, at depths x_C much less than the mean free path $v_0\tau$, the amplitude of the ratio $\delta E/E_\infty$ can turn out to be rather large in magnetic fields close to $H_1 = 2\mu_0/\beta$. Indeed, the maximum absolute value of the h-dependent factor in (9) is reached at $h \approx 1 - (x_C/v_0\tau)^2/8$ and is equal to $(2v_0\tau/ex_C)^2$, where e is the base of the natural logarithms (see Fig. 1).

4. MAGNETIC OSCILLATIONS

On the other hand, the wave under consideration represents antiphase oscillations of the partial densities of electrons with spins directed parallel and antiparallel to **H**, i.e., it should be accompanied by forced oscillations of the total magnetic moment. Its oscillatory part should obviously be written as

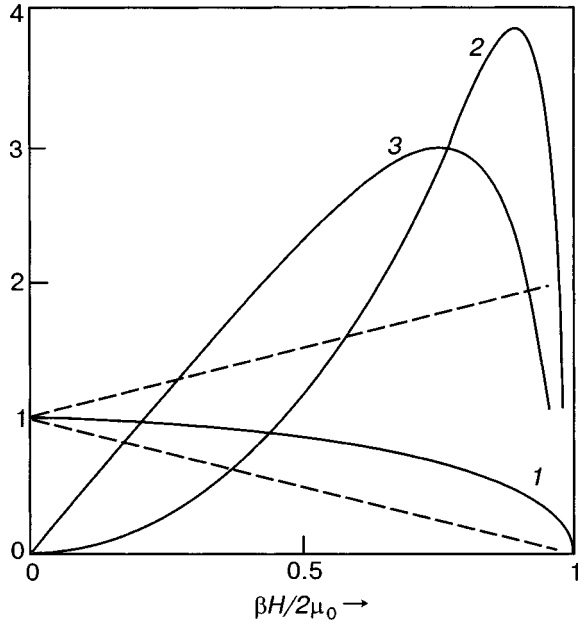

FIG. 1. Curves: *1*) the velocity of spin–plasma waves (in units of v_0); *2*,*3*) amplitudes of the oscillations of the electric field (in units of E_∞; see Eq. (10)) and magnetic moment (in arbitrary units), as functions of the applied static magnetic field. The parameter $x_C/v_0\tau = 1.15$. The dashed lines show the Fermi frequencies of electrons in the spin subbands.

$$\delta M_k = \beta(\langle\psi_k\rangle_+ - \langle\psi_k\rangle_-) = \beta\frac{ieE_k}{k}(P_+ - P_-). \tag{11}$$

Using formulas (3), (6), and (7) and introducing, as above, the dimensionless Fourier index $z \equiv kv_0/\tilde{\omega}$, we find the transform of the magnetization as

$$4\pi\delta M_k \approx \frac{\hbar\omega}{mc\tilde{\omega}}E(0)\frac{P_+ - P_-}{P_+ + P_-}$$

$$= \frac{\hbar\omega}{mc\tilde{\omega}}E(0)h\frac{1 + z^2(1-h^2)}{1 - z^2(1-h^2)} \tag{12}$$

and, by the inverse Fourier transformation, the distribution of the magnetization in the sample:

$$4\pi\delta M(x_C,t) \approx \frac{\hbar\omega}{imcv_0}E(0)\frac{h}{\sqrt{1-h^2}}$$

$$\times \exp\left(\frac{i\tilde{\omega}x_C}{v_0\sqrt{1-h^2}} - i\omega t\right). \tag{13}$$

As expected, the coefficient in front of $E(0)$ is small: even at comparatively low Fermi velocities $v_0 \simeq 10^6$ cm/s, taking $\omega \simeq 10^{12}$ s^{-1} we obtain $\hbar\omega/mcv_0 \simeq 3\times 10^{-5}$, i.e., an hf electric field $\simeq 1$ c.g.s. e.s.u. applied to the sample will produce magnetization oscillations with an amplitude of $\simeq 3\times 10^{-5}$ G. As in the case (9), the assessment may be more favorable for samples of small thickness compared to the mean free path $v_0\tau$, in fields close to H_1, so that for small $x_C/v_0\tau$ the h-dependent factor in (13) has a maximum amplitude there, with a value $\simeq v_0\tau/x_C$.

It is possible that the magnetic oscillations (13) will be easier to identify in experiment than the electric oscillations (9), since here there is no homogeneous term like (10).

5. SPECIAL TWO-DIMENSIONAL CASE

Of course, at a high enough magnetic field, the situation in which only the two lowest subbands (with opposite carrier spins) are filled is possible, even in systems of higher dimensionality. However, in that case for a wave of the acoustic plasmon type—with a velocity V in the interval $((v_{k-})_{\max},(v_{k+})_{\max})$—electrons can be found which are moving ''in phase'' with the wave, and that leads to its collisionless damping. The latter can be made weak only in fields corresponding to a relatively low occupation of the next-to-last subband, i.e., fields close to the critical value $H_c = \mu(H_c)/\beta$.

As an example, let us consider the two-dimensional electron spectrum in the special case mentioned above, when the field **H** applied along the plane of motion of the particles gives only spin splitting of the levels:

$$\varepsilon_{\pm}(\mathbf{p}) = \frac{p_x^2+p_y^2}{2m_{\perp}} \pm \beta H. \tag{14}$$

The total longitudinal conductivity calculated according to formula (2) (see also Refs. 7 and 8) here is equal to

$$\sigma_x(k,\omega) = \frac{ie^2}{k^2}\langle 1\rangle \sum_{\pm}\left(1-\frac{\tilde{\omega}}{\sqrt{\tilde{\omega}^2-k^2v_{\pm}^2}}\right);$$

$$v_{\pm} = \sqrt{2\frac{\mu_0 \pm \beta H}{m_{\perp}}} \equiv v_0\sqrt{1\pm\bar{h}} \tag{15}$$

—the maximum carrier velocities; $\langle 1\rangle$ is the energy density of states; for $D=2$ it is independent of energy and is therefore the same for both subbands. It is easy to check that for $\bar{h}\approx 1$ expression (15) goes to zero if the following dispersion relation holds:

$$k(\omega) \approx \frac{\tilde{\omega}}{V_2}\left(1+\frac{i}{3\sqrt{3}}\sqrt{\frac{1-\bar{h}}{1+\bar{h}}}\right); \quad V_2 \approx 2v_0\sqrt{\frac{1-\bar{h}}{3}}. \tag{16}$$

6. DISCUSSION OF THE RESULTS

The waves under discussion exist in an extremely wide range of magnetic field strengths. However, as may be seen from what we have said, conditions for realization of the effect (and, possibly, for applications in the controllable delay of hf signals) are more favorable in the case of relatively low occupations of the upper spin subband, i.e., for fields close to the maximum H_c. Let us estimate it, returning to the case $D=1$:

$$H_1 = \frac{2\mu_0}{\beta} = \frac{\hbar c}{e}\frac{m}{2m_C}\left(\frac{\pi n}{a_C}\right)^2, \tag{17}$$

where $n = Na_Ca_{\perp}^2$ is the number of carriers per cell of the crystal. For a ''good'' metal with $n\simeq 1$ (and $m_C \simeq m$) formula (17) would give $H_1 \simeq 10^8$ Oe, whereas it is ordinarily not technically feasible to obtain a static magnetic field greater than 10^6 Oe. However, a peculiarity of the one-dimensional case, for which $\mu_0 \propto n^2$, leads to rapid improvement of the assessment with decreasing free carrier density, i.e., for substances such as organic metals with an ordinarily narrow conduction band, and doped (degenerate) semiconductors. Thus for values $n\simeq 0.01$ the quantum limit in terms of the magnetic field would be achieved at quite realistic field strengths $H_1 \simeq 10^4$ Oe. At that value the necessary temperature regime ($T<\mu_0$) would be achieved for $T<1$ K.

Of course, the simple calculations presented here only illustrate the possibility of a new type of plasmons propagating in quasi-one-dimensional conductors: for example, dispersion relation (5) may be altered somewhat in the case of a strong Fermi-liquid interaction; the situation would also be complicated by the presence of several valleys in the electron spectrum. In addition, for magnetic fields very close to H_1 and/or frequencies comparable to the plasma frequency a more detailed treatment is necessary; in particular, the finiteness of the temperature should be taken into account. These and other refinements are planned for future publications.

The author is grateful to V. G. Peschansky and Yu. G. Pashkevich for a discussion of the results.

*E-mail: gokhfeld@host.dipt.donetsk.ua

[1)] This is because there is no orbital motion and, hence, no Landau quantization in the one-dimensional case. An analogous situation exists in a two-dimensional electron system in a magnetic field parallel to the plane of motion of the particles (see Sec. 5).

[2)] For this it is necessary that the electron spectrum have at least two valleys with substantially different Fermi velocities.[3,4]

[3)] In the 1D case the Fermi surface in **p** space consists of planes $|p_C| = \sqrt{2m_C\mu_{\pm}}$.

[4)] This term is due to the continuity of the electric displacement and is described by one-half the residue of the function (6) at the point $k=0$. Strictly speaking, the electric field in the sample also contains a screened part that decays with a decrement $\approx\sqrt{4\pi e^2\langle 1\rangle}$. However, in view of the macroscopic depths x_C, the latter can be ignored; this corresponds to the neglect (here and below) of the term of unity in the dielectric function $\epsilon(k,\omega)$.

[1] L. P. Gor'kov, Usp. Fiz. Nauk **144**, 381 (1984) [Sov. Phys. Usp. **27**, 809 (1984)].
[2] A. I. Buzdin and L. N. Bulaevskiĭ, Usp. Fiz. Nauk **144**, 415 (1984) [Sov. Phys. Usp. **27**, 830 (1984)].
[3] O. V. Konstantinov and V. I. Perel', Fiz. Tverd. Tela (Leningrad) **9**, 3051 (1967) [Sov. Phys. Solid State **9**, 2409 (1967)].
[4] D. Pines and J. Schriffer, Phys. Rev. A **124**, 1387 (1961).
[5] V. M. Gokhfel'd, M. A. Gulyanskiĭ, M. I. Kaganov, and A. G. Plyavenek, Zh. Éksp. Teor. Fiz. **89**, 985 (1985) [Sov. Phys. JETP **62**, 566 (1985)].
[6] V. M. Gokhfel'd, M. I. Kaganov, and G. Ya. Lyubarskiĭ, Zh. Éksp. Teor. Fiz. **92**, 523 (1987) [Sov. Phys. JETP **65**, 295 (1987)].
[7] T. Ando, A. B. Fowler, and F. Stern, Rev. Mod. Phys. **54**, 437 (1982).
[8] V. M. Gokhfeld, Fiz. Nizk. Temp. **28**, 304 (2002) [Low Temp. Phys. **28**, 215 (2002)].

Translated by Steve Torstveit

TECHNIQUE OF SUPERLOW TEMPERATURES

Setup for calorimetric measurements at temperatures below 1 K

V. N. Eropkin† and T. V. Chagovets*

B. Verkin Institute for Low Temperature Physics and Engineering, National Academy of Sciences of Ukraine, pr. Lenina 47, 61103 Kharkov, Ukraine

(Submitted April 16, 2003)
Fiz. Nizk. Temp. **29**, 1260–1264 (November 2003)

A compact, top-loading ^{3}He evaporation refrigerator is built for doing heat-capacity studies on various samples at temperatures below 1 K. It uses adsorption pumping and utilizes a portable helium Dewar of the STG-40 type as the cryostat. A calorimetric cell is built which permits investigation of the heat capacity of samples with masses of less than one gram. The lowest measurement temperature is 0.32 K. The dependence of the temperature of the ^{3}He evaporation chamber on the power delivered to it is established. The refrigerator can operate continuously for two hours at a heat load of 50 μW. © *2003 American Institute of Physics.* [DOI: 10.1063/1.1614242]

INTRODUCTION

Many physical problems now require calorimetric measurements at temperatures below 1 K in magnetic fields above 1 T. In particular, such problems include the investigation of ternary intermetallic compounds, which are characterized by an extremely wide spectrum of transformations in all of their subsystems of elementary excitations. Among these compounds are some for which a strong correlation of the electrons leads to the formation of heavy fermions, which is manifested as growth of the electronic component of the heat capacity with decreasing temperature below 4 K. Other compounds of this class display non-Fermi-liquid behavior of the electron subsystem, which is also accompanied by unusual behavior of the low-temperature heat capacity.

As the magnetic subsystem of these compounds can undergo phase transitions in the low-temperature region, it is necessary to study the heat capacity in magnetic fields.

In a number of compounds we have previously observed a superconducting transition at temperatures ranging from 5 to 25 K, depending on the composition.[1] It has not been ruled out that other compounds may exhibit superconductivity at lower temperatures.

One can extract the most information from studies of single-crystal samples, but their masses are usually small, less than a gram, and therefore the measurement cell itself must have small dimensions and a small intrinsic heat capacity.

For these tasks we have designed and built an apparatus for calorimetric measurements, based on a ^{3}He evaporation refrigerator with a loading lock and adsorption pumping, having a short cooling time to the base temperature. The low weight and knock-down construction of the refrigerator makes it transportable; a standard portable Dewar of the STG-40 type may be used as the cryostat, making it possible to use the refrigerator in any laboratory equipped with a helium system.

There are various designs of ^{3}He (Ref. 2) evaporation refrigerators. We tried to choose the variant which would best suit the problems at hand. The refrigerator was designed with the following requirements: working temperature interval $\sim 0.3-3$ K, compactness, short cooldown and heatup time, low consumption of liquid helium and electrical energy.

Heat-capacity measurements are usually made by adiabatic methods of calorimetry, with pulsed or continuous heating. However, the use of such methods in experiments at temperatures below 1 K requires large samples and good thermal isolation, which make for longer cooling times to get the sample down to the lowest temperature. Thermal switches are usually used to reduce this time, but at the expense of additional heat released into the evaporation chamber. For this reason we chose the thermal relaxation method, which does not require adiabatic conditions.

CONSTRUCTION AND WORKING PRINCIPLE OF THE REFRIGERATOR

We designed and built a compact, top-loading evaporation refrigerator intended for physical research at temperatures down to ~ 0.3 K. The height of the part of the refrigerator immersed in the cryostat is 1 m, and the outer diameter is 24 mm. These parameters and the specially designed hermetic locks made it possible to use a standard portable helium Dewar of the STG-40 type as the cryostat. For measurements in magnetic fields we designed and made transition flanges, making it possibility to use a Dewar with a small volume (~ 5 liters) and a diameter of 105 mm as the cryostat. The small diameter of the cryogenic insert makes it possible to use solenoids with a small inner diameter (~ 30 mm), in which one can obtain magnetic fields up to 8 T with good uniformity.

Either ^{3}He or ^{4}He can be used as the coolant in the refrigerator. Its low-temperature part is made as a unit, with control and coolant storage systems. Everything is mounted

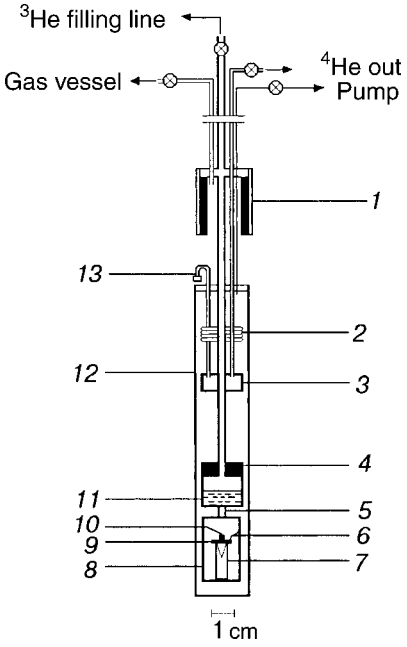

FIG. 1. Diagram of the ^{3}He evaporation refrigerator: *1*—adsorption pump, *2*—throttle, *3*—^{4}He pumping chamber, *4*—adsorbent of the vacuum can, *5*—threaded contact, *6*—thermal coupler, *7*—graphite rod, *8*—jacket of the calorimetric cell, *9*—sapphire substrate with heater deposited on it, *10*—germanium resistance thermometer, *11*—^{3}He evaporation chamber, *12*—vacuum can, *13*—intake tube with filter.

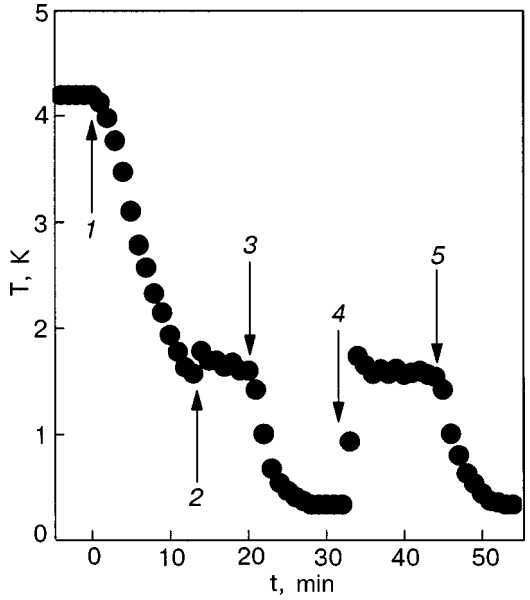

FIG. 2. Diagram of the cooling cycles of the refrigerator: *1*—pumping down of the ^{4}He evaporation chamber; *2*—condensation of ^{3}He into the ^{3}He evaporation chamber; *3*—pumping down of the ^{3}He evaporation chamber; *4*—heating of the adsorption pump and repeated condensation of ^{3}He; *5*—pumping down of the ^{3}He evaporation chamber.

on a movable platform, making the refrigerator an autonomous unit.

The evaporation refrigerator, illustrated schematically in Fig. 1, consists of the following units: ^{3}He evaporation chamber *11* and ^{4}He pumping chamber *3*, placed in vacuum can *12*, adsorption pump *1*, and systems for communications and for the storage and collection of residual helium (not shown in the figure).

The ^{4}He pumping chamber, of toroidal form, was made of copper and was placed on the pumping tube of the ^{3}He evaporation chamber. It serves for condensation of the coolant inside the evaporation chamber and to reduce external heat leakage. It is filled automatically from the outer bath of the cryostat through a throttle *2* and an intake tube with a filter *13*. The throttle had a hydrodynamic resistance to flow of 10^{11} cm^{-3}. The filter is a copper cylinder filled with pressed and baked ultradisperse copper powder. The use of the ^{4}He pumping chamber reduced the expenditure of helium substantially, rendering it unnecessary to to pump out the whole helium bath and making it possible to add helium during an experiment. The ^{4}He evaporation chamber works continuously if the helium level in the external bath of the cryostat is kept above the intake tube. The working temperature of the chamber is $\sim$1.5–1.8 K.

The ^{3}He evaporation chamber is a copper vessel with a volume of 2 cm^3. The bottom of the chamber has a threaded socket for mounting the measurement cell. The vapor is pumped out by an adsorption pump placed in the helium bath of the cryostat and having its own vacuum can. The synthetic adsorbent SKN is used in the pump. The amount of adsorbent was calculated to be able to absorb all the coolant from the evaporation chamber.[3] The vacuum can of the adsorption pump is an inverted cup, from under which a drainage tube discharges into the vapor region of the cryostat (gas vessel). The pump is equipped with a heater for regeneration of the adsorbent, the electrical resistance of which is 130 Ω.

The refrigerator works as follows. At room temperature a small amount of ^{4}He ($\sim$1 mm Hg) is admitted into the evacuated vacuum can to improve the heat exchange. At low temperature this helium is absorbed by the inner adsorption pump *4*, which is placed on the ^{3}He evaporation chamber. During cooling the insert is immersed in liquid helium and the pump evacuating the ^{4}He chamber is turned on. The drainage tube of the pump is closed off at this stage to prevent the liquid from penetrating under the cup and cooling the adsorbent. The ^{4}He pumping chamber and the ^{3}He evaporation chamber come to a temperature of $\sim$1.5 K in 15 min (Fig. 2), after which the condensation of ^{3}He from the storage cylinder into the ^{3}He chamber can begin. The condensation of the gaseous ^{3}He occurs on the wall of the ^{4}He pumping chamber. To improve the condensation process a screw thread was deposited on the surface of this wall. The condensation of ^{3}He takes 5 min. Then the adsorption pump is cooled. This is done by opening the drainage tube and admitting liquid ^{4}He under the cup, thereby cooling the pump. The time required to establish the working temperature ($\sim$0.3 K) is not more than 10 min.

When all the liquid from the evaporation chamber has been pumped out, the cooling process can be repeated. For this the pump must be warmed to a temperature of $\sim$20–25 K. At such temperatures the desorption of helium from the pump and repeated condensation occurs (Fig. 2). The pump can be warmed in two ways: either it can be raised above the helium level in the outer bath of the cryostat or helium can be evaporated from under the cup with the aid of a heater mounted on the wall of the pump. The recondensation process takes 10 min. After the heater of the adsorption pump is turned off, a new cooling cycle begins.

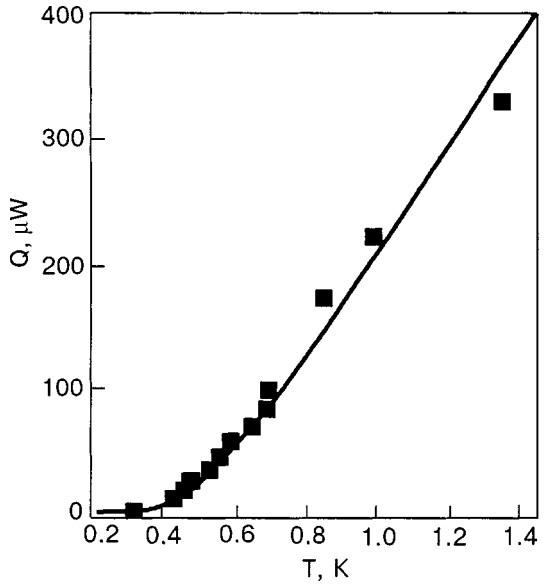

FIG. 3. Dependence of the temperature of the ^{3}He evaporation chamber on the power delivered to it.

The communications system of the evaporation refrigerator is mounted on a separate panel and serves for monitoring and control during operation. The system for storage and collection of residual coolant from the communications system (when taking down the apparatus) is assembled as an individual unit and is connected to the communications system of the refrigerator by a flexible metal hose. For collecting the residual coolant a special adsorption pump is used which may be cooled in a standard portable helium Dewar. A cylinder with a capacity of 1.8 liters is used to store the main supply of ^{3}He.

The operating time and minimum temperature of the refrigerator depend on the heat load. To determine the relationships a copper cylinder equipped with a heater ($\sim 60\ \Omega$) and a RuO_2 resistance thermometer was mounted to the threaded socket. As a test, different voltages were fed to the heater and the temperature was tracked. Figure 3 shows the dependence of the temperature on the power delivered. The external parasitic heat leakage is estimated to be 0.5 μW.

In addition, we performed several tests on the length of time the temperature was maintained. With a constant external heat leak of 50 μW a temperature of 0.6 K was maintained for 2 h. With no external heat leak a temperature of 0.32 K was maintained for more than 4 h and then the test was terminated. In the heat-capacity measurements the heat leak was less than 1 μW.

CONSTRUCTION AND WORKING PRINCIPLE OF THE CALORIMETER

The copper jacket of the calorimetric cell *8* (see Fig. 1) is made in the form a hollow cylinder 15 mm in diameter and is mounted in the ^{3}He evaporation chamber with the aid of a threaded contact *5*. It is equipped with a heater ($\sim 60\ \Omega$) and a resistance thermometer and plays the role of an isothermal shield. Inside the shield is a sapphire substrate with a heater *9* deposited on it and a small germanium resistance thermometer *10* placed at the center of the substrate. Cold is transferred from the shield to the sample, which is mounted on the substrate, through a thermal coupler—a fine copper wire *6* of small diameter, the length and diameter of which must be chosen experimentally. Since the thermal coupling element should be the main path of heat exchange between the shield and substrate, the substrate was thermally isolated from the shield and rested on a graphite rod *7* (9 mm in diameter). Thus the construction has a low thermal conductivity and a long heat-transfer path, since the relaxation time in the sample should be shorter than the relaxation time between the sample and the jacket of the calorimeter.

In the thermal relaxation method used in this device, the temperature of the bath is held constant. The jacket of the calorimeter is stabilized at the necessary temperature, the sample is heated above the temperature of the bath, and then the sample cools exponentially to the initial temperature. The variation of the sample temperature with time t corresponds to the equation

$$T(t)_s = \Delta T \exp(-t/\tau) + T_0, \tag{1}$$

where T_s is the sample temperature, T_0 is the bath temperature, ΔT is the initial temperature difference between sample and bath, τ is a time constant (C_p/K), C_p is the heat capacity of the sample, and K is the thermal conductivity of the thermal coupling element.[4] The thermal conductivity of the thermal coupling element is determined by measuring the temperature difference ΔT between the sample and bath at various heating powers $\dot{Q}$ according to the relation

$$K = \Delta \dot{Q}/\Delta T. \tag{2}$$

If τ and K are measured, the heat capacity C_P is determined from the equation

$$C_p = \tau K. \tag{3}$$

In conclusion we note that in working with this device, which is based on the top-loading transportable ^{3}He evaporation refrigerator with adsorption pumping described above, we have found it to be convenient and reliable. While our tasks include making heat-capacity measurements below 1 K, the refrigerator can also be used to study other physical characteristics, such as thermal conductivity, electrical conductivity, magnetoresistance, etc., since the measurement cell is dismountable from the ^{3}He evaporation chamber. Its compactness and economy makes it extremely useful for doing physical research at ultralow temperatures.

The authors thank Prof. V. M. Dmitriev and A. M. Gurevich for their support and interest in this topic, and V. A. Maidanov for consultation and fruitful discussions.

†Deceased
*E-mail: tchagovets@ilt.kharkov.ua

[1] A. M. Gurevich, V. M. Dmitriev, V. N. Eropkin, B. Yu. Kotur, N. N. Prentslau, V. Suski, A. V. Terekhov, and L. V. Shlyk, Fiz. Nizk. Temp. **27**, 11 (2001) [Low Temp. Phys. **27**, 967 (2001)].
[2] F. Pobell, *Matter and Methods at Low Temperatures*, Springer-Verlag, Berlin (1992).
[3] R. I. Shcherbachenko and V. N. Grigor'ev, Fiz. Nizk. Temp. **24**, 11 (1998) [Low Temp. Phys. **24**, 831 (1998)].
[4] V. N. Bakhman *et al.*, Prib. Nauchn. Issled., No. 2, 21 (1972).

Translated by Steve Torstveit

SHORT NOTES

Anomalous charge transport in a quasi-one-dimensional electron system over liquid helium

S. P. Gladchenko,* Yu. Z. Kovdrya, and V. A. Nikolaenko

B. Verkin Institute for Low Temperature Physics and Engineering, National Academy of Sciences of Ukraine, pr. Lenina 47, 61103 Kharkov, Ukraine

(Submitted April 8, 2003)
Fiz. Nizk. Temp. **29**, 1264–1268 (November 2003)

The conductivity σ in a quasi-one-dimensional electron system over liquid helium is measured in the temperature interval 0.5–1.7 K over a wide range of electron densities n. It is shown that the quantity σ/ne (e is the charge of the electron) initially increases with decreasing temperature and then, after passing through a maximum, begins to decline for $T\approx 1$ K. In this temperature region the value of σ/ne, above a certain value of the drift potential V_d, decreases with increasing V_d. It is conjectured that the anomalous charge transport observed in this study is due either to spatial ordering of the electrons in the quasi-one-dimensional channels or to the formation of many-electron polarons in the nonuniform potential along the channels. © *2003 American Institute of Physics.* [DOI: 10.1063/1.1614243]

Progress in nanoelectronic technology is stimulating active research on two-dimensional conducting systems with restricted geometry. A quasi-one-dimensional electron system over liquid helium was realized in Ref. 1, and in Refs. 2 and 3 the transport of carriers in such a system was considered in detail. It was found that, as in the case of two-dimensional electron systems over liquid helium, the mobility of the carriers for $T>0.8$ K is governed by their interaction with the helium atoms in the vapor, while for $T<0.8$ K the transport characteristics are governed by the interaction of the electrons with thermal oscillations of the liquid surface—ripplons. It has been found[3] that the conductivity of electrons in a quasi-one-dimensional electron system over liquid helium falls off at $T<0.8$ K, that the electron drift velocity v has a nonlinear dependence on the driving electric field $E_\parallel$ in this temperature region, similar to the dependence of v on $E_\parallel$ for a two-dimensional electron crystal. Therefore the authors have concluded that a spatial ordering of the electrons in quasi-one-dimensional channels occurs.

In this paper we report a study of the conductivity σ of electrons over liquid helium in quasi-one-dimensional channels over a wide range of electron densities n in holding fields of up to 900 V/cm. Studies were done in the temperature interval 0.5–1.7 K at a frequency of the measured signal of 100 kHz. In contrast to Ref. 3, where the electrons were held across the channel by a square potential well, the conducting channels in this study were formed by a potential well of quadratic form. In this study we used a profiled dielectric substrate placed a certain height above the liquid helium level. Liquid helium leaking onto the substrate formed ''grooves'' on the surface of the liquid, which in the presence of the holding electric field $E_\perp$ made it possible to create a potential well across the channel. Electrons localized in such a channel move freely along the channel, while their motion perpendicular to the channel is quantized and is oscillatory with a frequency $\omega_0=\sqrt{eE_\perp/mr}$ (here e and m are the charge and mass of the electron, and r is the radius of curvature of the surface of the liquid in the channel). The experimental cell and measurement techniques are described in detail in Ref. 2.

The results obtained are presented in Fig. 1 in the form

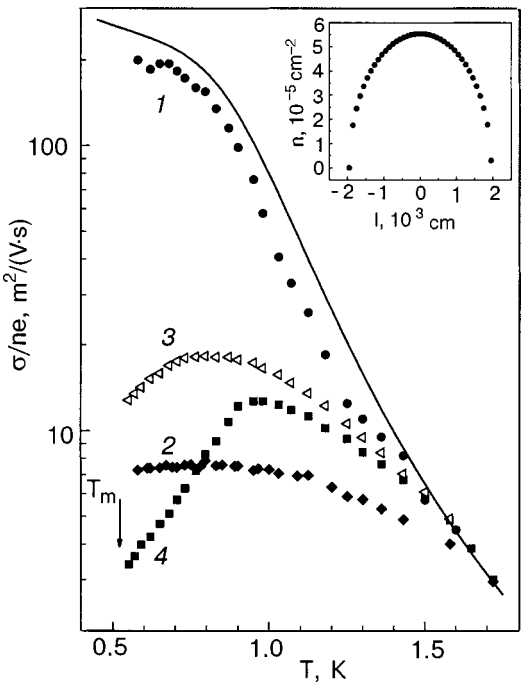

FIG. 1. Temperature dependence of the value of σ/ne for different values of the electron density n [cm^{-2}]: 2.18×10^5 (*1*), 5.77×10^6 (*2*), 1.35×10^8 (*3*), 1.7×10^8 (*4*). The solid curve is the theoretical calculation for a quasi-one-dimensional system.[6] The inset shows the calculated distribution of the electron density across the channel.

the dependence of σ/ne on the temperature T for different values of the electron density in the channel. The technique used to measure σ is analogous to that of Ref. 2. In constructing the curves *1*, *3*, and *4* we used the theoretical value of the mobility at 1.6 K. The inset shows the distribution of electrons across the channel for an average density of 1.4×10^8 cm^{-2}, obtained with the use of the calculation of Ref. 4. It is seen that n is substantially nonuniform along the channel. Curve *1* in Fig. 1 was obtained for an electrically neutral substrate and pertains to the case of a low electron density in the channel, when the electrons form a linear chain. The value of σ/ne for this curve increases exponentially in the region of gas scattering of electrons. At lower temperatures, in the region of ripplon scattering, the temperature dependence of σ/ne is smoother. Curve *2* describes the case when an electric charge is deposited on the substrate. It is seen that the electron mobility is substantially lower for a charged substrate and is practically independent of T at low temperatures. In the low-temperature region the mobility is apparently governed by the tunneling of electrons between the potential wells formed by electrons localized on the solid dielectric substrate. The values of σ/ne for curve *2* were determined under the assumption that there are two channels of carrier scattering: 1) scattering of electrons on helium atoms in the vapor and on ripplons, as in the case of the uncharged substrate; 2) scattering on potential variations caused by the presence of charges on the solid substrate. Furthermore, it was assumed that the electron mobility arising due to the presence of variations of the potential is independent of temperature.

Curves *3* and *4*, taken at a value of the drift potential $V_d \approx 30$ mV, pertain to the case of wide conducting channels with a high electron density. It is seen that the temperature dependence of σ/ne for such channels differs from that represented by curves *1* and *2*. The value of σ/ne, after passing through a maximum, the position of which depends on the electron density, begins to decrease with decreasing T.

Figure 2 shows the dependence of the quantity σ/ne on the value of the drift potential V_d, corresponding to curve *3* in Fig. 1. It is seen in Fig. 2 that in the high-temperature region (1.5 K) the value of σ/ne is practically independent of V_d. In the low-temperature region, where the anomalous temperature dependence is observed, it is seen that above a certain value of V_d the value of σ/ne decreases with increasing V_d. In that temperature region the carrier transport is of a nonlinear characteristic at sufficiently high values of the driving field.

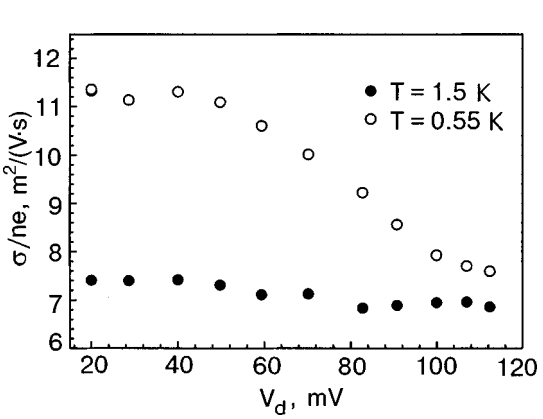

FIG. 2. Dependence of σ/ne on the value of the drift potential V_d in a quasi-one-dimensional electron system.

One of the possible explanations for the anomalous electron transport in narrow channels, which was proposed in Ref. 3, consists in the fact that in quasi-one-dimensional channels as in the case of a two-dimensional electron system, spatial ordering of the electrons occurs, with the formation of dimples beneath them. It was shown in Ref. 5 that in narrow channels formed by a parabolic potential (as was the case in the present study) the effective mass of a dimple is anisotropic and extremely large ($\sim 10^5 m_e$). It can be assumed that at sufficiently low temperatures the motion of these massive dimples will be determined by the viscosity η of the liquid helium. Since the viscosity η of liquid helium increases with temperature for $T \leqslant 1.1$ K, the mobility of the electron–dimple complexes should decrease. Here it should be kept in mind that, since the average distance between electrons and, hence the dimensions of the dimples was $\sim 10^{-4}$ cm, it is possible that the motion of the dimples takes place in a transitional regime between viscous and Knudsen, so that the temperature dependence of the mobility of the dimple will not be governed entirely by the dependence of η on T. It is not ruled out that the character of the motion of the dimples is influenced to some degree by the surface viscosity of liquid helium.

The conjecture that dimples are formed in the quasi-one-dimensional channels at $T < 0.8$ K is also supported by the dependence of σ/ne on the drift potential. For a quasi-one-dimensional system in the ripplon scattering region the mobility should increase with increasing value of the driving electric field.[7] In the present study we observed the opposite tendency for the quasi-one-dimensional channels: σ/ne decreases with increasing V_d. Such a dependence, which was also observed in Ref. 3, may serve as additional evidence of ordering in the electron system.

It is interesting to note that the temperature at which the decrease in σ/ne starts is considerably higher than the melting temperature of the two-dimensional electron crystal of the same density. Crystallization in a two-dimensional electron layer of restricted geometry has been studied theoretically in Refs. 8–10 by the Monte Carlo and molecular dynamics methods. It was shown that, depending on the conditions for realization of the two-dimensional electron system of restricted geometry, the crystallization temperature can be higher or lower than the analogous value for a system of large dimensions with the same particle density.

Another possible mechanism that could lead to anomalous transport in quasi-one-dimensional channels may be due to the formation of many-electron polarons. Such polarons can form, e.g., as a consequence of the variation of the potential along the channels due to the nonuniform charge density on the thin film along the sides of the conducting channels or because of a variation of the depth of the channels due to ellipticity of the nylon filaments forming the ''liquid'' channel. At those places where the potential wells are located the electron density is higher, and that leads to a microscopic

deflection of the liquid and, consequently, to the formation of many-electron polarons. The effective mass of such polarons will be very large, and the kinetic characteristics should be largely analogous to those of dimples in an electron crystal. Unfortunately, calculations of the properties of such polarons are lacking at the present time.

Thus in this study we have observed anomalous transport in quasi-one-dimensional electron channels formed by a parabolic potential well. We have conjectured that this anomalous transport is due to either spatial ordering of the electrons in one-dimensional channels or to the formation of many-electron polarons.

The experiments will be continued into the region of higher electron densities and holding electric fields.

The authors thank Yu. P. Monarkha and S. S. Sokolov for interest in this study and a discussion of the results.

*E-mail: sgladchenko@ilt.kharkov.ua

[1] Yu. Z. Kovdrya and V. A. Nikolaenko, Fiz. Nizk. Temp. **18**, 1278 (1992) [Low Temp. Phys. **18**, 894 (1992)].
[2] S. P. Gladchenko, V. A. Nikolaenko, Yu. Z. Kovdrya, and S. S. Sokolov, Fiz. Nizk. Temp. **27**, 3 (2001) [Low Temp. Phys. **27**, 1 (2001)].
[3] P. Glasson, V. Dotsenko, P. Fozooni, M. J. Lea, W. Bailey, G. Papageorgiou, S. E. Anderson, and A. Kristinsen, Phys. Rev. Lett. **87**, 176802-1 (2001).
[4] O. I. Kirichek, Yu. P. Monarkha, Yu. Z. Kovdrya, and V. N. Grigor'ev, Fiz. Nizk. Temp. **19**, 458 (1993) [Low Temp. Phys. **19**, 323 (1993)].
[5] S. S. Sokolov and N. Studart, Phys. Rev. B **60**, 1556 (1999).
[6] S. S. Sokolov, Guo-Qiang Hai, and N. Studart, Phys. Rev. B **51**, 5977 (1995).
[7] S. S. Sokolov, Guo-Qiang Hai, and N. Studart, Phys. Rev. B **52**, 15509 (1995).
[8] Yu. E. Lozovik, Usp. Fiz. Nauk **153**, 356 (1987).
[9] G. A. Farias and F. M. Peeters, Phys. Rev. B **55**, 3763 (1997).
[10] K. M. S. Bajaj and R. Mehrotra, Physica B **194–196**, 1235 (1994).

Translated by Steve Torstveit

Phonon Raman scattering in $LaMn_{1-x}Co_xO_3$ ($x=0$, 0.2, 0.3, 0.4, and 1.0)

V. P. Gnezdilov* and A. V. Yeremenko

B. Verkin Institute for Low Temperature Physics and Engineering of the National Academy of Sciences of Ukraine, 47 Lenin Ave., Kharkov 61164, Ukraine

Yu. G. Pashkevich

A. A. Galkin Donetsk Phystech of the National Academy of Scienses of Ukraine, 72 R. Luksemburg Str., Donetsk 83114, Ukraine

P. Lemmens

Physikalisches Institut, RWTH Aachen, D-52056 Aachen, Germany; Max Planck Institute for Solid State Research, D-70569 Stuttgart, Germany

G. Güntherodt

Physikalisches Institut, RWTH Aachen, D-52056 Aachen, Germany

S. V. Shiryaev, G. L. Bychkov, and S. N. Barilo

Institute of Physics of Solids & Semiconductors, Academy of Sciences, Minsk 220072, Belarus
(Received April 24, 2003)
Fiz. Nizk. Temp. **29**, 1269–1272 (November 2003)

The Raman-active phonons in perovskite-like $LaMn_{1-x}Co_xO_3$ ($x=0$, 0.2, 0.3, 0.4, and 1.0) are studied by measuring the Raman spectra at temperatures of 295 and 5 K. The changes in the spectra with Co doping are correlated with the decrease of the orthorhombic distortions. Surprisingly, more phonon lines are observed than are allowed for the rhombohedral $LaCoO_3$ structure. © *2003 American Institute of Physics.* [DOI: 10.1063/1.1614244]

The manganese perovskites of the type $R_{1-x}A_xMnO_3$ (R=rare earth, A=Ca, Sr, Ba, or Pb) have been subject of scientific investigations for many decades. Recently, this interest has been renewed due to the observation of a colossal magnetoresistance[1,2] and of charge, spin, and orbital ordering effects as a function of the Mn^{3+}/Mn^{4+} ratio.[3–5] Another system, Mn-site-doped, with the composition $LaMn_{1-x}D_xO_3$ (D=Cr, Fe, Co, or Ni) was intensively studied in the 1960s, but colossal magnetoresistance in those compounds was not mentioned until the 1990s.[6] While Raman spectra of La-site-doped compounds have been reported in numerous of publications,[7–13] surprisingly nothing was done on Mn-site-doped compounds. In this work we report the results of an optical phonon study in the perovskite oxides $LaMn_{1-x}Co_xO_3$ ($x=0$, 0.2, 0.3, 0.4, and 1.0). The end member of this system, $LaCoO_3$, has been the subject of continuing interest since the 1950s due to unusual magnetic properties and two spin-state transitions.[14,15]

Raman scattering measurements were carried out in quasi-backscattering geometry using 514.5 nm argon laser line. The incident laser beam of 10 mW power was focused onto a 0.1 mm spot of the mirror-like chemically etched as-grown crystal surface. The sample was mounted on the holder of a He-gas-flow cryostat using silver glue. The scattering light was analyzed with a DILOR XY triple spectrometer combined with a nitrogen-cooled CCD detector. The measurements were done in the $xx(zz)$ scattering configuration, where x and z are the [100] and [001] quasicubic directions, respectively.

The structural properties of $LaMn_{1-x}Co_xO_3$ have been characterized in several publications.[15–19] The crystal structures of the end members, $LaMnO_3$ and $LaCoO_3$, were found to be orthorhombic (space group $Pnma$, $Z=4$)[16] and rhombohedral (space group $R\bar{3}c$, $Z=2$),[17] respectively. The compounds with $0.15<x<0.50$ have been found to be orthorhombic.[18,19] When $x>0.50$ and near to 1.0, the compounds have a rhombohedral structure.[19] Around the 0.5 doping level the compounds show a mixture of two structural

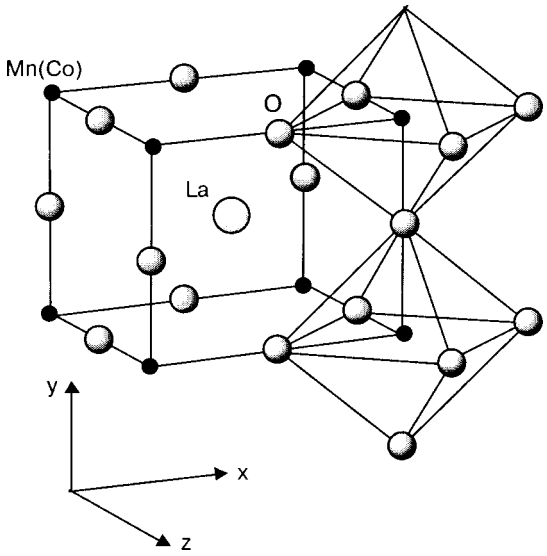

FIG. 1. Unit cell of the simple perovskite structure.

TABLE I. Factor group analysis and selection rules for the zone-center vibrational modes of orthorhombic $LaMnO_3$ and rhombohedral $LaCoO_3$.

Sample and space group	Atom	Number of equivalent positions (Wyckoff notation)	Site symmetry	Irreducible representation of modes	Activity and selection rules
$LaMnO_3$	La	4(c)	C_s	$2A_g + B_{1g} + 2B_{2g} + B_{3g} +$	$\Gamma_{\text{Raman}} = 7A_g + 5B_{1g} +$
Pnma				$+A_u + 2B_{1u} + B_{2u} + 2B_{3u}$	$+7B_{2g} + 5B_{3g}$
(D_{2h}^{16})	Mn	4(b)	C_i	$3A_u + 3B_{1u} + 3B_{2u} + 3B_{3u}$	$\Gamma_{IR} = 9B_{1u} + 7B_{2u} + 9B_{3u}$
$Z = 4$	O_1	4(c)	C_s	$2A_g + B_{1g} + 2B_{2g} + B_{3g} +$	$\Gamma_{\text{acoustic}} = B_{1u} + B_{2u} + B_{3u}$
				$+ A_u + 2B_{1u} + B_{2u} + 2B_{3u}$	$\Gamma_{\text{silent}} = 8A_u$
	O_2	8(d)	C_1	$3A_g + 3B_{1g} + 3B_{2g} +$	A_g: a_{xx}, a_{yy}, a_{zz}
				$+ 3B_{3g} + 3A_u + 3B_{1u} +$	B_{1g}: a_{xy}; B_{2g}: a_{xz}; B_{3g}: a_{yz}
				$+ 3B_{2u} + 3B_{3u}$	
$LaCoO_3$	La	2(b)	C_{3i}	$A_{1u} + 2A_{2u} + B_{2u} + 2E_u$	$\Gamma_{\text{Raman}} = A_{1g} + 4E_g$
$R\bar{3}c$	Co	2(a)	D_3	$A_{2g} + A_{2u} + E_g + E_u$	$\Gamma_{IR} = 3A_{2u} + 5E_u$
(D_{3d}^6)	O	6(e)	C_2	$A_{1g} + 2A_{2g} + 3B_g + 3E_g +$	$\Gamma_{\text{acoustic}} = A_{2u} + E_u$
$Z = 2$				$+ A_{1u} + 2A_{2u} + 3E_u$	$\Gamma_{\text{silent}} = 3A_{2g} + 2A_{1u}$
					A_{1g}: $a_{xx} + a_{yy}$, a_{zz}
					E_g: $(a_{xx} - a_{yy}, a_{xy})$, (a_{xz}, a_{yz})

phases, the orthorhombic and rhombohedral.[19] The idealized cubic perovskite structure of the $LaMn(Co)O_3$ crystal is shown in Fig. 1. The orthorhombic *Pnma* structure can be obtained by two consecutive rotations of the $Mn(Co)O_6$ octahedra around the [010] and [101] directions of cubic perovskite. The rhombohedral *R*3*c* structure is generated by the rotation of the same octahedral about the cubic [111] direction.

Results of a group-theoretical analysis for zone-center vibrations are presented in Table I for orthorhombic $LaMnO_3$ and rhombohedral $LaCoO_3$. Of the total 30 Γ-point phonon modes, only 5 $(A_{1g}+4E_g)$ are Raman active for the rhombohedral $LaCoO_3$ structure, and of 60 Γ-point phonon modes, 24 $(7A_g+5B_{1g}+7B_{2g}+5B_{3g})$ are Raman active for the orthorhombic $LaMnO_3$ structure. The increase in the phonon modes from 5 to 24 on going from rhombohedral to orthorhombic structure is due to (i) lowering of crystal symmetry which splits the doubly degenerate E_g modes into nondegenerate $B_{2g}+B_{3g}$, (ii) displacement of oxygen atoms into the lower symmetry site of the La plane, which introduces new Raman-active vibrations, (iii) doubling of the unit cell, which folds the zone-boundary modes of the rhombohedral structure into zone-center modes of the orthorhombic structure.

Raman spectra of $LaMn_{1-x}Co_xO_3$ compounds at 295 K are shown in Fig. 2. Room-temperature measurements, lattice dynamical calculations, and an assignment of the Raman modes of undoped $LaMnO_3$ were done previously by Iliev *et al.*[20] Our spectra of $LaMnO_3$ are consistent with the spectra at 300 K reported earlier.[9,20] Three broad bands centered near 280, 490, and 610 cm^{-1} are observed. The line near 280 cm^{-1} was assigned to a rotation-like mode.[20] The other two bands near 490 and 610 cm^{-1} are related to Jahn–Teller octahedral distortions.[20] Given that the Jahn–Teller distortions are static and ordered in orthorhombic $LaMnO_3$, these bands are Raman-allowed modes of bending- and stretching-type character, respectively. The fourth peak in the spectrum at $\sim$310 cm^{-1} is associated with vibrations of the apical

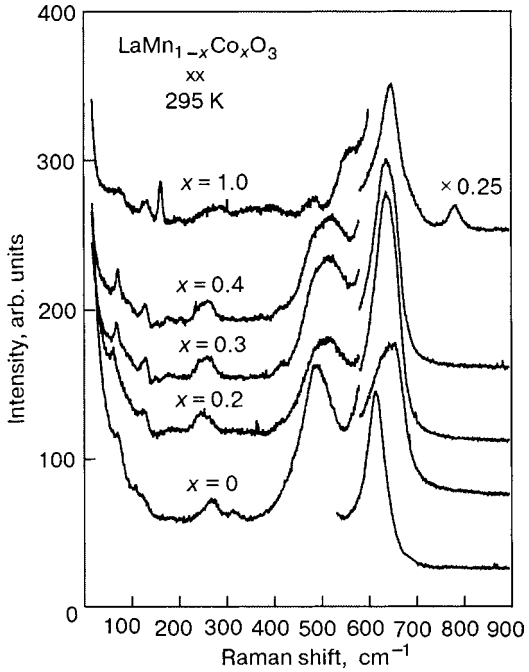

FIG. 2. Raman spectra of single crystals of $LaMn_{1-x}Co_xO_3$ at 295 K. The spectra are shifted for clarity. The right part of the spectra are multiplied by a factor indicated there.

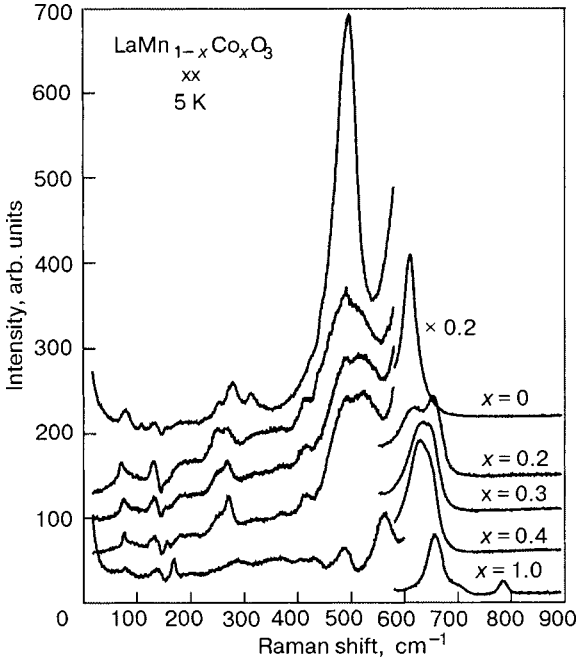

FIG. 3. Raman spectra of single crystals of $LaMn_{1-x}Co_xO_3$ at 5 K. The spectra are shifted for clarity. The right part of the spectra are multiplied by a factor indicated there.

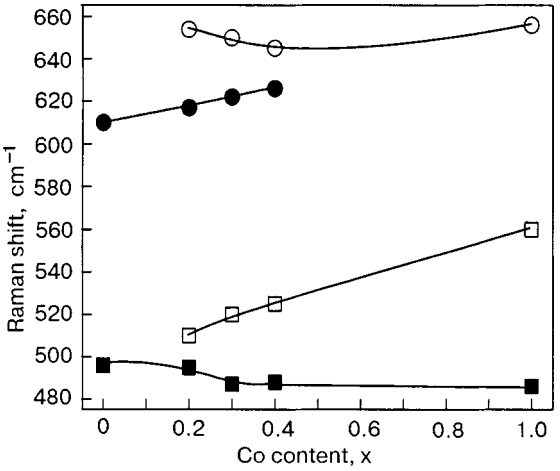

FIG. 4. Raman shift of some high-frequency phonon modes versus x in $LaMn_{1-x}Co_xO_3$ single crystals. The lines are a guide to the eye.

oxygen (O_1) atoms along the x direction. The spectra of the $x=0.2$, 0.3, and 0.4 samples look quite similar to the $x=0$ sample, except for the width and position of the bands in the region of 500 and 600 cm^{-1}. At room temperature the spectra of the $LaCoO_3$ sample exhibit peaks centered near 130, 160, 480, 555, 610, and 780 cm^{-1}, and four broad bands at 70, 270, 340, and 400 cm^{-1}.

Upon lowering of the temperature, more phonon peaks become visible in the Raman spectra of $LaMn_{1-x}Co_xO_3$. In Fig. 3 we present spectra measured at 5 K.

$LaMnO_3$: The spectra on the $LaMnO_3$ sample show 10 resolved peaks at 80, 110, 130, 154, 184, 257, 280, 314, 496, and 610 cm^{-1}. The strong high-frequency lines in the sample studied are broader than the corresponding lines in the spectra measured earlier.[9,20] The reason for this broadening is the presence of a small amount of excess oxygen in our sample. By using x-ray diffraction, magnetic susceptibility, and chemical analysis, the oxygen content was estimated to be 3.071.

$LaMn_{1-x}Co_xO_3$ (x=0.2, 0.3, 0.4): It is well known that Raman spectroscopy is a sensitive tool for the study of both local and spatially coherent structural changes. The spectra of the samples with $x>0$ differ from that of pure $LaMnO_3$, and in the following we will concentrate on the effect of Mn substitution by Co on the rotation-, bending-, and stretching-like vibrations of the MnO_6 octahedra. The rotational mode at 280 cm^{-1} in $LaMnO_3$ shifts to lower energy ($\sim$270 cm^{-1}) in the samples with $x=0.2$, 0.3, and 0.4. The frequency of this mode is a measure of the degree of the rotational distortions (the averaged angle of octahedral tilts). For example, in comparing the spectra of the more-distorted $YMnO_3$ and less-distorted $LaMnO_3$, a large shift from 396 to 284 cm^{-1} was observed.[20] Therefore, the softening of the rotation-like mode with Co doping is an indication of a decreasing orthorhombic distortion.

The scattering intensity of the phonon modes at 496 and 610 cm^{-1} decreases in the Co-doped samples. The decreasing intensity of these modes can reasonably be related with the reduction of the Jahn–Teller distortions in the averaged structure, introduced by the presence of Co. Moreover, each of these modes splits into two components. This splitting can be attributed to the coexistence of two types of octahedra, namely MnO_6 and CoO_6, in the composition. The frequency positions of some high-frequency lines are plotted in Fig. 4.

$LaCoO_3$: The spectra of $LaCoO_3$ are, however, somewhat surprising since (i) they are not similar to the spectra of isostructural rhombohedral $LaMnO_{3+\delta}$,[9,10,21,22] $La_{1-x}A_xMnO_3$,[9,10] and $LaAlO_3$;[22] (ii) according to the neutron-diffraction data the sample should have a rhombohedral symmetry D^6_{3d} and only 5 Raman-active phonon modes are expected. The main peaks in the spectra are at 75, 135, 169, 486, 560, 656, and 785 cm^{-1}. Note that high-frequency lines, with large intensity in $LaCoO_3$ even at room temperature, are not observed in the spectra of isostructural compounds. Moreover, wide bands centered approximately at 198, 281, 366, 407 cm^{-1} and a shoulder at 702 cm^{-1} are present in the spectrum. Probably a part of the features observed in these spectra are a contribution of second-order Raman processes, but it is more reasonable to assume that the $LaCoO_3$ crystal has a lower than rhombohedral symmetry. Precise measurements of polarized Raman spectra could provide valuable information about the structure of this compound.

In conclusion, we have performed a phonon Raman study on the $LaMn_{1-x}Co_xO_3$ ($x=0$, 0.2, 0.3, 0.4, and 1.0) system at temperatures of 295 and 5 K. Characteristic changes have been observed in the phonon spectra with Co concentration and are assigned to the reduction of octahedral distortions. The spectra of pure $LaCoO_3$ exhibit a larger number of peaks than are allowed for the rhombohedral (D^6_{3d}) symmetry, and a more accurate determination of the crystal structure of this compound is necessary.

This work was supported by INTAS Grant No. 01-0278 and NATO Collaborative Linkage Grant PST.CLG.977766.

*E-mail: gnezdilov@ilt.kharkov.ua

[1] R. Von Helmolt, J. Wecker, B. Holzapfel, L. Schultz, and K. Samwer, Phys. Rev. Lett. **71**, 2331 (1993).
[2] S. Jim, T. H. Tiefel, M. McCormack, R. A. Fastnacht, R. Manesh, and L. H. Chen, Science **264**, 413 (1994).
[3] H. Yoshizawa, H. Kawano, T. Tomioka, and Y. Tokura, Phys. Rev. B **52**, 13145 (1995).
[4] J. B. Googenough, Phys. Rev. **164**, 785 (1967).
[5] C. N. Rao, J. Phys. Chem. B **104**, 5877 (2000).
[6] J. H. Park, S. W. Cheong, and C. T. Chen, Phys. Rev. B **55**, 11072 (1997).
[7] V. B. Podobedov, A. Weber, D. B. Roberto, J. P. Rice, and H. D. Drew, Solid State Commun. **105**, 589 (1998).
[8] V. B. Podobedov, A. Weber, D. B. Roberto, J. P. Rice, and H. D. Drew, Phys. Rev. B **58**, 43 (1998).
[9] E. Granado, N. O. Moreno, A. Garcia, J. A. Sanjurjo, C. Rettori, I. Torriani, S. B. Oseroff, J. J. Neumeier, K. J. McClellan, S.-W. Cheong, and Y. Tokura, Phys. Rev. B **58**, 11435 (1998).
[10] Chaitali Roya and R. S. Budhari, J. Appl. Phys. **85**, 3124 (1999).
[11] E. Granado, A. Garcia, J. A. Sanjurjo, C. Rettori, I. Torriani, F. Prado, R. D. Sanchez, A. Caneiro, and S. B. Oseroff, Phys. Rev. B **60**, 11879 (1999).
[12] E. Liarokapis, Th. Leventouri, D. Lampakis, D. Palles, J. J. Neumeier, and D. H. Goodwin, Phys. Rev. B **60**, 12758 (1999).
[13] M. V. Abrashev, J. Bäckström, L. Börjesson, M. Pissas, N. Kolev, and M. N. Iliev, Phys. Rev. B **64**, 144429 (2001).
[14] Kichizo Asai, Atsuro Yoneda, Osamu Yokokura, J. M. Tranquada, G. Shirane, and Key Kohn, J. Phys. Soc. Jpn. **67**, 290 (1998) (and references therein).
[15] P. G. Radaelli and S.-W. Cheong, Phys. Rev. B **66**, 094408 (2002).
[16] J. B. A. A. Elemans, B. Van Laar, K. R. Van der Veen, and B. O. Loopstra, J. Solid State Chem. **3**, 238 (1971).
[17] G. Thornton, B. C. ToField, and A. W. Hewat, J. Solid State Chem. **61**, 301 (1986).
[18] G. H. Jonker, J. Appl. Phys. **37**, 1424 (1966).
[19] J. B. Goodenough, A. Wold, R. J. Arnott, and N. Menyuk, Phys. Rev. **124**, 372 (1961).
[20] M. N. Iliev, M. V. Abrashev, H.-G. Lee, V. N. Popov, Y. Y. Sun, C. Thomsen, R. L. Meng, and C. W. Chu, Phys. Rev. B **57**, 2872 (1998).
[21] E. Granado, J. A. Sanjurjo, C. Rettori, F. Prado, R. D. Sanches, A. Caneiro, and S. B. Oseroff, Phys. Status Solidi **220**, 609 (2000).
[22] M. V. Abrashev, A. P. Litvinchuk, M. N. Iliev, R. L. Meng, V. N. Popov, V. G. Ivanov, R. A. Chakalov, and C. Thomsen, Phys. Rev. B **59**, 4146 (1999).

Translated by Steve Torstveit

ERRATA

This paper was originally published in the June 2003 issue of *Low Temperature Physics*. It is reprinted here with the corrections reported by one of the authors. The publisher apologizes for the errors.

Erratum: Thermal conductivity of solid parahydrogen with methane admixtures [Low Temp. Phys. 29, 527–529 (June 2003)]

A. I. Krivchikov* and O. A. Korolyuk

B. Verkin Institute for Low Temperature Physics and Engineering of the National Academy of Sciences of Ukraine, 47, Ave. Lenin, Kharkov, 61103, Ukraine

V. V. Sumarokov, J. Mucha, P. Stachowiak, and A. Jeżowski

W. Trzebiatowski Institute for Low Temperature Physics and Structure Research of the Polish Academy of Sciences, P.O. Box 937, 50-950 Wroclaw, Poland

The thermal conductivity of a solid parahydrogen crystal with methane admixtures was measured in the temperature range 1.5 to 8 K. Solid samples were grown from the gas mixtures at 13 K. The concentration of CH_4 admixture molecules in the gas varied from 5 to 570 ppm. A very broad thermal conductivity peak with an absolute value of about 110 W/(m·K) was observed at 2.6 K. The data were interpreted using Callaway's model with resonance scattering of phonons by quasilocal vibrations of CH_4 molecules and phonon–grain boundary and phonon–phonon scattering. As grain boundary scattering increases, the broadening of the peak decreases. The analysis shows that a solid mixture of p-H_2 and CH_4 is a heterogeneous solution for CH_4 concentration higher than 0.1 ppm. © *2003 American Institute of Physics.*
[DOI: 10.1063/1.1582336]

Crystalline parahydrogen can be used as an ''inert'' matrix to study the dynamics of matrix-isolated atoms and molecules and their interaction with the crystal environment.[1–5] The thermal conductivity is very sensitive to the dynamic impurity–matrix interaction. At liquid-helium temperatures ($T<\Theta$) the inelastic anharmonic phonon–phonon U processes in p-H_2 freeze out. A considerable fraction of the p-H_2 molecules are in the rotational ground state. As a result, a defect-free pure p-H_2 crystal has a very high thermal conductivity.[6–9] The introduction of even small amounts of molecular or atomic impurity decreases strongly the value and temperature dependence of the thermal conductivity $K(T)$ at temperatures near the phonon peak.[9–11] The main source of phonon scattering is the dynamic disorder produced in the crystal by the sharp mass difference between the substitution impurity and the matrix molecule. Another factor reducing $K(T)$ could be resonance phonon scattering by molecular clusters—orthohydrogen clusters or impurity molecules with rotational degrees of freedom.[12,13]

In the present study $K(T)$ of pure p-H_2 and CH_4-doped p-H_2 was measured to determine how the rotational motion of the CH_4 molecules affects $K(T)$ in p-H_2. A CH_4 molecule in a H_2 matrix can be treated as a heavy point defect $[(m_{CH_4}-m_{H_2}/m_{H_2})=7]$ and as a weakly hindered quantum CH_4 rotor.[1,2] Strong resonance phonon scattering by the rotational CH_4 excitations has been detected previously. It is manifested as a dip in the temperature dependence $K(T)$ for solid krypton with CH_4 impurity.[14]

The experiment was performed using a specially designed liquid-^{4}He cryostat.[15] The samples were prepared and $K(T)$ was measured directly in a glass ampul (6.7 mm in diameter and 67 mm long) in the sample chamber of the cryostat. The samples were grown from p-H_2 gas near 13 K. After controlled cooling down to 4.2 K, $K(T)$ of the sample was measured by the steady-state flow method in the temperature range 1.5–8 K. The samples were prepared using H_2 gas, 6.0 (99.9999 vol %, Messer Co.) and CH_4 gas (99.95%). The chemical impurities in H_2 were $O_2 \leqslant 0.5$ ppm, $N_2 \leqslant 0.5$ ppm, $H_2O \leqslant 0.5$ ppm, $HC \leqslant 0.1$ ppm, $CO(CO_2) \leqslant 0.1$ ppm. The CH_4 gas contained 1.76% CH_3D, 0.12% CHD_3, 0.043% N_2, and 0.007% O_2. Parahydrogen containing less than 0.2% orthohydrogen was obtained by conversion of L-H_2 in contact with $Fe(OH)_3$ below 20 K. The gas mixtures were prepared in a stainless steel vessel at room temperature. The error in the estimated CH_4 concentration in the mixture was less than 20%. Optical polarized light observation showed that the solid samples all consisted of several (two or three) parts, which differed with respect to the directions of the **c** axis of their hcp lattice. Unlike pure p-H_2, the p-H_2–CH_4 samples were multicolored and their colors changed with the angle between the light polarization vector and the **c** axis.

$K(T)$ was measured for several pure p-H_2 samples and $(p\text{-}H_2)_{(1-c)}(CH_4)_c$ solutions. The CH_4 concentration (c) in the initial gas mixture varied from 5 to 570 ppm. The experimental temperature dependences $K(T)$ for pure p-H_2 in this work and in the published data[7–9] are shown in Fig. 1. $K(T)$ for pure p-H_2 at temperatures near the phonon peak agrees

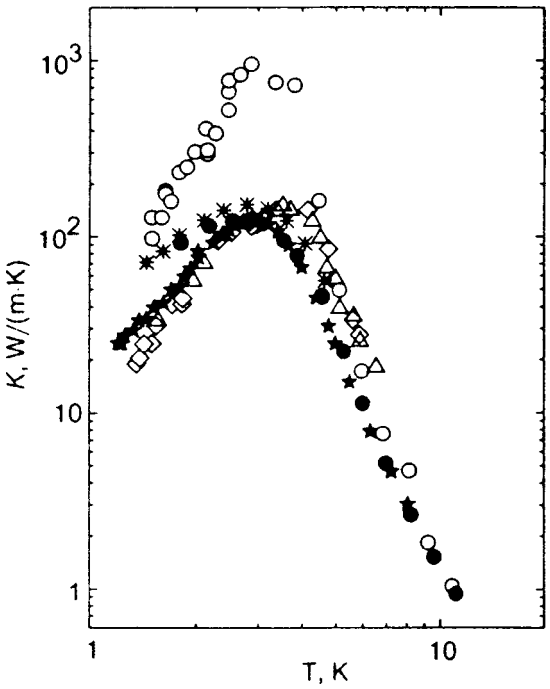

FIG. 1. The temperature dependence of the thermal conductivity of solid parahydrogen. ○ (Ref. 8); ● (Ref. 9); ◇, △ (Ref. 7)—for p-H_2 with 0.2% o-H_2 and p-H_2 with 0.34% o-H_2, accordingly; ⋆, *—present data for samples 1 and 2, respectively.

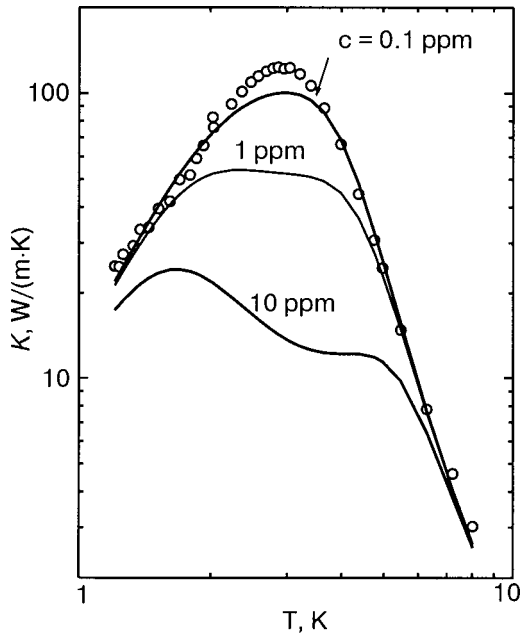

FIG. 2. The temperature dependence of the thermal conductivity of parahydrogen with a CH_4 admixture. The points are our experimental data for pure parahydrogen; the solid lines are the theoretical calculations for $c=0.1$, 1, and 10 ppm CH_4 in p-H_2.

well with the published data,[7,9] but it is one-tenth the record-high value reported in.[8] The good agreement observed for the thermal conductivity in pure p-H_2 measured in three independent experiments could be due to the close isotopic (natural) compositions of the H_2 gas used in this work. In other words $K(T)$ at its peak was limited by phonon scattering by H_2 isotopes, mainly HD molecules. The isotopic ratio $R=[D]/[H]$ for H_2 with the natural composition is $(1.39-1.56)\cdot 10^{-4}$. Mass-spectrometric analysis of H_2 gas showed that HD molecules were present in the initial gas. The large difference between the record-high value of $K(T)$ and the results of this study can be interpreted as an isotopic effect in $K(T)$ for p-H_2. The isotopic composition of H_2 was not specified in Ref. 8. However, judging from the value of the $K(T)$ peak, the HD content in H_2 is an order of magnitude lower than in gas with the natural isotopic composition. At temperatures below the phonon peak the structural imperfections of the sample affect $K(T)$. Above the peak $K(T)$ is influenced by U processes which are in turn sensitive to the hcp lattice anisotropy of p-H_2.[16] The contribution of the CH_4 impurity to $K(T)$ in solid p-H_2 can be detected only if it exceeds the isotopic effect. Figure 2 shows the calculated $K(T)$ curves for p-H_2 with different CH_4 concentrations (0.1, 1, and 10 ppm) assuming that the CH_4 molecules scatter phonons as heavy point defects.

The experimental curves $K(T)$ for pure p-H_2 and three p-H_2–CH_4 samples are shown in Fig. 3. $K(T)$ for a sample with 500 ppm CH_4 is only slightly lower than for pure p-H_2 and is even higher than for the sample with 28 ppm CH_4. The CH_4 effect on $K(T)$ in p-H_2 is found to be weak. One reason for this could be the very low solubility of CH_4 in solid H_2 (less than 0.1 ppm). The experimental samples were heterogeneous solid solutions. The main factors limiting the thermal conductivity are phonon scattering by grain boundaries, HD impurity, and U processes. We note that the spectroscopy of matrix-isolated molecules in solid H_2 samples with 10 ppm grown at $T\approx 8$ K detected no significant deviation of CH_4 from a random configuration distribution.[1,2]

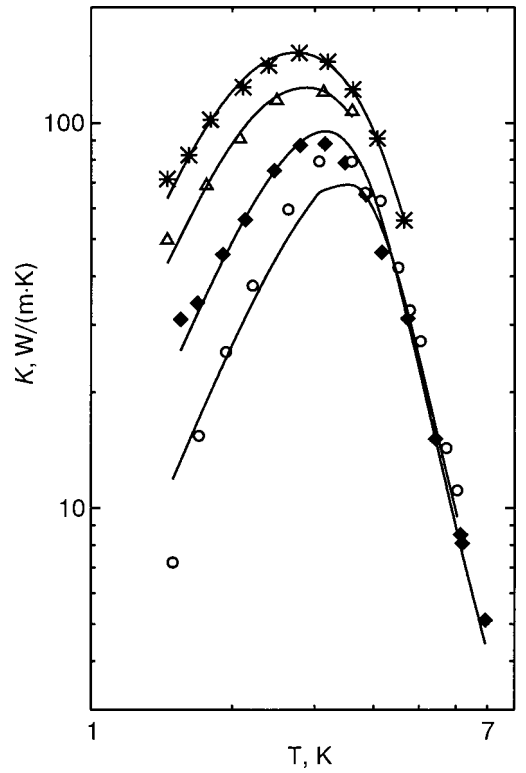

FIG. 3. The temperature dependence of the thermal conductivity of $(p\text{-}H_2)_{(1-c)}(CH_4)_c$. The points are the experimental data: pure hydrogen sample 2 (*); $c=28$ ppm CH_4 (◆); $c=116$ ppm CH_4 (○); $c=500$ ppm CH_4 (△). The solid lines are the best-fit curves.

TABLE I. The best-fit parameters, the phonon mean-free path L (boundary scattering), the HD concentration ξ, and the parameters A_U and E found by analyzing the experimental results for $K(T)$ in different samples of pure p-H_2 and p-H_2–CH_4.

Sample	ξ, ppm	L, mm	A_U, $10^7 K^{-3} s^{-1}$	E, K
p-H_2, sample 1	300±40	0.57±0.05	4.20	36
p-H_2, sample 2	300±40	1.11±0.05	2.11	36
p-H_2+28 ppm CH_4	300±40	0.34±0.05	4.80	36
p-H_2+116 ppm CH_4	300±40	0.17±0.05	4.20	36
p-H_2+500 ppm CH_4	300±40	0.71±0.05	4.20	36

The experimental results were analyzed using Callaway's theory allowing for the special role of normal phonon-phonon scattering processes in the thermal conductivity and using the Debye approximation to describe the phonon spectrum. In solid p-H_2 the resistive processes are due to phonon-phonon scattering, U processes ($\tau_U(x,T)$), scattering by the boundaries of crystalline grains and low-angle boundaries ($\tau_B(x,T)$), and scattering due to isotopic disorder (by HD molecules) ($\tau_I(x,T)$):

$$\tau_R^{-1}(x,T)=\tau_U^{-1}(x,T)+\tau_B^{-1}(x,T)+\tau_I^{-1}(x,T).$$

The characteristics of three-phonon U and N processes are determined only by the properties of the hcp lattice of H_2 and are virtually independent of the impurity molecules at low concentrations:

$$\tau_U^{-1}(x,T)=A_U x^2 T^3 e^{(-E/T)}, \quad \tau_N^{-1}(x,T)=A_N x^2 T^5.$$

The parameters A_U and E depend on the heat flow direction with respect to the **c** axis of the hcp lattice of H_2.[16] The boundary scattering is dependent on the mean crystal grain size L: $\tau_B^{-1}(x,T)=s/L$, where s is the sound speed. The intensity of N processes is taken from[17] ($A_N=6.7\times10^5$ $s^{-1}\cdot K^{-5}$).

The scattering due to isotopic disorder is characterized by the Rayleigh relaxation rate

$$\tau_I^{-1}=\xi\left(\frac{\Delta m}{m_{H_2}}\right)^2\frac{\Omega_0}{4\pi s^3}\omega^4,$$

where ξ is the HD concentration, Ω_0 is the volume per atom, and $\Delta m=1$ for HD impurity in H_2. The fit parameters used to match the calculated curves and the experimental results were the HD concentration ξ and the parameters L, A_U, and E (see Table I). It was assumed for p-H_2–CH_4 samples that the concentration ξ was invariable from sample to sample. Parameter L characterizes the structure of defects in the sample.[18] L varied nearly five-fold (see Table I). This variation of L in samples prepared from the gas mixtures p-H_2–CH_4 indicates that the density of low-angle boundaries in the sample increases as a result of stress appearing when the crystal is grown and cooled.

The new measurements for $K(T)$ in pure p-H_2 have been interpreted as a manifestation of the isotopic effect. $K(T)$ in the samples prepared by depositing gas mixtures $(p\text{-}H_2)_{(1-c)}(CH_4)_c$ in the interval $c=5-570$ ppm at temperatures near the triple point of p-H_2 varied only slightly with concentration. Because of the low solubility of CH_4 in p-H_2 we were unable (unlike in the Kr–CH_4 case) to detect resonance phonon scattering by the rotational excitations of the CH_4 molecules (a dip in the temperature dependence of $K(T)$ of solid H_2 with CH_4 impurity). The upper limit of CH_4 solubility in solid p-H_2 was estimated from the thermal conductivity values. It does not exceed 0.1 ppm.

We are grateful to Professor V. G. Manzhelii and Dr. B. Ya. Gorodilov for helpful discussions. The work described in this paper was made possible in part by grant N 2M/78-2000 from the Ukrainian Ministry of Education and Science.

*E-mail: krivchikov@ilt.kharkov.ua

[1] T. Momose, M. Miki, T. Wakabayashi, T. Shida, M.-Ch. Chan, S. S. Lee, and T. Oka, J. Chem. Phys. **107**, 7707 (1997).
[2] M. Miki and T. Momose, Fiz. Nizk. Temp. **26**, 899 (2000) [Low Temp. Phys. **26**, 661 (2000)].
[3] H. Katsuki and T. Momose, Phys. Rev. Lett. **84**, 3286 (2000).
[4] J. Z. Li, M. Suzuki, M. Katsuragawa, and K. Hakuta, J. Chem. Phys. **115**, 930 (2001).
[5] R. J. Hinde, D. T. Anderson, S. Tam, and M. E. Fajardo, Chem. Phys. Lett. **356**, 355 (2002).
[6] R. W. Hill and B. Schneidmesser, Z. Phys. Chem. (Munich) **16**, 257 (1958).
[7] R. G. Bohn and C. F. Mate, Phys. Rev. B **2**, 2121 (1970).
[8] N. N. Zholonko, B. Ya. Gorodilov, and A. I. Krivchikov, JETP Lett. **55**, 167 (1992).
[9] B. Ya. Gorodilov, O. A. Korolyuk, A. I. Krivchikov, and V. G. Manzhelii, J. Low Temp. Phys. **119**, 497 (2000).
[10] V. G. Manzhelii, B. Ya. Gorodilov, and A. I. Krivchikov, Fiz. Nizk. Temp. **22**, 174 (1996) [Low Temp. Phys. **22**, 131 (1996)].
[11] O. A. Korolyuk, B Ya. Gorodilov, A. I. Krivchikov, and V. G. Manzhelii, Fiz. Nizk. Temp. **25**, 944 (1999) [Low Temp. Phys. **25**, 708 (1999)].
[12] B. Ya. Gorodilov and V. B. Kokshenev, J. Low Temp. Phys. **81**, 45 (1990).
[13] T. N. Antsygina, V. A. Slyusarev, and K. A. Chishko, Zh. Eksp. Teor. Fiz. **87**(2), 555 (1998) [JETP **114**, 303 (1998)].
[14] V. V. Dudkin, B. Ya. Gorodilov, A. I. Krivchikov, and V. G. Manzhelii, Fiz. Nizk. Temp. **26**, 1023 (2000) [Low Temp. Phys. **26**, 762 (2000)].
[15] A. Jeżowski and P. Stachowiak, Cryogenics **32**, 601 (1992).
[16] O. A. Korolyuk, B. Ya. Gorodilov, A. I. Krivchikov, A. S. Pirogov, and V. V. Dudkin, J. Low Temp. Phys. **111**, 515 (1998).
[17] T. N. Antsygina, B. Ya. Gorodilov, N. N. Zholonko, A. I. Krivchikov, and V. G. Manzhelii, Fiz. Nizk. Temp. **18**, 417 (1992) [Low Temp. Phys. **18**, 283 (1992)].
[18] O. A. Korolyuk, A. I. Krivchikov, and B. Ya. Gorodilov, J. Low Temp. Phys. **122**, 203 (2001).

This article was published in English in the original Russian journal Reproduced here with stylistic changes by AIP.